



ROTORCRAFT SMOOTHING VIA LINEAR TIME PERIODIC METHODS

DISSERTATION

Christopher S. Schulz, Captain, USAF

AFIT/DS/ENY/07-10

DEPARTMENT OF THE AIR FORCE  
AIR UNIVERSITY

**AIR FORCE INSTITUTE OF TECHNOLOGY**

Wright-Patterson Air Force Base, Ohio

APPROVED FOR PUBLIC RELEASE; DISTRIBUTION UNLIMITED.

The views expressed in this dissertation are those of the author and do not reflect the official policy or position of the United States Air Force, Department of Defense, or the United States Government.

AFIT/DS/ENY/07-10

# ROTORCRAFT SMOOTHING VIA LINEAR TIME PERIODIC METHODS

## DISSERTATION

Presented to the Faculty

Department of Aeronautical and Astronautical Engineering

Graduate School of Engineering and Management

Air Force Institute of Technology

Air University

Air Education and Training Command

In Partial Fulfillment of the Requirements for the  
Degree of Doctor of Philosophy in Aeronautical Engineering

Christopher S. Schulz, B.S.M.E., B.S.A.E., M.S.A.E.

Captain, USAF

July 2007

APPROVED FOR PUBLIC RELEASE; DISTRIBUTION UNLIMITED.

## ROTORCRAFT SMOOTHING VIA LINEAR TIME PERIODIC METHODS

Christopher S. Schulz, B.S.M.E., B.S.A.E., M.S.A.E.

Captain, USAF

Approved:

_____ Dr. Donald L. Kunz Dissertation Advisor	_____ date
_____ Dr. Raul Ordonez Committee Member	_____ date
_____ Dr. Norman Wereley Committee Member	_____ date
_____ Dr. William L. Wiesel Committee Member	_____ date
_____ Dr. Mark Oxley Deans Representative	_____ date

Accepted:

_____ M. U. Thomas Dean, Graduate School of Engineering and Management	_____ Date
--	---------------

*Abstract*

Helicopter flight, relying on rotary motion of a complex mechanical system, is predisposed to vibration. While the helicopter has many sources of vibrations the main rotor system generates by far the largest magnitude vibrations, and can render the vehicle inoperable if left unaddressed. Thus, proper maintenance to reduce vibrations is essential to the safe operation of any helicopter. This maintenance, however, is costly and time consuming. Improving the maintenance procedure for balancing the main rotor system has been an area of active interest since the inception of the helicopter. However, the state of the art in rotor balancing still requires several iterations of rotor adjustments, each necessitating a separate test flight and then time consuming maintenance, to reduce the vibrational level to an acceptable amount. This research provides the basis for an improved rotor vibrational reduction methodology that significantly reduces the number of adjustment iterations required to reduce main rotor vibrations.

To address these issues, it was the intent of this research to develop an on-line, linear time periodic rotor vibration controller. The Cramer-Rao bound was developed for a linear time periodic system in order to identify the quality of identified system parameters that are used in system models for controller development. The methods developed in this work have allowed model parameters to be verified for accuracy and likewise adjusted to improve controller accuracy. To achieve these goals several steps were undertaken as enumerated below.

1. Describe the methodology defined by Wereley [42] to model a linear system with time periodic coefficients as a state space model, in a manner similar to a linear time invariant system.

2. Develop the Cramer-Rao Bound to validate the parameters of the linear time parametric system in state space form, as in the case of a helicopter rotor model.
3. Model a helicopter rotor system which incorporates time periodic system coefficients to accurately describe the system in forward flight.
4. Using the linear time periodic state space model, perform system identification of the main rotor system to identify the time periodic parameters of the model.
5. Develop an optimal control methodology for a linear time periodic rotor model as to provide a vibration smoothing solution for an unbalanced model.

## *Acknowledgements*

This work is dedicated to Kelly, Chloe, and Oliver, who are known in research circles as the worlds best study partners.

Christopher S. Schulz

## *Table of Contents*

	Page
Abstract . . . . .	iv
Acknowledgements . . . . .	vi
List of Figures . . . . .	x
List of Symbols . . . . .	xviii
List of Abbreviations . . . . .	xix
 I. Introduction . . . . .	 1
1.1 Present Rotor Vibrational Reduction Techniques . . . . .	1
1.2 Current Advances in Rotor Smoothing . . . . .	2
1.3 Research Objectives . . . . .	3
 II. Historical Development for Research in Rotorcraft Smoothing . .	 5
2.1 Smoothing of Rotorcraft Vibrations . . . . .	5
2.1.1 The Need for Rotorcraft Vibration Reduction . .	5
2.1.2 Rotor Smoothing, Track and Balance . . . . .	6
2.1.3 Cause of Rotor Vibrations . . . . .	8
2.2 Rotor Smoothing Methods . . . . .	8
2.2.1 Rotor Adjustment Options . . . . .	8
2.2.2 Historical Methods . . . . .	12
2.2.3 Current Methods . . . . .	16
2.3 Smoothing Performance Of Current Methods . . . . .	20
2.4 Current Method Deficiencies . . . . .	21
2.5 Summary . . . . .	22
 III. Scope of Research . . . . .	 23
3.1 Scope of current research . . . . .	24
3.1.1 Objective 1: Model linear systems with time pe- riodic coefficients as a state space model . . . . .	24
3.1.2 Objective 2: Adapt the Cramer-Rao Bound to Validate the Parameters of the Linear Time Para- metric Rotor Model . . . . .	26
3.1.3 Objective 3: Develop a Parametric Main Rotor System Model . . . . .	29
3.1.4 Objective 4: Perform System Identification of the Main Rotor System . . . . .	29
3.1.5 Objective 5: Develop an LTP Optimal Control Methodology for Rotor Vibration Smoothing . .	30

	Page
IV. Mathematic Foundations of Linear Time Periodic Systems . . . .	33
4.1 The Fourier Series . . . . .	33
4.1.1 Linear Independence, Orthogonality, and Orthonormal Function Sets . . . . .	34
4.1.2 Trigonometric and Complex Forms of the Fourier Series . . . . .	36
4.2 Eigenvalues and Eigenvectors . . . . .	37
4.3 Singular Value Decomposition . . . . .	39
4.4 The Toeplitz Transformation . . . . .	40
V. Linear Time Periodic System Theory . . . . .	43
5.1 The Continuous Time Invariant Linear State Model . . .	43
5.1.1 Transfer Functions for LTI Systems . . . . .	45
5.1.2 Frequency Response for LTI Systems . . . . .	46
5.2 Signal Spaces for LTI and LTP Systems . . . . .	48
5.2.1 Geometrically Periodic Signals . . . . .	50
5.2.2 Exponentially Modulated Periodic Signals . . .	50
5.3 LTP Transfer Functions . . . . .	51
5.3.1 Harmonic Balance . . . . .	52
5.3.2 Harmonic Balance State Space Model . . . . .	54
VI. Linear Time Periodic System Parameter Validation via the Cramer-Rao Lower Bound . . . . .	60
6.1 Introduction . . . . .	60
6.2 General Description of the Cramer-Rao Lower Bound . .	62
6.3 The Maximum Likelihood Estimator . . . . .	63
6.4 The Cramer-Rao Inequality . . . . .	66
6.4.1 Statistical Methods Defined . . . . .	66
6.4.2 The Cramer-Rao Inequality . . . . .	68
6.5 Cramer-Rao Lower Bound for LTI Systems . . . . .	71
6.6 Cramer-Rao Methodology for LTP Systems . . . . .	75
6.6.1 LTP State Space Operator . . . . .	75
6.6.2 Cramer-Rao Definition for LTP Systems . . . .	79
6.7 Illustrative Example . . . . .	83
6.8 Concluding Remarks . . . . .	87
VII. Rotor Vibration Smoothing Using Cramer-Rao Parameter Validation . . . . .	89
7.1 Needed Improvements in Rotor Smoothing Algorithms .	89
7.2 Outline of Cramer-Rao Validated Controller Development	91
7.3 Rotor System LTP Equations of Motion . . . . .	92

	Page
7.4 Design of a Optimal Vibration Attenuation Controller for a Linear Time Periodic Rotor System . . . . .	105
7.5 The Linear Time Periodic Linear Quadratic Regulator . . . . .	105
7.5.1 The Riccati Equation . . . . .	106
7.6 Vibration Reduction via Reference Tracking Control . . . . .	109
7.6.1 Tracking Control Applied to Out of Plane Rotor Vibrations . . . . .	115
7.7 Controller Model Parameter Validation via the Cramer-Rao Bound . . . . .	118
7.7.1 Cramer-Rao Bound Calculation for a LTP Rotor Model . . . . .	118
7.7.2 Cramer-Rao Bounds of Lock Number, $\gamma$ . . . . .	121
7.7.3 Determination of Model Dimension . . . . .	130
7.8 Vibration Controller Validation via the Cramer-Rao Bound . . . . .	130
7.8.1 Vibration Controller Performance Evaluated By Cramer-Rao Bound . . . . .	132
7.9 Concluding Remarks . . . . .	145
VIII. Summary . . . . .	148
8.1 Summary and Conclusions . . . . .	148
8.2 Recommendations for Future Research . . . . .	151
Appendix A. Lock Number Validation Plots via the Cramer-Rao Bound . . . . .	153
Appendix B. Cramer-Rao Bound Plots for an Individual Rotor Blade . . . . .	158
Appendix C. Vibration Controller Comparison Plots, Noise Case $S_v = 1$ . . . . .	162
Appendix D. Vibration Controller Comparison Plots, Noise Case $S_v = 2$ . . . . .	191
Appendix E. Vibration Controller Comparison Plots, Noise Case $S_v = 3$ . . . . .	220
Appendix F. Vibration Controller Comparison Plots, Noise Case $S_v = 4$ . . . . .	249
Appendix G. Cramer-Rao Bound Relationship to Maximum Control Requirements . . . . .	278
Bibliography . . . . .	287

## *List of Figures*

Figure		Page
2.1.	Rotor Blade Tracking [1]. . . . .	7
2.2.	Image of Rotor Blade Split [4]. . . . .	7
2.3.	Blade Weights Applied at the Blade Root [23]. . . . .	9
2.4.	Rotorcraft Pitch Linkage Adjustment [23]. . . . .	10
2.5.	Rotorcraft Dynamic Pitch Linkage [20]. . . . .	11
2.6.	BO 105 Rotor Head With Dynamic Pitch Linkages [20]. . . . .	12
2.7.	Individual Dynamic Pitch Linkage on a BO 105 [20]. . . . .	13
2.8.	Rotor Blade Trim Tab at Trailing Edge [33]. . . . .	14
2.9.	Biological Neural Network [21]. . . . .	18
2.10.	Artificial Neural Network [21]. . . . .	19
3.1.	Multiharmonic Response of an LTP System [20]. . . . .	26
3.2.	Example of Cramer-Rao Bounds for Parameter Estimates [34].	28
4.1.	Sinusoidal input functions [22]. . . . .	34
4.2.	Periodic non-sinusoidal input signal [22]. . . . .	35
5.1.	Principal Gains of a MIMO LTI system [2]. . . . .	48
5.2.	A Simple LTP System [42]. . . . .	49
6.1.	Example of Cramer-Rao Bounds for Parameter Estimates [34].	64
6.2.	Example of a simple LTP system represented by a modulating gain. . . . .	76
6.3.	Multiharmonic Response of an LTP System [20]. . . . .	81
6.4.	Example LTP system with time invariant A,C matrices and time periodic B(t) matrix. . . . .	83
6.5.	Cramer-Rao bound of the system in Equation 6.52 with respect to the parameter $\zeta$ . . . . .	85
6.6.	Values of $\zeta$ derived by system identification at input frequency $\omega_f$ with superimposed Cramer-Rao bounds. . . . .	86

Figure		Page
7.1.	Diagram of AH-64 rotor system [14]. . . . .	93
7.2.	Rigid Rotor Blade Flapping Moments [16]. . . . .	95
7.3.	Reference Tracking Controller Block Diagram. . . . .	111
7.4.	Individual Flap Angles of the Four Blades. . . . .	116
7.5.	Combined Flap Angles of the Four Blades. . . . .	117
7.6.	Cramer-Rao Bounds for all Frequencies, $\omega_f$ , all Noise Values, $S_v$ . . . . .	123
7.7.	Cramer-Rao Bounds for all Frequencies, $\omega_f$ , at Noise Value, $S_v = 4$ . . . . .	125
7.8.	Cramer-Rao Bounds for all Frequencies, $\omega_f$ , at Noise Value, $S_v = 1$ . . . . .	126
7.9.	Cramer-Rao Bounds vs. Data Scatter of 100 runs for all Frequencies, $\omega_f$ , at Noise Value, $S_v = 1$ . . . . .	128
7.10.	Cramer-Rao Bounds vs. Data Scatter of 100 runs for all Frequencies, $\omega_f$ , at Noise Value, $S_v = 4$ . . . . .	129
7.11.	Blade Flapping Angles For an Unbalanced Rotor. . . . .	134
7.12.	Summation of the Blade Flapping Angles For an Unbalanced Rotor. . . . .	135
7.13.	Best Case: Tracking Performance of Vibration Controller for case $\omega_f = 0.5\omega_p$ , $S_v = 1$ . . . . .	137
7.14.	Worst Case: Tracking Performance of Vibration Controller for case $\omega_f = 0.0\omega_p$ , $S_v = 4$ . . . . .	138
7.15.	Best Case: Control Usage for case $\omega_f = 0.5\omega_p$ , $S_v = 1$ . . . . .	139
7.16.	Worst Case: Control Usage for case $\omega_f = 0.0\omega_p$ , $S_v = 4$ . . . . .	140
7.17.	Comparison of Cramer-Rao Bound to Maximum Negative Control Deflection For Blade 4: $\omega_f = \omega_p(0, 0.05, 0.1, 0.2, 0.3, 0.4, 0.5)$ , $S_v = 1$ . . . . .	142
7.18.	Comparison of Cramer-Rao Bound to Maximum Negative Control Deflection For Blade 4: $\omega_f = \omega_p(0, 0.05, 0.1, 0.2, 0.3, 0.4, 0.5)$ , $S_v = 1, 2, 3, 4$ . . . . .	143
A.1.	Comparison of Identified Lock Number to Cramer-Rao Bound, $S_v = 1$ . . . . .	154

Figure		Page
A.2.	Comparison of Identified Lock Number to Cramer-Rao Bound, $S_v = 2$ . . . . .	155
A.3.	Comparison of Identified Lock Number to Cramer-Rao Bound, $S_v = 3$ . . . . .	156
A.4.	Comparison of Identified Lock Number to Cramer-Rao Bound, $S_v = 4$ . . . . .	157
B.1.	Cramer-Rao Bound of Blade, $S_v = 1$ . . . . .	158
B.2.	Cramer-Rao Bound of Blade, $S_v = 2$ . . . . .	159
B.3.	Cramer-Rao Bound of Blade, $S_v = 3$ . . . . .	160
B.4.	Cramer-Rao Bound of Blade, $S_v = 4$ . . . . .	161
C.1.	Individual Flap Angles, $\beta$ , for case $\omega_f = 0.5\omega_p$ , $S_v = 1$ . . . . .	163
C.2.	All LQR Gains for case $\omega_f = 0.5\omega_p$ , $S_v = 1$ . . . . .	164
C.3.	Control Usage for case $\omega_f = 0.5\omega_p$ , $S_v = 1$ . . . . .	165
C.4.	Tracking Performance of Vibration Controller for case $\omega_f = 0.5\omega_p$ , $S_v =$ 1 . . . . .	166
C.5.	Individual Flap Angles, $\beta$ , for case $\omega_f = 0.4\omega_p$ , $S_v = 1$ . . . . .	167
C.6.	All LQR Gains for case $\omega_f = 0.4\omega_p$ , $S_v = 1$ . . . . .	168
C.7.	Control Usage for case $\omega_f = 0.4\omega_p$ , $S_v = 1$ . . . . .	169
C.8.	Tracking Performance of Vibration Controller for case $\omega_f = 0.4\omega_p$ , $S_v =$ 1 . . . . .	170
C.9.	Individual Flap Angles, $\beta$ , for case $\omega_f = 0.3\omega_p$ , $S_v = 1$ . . . . .	171
C.10.	All LQR Gains for case $\omega_f = 0.3\omega_p$ , $S_v = 1$ . . . . .	172
C.11.	Control Usage for case $\omega_f = 0.3\omega_p$ , $S_v = 1$ . . . . .	173
C.12.	Tracking Performance of Vibration Controller for case $\omega_f = 0.3\omega_p$ , $S_v =$ 1 . . . . .	174
C.13.	Individual Flap Angles, $\beta$ , for case $\omega_f = 0.2\omega_p$ , $S_v = 1$ . . . . .	175
C.14.	All LQR Gains for case $\omega_f = 0.2\omega_p$ , $S_v = 1$ . . . . .	176
C.15.	Control Usage for case $\omega_f = 0.2\omega_p$ , $S_v = 1$ . . . . .	177
C.16.	Tracking Performance of Vibration Controller for case $\omega_f = 0.2\omega_p$ , $S_v =$ 1 . . . . .	178

Figure		Page
C.17.	Individual Flap Angles, $\beta$ , for case $\omega_f = 0.1\omega_p$ , $S_v = 1$ . . . . .	179
C.18.	All LQR Gains for case $\omega_f = 0.1\omega_p$ , $S_v = 1$ . . . . .	180
C.19.	Control Usage for case $\omega_f = 0.1\omega_p$ , $S_v = 1$ . . . . .	181
C.20.	Tracking Performance of Vibration Controller for case $\omega_f = 0.1\omega_p$ , $S_v = 1$ . . . . .	182
C.21.	Individual Flap Angles, $\beta$ , for case $\omega_f = 0.05\omega_p$ , $S_v = 1$ . . . . .	183
C.22.	All LQR Gains for case $\omega_f = 0.05\omega_p$ , $S_v = 1$ . . . . .	184
C.23.	Control Usage for case $\omega_f = 0.05\omega_p$ , $S_v = 1$ . . . . .	185
C.24.	Tracking Performance of Vibration Controller for case $\omega_f = 0.05\omega_p$ , $S_v = 1$ . . . . .	186
C.25.	Individual Flap Angles, $\beta$ , for case $\omega_f = 0.0\omega_p$ , $S_v = 1$ . . . . .	187
C.26.	All LQR Gains for case $\omega_f = 0.0\omega_p$ , $S_v = 1$ . . . . .	188
C.27.	Control Usage for case $\omega_f = 0.0\omega_p$ , $S_v = 1$ . . . . .	189
C.28.	Tracking Performance of Vibration Controller for case $\omega_f = 0.0\omega_p$ , $S_v = 1$ . . . . .	190
D.1.	Individual Flap Angles, $\beta$ , for case $\omega_f = 0.5\omega_p$ , $S_v = 2$ . . . . .	192
D.2.	All LQR Gains for case $\omega_f = 0.5\omega_p$ , $S_v = 2$ . . . . .	193
D.3.	Control Usage for case $\omega_f = 0.5\omega_p$ , $S_v = 2$ . . . . .	194
D.4.	Tracking Performance of Vibration Controller for case $\omega_f = 0.5\omega_p$ , $S_v = 2$ . . . . .	195
D.5.	Individual Flap Angles, $\beta$ , for case $\omega_f = 0.4\omega_p$ , $S_v = 2$ . . . . .	196
D.6.	All LQR Gains for case $\omega_f = 0.4\omega_p$ , $S_v = 2$ . . . . .	197
D.7.	Control Usage for case $\omega_f = 0.4\omega_p$ , $S_v = 2$ . . . . .	198
D.8.	Tracking Performance of Vibration Controller for case $\omega_f = 0.4\omega_p$ , $S_v = 2$ . . . . .	199
D.9.	Individual Flap Angles, $\beta$ , for case $\omega_f = 0.3\omega_p$ , $S_v = 2$ . . . . .	200
D.10.	All LQR Gains for case $\omega_f = 0.3\omega_p$ , $S_v = 2$ . . . . .	201
D.11.	Control Usage for case $\omega_f = 0.3\omega_p$ , $S_v = 2$ . . . . .	202

Figure		Page
D.12.	Tracking Performance of Vibration Controller for case $\omega_f = 0.3\omega_p$ , $S_v = 2$ . . . . .	203
D.13.	Individual Flap Angles, $\beta$ , for case $\omega_f = 0.2\omega_p$ , $S_v = 2$ . . . . .	204
D.14.	All LQR Gains for case $\omega_f = 0.2\omega_p$ , $S_v = 2$ . . . . .	205
D.15.	Control Usage for case $\omega_f = 0.2\omega_p$ , $S_v = 2$ . . . . .	206
D.16.	Tracking Performance of Vibration Controller for case $\omega_f = 0.2\omega_p$ , $S_v = 2$ . . . . .	207
D.17.	Individual Flap Angles, $\beta$ , for case $\omega_f = 0.1\omega_p$ , $S_v = 2$ . . . . .	208
D.18.	All LQR Gains for case $\omega_f = 0.1\omega_p$ , $S_v = 2$ . . . . .	209
D.19.	Control Usage for case $\omega_f = 0.1\omega_p$ , $S_v = 2$ . . . . .	210
D.20.	Tracking Performance of Vibration Controller for case $\omega_f = 0.1\omega_p$ , $S_v = 2$ . . . . .	211
D.21.	Individual Flap Angles, $\beta$ , for case $\omega_f = 0.05\omega_p$ , $S_v = 2$ . . . . .	212
D.22.	All LQR Gains for case $\omega_f = 0.05\omega_p$ , $S_v = 2$ . . . . .	213
D.23.	Control Usage for case $\omega_f = 0.05\omega_p$ , $S_v = 2$ . . . . .	214
D.24.	Tracking Performance of Vibration Controller for case $\omega_f = 0.05\omega_p$ , $S_v = 2$ . . . . .	215
D.25.	Individual Flap Angles, $\beta$ , for case $\omega_f = 0.0\omega_p$ , $S_v = 2$ . . . . .	216
D.26.	All LQR Gains for case $\omega_f = 0.0\omega_p$ , $S_v = 2$ . . . . .	217
D.27.	Control Usage for case $\omega_f = 0.0\omega_p$ , $S_v = 2$ . . . . .	218
D.28.	Tracking Performance of Vibration Controller for case $\omega_f = 0.0\omega_p$ , $S_v = 2$ . . . . .	219
E.1.	Individual Flap Angles, $\beta$ , for case $\omega_f = 0.5\omega_p$ , $S_v = 3$ . . . . .	221
E.2.	All LQR Gains for case $\omega_f = 0.5\omega_p$ , $S_v = 3$ . . . . .	222
E.3.	Control Usage for case $\omega_f = 0.5\omega_p$ , $S_v = 3$ . . . . .	223
E.4.	Tracking Performance of Vibration Controller for case $\omega_f = 0.5\omega_p$ , $S_v = 3$ . . . . .	224
E.5.	Individual Flap Angles, $\beta$ , for case $\omega_f = 0.4\omega_p$ , $S_v = 3$ . . . . .	225
E.6.	All LQR Gains for case $\omega_f = 0.4\omega_p$ , $S_v = 3$ . . . . .	226

Figure		Page
E.7.	Control Usage for case $\omega_f = 0.4\omega_p$ , $S_v = 3$ . . . . .	227
E.8.	Tracking Performance of Vibration Controller for case $\omega_f = 0.4\omega_p$ , $S_v = 3$ . . . . .	228
E.9.	Individual Flap Angles, $\beta$ , for case $\omega_f = 0.3\omega_p$ , $S_v = 3$ . . . . .	229
E.10.	All LQR Gains for case $\omega_f = 0.3\omega_p$ , $S_v = 3$ . . . . .	230
E.11.	Control Usage for case $\omega_f = 0.3\omega_p$ , $S_v = 3$ . . . . .	231
E.12.	Tracking Performance of Vibration Controller for case $\omega_f = 0.3\omega_p$ , $S_v = 3$ . . . . .	232
E.13.	Individual Flap Angles, $\beta$ , for case $\omega_f = 0.2\omega_p$ , $S_v = 3$ . . . . .	233
E.14.	All LQR Gains for case $\omega_f = 0.2\omega_p$ , $S_v = 3$ . . . . .	234
E.15.	Control Usage for case $\omega_f = 0.2\omega_p$ , $S_v = 3$ . . . . .	235
E.16.	Tracking Performance of Vibration Controller for case $\omega_f = 0.2\omega_p$ , $S_v = 3$ . . . . .	236
E.17.	Individual Flap Angles, $\beta$ , for case $\omega_f = 0.1\omega_p$ , $S_v = 3$ . . . . .	237
E.18.	All LQR Gains for case $\omega_f = 0.1\omega_p$ , $S_v = 3$ . . . . .	238
E.19.	Control Usage for case $\omega_f = 0.1\omega_p$ , $S_v = 3$ . . . . .	239
E.20.	Tracking Performance of Vibration Controller for case $\omega_f = 0.1\omega_p$ , $S_v = 3$ . . . . .	240
E.21.	Individual Flap Angles, $\beta$ , for case $\omega_f = 0.05\omega_p$ , $S_v = 3$ . . . . .	241
E.22.	All LQR Gains for case $\omega_f = 0.05\omega_p$ , $S_v = 3$ . . . . .	242
E.23.	Control Usage for case $\omega_f = 0.05\omega_p$ , $S_v = 3$ . . . . .	243
E.24.	Tracking Performance of Vibration Controller for case $\omega_f = 0.05\omega_p$ , $S_v = 3$ . . . . .	244
E.25.	Individual Flap Angles, $\beta$ , for case $\omega_f = 0.0\omega_p$ , $S_v = 3$ . . . . .	245
E.26.	All LQR Gains for case $\omega_f = 0.0\omega_p$ , $S_v = 3$ . . . . .	246
E.27.	Control Usage for case $\omega_f = 0.0\omega_p$ , $S_v = 3$ . . . . .	247
E.28.	Tracking Performance of Vibration Controller for case $\omega_f = 0.0\omega_p$ , $S_v = 3$ . . . . .	248
F.1.	Individual Flap Angles, $\beta$ , for case $\omega_f = 0.5\omega_p$ , $S_v = 4$ . . . . .	250

Figure		Page
F.2.	All LQR Gains for case $\omega_f = 0.5\omega_p$ , $S_v = 4$ . . . . .	251
F.3.	Control Usage for case $\omega_f = 0.5\omega_p$ , $S_v = 4$ . . . . .	252
F.4.	Tracking Performance of Vibration Controller for case $\omega_f = 0.5\omega_p$ , $S_v = 4$ . . . . .	253
F.5.	Individual Flap Angles, $\beta$ , for case $\omega_f = 0.4\omega_p$ , $S_v = 4$ . . . . .	254
F.6.	All LQR Gains for case $\omega_f = 0.4\omega_p$ , $S_v = 4$ . . . . .	255
F.7.	Control Usage for case $\omega_f = 0.4\omega_p$ , $S_v = 4$ . . . . .	256
F.8.	Tracking Performance of Vibration Controller for case $\omega_f = 0.4\omega_p$ , $S_v = 4$ . . . . .	257
F.9.	Individual Flap Angles, $\beta$ , for case $\omega_f = 0.3\omega_p$ , $S_v = 4$ . . . . .	258
F.10.	All LQR Gains for case $\omega_f = 0.3\omega_p$ , $S_v = 4$ . . . . .	259
F.11.	Control Usage for case $\omega_f = 0.3\omega_p$ , $S_v = 4$ . . . . .	260
F.12.	Tracking Performance of Vibration Controller for case $\omega_f = 0.3\omega_p$ , $S_v = 4$ . . . . .	261
F.13.	Individual Flap Angles, $\beta$ , for case $\omega_f = 0.2\omega_p$ , $S_v = 4$ . . . . .	262
F.14.	All LQR Gains for case $\omega_f = 0.2\omega_p$ , $S_v = 4$ . . . . .	263
F.15.	Control Usage for case $\omega_f = 0.2\omega_p$ , $S_v = 4$ . . . . .	264
F.16.	Tracking Performance of Vibration Controller for case $\omega_f = 0.2\omega_p$ , $S_v = 4$ . . . . .	265
F.17.	Individual Flap Angles, $\beta$ , for case $\omega_f = 0.1\omega_p$ , $S_v = 4$ . . . . .	266
F.18.	All LQR Gains for case $\omega_f = 0.1\omega_p$ , $S_v = 4$ . . . . .	267
F.19.	Control Usage for case $\omega_f = 0.1\omega_p$ , $S_v = 4$ . . . . .	268
F.20.	Tracking Performance of Vibration Controller for case $\omega_f = 0.1\omega_p$ , $S_v = 4$ . . . . .	269
F.21.	Individual Flap Angles, $\beta$ , for case $\omega_f = 0.05\omega_p$ , $S_v = 4$ . . . . .	270
F.22.	All LQR Gains for case $\omega_f = 0.05\omega_p$ , $S_v = 4$ . . . . .	271
F.23.	Control Usage for case $\omega_f = 0.05\omega_p$ , $S_v = 4$ . . . . .	272
F.24.	Tracking Performance of Vibration Controller for case $\omega_f = 0.05\omega_p$ , $S_v = 4$ . . . . .	273

Figure		Page
F.25.	Individual Flap Angles, $\beta$ , for case $\omega_f = 0.0\omega_p$ , $S_v = 4$ . . . . .	274
F.26.	All LQR Gains for case $\omega_f = 0.0\omega_p$ , $S_v = 4$ . . . . .	275
F.27.	Control Usage for case $\omega_f = 0.0\omega_p$ , $S_v = 4$ . . . . .	276
F.28.	Tracking Performance of Vibration Controller for case $\omega_f = 0.0\omega_p$ , $S_v = 4$ . . . . .	277
G.1.	Comparison of Cramer-Rao Bound to Maximum Negative Control Deflection For Blade 1: $\omega_f = \omega_p(0, 0.05, 0.1, 0.2, 0.3, 0.4, 0.5)$ , $S_v = 1$ . . . . .	279
G.2.	Comparison of Cramer-Rao Bound to Maximum Negative Control Deflection For Blade 1: $\omega_f = \omega_p(0, 0.05, 0.1, 0.2, 0.3, 0.4, 0.5)$ , $S_v = 1, 2, 3, 4$ . . . . .	280
G.3.	Comparison of Cramer-Rao Bound to Maximum Negative Control Deflection For Blade 2: $\omega_f = \omega_p(0, 0.05, 0.1, 0.2, 0.3, 0.4, 0.5)$ , $S_v = 1$ . . . . .	281
G.4.	Comparison of Cramer-Rao Bound to Maximum Negative Control Deflection For Blade 2: $\omega_f = \omega_p(0, 0.05, 0.1, 0.2, 0.3, 0.4, 0.5)$ , $S_v = 1, 2, 3, 4$ . . . . .	282
G.5.	Comparison of Cramer-Rao Bound to Maximum Negative Control Deflection For Blade 3: $\omega_f = \omega_p(0, 0.05, 0.1, 0.2, 0.3, 0.4, 0.5)$ , $S_v = 1$ . . . . .	283
G.6.	Comparison of Cramer-Rao Bound to Maximum Negative Control Deflection For Blade 3: $\omega_f = \omega_p(0, 0.05, 0.1, 0.2, 0.3, 0.4, 0.5)$ , $S_v = 1, 2, 3, 4$ . . . . .	284
G.7.	Comparison of Cramer-Rao Bound to Maximum Negative Control Deflection For Blade 4: $\omega_f = \omega_p(0, 0.05, 0.1, 0.2, 0.3, 0.4, 0.5)$ , $S_v = 1$ . . . . .	285
G.8.	Comparison of Cramer-Rao Bound to Maximum Negative Control Deflection For Blade 4: $\omega_f = \omega_p(0, 0.05, 0.1, 0.2, 0.3, 0.4, 0.5)$ , $S_v = 1, 2, 3, 4$ . . . . .	286

## *List of Symbols*

Symbol		Page
$\omega_p$	Pumping Frequency . . . . .	33
$\delta$	Kronecker Delta . . . . .	35
$e^{At}$	Matrix Exponential function . . . . .	37
$\lambda$	Eigenvalue . . . . .	38
$\zeta$	Eigenvector . . . . .	38
$[\lambda I - A]$	Resolvent Matrix . . . . .	38
$\Delta(\lambda)$	characteristic polynomial . . . . .	38
$\mathbb{C}^{m \times n}$	set of complex $m \times n$ matrices . . . . .	39
$\dagger$	transpose operator . . . . .	40
$\sigma$	set of singular values . . . . .	40
$\mathcal{T}$	Toeplitz Transform . . . . .	41
$\Phi(t, t_0)$	State Transition matrix . . . . .	44
$\mathcal{L}$	Laplace Transform . . . . .	45
$u_0 e^{st}$	exponentially modulated sinusoid . . . . .	46
$\omega_f$	sinusoidal input signal . . . . .	48
$\psi(t)$	parametric excitation . . . . .	53
$\beta$	Flap angle . . . . .	94
$\rho$	Air Density Coefficient . . . . .	96
$\gamma$	Lock number . . . . .	96
$\Theta$	Blade pitch angle . . . . .	97
$\psi$	Rotor azimuth . . . . .	97
$\mu$	Rotor advance ratio, $\frac{V \cos \alpha}{\Omega R}$ . . . . .	97
$\lambda$	Rotor inflow ratio, $\frac{V \sin \alpha + \nu}{\Omega R}$ . . . . .	97
$\Theta_{con}$	Control input for blade pitch . . . . .	98
$\Theta_{tw}$	Blade twist . . . . .	98

## *List of Abbreviations*

Abbreviation		Page
AVA	Aviation Vibration Analyzer . . . . .	2
VMEP	Vibration Management Enhancement Program . . . . .	2
1/Per	Once Per Revolution Vibration . . . . .	8
HHC	Higher Harmonic Control . . . . .	8
LTI	Linear Time Invariant . . . . .	25
LTP	Linear Time Periodic . . . . .	25
FFT	Fast Fourier Transform . . . . .	30
T	System period . . . . .	33
SVD	Singular Value Decomposition . . . . .	39
$x(t)$	System State vector . . . . .	43
$A(t)$	State Matrix . . . . .	43
$u(t)$	System Control vector . . . . .	43
$B(t)$	Control Matrix . . . . .	43
$C(t)$	Output Matrix . . . . .	43
$D(t)$	Feed Forward Matrix . . . . .	43
$g(t)$	time domain impulse response matrix . . . . .	45
$G(s)$	Laplace Transfer function . . . . .	45
SISO	Single Input-Single Output . . . . .	46
$ G(s) $	System magnitude . . . . .	46
$\angle(G(s))$	Phase angle . . . . .	47
MIMO	Multi Input-Multi Output . . . . .	47
GP	Geometrically Periodic Signal . . . . .	50
EMP	Exponentially Modulated Periodic Signal . . . . .	51
q	pumping amplitude . . . . .	53
MLE	Maximum Likelihood Estimator . . . . .	62

Abbreviation		Page
$iid$	Independent and Identically Distributed random values . .	63
pdf	Probability density function . . . . .	64
R	Prediction error covariance matrix . . . . .	65
$E_X, \mu_X$	Expected Values . . . . .	66
$Var X, \sigma_X^2$	Variance . . . . .	66
$Cov(X, Y)$	Covariance . . . . .	66
I	Identity matrix . . . . .	70
M	Fisher Information Matrix . . . . .	70
LQR	Linear Quadratic Regulator . . . . .	89
$I_b$	Blade moment of inertia . . . . .	96
a	blade section two dimensional lift curve slope . . . . .	96
c	Blade chord width . . . . .	96
$M_F$	Aerodynamic flap moment . . . . .	96
$U_T$	Air velocity of the blade section, tangential to the rotor disk	97
$U_P$	Air velocity of the blade section, perpendicular to the rotor disk . . . . .	97
$B_u$	Controllable input matrix . . . . .	106
J	Quadratic cost function . . . . .	106
<b>Q,H</b>	State weighting matrix . . . . .	106
<b>R</b>	Control weighting matrix . . . . .	106
<b>P(t)</b>	Costate proportionality matrix . . . . .	106
<b>K(t)</b>	Time varying gain matrix for LTI systems . . . . .	107
$\mathcal{K}(t)$	Time periodic gain matrix . . . . .	108
$e$	Error state . . . . .	109
r	Reference input . . . . .	109
$C_m$	Measurement output matrix . . . . .	109
$C_y$	State output matrix . . . . .	109

## I. Introduction

Helicopter flight, relying on rotary motion of a complex mechanical system, is predisposed to vibration. While the helicopter has many sources of vibrations the main rotor system generates by far the largest magnitude vibrations, and can render the vehicle inoperable if left unaddressed. Thus, proper maintenance to reduce vibrations is essential to the safe operation of any helicopter. This maintenance, however, is costly and time consuming.

Improving the maintenance procedure for balancing the main rotor system has been an area of active interest since the inception of the helicopter. However, the state of the art in rotor balancing still requires several iterations of rotor adjustments, each necessitating a separate test flight and then time consuming maintenance, to reduce the vibrational level to an acceptable amount. The intent of this research is to provide an improved rotor vibrational adjustment methodology that significantly reduces the number of adjustment iterations required to reduce main rotor vibrations.

### 1.1 *Present Rotor Vibrational Reduction Techniques*

Vibrations of the largest magnitude in the main rotor system are primarily the result of unbalanced hub mass and aerodynamic forces. These forces are the result of the individual blades exhibiting unequal lift forces as they perform one complete rotation about the system hub. By summing the resulting forces of each blade about the entire azimuth of the main rotor a resultant force is determined that nutates about the main rotational axis, thus creating a vibration. Vibrational reduction is performed by adjusting individual main rotor blades to balance out the lift forces. Historically, this maintenance was referred to as *track and balance* as the general idea was to adjust the rotor blades so each blade's tip followed the same path, or 'track'. With each tip following in the same plane of rotation, the idea was that each blade

would then produce the same lift. This is based on the assumption that if the blades are identical then identical loads will be imparted on each blade that follows a common track. Identical blades, however, do not truly exist and thus track and balance is not ideal for eliminating vibrations. Modern rotorcraft vibration reduction methods rely on adjustments to each blade to reduce measured vibrations. This method is referred to as rotor *smoothing* as blade adjustments are made to 'smooth' the overall system vibration to an acceptable level.

## ***1.2 Current Advances in Rotor Smoothing***

Rotor smoothing relies on a defined mapping from blade adjustment space to system vibration space in order to reduce overall system vibrations. Historic rotor smoothing methods have relied on empirically determined non-parametric linear mappings to compute a rotor balance adjustment solution to minimize main rotor vibrations. Examples of such an approach are the US Army Aviation Vibration Analyzer (AVA) system [1]. These methods, while performing better than simple track and balance, produce inaccurate blade adjustment solutions as the mappings do not completely represent the system under test. The focus of current research has been to improve the system response mapping, as inaccurate mappings result in the iterative adjustments that rotor smoothing is plagued with.

One suggested approach to improving the system mapping is to replace the linear non-parametric mapping by a non-linear neural network model. This model has been successfully applied to the US Army Vibration Management Enhancement Program (VMEP) program [6]. While this method has been shown to outperform AVA, it relies on a non parametric mapping, which precludes any attempt to identify modeling errors by reviewing the model parameters for accuracy. By identifying incorrectly identified model parameters, the VMEP approach has the ability to correct inaccurate mappings. This will ultimately reduce the iterations exhibited by current approaches as the result of using a more accurate model for control solution development.

### **1.3 Research Objectives**

It is the intent of this research to develop a linear parametric mapping based method for rotor vibrational adjustment in which individual model parameters can be verified for accuracy and likewise adjusted to improve model accuracy. To achieve these goals several steps will be undertaken as enumerated below.

**Objective 1: Replace the non parametric mapping of the rotor system dynamics with a parametric approach applicable to system identification methods.** This step will describe the methodology defined by Wereley [42] to model a linear system with time periodic coefficients as a state space model, in a manner similar to a linear time invariant system.

**Objective 2: Adapt the Cramer-Rao Bound to Validate the Parameters of the Linear Time Parametric Rotor Model.** The Cramer-Rao Bound is a method commonly used in flight testing to establish the accuracy of identified parameters of a linearized vehicle model. The effort of this step is to develop a method to adopt the Cramer-Rao bound to the parametric model defined by Objective 1.

**Objective 3: Develop a Parametric Main Rotor System Model.** The next step in achieving the proposed research goals is to develop a parametric time periodic main rotor system model for the purposes of simulation. The model will include dynamically actuated and fixed pitch linkages for each blade so it will be possible to explore both static and dynamic smoothing cases.

**Objective 4: Perform System Identification of the Main Rotor System.** This step in the proposed research goals is to adapt a system identification technique to determine the dynamics of the main rotor in both hover and forward flight. An accurate rotor model is necessary for the development of an effective vibration controller, as will be done as the final objective in this research.

**Objective 5: Develop a Control Methodology for Rotor Vibration Smoothing.** The final objective of this research is to develop a robust controller capable of attenuating the hub vibrations caused by aerodynamic imbalances of the

rotor system. The control methodology must be adaptable to the periodic nature of the helicopter rotor model in forward flight. This will use the verified model developed by objectives 1-4.

The presentation of this work is now described. The next chapter presents the historical developments of rotorcraft smoothing. This is to familiarize the reader with the successes, but more importantly, the deficiencies with the existing rotor vibration reduction methods.

## II. Historical Development for Research in Rotorcraft Smoothing

The practice of reducing main rotor induced vibrations in rotorcraft has been around since the first helicopters were developed. This chapter presents a brief history of the evolution of these practices with the intent of highlighting their successes and deficiencies. Recommendations to overcome the existing deficiencies of the methods covered in this chapter are presented as a basis for the work this research will undertake.

### *2.1 Smoothing of Rotorcraft Vibrations*

In this Section we discuss the effects of vibrations on a rotorcraft and the methods that exist to reduce them.

#### *2.1.1 The Need for Rotorcraft Vibration Reduction.*

Helicopters, as with any rotating system generate an oscillatory vibration whenever the forces acting on the system are imbalanced. This phenomenon is commonplace, as all who have driven an automobile have experienced the vibrations of an unbalanced tire. This problem is not only an annoying disturbance to the driver, but if left untended to can lead to costly repairs. In the case of the automobile the proper maintenance required is simply to rebalance the tire by determining the magnitude of the disturbance force and at what phase of rotation does it occur. A mass that generates an equal magnitude force is placed 180 degrees out of phase with the disturbance. This procedure is repeated until the measured vibrations are below a predetermined threshold.

The vibrations exhibited by a helicopter's rotating blade systems, being either the main or tail rotor, are similar in concept to the automotive example above. These vibrations generate the highest magnitude vibrations in the airframe and must be balanced out to prevent crew fatigue, premature airframe fatigue, and catastrophic system failures. The balancing procedure for a helicopter is in principal the same as

for balancing a tire, but the disturbance forces are slightly different and the system complexity is greater and must be considered. The rotating automotive tire has only imbalanced inertial forces to cause a vibration, whereas the helicopter must also contend with aerodynamic force imbalance caused by the individual blades. The aerodynamic forces can also vary periodically as the helicopter transitions from a hover state to a forward flight state. Aerodynamic disturbance forces are corrected by adjusting the angle of attack on the requisite blades as required to meet magnitude and phase requirements. These adjustments can be made by changing the length of a pitch linkage or by adjusting a trim tab on a blade. By changing the length of the pitch linkage for a particular blade the pitch of the blade is adjusted for the entire blade, whereas an adjustment to a trim tab adjusts the camber of the blade at the portion the blade in which it is attached. This procedure is generally referred to as *Track and Balance* or more commonly *Rotor Smoothing*.

Rotational vibrations in helicopters generate three distinct problems; increased maintenance downtime, flight crew fatigue, and increased vehicle life cycle costs. Renzi [33] emphasizes the financial impact of performing maintenance to alleviate them. He points out that the cost of rotor smoothing maintenance is not considered as a significant cost driver during vehicle acquisition but becomes one of the most costly operations in the vehicle's lifespan. A more efficient method of rotor smoothing will greatly improve the operational availability of the vehicle, crew alertness, and significantly reduce the maintenance cost of the vehicle over its lifetime.

### 2.1.2 *Rotor Smoothing, Track and Balance.*

There are two common terms used to define the process of alleviating helicopter 1 per revolution rotor vibrations and will now be addressed to alleviate any confusion. The first, *track and balance*, is a more historical term used when reducing rotor vibrations. The term arises from the earliest methods of rotor vibration reduction when the blades of the helicopter were adjusted so their individual blade tips are aligned in the same plane of rotation. This approach noted the difference in vertical spacing

between the individual blade tips, usually by marking them in different colors. The individual blade spacings were noted, then the necessary adjustments to each blade are made to bring the blade tips into alignment in the same plane, or as commonly referred to, in the same 'track'. An example of this is depicted in Figures 2.1 and 2.2. This was the first method to attempt to balance the aerodynamic forces of each blade [33,35].

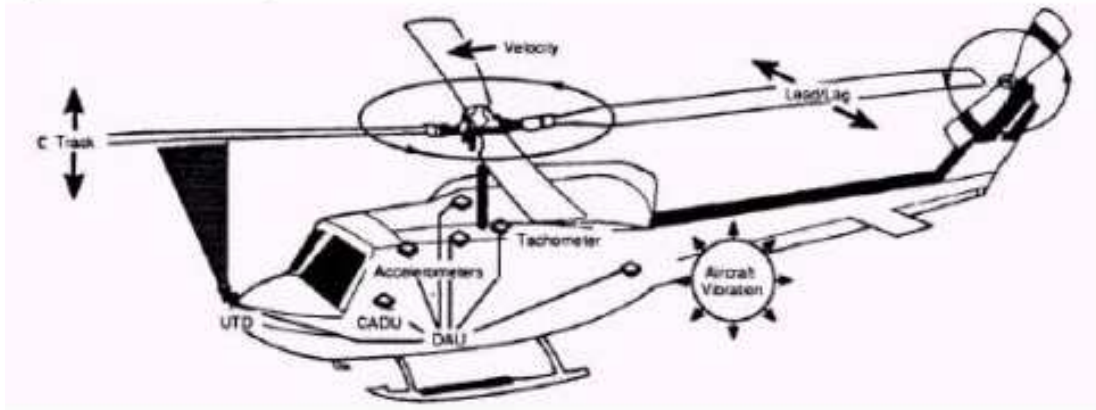


Figure 2.1: Rotor Blade Tracking [1].

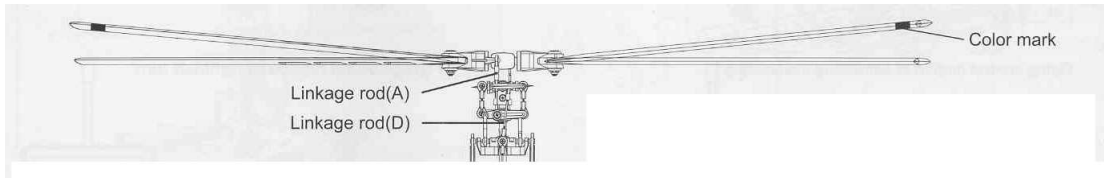


Figure 2.2: Image of Rotor Blade Split [4].

The second term used when defining rotor vibration alleviation is *smoothing*. This term more accurately defines the modern process of vibration alleviation as the requirement to force the blades to track in the same plane of rotation is relaxed. This process usually relies on performing individual blade adjustments that will reduce the overall chassis vibrations [39]. Taitel notes that since the reduction of rotor vibrations are the main goal of rotor smoothing, the tracking of each blade may not be perfect, as the adjustment to reduce vibrations may result in a split track. Rotor smoothing

views the requirement of perfect tracking as aesthetic and not necessary for reduced vibration levels.

*2.1.3 Cause of Rotor Vibrations.* An unbalanced cantilevered spinning rotor can emit both vertical and lateral vibrations. This is the case for both the main rotor and tail rotor of a helicopter. Lateral vibrations are due to mass imbalances, such as the individual blades of the rotor system having unequal masses. Vertical vibrations are due to the individual blades in the rotor system having unequal lift, thus causing a nutating lift vector about the rotational axis of the rotor system.

Rotor systems emit vibrations across an infinite frequency band. The largest magnitude vibrations are those occurring at the system fundamental frequency, which is once per revolution (1/Per) [5]. The current methods that exist for rotor smoothing can only reduce vibrations at the fundamental rotor frequency. This is due to current helicopter control systems inability to command anything but a cyclic control at the fundamental frequency of the rotor system. Higher multiples of the fundamental rotor frequency are also noticeable sources of vibration but have vibrations that are orders of magnitude lower than the fundamental frequency. These vibrations are primarily due to the harmonic forces generated in forward flight, which are due in part to the flexible nature of the rotor system. The research area of Higher Harmonic Control (HHC) [12, 20] is addressing this problem.

## ***2.2 Rotor Smoothing Methods***

Rotor smoothing generally is the process of adjusting rotor blade properties to reduce the vibrations due to unbalanced loads across the rotor disk. This Section will review the adjustments to the rotor system used in this process.

*2.2.1 Rotor Adjustment Options.* Vibrations, as stated previously, are due to asymmetrical forces acting on a spinning rotor system. In order to perform any adjustments to correct the vibrations the control inputs that are available to a heli-

copter must first be know. This Section will cover commonly available control inputs on modern rotorcraft.

*2.2.1.1 Mass Adjustment.* Mass adjustments are necessary to correct the lateral vibrations of a spinning rotor. The rotor system provides for this correction by applying masses to the root of an individual blade of the rotor system, as seen in Figure 2.3. These masses are usually in the form of plates or pellets. It is important to note the effect of adding mass to a blade can be replicated by removing an equal mass from the opposite blade, or opposite blades if the rotor system has an odd number of blades. Adjusting the masses on rotor blades has no aerodynamic effect and thus provides no direct input to vertical vibrations.



Figure 2.3: Blade Weights Applied at the Blade Root [23].

*2.2.1.2 Pitch Link Adjustment.* In order to affect the rotor's vertical vibrations an aerodynamic input must be imparted on the system. One method for this is by adjusting the pitch linkage of an individual blade. A pitch linkage is a rod of adjustable length which connects the blade to the swashplate of the helicopter. This adjustment is seen in Figure 2.4.



Figure 2.4: Rotorcraft Pitch Linkage Adjustment [23].

The pitch linkage controls the pitch of the blade it is connected to. Increasing or decreasing the length of a pitch linkage will likewise increase or decrease the angle of attack of the modified blade. The angle of attack of the blade will determine the lift the blade will produce. Thus, for positive vertical forces to be reduced on the rotor, a blade that is 180 degrees out of phase of the disturbance has the pitch linkage set to increase positive pitch to impart an equal and opposite force. Alternately, negative pitch can be applied to a blade that is directly in phase to the disturbance to achieve the same effect. Pitch linkages on modern helicopters are not dynamically adjustable,

thus any change in pitch length must occur when the helicopter's rotor system is not spinning. Research is underway to provide for dynamically adjustable pitch linkages. The concept is seen in Figure 2.5.

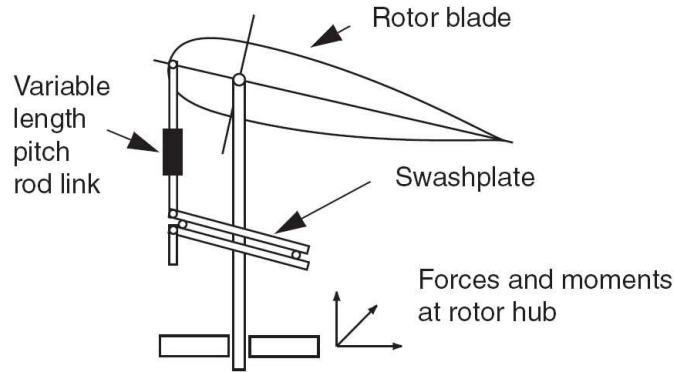


Figure 2.5: Rotorcraft Dynamic Pitch Linkage [20].

Mannchen [20] and Hwang [12] review the various aspects of implementing HHC via dynamically adjustable control linkages. A BO 105 has been modified to replace the static pitch linkages with dynamically adjustable linkages, as seen in Figures 2.6 and 2.7.

*2.2.1.3 Trim Tab Adjustment.* Trim tab adjustments are another method of adjusting the rotor system's vertical vibrations. A trim tab is a flap-like device attached to the trailing edge of a rotor blade. An example of a trim tab is seen in Figure 2.8. It operates in much the same manner as an aileron on a fixed wing aircraft by changing the overall camber of the wing section to which it is attached. Thus, reduced camber will reduce or change the direction of lift on the wing at the section to which it is connected. Likewise, an increase in camber will cause an increase in lift at the airfoil section. Trim tabs are not dynamically adjustable, but similar research as discussed by Hwang and Mannchen [12, 20] allows for such capability.



Figure 2.6: BO 105 Rotor Head With Dynamic Pitch Linkages [20].

*2.2.2 Historical Methods.* Rotor smoothing methods have been around as long as helicopters have been vibrating, which is to say since their inception. This



Figure 2.7: Individual Dynamic Pitch Linkage on a BO 105 [20].



Figure 2.8: Rotor Blade Trim Tab at Trailing Edge [33].

Section will briefly cover the methods used from the 1930's to the 1980's, as outlined by Johnson [15].

*2.2.2.1 Touch Flag Method.* The touch flag method was the forerunner in rotor track and balance techniques. This method was devised to align the blade tips in the same plane of rotation, or 'track'. This method employed a pole mounted flag with which the operator would allow to come in contact with the rotating blade tips. As each blade tip, which was colored with chalk or crayon, struck the flag the blade gap separation was then noted, thus providing track information.

*2.2.2.2 1960's Electro-Optical Track Adjustment.* In the 1960's a method to measure the blade track using electro-optical equipment was devised by Chicago Aerial. This method provided for very accurate measurement of blade track

via a vertical height measurement from the sensor datum. This method, however, only provided track information while the vehicle was on the ground. A second product was devised to provide in-flight tracking but produce lower accuracy results as compared to the the high accuracy method.

*2.2.2.3 1970's Strobe Light Tracking.* A method to identify blade track information while the vehicle was in flight was devised in the 1970's using a synchronized strobe and reflective targets. The targets were affixed to the individual blade tips. This method required the operator to remember individual blade positions, which required not only training but high proficiency. While this method was capable of blade tracking while the vehicle was in flight, it was deemed too unreliable due to the high operator proficiency requirement and thus abandoned.

Rotor smoothing during 1970's moved from the purely static mass balance method used up until this point to a method which measured rotational vibrations. This method was adopted from spin balancing techniques for large industrial blowers. The data from the accelerometers was synchronized with a strobe light to establish the phase relationship of the vibration. This provided the operator information of how much and where to place mass. This method did not address blade adjustments for vibration reduction.

*2.2.2.4 1980's to late 1990's.* Rotor vibrational reduction methods during the 1980's began to adopt a mathematical model-based approach by using a linearized model of the rotor dynamics to determine the appropriate rotor adjustments. This approach was intended to eliminate the multi-step process of previous rotor track and smoothing processes by identifying the relationship between rotor adjustments and vibrations via a mathematical model. This procedure worked well as long as the vehicle is a close match to the mathematic model used by the smoothing algorithm. The mathematical models used primarily non-parametric transfer function models. As the mathematical model did not adjust to match the characteristics of the test aircraft, the reliability of the recommended adjustments were valid only 50 to 75

percent of the time [15]. This type of algorithm is referred to as a non-learning type as the model is rigidly fixed to one aircraft configuration. This has led to the development of learning algorithms so that the internal model can adjust to match the test aircraft, as discussed in reference [41] and in Section 2.2.3.2. The research covered in this dissertation primarily focuses on the improvement of learning algorithms.

*2.2.3 Current Methods.* Modern developments in rotor vibration reduction are focused on providing an adaptive mathematical model which can 'learn' the individual characteristics of the the vehicle under test. These methods attempt to match the input-output relationship of test data to that of the mathematical model used by the smoothing algorithm. These algorithms are based on both *linear* and *nonlinear* models. In this Section we will briefly describe the linear and nonlinear algorithms used to smooth rotor vibrations. The cases considered here are for a single main rotor, however the same methodology applies for the tail rotor or any rotor in a counter rotating main rotor configuration, such as a Kamov Ka-26.

*2.2.3.1 Linear Smoothing Algorithms.* Linear algorithms were the first of the numerically based approaches to rotor vibration smoothing to appear in the helicopter community. This approach is based on a non-parametric input-output relationship of the change in vibrations to the change in a rotor adjustment, such as changing the length of a pitch link or changing the angle of a trim tab. The input-output relationship is considered linear in this approach and thus results in a simplified transfer function model. The transfer function is expressed simply as a Least-Squares Equation 2.1 [33]

$$\alpha_{ij} = \Delta_j \text{Vibration} / \Delta \text{Adjustment}_i \quad (2.1)$$

where  $\alpha_{ij}$  is the sensitivity coefficient matrix,  $\Delta_j \text{Vibration}$  is the change in vibrations for time  $j$  and  $\Delta \text{Adjustment}_i$  is the change in adjustment  $i$  to the rotor. It is

important to note that the linear sensitivity coefficients are determined a priori to any adjustment calculations through a series of flight tests at select altitudes and velocities within the helicopter's flight envelope. The individual elements of the sensitivity coefficient matrix  $\alpha$  are determined by making incremental changes to  $\Delta Adjustment_i$  in Equation 2.1. This process is repeated for all incremental changes of adjustments at all the selected points within the helicopter's flight envelope. In most cases in linear smoothing algorithms the sensitivity coefficient remains unchanged after the initial matrix development. This approach is referred to as a *non-learning* approach as the algorithm does not adjust the sensitivity coefficients after they have been developed.

Non-learning algorithms have problems with accuracy in their adjustment calculations due to error in the individual elements within the sensitivity coefficient matrix. These errors arise from the method in which the linear coefficients are calculated, namely that they are calculated from one helicopter. Individual helicopters have variances in their input-output relationships, thus the sensitivity coefficient matrix does not accurately apply to all helicopters. Additionally, error arises in the sensitivity coefficients due to poor reproducibility of the vibration data at each flight condition. An individual linear coefficient within the sensitivity matrix is formed from the average value of several tests at the same flight condition and same adjustment setting. Wroblewski [5] indicates that the statistical variance between tests at one point is 30%. This is due to measurement noise, aircraft gross weight, and the interaction of aircraft modes that are weakly dependent on rotor adjustments [5].

The required adjustment is determined by adjusting Equation 2.1 as seen in Equation 2.2

$$\Delta Adjustment_i = \alpha_{ij} / \Delta_j Vibration /. \quad (2.2)$$

Once again, a Least-Squares approach is used to calculate the required rotor adjustment necessary to minimize the measured vibration.

#### 2.2.3.2 Artificial Neural Network Smoothing Algorithms.

Artificial

neural networks are another method of describing the input-output relationship of a dynamic system. Based on biological neural networks, artificial neural networks mimic the functions of the axon, the cell body, and the dendrites as seen in Figure 2.9. The dendrites act to accept inputs to the system, the cell body assigns weightings to inputs and then passes this value through an internal transfer function, and these signals are then carried out of the cell body by the axon. The synapse acts as the output of the system [21].

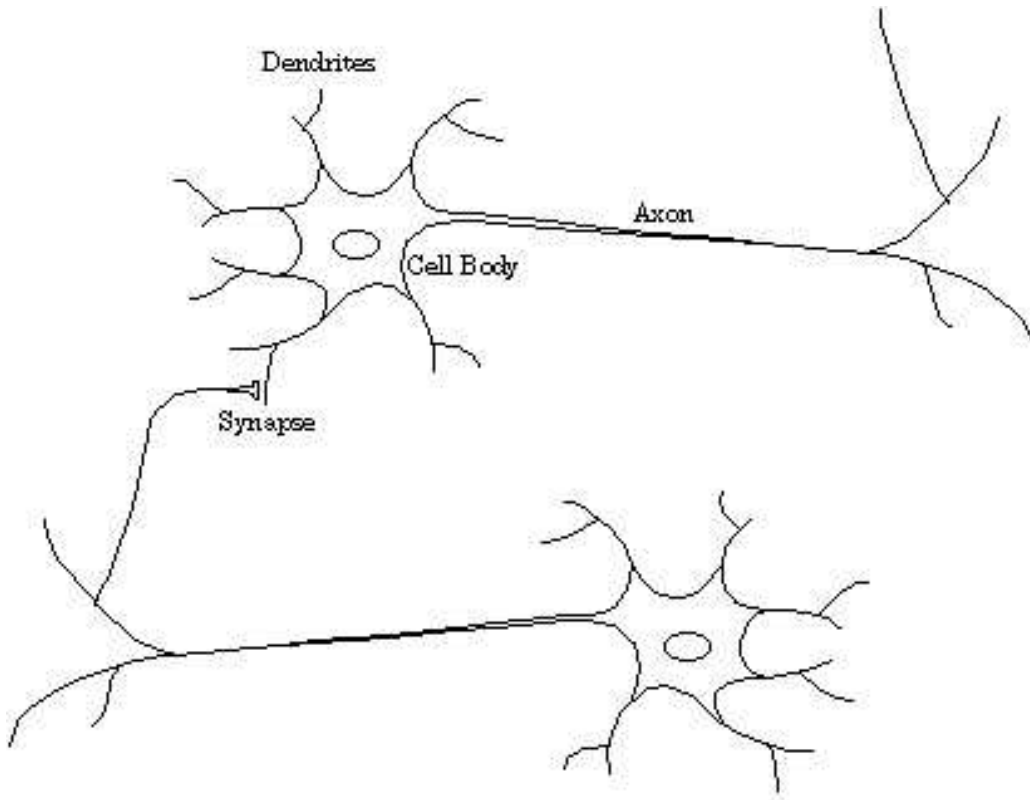


Figure 2.9: Biological Neural Network [21].

Artificial neural networks allow for both linear and nonlinear transfer functions within the "cell body," thus allowing for both nonlinear or linear mappings of input-to-output. A depiction of an artificial network is seen in Figure 2.10. This has a

great advantage over linear transfer function models, as they are constrained to only linear mappings from the input space to the output space. Neural networks are non-parametric in that no explicit relationship, such as a multivariable dynamic model, is needed to describe the relationship of helicopter rotor adjustments to vibrational output [6]. The model is therefore represented by the input-to-output interactions of the network.

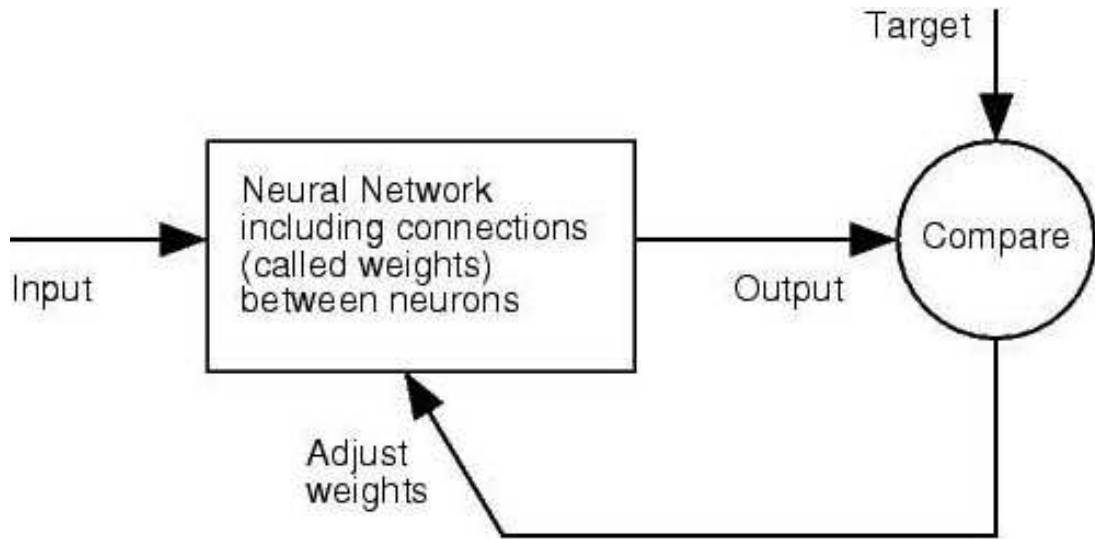


Figure 2.10: Artificial Neural Network [21].

Artificial neural networks establish the input-to-output mapping through a ‘learning’ process in which true input and output data is observed and then reproduced. The data is reproduced by first passing the input data through the network and then comparing the network calculated output to the true output. A gradient of the magnitude of the error in the output is then used to adjust the weightings in the individual neurons within the network which will allow the network to then calculate a more precise output. This process is repeated until the error between the output of the neural network and the real data falls below a predetermined threshold.

In the case of using artificial neural networks for smoothing main rotor vibrations a set of training data must first exist. This set of data is referred to as the training set. The training set can come from either real aircraft or simulation of a linear or

nonlinear parametric model. In the establishment of the training set a range of rotor adjustments is performed and the resulting change in helicopter vibration is then recorded for each change. Wroblewsky [6] indicates the training set must be selected to exhaustively cover the entire flight envelope of the vehicle. As the data required to adequately train a neural network for this task is quite large, simulation data is typically used as a reasonable first approximation [6]. As more flight data becomes available the training set is modified by replacing the simulated data with actual flight data. A typical training set will require between 20 to 30 flights.

### ***2.3 Smoothing Performance Of Current Methods***

Smoothing performance can be considered in terms of:

1. Quality of final rotor adjustments
2. Number of rotor adjustment iterations required to achieve minimum vibrations
3. Number of individual rotor adjustments required per iteration
4. Amount of data necessary for initial non-parametric mapping

The linear non-parametric mapping method presented in Section 2.2.3.1 and the neural network based method presented in Section 2.2.3.2 both have been shown to produce adequate adjustment solutions, thus resulting in minimum rotor vibration [8,23,28–30]. In this comparison there is no clear advantage to either method as they both arrive at an acceptable vibration measurement at the final adjustment solution. In terms of speed of maintenance there also seems to be no clear leader. Both methods generally require two to three smoothing iterations including adjustments and test flights to reach an acceptable level of rotor vibrations. This is interesting as the neural network method was reported to provide a solution in fewer iterations by including the system nonlinearities in the adjustment to vibration mapping [6]. Miller [23] disputes this claim by demonstrating that rotor adjustments show a linear mapping to the vibration changes. Furthermore, the number of changes required per iteration appears to be independent of method. Both methods have minimum adjustment

optimized solutions available and perform generally the same [6, 8]. Finally, both methods require a large database of system adjustments and resulting vibrational data to build the initial input-output mapping. In this area there appears to be no clear leader, as both methods can use either flight data or data from simulation to create the initial mapping. Furthermore, once the initial mappings have been established each method provides no method to adjust them to an individual aircraft that has slightly different dynamics due to wear, environment, and variances in vehicle components. Finally, this method cannot provide adjustment solutions outside of the training set.

## ***2.4 Current Method Deficiencies***

The rotor smoothing methods covered up to this point represent the evolution of the state of the art in this area. The methods have emerged from flags and grease pencils used to make rotor track adjustment methods to using linear or nonlinear non-parametric transfer functions used to compute rotor changes. While the non-parametric transfer function methods produce an adequate rotor adjustment solution to reduce vibrations they have several deficiencies that need further attention. These deficiencies are listed below:

1. Extensive data collection required before any use of system
2. Inability to adjust mapping after establishment
3. Both methods are non-parametric, thus it is impossible to check the individual parameters for accuracy

This Section will address the above deficiencies and briefly suggest solutions that this work will be based on.

The first deficiency in the current smoothing methods is the extensive data collection necessary to create the input-output mappings of rotor adjustments to changes in vibration. This requirement is necessary regardless of method used, as the neural networks require this data for the training set. As stated in 2.2.3.2, the data

collection can require up to 30 test flights, depending on the number of test points used to create the mapping. To improve the state of the art in rotor smoothing methods this requirement must be greatly reduced.

The inability to adjust the input-output mapping after it is created is the second area of improvement in rotor smoothing algorithms. Generally, only one helicopter with one fixed configuration is used to collect the initial data, which is then applied to the entire fleet. Individual aircraft modifications and repairs can cause differences in the input-output mappings as the vehicle dynamics are different from the vehicle used to create the original mapping. Thus, the accurate reduction in vibrations requires adjustments based on the current vehicle, not the one from which the mapping was created. The second improvement to rotor smoothing algorithms is to allow for changes in the input-output mapping to match a helicopter undergoing smoothing operations.

It is difficult to verify the accuracy of Non parametric derived input-output relationships to known, or *truth* models, as they do not contain discernible parameters such as lift coefficients, etc. Thus, after the initial data is collected and the mapping is created there is no method to verify the validity of the input-output relationships except further empirical testing and statistical analysis. A third improvement to rotor smoothing is to incorporate parametric models that use specific parameters that can be checked for validity.

## **2.5 Summary**

In this chapter, we exhibited an overview of previous work from the pertinent research areas and noted the research objectives of this present study as they arose from previous works. In the next chapter, the objectives for the proposed research are discussed in sequential order.

### III. Scope of Research

Rotor smoothing has an extensive history, as seen in the historic view taken by the previous chapter. Focusing on future developments in rotor smoothing, this chapter will briefly glimpse at the research objectives of this work and outline their significance to improvements in this field.

The objectives described in this chapter layout the framework that this research will use to produce a *parametric model-based rotor smoothing algorithm*. In principle, this research is based upon a proposed rotor smoothing method, which works as follows:

1. Perform system identification to populate the rotor system parametric model.
2. Validate the accuracy of the parameters of the rotor system model.
3. Produce a vibration control solution using linear optimal methods.

The effort of this research is to redefine how rotor smoothing is performed by evaluating the following items:

1. Replace the non-parametric mapping of the rotor system dynamics with a parametric approach applicable to system identification methods. This will be done by using a linear time periodic system modeling approach developed by Wereley [42] that produces the convenient state space linear operator form.
2. Identify a method that is capable of validating parameters of the parametric rotor model used in the above item.
3. Identify a System Identification methodology that is compatible with a rotor in both hover and forward flight.
4. Produce a control solution that reduces rotor vibration levels to an acceptable level base on the above items.

The remainder of this chapter will discuss each of the items listed above as objectives within the scope of this work.

### 3.1 Scope of current research

The primary objective of this research is to develop a robust rotor smoothing algorithm based on frequency domain system identification methodology. As mentioned above, this method will be compatible with a helicopter rotor in forward flight, which is best represented as a linear time periodic system [12, 42]. The proposed research outlined below is to extend the works of [12, 42] by introducing a theory to validate system parameters of the identified model based on the Cramer-Rao bound [34]. Additionally, this work intends to address the feasibility of optimal control of linear time periodic systems for vibration smoothing of current and future helicopter main rotor systems. The following Sections review the objectives of this research in a step by step approach.

*3.1.1 Objective 1: Model linear systems with time periodic coefficients as a state space model.* This Section will describe the methodology defined by Wereley [42] to model a linear system with time periodic coefficients as a state space model, in a manner similar to a linear time invariant system. The rationale is described below.

The first step in achieving the proposed research goals is to develop a parametric main rotor system model for the purposes of simulation. While the rotor model is inherently nonlinear, based on the analysis by [23], a linear model is deemed adequate for investigations into rotor smoothing and thus will be used here. This is advantageous such that the linear model approach will allow the use of developed system identification, analysis, and control methodologies for linear models. Before this can begin, however, a distinction must be made concerning the *periodicity* of the system dynamics and how to address them.

The rotor system model proposed above, while being linear, will retain the time periodic terms in the system dynamics, control input, and system output matrices. This is critical in order to retain the system response fidelity in forward flight, where the time periodic terms play a major part in the total system response. Historically, these terms have been averaged over the system time interval  $T$ , as in [20, 31], but this

results in an inaccurate dynamics model and ultimately to poor control development. This averaging is due to the inability of incorporating the time periodic terms in the state space form of the linear model. To explain this further, it is important to differentiate between a model with *Time Invariant* dynamics as opposed to one with *Time Periodic* dynamics.

In forward flight, a helicopter cannot accurately be considered as a Linear Time Invariant (LTI) model as the rotor system produces periodic aerodynamic forces. This requires the use of a Linear Time Periodic (LTP) system to describe the rotor dynamics in forward flight. This is not to say that LTI models are improper to use as a system model of a helicopter rotor, but rather that the flight condition must be taken into account. For example, Kvaternik et al. [31] successfully used a LTI model of the Bell-Boeing XV-15 tiltrotor to perform real time system identification and control to reduce rotor vibrations in hover. This is not the case in forward flight, however, as Hwang [12] demonstrates that system identification based on LTI models fails due to poor model matching as compared to LTP based system identification of a helicopter in forward flight. In a frequency domain sense, this is due to the inability of the LTI system to account for the sideband power generated by the LTP system, as LTI systems can only account for power at the excitation frequency. This is explained in more detail in Section 3.1.1.1.

#### *3.1.1.1 Frequency Response Differences in LTI and LTP Systems.* As

stated above, the frequency response of a LTI system and a LTP system vary in output to the same forced input. This is due to the fact that a LTP system can change the amplitude and phase of the input signal in addition to causing frequency translation of the input signal. LTI systems can only effect the amplitude and phase of the input signal. Hwang states [12] the frequency translation of the input signal in LTP systems is represented by an output that is the the product of the sinusoidal excitation signal and a Fourier series expansion of the fundamental frequency, which in this case is the

rotational frequency of the rotor system. An example of this is shown in Figure 3.1. Linear time periodic system theory will be covered in detail in chapter V.

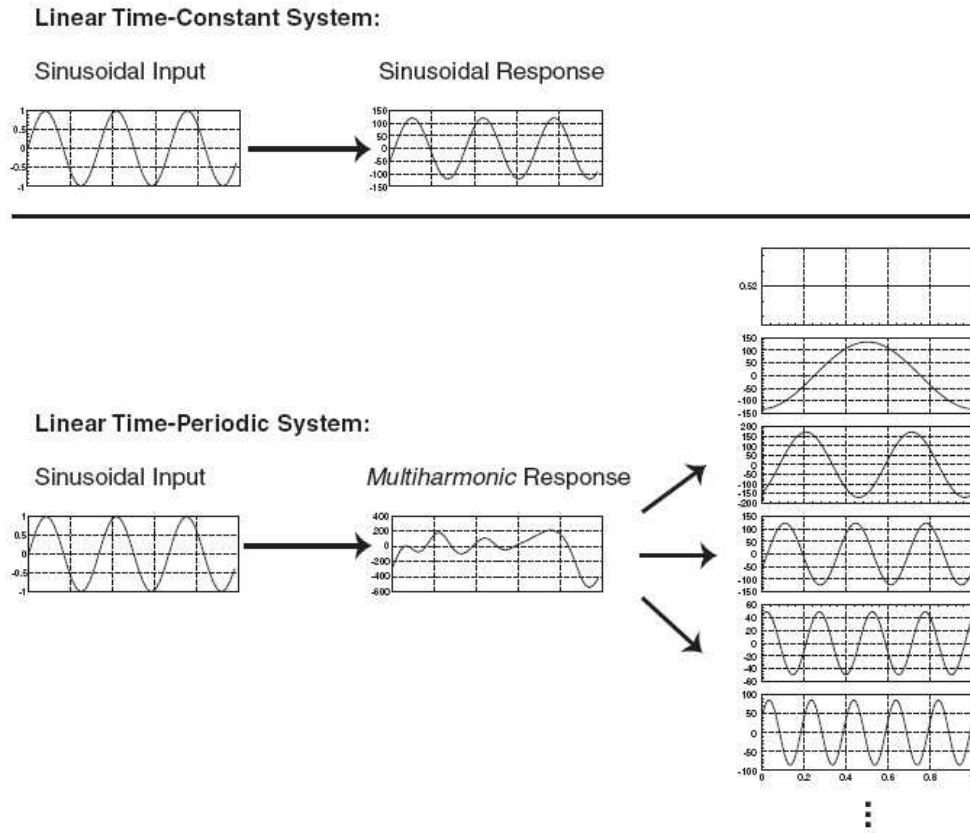


Figure 3.1: Multiharmonic Response of an LTP System [20].

Therefore, a LTP system will produce power at the excitation frequency as well as sideband power due to the fundamental frequency of the system. It is clear to point out that any system identification techniques that do not account for the additional sideband powers will result in inaccurate results.

*3.1.2 Objective 2: Adapt the Cramer-Rao Bound to Validate the Parameters of the Linear Time Parametric Rotor Model.* This Section will cover the necessity to develop the Cramer-Rao Bound to validate the parameters of the linear time parametric system in state space form, as in the case of a helicopter rotor model.

System models, as in the LTP model in Section 3.1.1, are initially described by parameters derived from mathematical models of the system dynamics. These models, while generally good, need to be validated so that they accurately describe the real system upon which they are based such as a real helicopter rotor. This validation is referred to as *system identification*, where the individual system parameters are derived from data collected from a test of the real system, such as a flight test.

The parameters developed by system identification methods define a linearized vehicle model, which in turn defines the dynamic characteristics of that vehicle. These models are in turn used in simulators, control system design, and to validate wind tunnel parameter predictions. Maine and Liff [34] point out that it is important to remember that parameters obtained from testing are only estimates and not exact values. This, unfortunately, is often disregarded and rarely are the parameters ever verified for accuracy. Maine and Liff [34] further state that if accurate parameter estimates cannot be distinguished from worthless estimates all estimates must be assumed to be of questionable accuracy. It is for these reasons that parameter validation methods have been developed for LTI systems such as those cited in [3, 34]

As stated in Section 3.1 the intent of this research is to develop an adaptive control algorithm to alleviate the main rotor vibrations for the purpose of rotor smoothing. The measure of accuracy of the model parameters of the identified rotor system are of critical importance in this application as they will determine the effectiveness of the implemented vibration controller. To implement a controller based on an unverified model may have disastrous results as the commanded control inputs are based on a model that does not match the true rotor system dynamics.

The Cramer-Rao bound [34] is a method commonly used in flight testing to establish the accuracy of identified parameters of a linearized vehicle model. This measure of accuracy is based on the Uncertainty Ellipsoid and is similar to other measures of accuracy such as estimated variance and standard deviation. The Cramer-Rao bound is the same as these methods except that the Cramer-Rao bound is the

square root of the variance. By reviewing the Cramer-Rao bound for each parameter estimate from flight test, one can determine the data accuracy by evaluating the size of the bounds themselves. The Cramer-Rao bound established the standard deviation of an identified model parameter, and therefore large bounds indicate a poor estimation performance. This method provides greater insight into the accuracy of estimated parameters than simply reviewing the scatter of parameter estimates from flight test data at each point, as seen in Figure 3.2. Upon review of Figure 3.2,

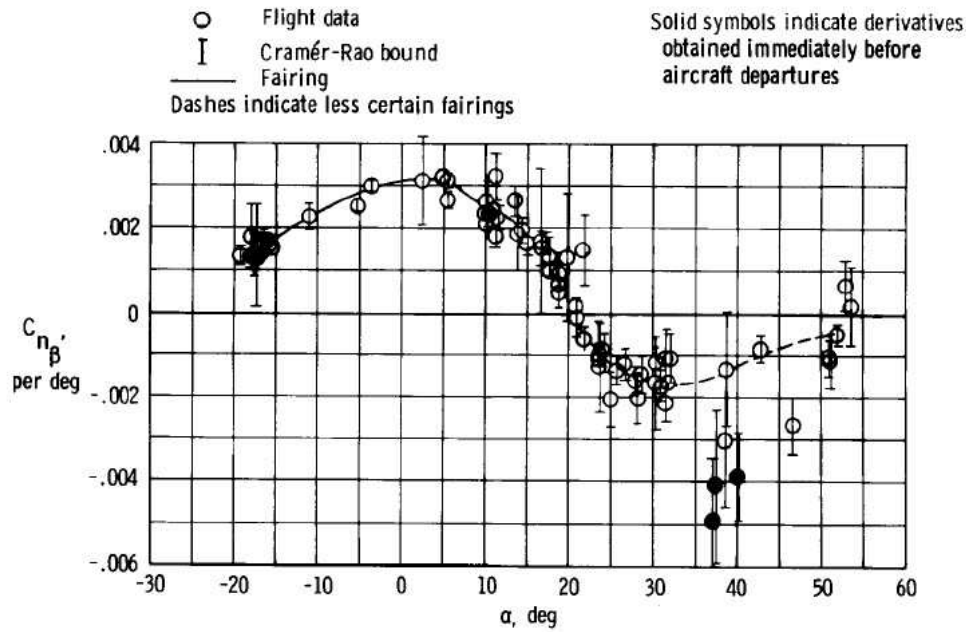


Figure 3.2: Example of Cramer-Rao Bounds for Parameter Estimates [34].

one can see the Cramer-Rao bound shows that data below -10 degrees is unreliable even as the data scatter is not very large. Likewise, at +10 degrees  $\alpha$  the Cramer-Rao bound matches the spread of the collected data. In this case the parameter is poor based upon both data scatter analysis and the Cramer-Rao bound. This shows that the Cramer-Rao bound can detect both small and large data scatter cases where parameter estimation is poor. Thus, a review of the Cramer-Rao bounds for estimated vehicle models parameters allows for an evaluation of whether the parameters have been estimated properly, and thus whether they should either be re-evaluated or adjusted by the engineer before they are used in the vibration control model.

This research will develop this method further by allowing for Cramer-Rao bounds to be identified for LTP model parameters.

*3.1.3 Objective 3: Develop a Parametric Main Rotor System Model.* The system identification and control processes used in the proposed method of rotor smoothing will require a linear time periodic model of a helicopter rotor. This Section will develop a linear model of a helicopter rotor system which incorporates time periodic system coefficients to accurately describe the system in forward flight.

The model will include dynamically actuated pitch linkages for each blade so it will be possible to explore dynamic smoothing cases allowed by using an optimal control approach. The flap equations of motion for a rigid blade will be derived. Candidate models to be considered are those based on the work presented by Johnson [15] and Webb [37]. This research will consider main helicopter rotor in forward flight and in hover, however the emphasis will be on a helicopter in forward flight. The inflow will be simplified to consider a uniform inflow model.

*3.1.4 Objective 4: Perform System Identification of the Main Rotor System.* The next step in the proposed research goals is to adapt a system identification technique to determine the dynamics of the main rotor in both hover and forward flight. An accurate rotor model is necessary for the development of an effective vibration controller. Therefore, the linear time periodic model proposed in Section 3.1.3 will be used for this step. The choice of system identification techniques is constrained due to the inherent dynamics of a helicopter. As stated in Section 3.1.1, in forward flight a helicopter cannot accurately be considered as a linear time invariant model as the rotor system produces periodic aerodynamic forces. This requires the use of a linear time periodic system to describe the rotor dynamics in forward flight.

*Candidate System Identification Methods.* System identification methods generally fall into two categories for linear systems, Frequency Domain methods and Time Domain Methods. Frequency domain methods dominated the early

history of system identification with non-parametric transfer function analysis. This method was improved upon by the developments of Cooley and Tukey [13] with the Fast Fourier Transform(FFT), which greatly decreased the testing time required to generate the model. Frequency domain methods are popular in system identification as they have the ability to reject low frequency drift and DC bias in sampled data. However, Juang [17] states that frequency domain methods have lost their popularity in control model identification. Modern control methods rely on parametric models such as state-space models. Time domain methods are capable of generating parametric models and for this reason it is the leading system identification method used for the development of control model identification. Time domain methods lack some of the desirable features of frequency domain methods such as reduced amounts of sampled data. Additionally, time domain methods do not inherently have the ability to handle bias and low frequency drift. These problems can be addressed, but require the use of additional algorithms and thus are not as efficient as frequency domain methods. Recently, several researchers [12, 42] have improved frequency domain system identification methods by developing a method to identify model parameters to match the frequency response characteristics. Hwang [12] has developed a parametric frequency domain identification method for LTP systems which is directly applicable to control model identification. This method will be adapted to the main rotor smoothing problem of this research due to its inherent ability to handle LTP methods and generate a parametric model.

*3.1.5 Objective 5: Develop an LTP Optimal Control Methodology for Rotor Vibration Smoothing.* The final objective of this research is to develop a robust controller capable of attenuating the hub vibrations caused by aerodynamic imbalances of the rotor system. The general idea behind attenuating rotor vibrations is simply inducing equal magnitude forces and moments into the rotor system that are  $180^\circ$  opposite in phase of the disturbance force. This produces destructive interference of the vibrations caused by the imbalance loading on the rotor system, effectively

eliminating the vibration felt at the rotor hub if performed precisely. It is the matter of model precision that the previous Section 3.1.3 dealt with, which is essential to produce a linear model for effective controller development. The research of *Objective 5* will explore the use of active control to arrive at a steady state control solution to reduce or eliminate rotor induced 1/rev vibrations. The following Section will briefly discuss candidate control methodologies in which the vibration attenuation system, or simply rotor smoothing, will be based upon.

*3.1.5.1 Candidate Control Methodologies.* Several control methodologies currently exist in the area of rotorcraft control including Optimal [7,36,40], Modal Control [37], and Periodic system control [19,27]. Due to the constraints imposed by the modeling requirements, namely that the model must be represented as LTP for accuracy, only methods that are capable of handling LTP models will be considered.

Optimal control has successfully been used in active rotorcraft vibration control, as cited in the references above. Namely, linear optimal methods are of interest to explore as they inherently use parametric models for the controller development. This is especially attractive as the intent of this research is to both identify and verify a parametric linear model. The application optimal LTP control has, however, only focused on active vibration reduction for an already smoothed rotor system. This research will explore the usage of optimal LTP control for the purpose of producing a smoothed rotor system by producing a steady state control solution. As this is the case, only the 1 per rev vibrations will be considered in terms of a disturbance input. All higher multiples of disturbance input vibrations will be disregarded as this research is not focusing on higher harmonic control. Steady state input will be possible for the periodic system by considering all control inputs in the fixed coordinate system of the rotor.

This chapter presented an overview of the overall methodology for the proposed research, including a step-by-step road map of the sequential research objectives. The

next chapter will introduce the mathematical concepts of the LTP system, which will serve as the basis upon this work will be built.

## IV. Mathematic Foundations of Linear Time Periodic Systems

Linear models can be assumed to have *time invariant* or *time periodic* dynamics, as discussed in Chapter III. While the principals of linear time invariant models are well understood, many of the mathematical foundations of linear time periodic systems are not in the engineering community. Therefore, this Chapter will present several of the required mathematical elements of linear time periodic systems, as they will be used extensively in later Chapters to develop the LTP system model.

### 4.1 The Fourier Series

Harmonic system excitation, in the case of input signals to a linear transfer function, repeat at a time interval,  $[0, T]$ . The term  $T$  is referred to as the *system period* and is defined as

$$T = \frac{2\pi}{\omega_p} \quad (4.1)$$

where  $\omega_p$  is the system Fundamental frequency or *Pumping frequency* ( $\omega_p$ ) . Any function that repeats itself over the time interval  $[0, T]$  is known as a *periodic function*. Meirovitch [22] states that any periodic function satisfies the relation of the type

$$f(t) = f(t + T) \quad \forall t \in \mathfrak{R} . \quad (4.2)$$

By the definition stated in Equation 4.2 it is evident that the even and odd trigonometric functions,  $\sin nt$  and  $\cos nt$  , ( $n = 1, 2, \dots$ ), are periodic over the period  $T$  as  $\sin nt = \sin n(t + T)$  and likewise for  $\cos nt$  when  $\omega_p = 1$ .

An example of a periodic system excitation is a sinusoidal function as seen in Figure 4.1. From this graphic it is clear that the input function is both periodic over  $T$  and purely sinusoidal over that period.

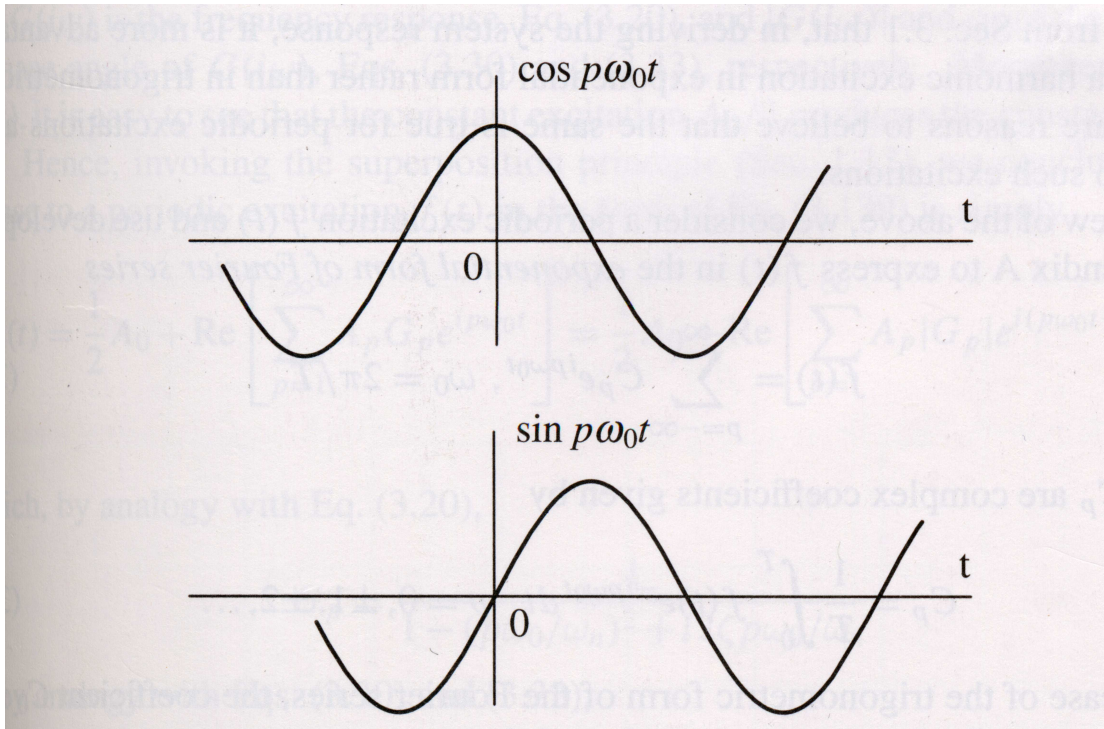


Figure 4.1: Sinusoidal input functions [22].

It is important to note that a harmonic function can undergo a motion that is not purely sinusoidal while cycling through a period  $T$ . The saw tooth wave function seen in figure 4.2 represents an example of a non-sinusoidal harmonic function that is periodic with period  $T$ . Thus, the purely sinusoidal input signal is a general case of the harmonic input signal. Non-sinusoidal functions, while still periodic, can be represented as a linear combination of harmonic functions. This combination is referred to as the *Fourier Series* [22].

To develop the definition of the Fourier series the concept of linear independence, orthogonality, and orthonormal function sets must first be defined. These subjects will now be covered.

#### 4.1.1 Linear Independence, Orthogonality, and Orthonormal Function Sets.

Over the interval  $[0, T]$  a set of functions  $\psi_r(t) : r = 1, 2, \dots$  is said to be an *orthogonal*

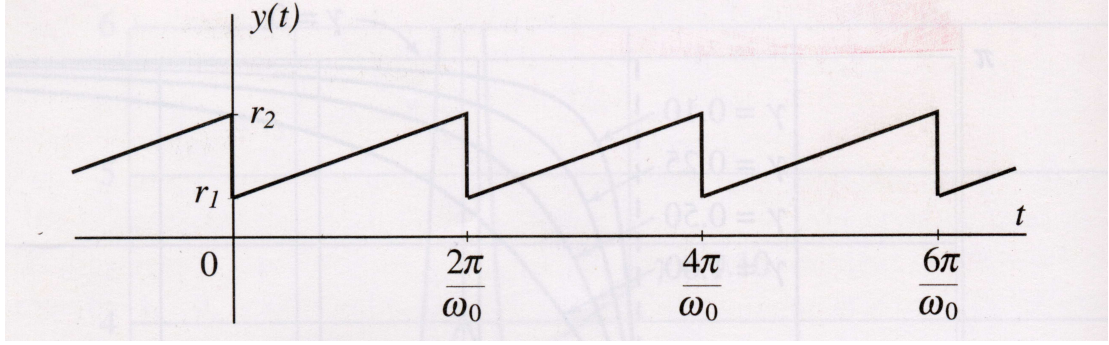


Figure 4.2: Periodic non-sinusoidal input signal [22].

set of functions defined on  $[0, T]$  if

$$\int_0^T \psi_r(t) \psi_s(t) dt = 0 \quad \forall r \neq s. \quad (4.3)$$

Furthermore, the set of functions  $\psi_r(t) : r = 1, 2, \dots$  is said to be *orthonormal* if

$$\int_0^T \psi_r^2(t) dt = 1 \quad \forall r \in \mathbb{N}. \quad (4.4)$$

For any function within the orthonormal set, the *Kronecker Delta* ( $\delta$ ) can be defined as

$$\int_0^T \psi_r(t) \psi_s(t) dt = \delta_{rs} \quad \forall r, s. \quad (4.5)$$

Finally, considering the set of functions  $\psi_r(t) : r = 1, 2, \dots$  and a set of constants  $c_r \in \mathfrak{R} : r = 1, 2, \dots$  where  $c_r$  are not exclusively null. Then, a homogeneous linear relationship 4.6

$$\sum_{r=1}^n c_r \psi_r(t) \neq 0 \quad (4.6)$$

denotes the function set  $\psi_r$  is defined *linearly independent*. Likewise, if Equation 4.6 is equal to zero then the set  $\psi_r$  is defined as *linearly dependent*. It is important to note

that any set that is orthogonal is also linearly independent by noting that Equation 4.3 by definition satisfies the properties of Equation 4.6.

*4.1.2 Trigonometric and Complex Forms of the Fourier Series.* A piecewise linear function  $f(t)$  can be approximated by considering a orthonormal set  $\psi_r$  in the linear relation of Equation 4.7.

$$\sum_{r=1}^n c_r \psi_r(t) . \quad (4.7)$$

Any function set  $\{\psi_r : r = 1 \dots n\}$  that approximates the piecewise continuous function in the Equation 4.7 is termed *complete* [22]. A well known complete function set [22] over the interval  $[0, 2\pi]$  is seen in 4.8.

$$\left( \frac{1}{\sqrt{2\pi}}, \frac{\sin t}{\sqrt{\pi}}, \frac{\cos t}{\sqrt{\pi}}, \frac{\sin 2t}{\sqrt{\pi}}, \frac{\cos 2t}{\sqrt{\pi}}, \frac{\sin 3t}{\sqrt{\pi}}, \dots \right) . \quad (4.8)$$

Using the complete orthonormal set defined in Equation 4.8 every continuous function  $f(t)$  defined over the interval  $[0, 2\pi]$  can be represented by the *Fourier Series*, as seen in Equation 4.9.

$$f(t) = \frac{1}{2}a_o + \sum_{r=1}^{\infty} (a_r \cos r\omega_o t + b_r \sin r\omega_o t) \quad (4.9)$$

noting  $\omega_o$  is referred to as the *fundamental frequency* . This form of the Fourier series is referred to as the *Trigonometric form* of the Fourier Series. The coefficients  $a_r, b_r$  ( $r = 1, 2, \dots$ ) in Equation 4.9 are referred to as *Fourier coefficients*. These coefficients are defined as

$$\begin{aligned} a_r &= \frac{2}{T} \int_0^T f(t) \cos r\omega_o t \, dt, r = 0, 1, 2, \dots \\ b_r &= \frac{2}{T} \int_0^T f(t) \sin r\omega_o t \, dt, r = 1, 2, \dots \end{aligned} \quad (4.10)$$

The Fourier coefficients define the contribution of the  $r=1,2,\dots$  trigonometric terms  $\cos r\omega_o t$  and  $\sin r\omega_o t$  to the approximation of the piecewise continuous function.

The Fourier series can also be expressed as an exponential series. This form, while mapping directly to the trigonometric form, is used as it more easily expresses a harmonic excitation in exponential as compared to the trigonometric form. The *exponential form of the Fourier Series* can be represented as follows

$$f(t) = \sum_{r=-\infty}^{\infty} C_r e^{ir\omega_o t} \quad (4.11)$$

where the *complex Fourier Coefficients* are represented as

$$C_r = \frac{1}{T} \int_0^T f(t) e^{-ir\omega_o t} dt, \quad r = 0, \pm 1, \pm 2, \dots \quad (4.12)$$

While both the trigonometric and exponential forms of the Fourier series are presented in this section, this work henceforward will extensively use the exponential form.

The Fourier series in Equation 4.9 represents an approximation of the piecewise continuous function having infinite dimension. In most cases an infinite approximation is not feasible and must therefore truncate the number of terms in the series. The number of terms included in the Fourier series is determined by the level of accuracy required to reproduce the piecewise continuous function it is approximating.

## 4.2 Eigenvalues and Eigenvectors

The study of linear systems rely heavily on the *matrix exponential function* ( $e^{At}$ ) when developing solutions to differential Equations. These solutions can be used to evaluate the system characteristics such as stability and frequency response. Key to these solutions are the *eigenvalues* and *eigenvectors* of the system. This section will define the properties of these terms as they are used extensively in this work.

Starting with the definition of a first order system of Equations in matrix form

$$\frac{du}{dt} = Au \quad (4.13)$$

where the constant matrix  $A$  is of dimension  $n \times n$ . Strang [38] notes a solution to the linear Equation 4.13 as

$$u(t) = e^{\lambda t} \zeta. \quad (4.14)$$

Now, directly substituting Equation 4.14 into 4.13 produces the Equation

$$A\zeta = \lambda\zeta. \quad (4.15)$$

The results of the form of Equation 4.15 can be transformed into the commonly recognised form

$$[\lambda I - A]\zeta = \mathbf{0} \quad (4.16)$$

where the scalar  $\lambda$  is termed the *Eigenvalue*( $\lambda$ ) and the vector  $\zeta$  is termed the *Eigenvector*( $\zeta$ ) of the matrix  $A$ . For clarification the matrix  $I$  is the *identity matrix* of dimension  $n$ . Reid [32] notes that considering the scalar first, it is seen that  $\lambda$  must be a real or complex value such that the coefficient matrix  $[\lambda I - A]$  is singular, thus not invertible. If the matrix is not singular then the trivial solution for the eigenvector would be the zero vector.

Reid [32] further notes that one condition for the matrix  $[\lambda I - A]$ , or *Resolvent Matrix*( $[\lambda I - A]$ ), to be non-singular is that the determinant be zero. Thus, the determinant of the resolvent matrix yields the *characteristic polynomial*( $\Delta(\lambda)$ ), an

$n$ th order polynomial in  $\lambda$ ,

$$\begin{aligned}\Delta(\lambda) &= \det[\lambda I - A] \\ &= \lambda^n + a_{n-1}\lambda^{n-1} + \cdots + a_1\lambda + a_0\end{aligned}\tag{4.17}$$

where  $a_i \in \mathbb{C}$ . The eigenvalues of the resolvent matrix are the distinct roots of the characteristic polynomial.

### 4.3 Singular Value Decomposition

One method of determining the eigenvalues and eigenvectors of a linear system is to use the *Singular Value Decomposition* (SVD). Burl [2] defines the *SVD* as a matrix factorization that provides the principal gains along with the resultant input and output direction vectors of the the given input-output relationship under evaluation. The SVD is essentially a *similarity transformation*, which is defined by Wereley [42] as in the following.

**Definition 4.3.1** (Similarity Transformation). *A matrix  $A \in \mathbb{R}^{n \times n}$  can be reduced to a diagonal matrix  $\Lambda$  by the similarity transformation  $\Lambda = WAV$  if and only if  $A$  has a linear independent set of  $n$  right eigenvectors. These right eigenvectors are the columns of  $V$ , with corresponding left eigenvectors that are the rows of  $W = V^{-1}$ , and corresponding eigenvalues that are the diagonal entries of  $\Lambda$ . Also, the original matrix  $A$  can be reconstructed from its eigenvectors and eigenvalues as  $A = V\Lambda W$ .*

Thus, Burl [2] states the *Singular Value Decomposition* is defined as a matrix  $A \in \mathbb{C}^{n_y \times n_u}$

$$A = V\Lambda W\tag{4.18}$$

where  $V \in \mathbb{C}^{n_y \times n_y}$  and  $W \in \mathbb{C}^{n_u \times n_u}$  are unitary matrices, noting  $\mathbb{C}^{m \times n}(\mathbb{C}^{m \times n})$  defines a set of complex matrices. Unitary matrices are defined as

**Definition 4.3.2** (Unitary Matrices). *A matrix  $V$  having the property*

$$V^\dagger V = VV^\dagger = I \quad \forall V \in \mathbb{C}^{n \times n} \quad (4.19)$$

*is thus considered a unitary matrix. The matrix transpose is represented by the symbol  $\dagger$ .*

The column vectors  $V$  and  $W$  are the left and right singular vectors of  $A$ , respectively. Furthermore, the matrix  $\Lambda \in \mathbb{R}^{n_y \times n_u}$  contains the eigenvalues of  $A$ , or *singular values*( $\sigma$ ), as seen in 4.20

$$\Lambda = \begin{bmatrix} \sigma_1 & & 0 \\ & \ddots & \\ 0 & & \sigma_p \end{bmatrix} \quad (4.20)$$

where the dimension  $n_y = n_u = n_p$ . Burl [2] defines similar singular value matrices of unequal dimensions y,u. As a note the singular values appearing on the diagonal of  $\Lambda$  appear in order of highest to lowest value such that  $\sigma_1 \geq \sigma_2 \geq \dots \sigma_p \geq 0$ .

By performing the singular value decomposition, Burl [2] states that one can clearly see how a matrix operates on a vector, or *input*. The singular values represent the range of matrix gains, which are referred to as the system *principal gains*. They provide a range of maximum and minimum gains over a range of frequencies. The right singular vectors define which inputs produce the maximum and minimum gains, where as the left singular vectors define which outputs result when the maximum and minimum gains are achieved [2].

#### 4.4 The Toeplitz Transformation

Many of the modern control theories have been based upon a state space representation of a linear operator form. In the case of linear operators that are expanded by a Fourier series the *Toeplitz* transformation is used when converting to state space form. This transformation allows the algebraically simplified representation of the

state space matrix representation while accounting for the Fourier series components. This section will define the Toeplitz transform and the properties that define it, as defined by Wereley [42].

**Definition 4.4.1** (Toeplitz Transform). *Let the  $T$  periodic matrix  $A(t)$  be described by the absolutely convergent Fourier series*

$$A(t) = \sum_{n=-\infty}^{\infty} A_n e^{jn\omega_p t} \quad (4.21)$$

where  $\omega_p$  is the fundamental frequency. The Toeplitz Transform,  $\mathcal{T}$  of  $A(t)$ ,  $\mathcal{T}\{A(t)\}$ , maps the set of complex Fourier coefficients,  $\{A_n | n \in \mathbb{Z}\}$  into the doubly infinite block Toeplitz matrix,  $\mathcal{A}$ , as seen in Equation 4.22

$$\mathcal{T}\{A\} = \mathcal{A} = \begin{bmatrix} \ddots & \vdots & \vdots & \vdots & \vdots & \vdots & \\ \cdots & \mathbf{A}_0 & \mathbf{A}_{-1} & \mathbf{A}_{-2} & \mathbf{A}_{-3} & \mathbf{A}_{-4} & \cdots \\ \cdots & \mathbf{A}_1 & \mathbf{A}_0 & \mathbf{A}_{-1} & \mathbf{A}_{-2} & \mathbf{A}_{-3} & \cdots \\ \cdots & \mathbf{A}_2 & \mathbf{A}_1 & \mathbf{A}_0 & \mathbf{A}_{-1} & \mathbf{A}_{-2} & \cdots \\ \cdots & \mathbf{A}_3 & \mathbf{A}_2 & \mathbf{A}_1 & \mathbf{A}_0 & \mathbf{A}_{-1} & \cdots \\ \cdots & \mathbf{A}_4 & \mathbf{A}_3 & \mathbf{A}_2 & \mathbf{A}_1 & \mathbf{A}_0 & \cdots \\ & \vdots & \vdots & \vdots & \vdots & \vdots & \ddots \end{bmatrix}. \quad (4.22)$$

The Toeplitz transform, as seen above, provides a convenient method of transforming periodic differential Equations into matrix form. Also several useful properties defined by Wereley [42] associated with the Toeplitz transform are listed below.

**Theorem 4.4.1** (Multiplicative Property of the Toeplitz Transform). *The Toeplitz transform of the product of two Toeplitz matrices,  $A(t)$  and  $B(t)$ , is the product of its transforms*

$$\mathcal{T}\{A B\} = \mathcal{T}\{A\}\mathcal{T}\{B\}. \quad (4.23)$$

**Theorem 4.4.2** (Additive Property of two Toeplitz Matrices). *The Toeplitz transform of the sum of two  $T$  periodic matrices of the same dimension,  $A(t)$  and  $B(t)$ , is the sum of its transforms*

$$\mathcal{T}\{A + B\} = \mathcal{T}\{A\} + \mathcal{T}\{B\} . \quad (4.24)$$

**Definition 4.4.2** (Unitary Matrices). *Consider the absolutely convergent series*

$$\dot{A}(t) = \sum_{n=-\infty}^{\infty} jn\omega_p A_n e^{jn\omega_p t}$$

as  $\dot{A} \in (L_2[0, T], \mathbb{C}^{n \times n})$ . *The Toeplitz transform of the matrix  $\dot{A}$  is defined as*

$$\mathcal{T}\{\dot{A}\} = \mathcal{N}\mathcal{T}\{A\} - \mathcal{T}\{A\}\mathcal{N} \quad (4.25)$$

where the matrix  $\mathcal{N}$ , which contains multiples of the pumping frequency  $\omega_p$  is defined as

$$\begin{aligned} \mathcal{N} &= \text{blkdiag}\{jn\omega_p I\} \forall n \in \mathbb{Z} \\ &= \begin{bmatrix} j\omega_p & & 0 \\ & \ddots & \\ 0 & & jn\omega_p \end{bmatrix} \forall n \in \mathbb{Z} . \end{aligned} \quad (4.26)$$

This Chapter presented an overview in the mathematical preliminaries necessary to construct the foundation of linear time periodic systems. The next Chapter will develop the linear time periodic system theory and define the state space representation of such a system.

## V. Linear Time Periodic System Theory

This Section will describe the formation of the Linear Time Periodic system in terms of the state space. The linear time periodic state space representation is essential to later chapters in system parameter validation and control. In the upcoming chapters linear time periodic analogues of system parameter validation and optimal control methods will build upon existing state space based LTI methods. These efforts will first require a linear time periodic state space operator, which this chapter will detail.

### 5.1 *The Continuous Time Invariant Linear State Model*

The linear continuous time state model is a matrix representation of several first order linear differential Equations. This matrix representation presents a linear mapping of the input to output response of the linearised system dynamics. The standard representation of the state space model is seen in Equations 5.1 and 5.2.

$$\dot{x}(t) = A(t)x(t) + B(t)u(t) \quad (5.1)$$

$$y(t) = C(t)x(t) + D(t)u(t) \quad (5.2)$$

In this form the states of the system are represented as the vector  $x(t) \in \mathbb{R}^{n_x}$  which act upon the system *State* or *Plant* matrix,  $A(t) \in \mathbb{R}^{n_x \times n_x}$ . The vector  $u(t) \in \mathbb{R}^{n_u}$  represents the system input which acts upon the system *Control* matrix  $B(t) \in \mathbb{R}^{n_x \times n_u}$ , as seen in the *state equation* 5.1. The system output,  $y(t)$ , as seen in the *output equation* 5.2, is composed of the the state vector  $x(t)$  acting upon the system *Output* matrix  $C(t) \in \mathbb{R}^{n_y \times n_x}$  and control vector  $u(t)$  acting upon the *Feed Forward* matrix  $D(t) \in \mathbb{R}^{n_y \times n_u}$ . It is important to note that the  $A(t)$ ,  $B(t)$ ,  $C(t)$  and  $D(t)$  matrices are functions of time, or *time varying*.

The state model in Equations 5.1 and 5.2 can be simplified by assuming the plant, control, output, and feed-forward matrices are not functions of time. By using

this assumption the *Linear Time Invariant*(LTI) state model can be described as

$$\dot{x}(t) = Ax(t) + Bu(t) \quad (5.3)$$

$$y(t) = Cx(t) + Du(t) . \quad (5.4)$$

As a note, the state model representation seen in Equations 5.3 and 5.4 is the most prevalent matrix form encountered when dealing with linear models, as most systems are simplified by assuming time invariance. This is seen in modern linear optimal control theory [25,26] and optimal state estimation theory [9].

In order to identify the state vector  $x(t) \forall t \geq 0$  for linear time invariant systems the input vector  $u(t)$  and the initial state vector at time zero,  $x(0)$  is used, as seen in Equation 5.5

$$x(t) = \Phi(t, t_0)x(0) + \int_0^t \Phi(t, \tau)Bu(\tau)d\tau . \quad (5.5)$$

In the above Equation 5.5 the *State Transition matrix*( $\Phi(t, t_0)$ ) is required. The state transition matrix is defined for a linear time invariant system as the matrix exponential in Equation 5.6

$$\Phi(t) = e^{At} \quad (5.6)$$

where the matrix exponential can be described by the power series of Equation 5.7.

$$e^{At} = I + At + \frac{1}{2!}A^2t^2 + \frac{1}{3!}A^3t^3 + \dots . \quad (5.7)$$

Thus, substituting the relation depicted in Equation 5.6 into Equation 5.5 the expression for the state vector  $x(t)$  is then redefined as seen below.

$$x(t) = e^{At}x(0) + \int_0^t e^{A(t-\tau)}Bu(\tau)d\tau \quad (5.8)$$

Using the same procedure as the state vector, the system output,  $y(t)$ , is defined in a similar fashion.

$$y(t) = Ce^{At}x(0) + \int_0^t Ce^{A(t-\tau)}Bu(\tau)d\tau + Du(t) . \quad (5.9)$$

*5.1.1 Transfer Functions for LTI Systems.* Determining the system response for LTI systems can be accomplished by way of the method outlined in Equation 5.9. This method, however, operates in the time domain and requires convolution, which generally limits its applicability. By transforming the LTI system into the frequency domain by the *Laplace* transform ( $\mathcal{L}$ ) the process of determining system response is greatly simplified.

In order to determine the frequency domain transfer function of the system,  $G(s)$ , the Laplace transform of the time domain state equations in Equations 5.3 and 5.4 is performed, producing

$$sX(s) - x(0) = AX(s) + BU(s) \quad (5.10)$$

$$Y(s) = CX(s) + DU(s) . \quad (5.11)$$

The notation  $X$ ,  $Y$  and  $U$  represent the Laplace transforms of  $x$ ,  $y$  and  $u$ . With the use of Equations 5.10 and 5.11 the Laplace transformed output Equation 5.9 is then  $Y(s) = \mathcal{L}[y(t)]$ , or as represented below.

$$Y(s) = C(sI - A)^{-1}x(0) + [C(sI - A)^{-1}B + D]U(s) \quad (5.12)$$

The Laplace transform of the time domain impulse response matrix( $g(t)$ ) results in the Laplace transfer function, or more commonly referred to, the *Transfer function*( $G(s)$ )

$$G(s) = \mathcal{L}[g(t)] \quad (5.13)$$

$$= C(sI - A)^{-1}B + D . \quad (5.14)$$

By using the relation in Equation 5.14 the output equation  $Y(s)$  in Equation 5.12 can be restated as seen below.

$$Y(s) = G(s)U(s) . \quad (5.15)$$

*5.1.2 Frequency Response for LTI Systems.* The term *frequency response* refers to the steady state response of a system to a sinusoidal input signal. Frequency response methods, such as the *Bode* [25] plot display the system response over a varying range of input frequencies. The system response is generally measured in terms of the magnitude of the output signal and the phase difference between the input and output.

Frequency response characteristics have varying properties depending on the description of the system model. In the case of LTI systems, the input and output frequencies are the same while having different magnitude and phase differences as noted above. Other systems, such as LTP models, the input and output frequencies vary. This is an important distinction and will be covered in

For LTI systems the input signal used for frequency response is the *exponentially modulated sinusoid* ( $u_0 e^{st}$ ) as seen in Equation 5.16.

$$u(t) = u_0 e^{st} \quad s \in \mathbb{C}, \quad u_0 \in \mathbb{C}^m . \quad (5.16)$$

By using the definition of the Laplace transfer function in Equation 5.14 the system output can be described as the product of it and the input of Equation 5.16.

$$Y(s) = G(s)u_0 e^{st} . \quad (5.17)$$

The magnitude for *single input-single output* (SISO) systems is defined as the modulus of the transfer function  $|G(s)|$ .

$$|G(s)| = \sqrt{\text{real}(G(s))^2 + \text{imag}(G(s))^2} \quad (5.18)$$

The magnitude of the system is also referred to as the system *gain*. The phase angle( $\angle(G(s))$ ) for SISO systems is defined as seen in Equation 5.19.

$$\angle(G(s)) = \text{Arctan}\left(\frac{\text{imag}(G(s))}{\text{real}(G(s))}\right) \quad (5.19)$$

For *multi input-multi output*(MIMO) systems the concept of magnitude and phase are interpreted differently then those of SISO systems. The response magnitude for MIMO system is defined as seen in 5.20.

$$\text{Magnitude} = \frac{\|G(s)u_0\|}{\|u_0\|} \quad (5.20)$$

where  $\|\cdot\|$  is the *2-Norm* or *Euclidean* norm

$$\|\alpha\| = \sqrt{\alpha_1^2 + \alpha_2^2 + \cdots + \alpha_n^2}. \quad (5.21)$$

The MIMO system response is different from that of the SISO system as the magnitude response is defined over a range

$$\min_{u_0} \frac{\|G(s)u_0\|}{\|u_0\|} \leq \text{Magnitude} \leq \max_{u_0} \frac{\|G(s)u_0\|}{\|u_0\|} \quad (5.22)$$

as the magnitude in this case is dependent on both  $u_0$  and  $\{s : s = j\omega\}$ . Conventionally,  $u_0$  is normalized to unity  $\|u_0\| = 1$ . An example of the principal gains of a MIMO system is seen in Figure 5.1 The SVD approach outlined in Section 4.3 is commonly used as a method for determining the MIMO system gains as the method outlined in Equation 5.20 can be overly complex for a large systems. By performing the SVD on the transfer function  $G(s)$  for ever frequency over  $\{s : s = j\omega\}$ , the system *principal gains* are then the frequency dependent singular values,  $\sigma$ . The principal gains are determined over a range, as outlined in Equation 5.22. The MIMO phase relation for frequency response is undefined as there is no convenient way to describe it. This is due to each input-output relationship having a different phase shift.

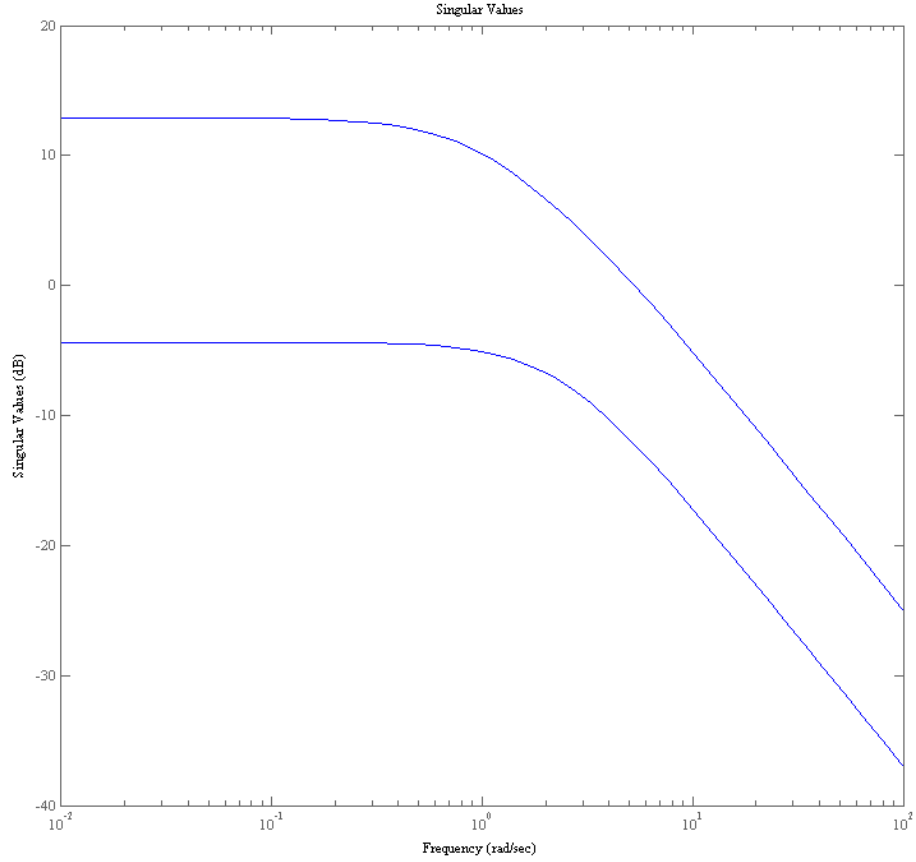


Figure 5.1: Principal Gains of a MIMO LTI system [2].

## 5.2 Signal Spaces for LTI and LTP Systems

Before the transfer function and frequency response of the LTP system are explained it is important to first describe the differences in the signal spaces of LTI vs. LTP systems.

A LTI system having a *sinusoidal input signal* of frequency ( $\omega_f$ ) will map an output signal of  $\omega_n$  but with different magnitude and phase than the input signal. Thus, the signal spaces are identical, as the input and output are both complex exponential sinusoids of frequency  $\omega_f$ . This response for a LTI system is clearly seen

in a Bode plot, as phase and magnitude of the system are plotted over the entire range of input frequency ,  $\omega_f \in (0, \infty)$ .

A LTP system differs from a LTI system by the system parameters varying periodically rather than remaining constant, or *time invariant*. Consider a LTP system defined as such by having a time periodic input matrix,  $B$ . In this case the steady state forced response signal of a LTP system will be composed of the sinusoidal input signal  $\omega_f$  and the pumping frequency input signal  $\omega_p$ , as seen in Figure 5.2. In this Figure

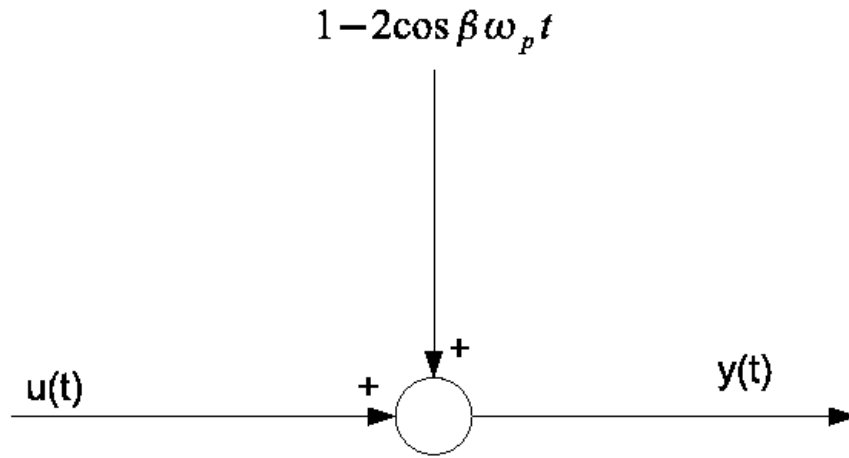


Figure 5.2: A Simple LTP System [42].

an input signal,  $u(t)$ , is convoluted with a time periodic gain  $1 - 2\beta \cos \omega_p t$ . Thus, the output signal,  $y(t)$ , is a convolution of signals best described by Fourier series containing the frequencies  $\omega_f \pm n\omega_p : \omega_f \in \mathbb{C}, n \in \mathbb{Z}$ , which is an infinite dimension signal space. Clearly the input and output spaces are not the same dimension as in the case of the LTI system spaces. This difference in signal spaces differentiates the LTP system from LTI systems, as the mapping of signal spaces from input to output is not an *isomorphism*, being *one-to-one* and *onto*, but rather a *one-to-many* mapping as seen in Figure 3.1. To overcome the difference in signal spaces, Wereley [42] devel-

opened the concepts of *Geometrically periodic signals* and the identical *Exponentially modulated periodic signal*, which will now be covered.

**5.2.1 Geometrically Periodic Signals.** From Floquet analysis of a LTP system the steady state response at the time  $t$  is related to the system response a full period later at time  $t + T$  by the relation in Equation 5.23

$$x(t + T) = zx(t), z \in \mathbb{C} \quad (5.23)$$

where the complex scalar  $z \in \mathbb{C}$  is defined as

$$z = e^{sT} \quad (5.24)$$

and as a note  $s = j\omega$ . By using the relation defined in Equation 5.23 the system response  $N$  periods later,  $(t + NT)$ , is defined in Equation 5.25

$$x(t + T) = z^N x(t), z \in \mathbb{C} . \quad (5.25)$$

In order to achieve a linear mapping Wereley [42] noted the input signal must be of the form of Equation 5.25, which led to his development of the *Geometrically periodic signal*, as defined in 5.2.1

**Definition 5.2.1** (Geometrically Periodic Signals [42]). *A geometrically periodic signal (GP),  $u(t)$ , having a pumping frequency  $\omega_p$  and period  $T$  is defined as*

$$u(t + T) = z^N u(t), z \in \mathbb{C} \quad (5.26)$$

*if there exists a nonzero  $z \in \mathbb{C}$  and  $N \in \mathbb{N}$ .*

**5.2.2 Exponentially Modulated Periodic Signals.** Wereley [42] further provided that the definition of the geometrically periodic signal can be similarly expressed as a complex exponential modulation of a periodic signal, as seen in definition 5.2.2

**Definition 5.2.2** (Exponentially Modulated Periodic Signals [42]). *A exponentially periodic signal (EMP),  $u(t)$ , is defined as the complex Fourier series expansion of a periodic signal having a pumping frequency  $\omega_p$  and period  $T$ , modulated by a complex exponential signal  $e^{sT} \forall s \in \mathbb{C}$*

$$\begin{aligned} u(t) &= e^{sT} \sum_{n=-\infty}^{\infty} u_n e^{jn\omega_p t} \\ &= \sum_{n=-\infty}^{\infty} u_n e^{s_n t} \quad |t \geq 0, s_n = s + jn\omega_p. \end{aligned} \quad (5.27)$$

The exponentially modulated periodic signal will be used extensively in the development of the the state space form of the LTP system, which will be covered next.

### 5.3 LTP Transfer Functions

The linear operator for LTI systems is the well known Transfer function ,  $G(s)$ . As was covered in Section 5.1.1 the Transfer function can be described by relating the matrices  $A, B, C, D$  of the state space form as seen in Equation 5.14, which is restated below

$$G(s) = C(sI - A)^{-1}B + D.$$

For LTI systems the frequency response is directly related to the transfer function  $G(s)$  due to the fact that in steady state the input to output signal maintains the same frequency but different magnitude and phase. Therefore, the input and output signal spaces are of the same dimension. As noted in Section 5.2 the differences in input to output signal spaces precludes the direct application of the LTI form of the transfer function for LTP systems. By modifying the input signal space by use of the *EMP* signal from Section 5.2.2, however, a convenient form similar to Equation

5.14 can be used for LTP systems. This is accomplished by the method of *Harmonic Balance*

*5.3.1 Harmonic Balance.* Analysis techniques, such as stability analysis, for LTP systems is the *method of Harmonic Balance*. This method originated in the late 19th century by Hill [11] on his work to determine the stability analysis techniques of linear periodic systems, in this case the Lunar perigee. This technique will be briefly described as it is the fundamental building block in the development of the state space linear operator form for LTP systems.

Before the *principle of Harmonic Balance* is defined a review of the properties of the Fourier series must first be covered. Fourier series expansions, being either Trigonometric or complex, of harmonic functions involve the expansion of the parametric excitation into a set of basis function. These basis functions, in this case sinusoids, form an orthonormal basis over the fundamental period. As was covered in Section 4.1.1, the elements of an orthonormal basis are linearly independent and therefore the coefficients that multiply each basis function in a Fourier series must vanish for each harmonic independently. For any linear periodic system whose periodic parameters are expanded by the Fourier series, that series expansion is referred to as the *Harmonic Balance*. The *Principle of Harmonic Balance* refers to the requirement that the individual coefficients that multiply the elements of the Harmonic must vanish independently.

The *principle of harmonic balance* as formed by Hill [11] used a exponential Fourier series which was modulated by a complex exponential. This can be seen by determining the state vector solution to a periodic dynamic equation, such as the *Hill* differential equation in Equation 5.28

$$\ddot{x} + [a - 2q\psi(t)]x(t) = 0 \quad (5.28)$$

where  $\psi(t)$  is defined as the *parametric excitation*( $\psi(t)$ ) having fundamental period  $T$ . Thus,  $\psi(t) = \psi(t + T)$ . Additionally, the parameter  $q$  is referred to as the *pumping amplitude*( $q$ ) and the parameter  $a$  is referred to as a *constant portion of the time periodic coefficient of  $x(t)$* . As  $\psi(t)$  is T-Periodic, it can be described as by the complex Fourier series, as seen in Equation 5.29.

$$\psi(t) = \sum_{n=-\infty}^{\infty} \psi_n e^{jn\omega_p t} \quad (5.29)$$

where  $\omega_p$  is the pumping frequency of the harmonic function. The assumed solution to the periodic Equation 5.28, as proposed by Hill [11] uses the Fourier series in Equation 5.30.

$$x(t) = e^{st} \sum_{n=-\infty}^{\infty} x_n e^{jn\omega_p t} . \quad (5.30)$$

By substituting Equation 5.30 and 5.29 into Equation 5.28 , and noting that the set of functions  $\{e^{jn\omega_p} : n \in \mathbb{Z}\}$  forms a set of orthonormal basis functions in  $L_2$  on the interval  $[0, T]$ , the principal of harmonic balance can be applied to the resulting equation, as seen in Equation 5.31

$$0 = [(s + jn\omega_p)^2 + a]x_n - 2q \sum_{m=-\infty}^{\infty} \psi_m x_{n-m} . \quad (5.31)$$

By the application of the principle of harmonic balance, the above equation results in an infinite set of simultaneous equations. Hill developed the determinant of the infinite set in Equation 5.31 to determine the stability characteristics of periodic functions as a function of the periodic parameters of the function, as in  $a$  and  $q$  in the Hill equation.

The form of the series expansion used in Equation 5.31 was adopted by Wereley [42] to develop a linear operator for periodic systems in state space form. This was principally done by adopting the use of the exponentially modulated periodic signal

from Section 5.2.2 in a similar manner as Hill took in Equation 5.30. This will be covered next as the *Harmonic Balance State Space Model* for LTP systems is discussed.

*5.3.2 Harmonic Balance State Space Model.* As discussed in Section 5.2 the signal spaces of LTP systems are not equal, which precludes the development of a linear operator describing the input-output mapping of a signal having the same input and output spaces. Wereley [42] has demonstrated that by using an exponentially modulated periodic signal (EMP) as an input signal to a LTP system, an input signal to a LTP system maps an EMP input signal to an EMP output signal having the same frequency but not the same magnitude or phase as the input signal. This is significant, as the input and output signal spaces are equal, thus the concept of a linear operator is now possible to describe for a LTP system. As a reminder, the exponentially modulated periodic signal is described in Section 5.2.2. Also, the magnitude differences in input-output mapping of a LTP system refer to the amplitude of all included harmonics in the input and output signals. As a linear operator has been shown to exist for LTP systems, as stated above, the principle of harmonic balance will now be applied to transform a LTP system to state space form.

The principal element to provide equal input and output signal spaces is the EMP input signal,  $u(t)$ , of Equation 5.27, and restated below

$$\begin{aligned} u(t) &= e^{sT} \sum_{n=-\infty}^{\infty} u_n e^{jn\omega_p t} \\ &= \sum_{n=-\infty}^{\infty} u_n e^{s_n t} \mid t \geq 0, s_n = s + jn\omega_p . \end{aligned}$$

Next, by using an approach similar to Hill to provide steady state response to of a LTP signal to an EMP signal, as in Equation 5.30, Wereley [42] and later Hwang [12]

provide the steady state response as

$$x(t) = \sum_{n=-\infty}^{\infty} x_n e^{s_n t} \quad |t \geq 0, s_n = s + jn\omega_p \quad (5.32)$$

$$\dot{x}(t) = \sum_{n=-\infty}^{\infty} s_n x_n e^{s_n t} \quad |t \geq 0, s_n = s + jn\omega_p . \quad (5.33)$$

In a likewise approach, the output signal of a LTP system,  $y(t)$ , is a linear combination of the state and control and thus is described as

$$y(t) = \sum_{n=-\infty}^{\infty} y_n e^{s_n t} \quad |t \geq 0, s_n = s + jn\omega_p . \quad (5.34)$$

Now, considering the form of a LTP system in state space form in Equations 5.1 and 5.2, as restated below

$$\begin{aligned} \dot{x}(t) &= A(t)x(t) + B(t)u(t) \\ y(t) &= C(t)x(t) + D(t)u(t) . \end{aligned}$$

It is important to note that the matrices  $[A(t), B(t), C(t), \text{ and } D(t)]$  are *T-periodic* and can be expanded by the Fourier series, as seen in Equation 5.35 for the plant matrix,  $A(t)$ .

$$A(t) = \sum_{n=-\infty}^{\infty} A_n e^{s_n t} \quad |t \geq 0, s_n = s + jn\omega_p . \quad (5.35)$$

As a note, all the remaining matrices  $[B(t), C(t), \text{ and } D(t)]$  can be expressed as in Equation 5.35. Next, by substituting Equations 5.32, 5.33, 5.34 and 5.35 along with the similar approaches for  $[B(t), C(t), \text{ and } D(t)]$  the LTP state space form can be

restated as in Equation 5.36

$$\begin{aligned}
\sum_{n=-\infty}^{\infty} x_n e^{s_n t} &= \sum_{n=-\infty}^{\infty} A_n e^{s_n t} \sum_{m=-\infty}^{\infty} x_m e^{s_m t} + \sum_{n=-\infty}^{\infty} B_n e^{s_n t} \sum_{m=-\infty}^{\infty} u_m e^{s_m t} \\
&= \sum_{n,m=-\infty}^{\infty} A_n x_m e^{s_{n+m} t} + \sum_{n,m=-\infty}^{\infty} B_n u_m e^{s_{n+m} t} \\
&= \sum_{n,m=-\infty}^{\infty} A_{n-m} x_m e^{s_n t} + \sum_{n,m=-\infty}^{\infty} B_{n-m} u_m e^{s_n t} .
\end{aligned} \tag{5.36}$$

A likewise approach can be made for the output,  $y(t)$ , as seen in Equation 5.37

$$\sum_{n=-\infty}^{\infty} y_n e^{s_n t} = \sum_{n,m=-\infty}^{\infty} C_{n-m} x_m e^{s_n t} + \sum_{n,m=-\infty}^{\infty} D_{n-m} u_m e^{s_n t} . \tag{5.37}$$

Next, by moving all terms of Equation 5.36 and 5.37 to the right hand side and then multiplying through by  $e^{-s t}$  results in

$$0 = \sum_{n=-\infty}^{\infty} \left[ s_n x_n - \sum_{m=-\infty}^{\infty} A_{n-m} x_m + \sum_{m=-\infty}^{\infty} B_{n-m} u_m \right] e^{s_n t} \tag{5.38}$$

$$0 = \sum_{n=-\infty}^{\infty} \left[ y_n - \sum_{m=-\infty}^{\infty} C_{n-m} x_m + \sum_{m=-\infty}^{\infty} D_{n-m} u_m \right] e^{s_n t} . \tag{5.39}$$

Now, by the *principle of harmonic balance* from Section 5.31, the terms within the brackets in Equation 5.39 are linearly independent and therefore must be null to avoid a trivial solution. Therefore, the state model of Equation 5.39 can be restated  $\forall n \in \mathbb{Z}$  as

$$s_n x_n = \sum_{m=-\infty}^{\infty} A_{n-m} x_m + \sum_{m=-\infty}^{\infty} B_{n-m} u_m \tag{5.40}$$

$$y_n = \sum_{m=-\infty}^{\infty} C_{n-m} x_m + \sum_{m=-\infty}^{\infty} D_{n-m} u_m . \tag{5.41}$$

The input-output relation stated in Equation 5.41, while functional, is difficult to use due to the summations. By applying the *Toeplitz* transformation from Section 4.4 to

the T-periodic matrices  $A(t)$ ,  $B(t)$ ,  $C(t)$ ,  $D(t)$ , Wereley [42] simplified Equation 5.41, as defined below.

**Definition 5.3.1** (Harmonic State Space Model [42]). *The Toeplitz transformation of the T-Periodic matrices of Equation 5.41 are expressed as the doubly infinite matrix equation*

$$sx = (\mathcal{A} - \mathcal{N})x + \mathcal{B}u \quad (5.42)$$

$$y = \mathcal{C}x + \mathcal{D}u \quad (5.43)$$

where  $\mathcal{N}$ , originally defined in Equation 4.26, represents a doubly infinite block diagonal matrix consisting of all of the pumping frequency harmonics,  $n\omega_p$

$$\mathcal{N} = \text{blkdiag}\{jn\omega_p I\} \forall n \in \mathbb{Z} . \quad (5.44)$$

Additionally the state, control, and output vectors are doubly infinite, as stated as

$$x = \begin{bmatrix} \vdots \\ \mathbf{x}_{-2} \\ \mathbf{x}_{-1} \\ \mathbf{x}_0 \\ \mathbf{x}_1 \\ \mathbf{x}_2 \\ \vdots \end{bmatrix} \quad u = \begin{bmatrix} \vdots \\ \mathbf{u}_{-2} \\ \mathbf{u}_{-1} \\ \mathbf{u}_0 \\ \mathbf{u}_1 \\ \mathbf{u}_2 \\ \vdots \end{bmatrix} \quad y = \begin{bmatrix} \vdots \\ \mathbf{y}_{-2} \\ \mathbf{y}_{-1} \\ \mathbf{y}_0 \\ \mathbf{y}_1 \\ \mathbf{y}_2 \\ \vdots \end{bmatrix}$$

The Toeplitz transformed T-periodic  $A, B, C, D$  matrices are made of the complex Fourier coefficients of the matrices, as covered in Section 4.22. For example, the plant matrix

$A(t)$  is defined as

$$\mathcal{A} = \begin{bmatrix} \ddots & \vdots & \vdots & \vdots & \vdots & \vdots & \\ \cdots & \mathbf{A}_0 & \mathbf{A}_{-1} & \mathbf{A}_{-2} & \mathbf{A}_{-3} & \mathbf{A}_{-4} & \cdots \\ \cdots & \mathbf{A}_1 & \mathbf{A}_0 & \mathbf{A}_{-1} & \mathbf{A}_{-2} & \mathbf{A}_{-3} & \cdots \\ \cdots & \mathbf{A}_2 & \mathbf{A}_1 & \mathbf{A}_0 & \mathbf{A}_{-1} & \mathbf{A}_{-2} & \cdots \\ \cdots & \mathbf{A}_3 & \mathbf{A}_2 & \mathbf{A}_1 & \mathbf{A}_0 & \mathbf{A}_{-1} & \cdots \\ \cdots & \mathbf{A}_4 & \mathbf{A}_3 & \mathbf{A}_2 & \mathbf{A}_1 & \mathbf{A}_0 & \cdots \\ & \vdots & \vdots & \vdots & \vdots & \vdots & \ddots \end{bmatrix} \quad (5.45)$$

where the matrices  $B, C,$  and  $D$  are described using the same methodology as described in Equation 5.45.

Now that the harmonic state space form has been defined in a manner similar to the LTI form, the transfer function for periodic systems can now be defined in a manner similar to a LTI system. By using the LTP harmonic state space model from definition 5.3.1 the input-output relationship between the input harmonics,  $\{u_n : n \in \mathbb{Z}\}$ , and the output harmonics,  $\{y_n : n \in \mathbb{Z}\}$ , can be described by the *harmonic transfer function*,  $\widehat{G}(s)$ .

**Definition 5.3.2** (Harmonic Transfer Function). *The harmonic transfer function,  $\widehat{G}(s)$ , is an infinite dimensional matrix of Fourier coefficients relating the input harmonics,  $\{u_n : n \in \mathbb{Z}\}$ , and the output harmonics,  $\{y_n : n \in \mathbb{Z}\}$ , described as*

$$y = \widehat{G}(s)u \quad (5.46)$$

where

$$\widehat{G}(s) = \mathcal{C}[s\mathcal{I} - (\mathcal{A} - \mathcal{N})]^{-1}\mathcal{B} + \mathcal{D} \quad (5.47)$$

as long as the inverse  $[s\mathcal{I} - (\mathcal{A} - \mathcal{N})]^{-1}$  exists.

This chapter presented the fundamentals of linear time periodic systems, with an emphasis on the state space form. The next chapter will develop the Cramer-Rao bound in a manner similar to LTI systems by using the LTP state space form developed in this chapter.

## VI. Linear Time Periodic System Parameter Validation via the Cramer-Rao Lower Bound

The intent of this research, as stated previously, is to develop a more accurate method of rotor smoothing by way of controlling a verifiably accurate rotor system model. In the last chapter the concept of the linear time periodic model was developed, which provides the foundation for an accurate helicopter rotor in forward flight. The identified parameters that populate that LTP model, however, must be accurate in order to provide a basis for an effective controller. This chapter will present the development of the Cramer-Rao lower bound for a linear periodic system in order to validate the identified system parameters.

### 6.1 *Introduction*

Helicopter rotors are subject to vibratory forces from a variety of sources. In forward flight, vibratory forces at integer harmonics of the rotor speed are generated because the velocity of the blades with respect to the air is inherently periodic. In hover, vibratory forces in the plane of the rotor disk are generated as a result of mass imbalances in the rotor blades; and out-of-plane vibratory forces result from an unsymmetric distribution of lift caused by aerodynamic dissimilarities among the blades. These vibratory forces have a period equal to the rotor period of revolution (one-per-rev). While other sources of vibration also exist, the main rotor system generates by far vibrations of the largest magnitude. Over time, the vibrations produced by the main rotor will result in damage to the aircraft, and can compromise the effectiveness of the crew. While vibratory loads in forward flight are to some degree unavoidable, the one-per-rev vibratory loads due to mass and aerodynamic imbalances can be minimized through proper and regular maintenance.

Improving maintenance procedures for eliminating one-per-rev vibrations for helicopter main rotors (rotor smoothing) has been an area of active interest since the early days of helicopters, when those procedures were called track and balance. The current state-of-the-art in rotor smoothing techniques, while improving, is still

costly and time consuming. One of the principle reasons for the inefficiency of current rotor smoothing maintenance methods is that they all require multiple iterations; each necessitating a separate test flight followed by maintenance actions to adjust blade mass, pitch link length, or trim tab angle, until the vibrations are reduced to an acceptable level. In order to minimize the number of iterations required to achieve an acceptable vibration level, one must accurately predict the optimal set of adjustments. These predictions rely exclusively on a having an accurate plant model of the entire aircraft, since fuselage characteristics affect where and how much vibration is sensed.

In order to develop an accurate model of a helicopter, the parameters that define the system must be accurately identified. While it is obvious that different helicopter types require different models, it may be less obvious that individual helicopters of the same type may have significant differences that require modifications to the parameters, and that those parameters may change over time [18]. Therefore, it is important to be able to identify an aircraft's parameters 'on the fly'. Several of the most current rotor smoothing methods use system identification methods based on either a linear least squares approximation [24], or a neural network approximation [39, 43]. Due to the high cost of flight tests, these methods typically depend on a very small dataset, usually obtained from a single aircraft.

Regardless of the size of the dataset used to create the aircraft model, or the number of different aircraft used, it is equally important that the parameters identified for an aircraft are verifiably accurate. For linear, time invariant (LTI) systems, the accuracy of identified parameters can be verified using the Cramer-Rao bound. However, a helicopter rotor is time periodic, so the Cramer-Rao bound for LTI systems is not valid. The objective of this chapter is to develop the theory necessary to define the Cramer-Rao bound for a linear, time periodic (LTP) system. With such a tool, plant models derived from identified parameters for LTP systems can be verified by examining the Cramer-Rao bound of each parameter for accuracy, and adjustments can be made to improve model accuracy.

This chapter begins briefly describing the Cramer-Rao bound as used to determine parameter accuracy. Next, the *Maximum Likelihood Estimator*(MLE) will be defined, as it forms a direct link to the formulation of the Cramer-Rao lower bound. Next, to provide a solid foundation for the reader, the definitions of several statistical methods used to define the Cramer-Rao inequality are presented. In turn, the Cramer-Rao inequality is then formulated based on the MLE. Finally, by way of the definition of the Cramer-Rao inequality, the Cramer-Rao lower bound is defined for individual parameters of a LTP system in state space form. The effectiveness of the Cramer-Rao lower bound is demonstrated at the conclusion to this chapter through a short example depicting parameter accuracy for a LTP system.

## **6.2 General Description of the Cramer-Rao Lower Bound**

The parameters determined by system identification methods define a linearized vehicle model, which in turn defines the dynamic characteristics of that vehicle. These models are then used in simulators, control system design, and are used to validate wind tunnel parameter predictions. Maine and Iliff [34] point out that it is important to remember that parameters obtained from testing are only estimates, and not exact values. This fact, unfortunately, is often disregarded and only rarely are the parameters ever verified for accuracy. Maine and Iliff [34] further state that if accurate parameter estimates cannot be distinguished from worthless estimates, then all estimates must be assumed to be of questionable accuracy. It is for these reasons that parameter validation methods have been developed for linear, time invariant (LTI) systems such as those cited in Refs. [34] and [3].

As stated in Section 6.1, the intent of this research is to improve LTP modeling for controller development, with specific application for alleviating main rotor vibrations through the use of rotor smoothing techniques. The measure of accuracy of the model parameters of the identified rotor system are of critical importance in this application as they will determine the effectiveness of the vibration control implementation. Implementing a controller based on an unverified model may have disastrous

results, as the commanded control inputs are based on a model that does not match the true rotor system dynamics.

The Cramer-Rao bound is a method commonly used in flight testing to establish the accuracy of identified parameters of a linearized vehicle model. As demonstrated by Maine and Iliff [34], the Cramer-Rao lower bound gives the theoretical lower limit to the accuracy of parameter estimates by an optimal estimator. This measure of accuracy is based on the *uncertainty ellipsoid* and is similar to other measures of accuracy such as estimated variance and standard deviation. The Cramer-Rao bound is similar to these methods except that the Cramer-Rao bound is the square root of the variance. By examining the Cramer-Rao bound for each parameter estimated from flight test, one can determine the accuracy of the data by evaluating the size of the bounds. The Cramer-Rao bound establishes the standard deviation of an identified model parameter, therefore, large bounds indicate poor estimation performance. This method provides greater insight into the accuracy of estimated parameters than simply examining the scatter of parameter estimates from flight test data at each point, as seen in Figure 6.1.

Upon review of Figure 6.1, one can see that the Cramer-Rao bound indicates that data below -10 degrees is unreliable, even though the data scatter is not very large. Thus, an examination of the Cramer-Rao bounds for estimated vehicle model parameters provides a basis for an evaluation of whether the parameters have been estimated properly, or whether they should either be re-evaluated or adjusted by the engineer before they are used in the vibration control model.

### ***6.3 The Maximum Likelihood Estimator***

As stated by References [34] and [10], the *Maximum Likelihood Estimator* (MLE) is by far the most commonly used technique for estimating parameters. The MLE is a method that relates the a sampled vector of *Independent and Identically Distributed random values* (*iid*) to a vector of 'true' values in an attempt to discern differences

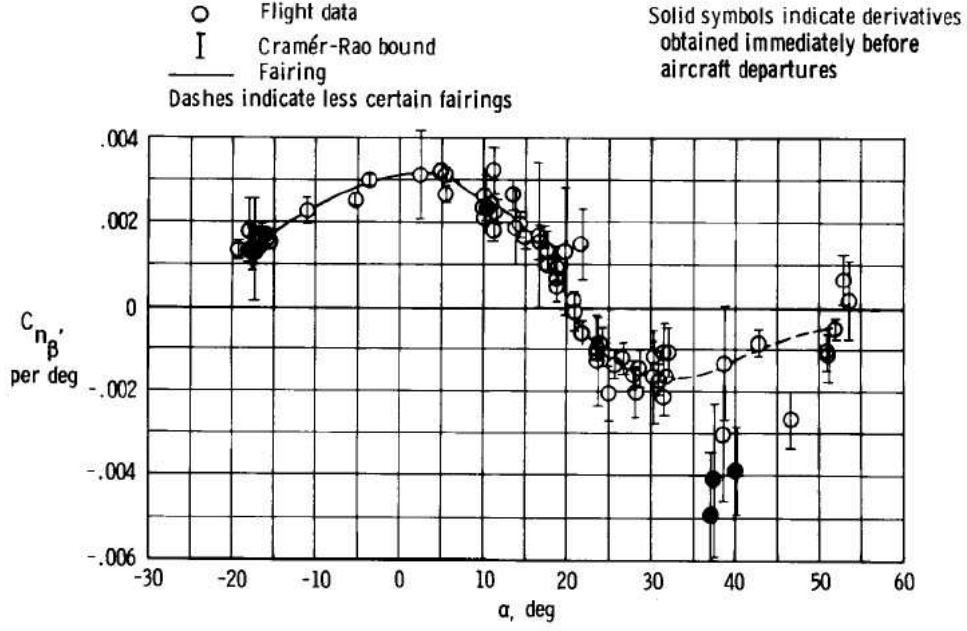


Figure 6.1: Example of Cramer-Rao Bounds for Parameter Estimates [34].

between the two vectors. Before the MLE is defined, the concept of an *iid* sample is first defined as follows:

**Definition 6.3.1** (Independent and identically distributed random variables(iid)).  
*The random variables  $X_1, \dots, X_n$  are defined as independent and identically distributed random variables if  $X_1, \dots, X_n$  are mutually independent random variables from a probability density function(pdf) of the same function  $F(x)$ .*

Thus, with a *iid* sample  $X_1, \dots, X_n$  from a pdf  $f(x|\theta_1, \dots, \theta_k)$ , the likelihood function is defined according to reference [10] in Equation 6.1.

$$L(\theta|\mathbf{X}) = \prod_{i=1}^n f(x_i|\theta_1, \dots, \theta_k) . \quad (6.1)$$

The likelihood function defined in Equation 6.1 is simply a measure of the plausibility, or *likelihood*, of the variable  $\theta_i$  to the vector of sample data points,  $\mathbf{X}$ . Having defined the likelihood function, the *maximum likelihood estimator* can now be stated as in definition 6.3.2.

**Definition 6.3.2** (Maximum Likelihood Estimator). *The maximum likelihood estimator of the variable  $\theta$  is defined as the estimate of the value  $\theta_1, \dots, \theta_k$  that maximises the likelihood function,  $L(\theta|\mathbf{x})$ . Thus, for each sample point  $\mathbf{x}$ , let  $\hat{\theta}(\mathbf{x})$  be a parameter value at which  $L(\theta|\mathbf{x})$  attains a maximum value as a function of  $\theta$  while holding  $\mathbf{x}$  fixed.*

The MLE can be produced by differentiation of the likelihood function, however direct maximization through an optimization function is generally the method of choice to identify the parameter  $\theta$ .

The form of the likelihood function commonly used for the MLE is based on *Gaussian* distribution, and is referred to as the *normal likelihood* function. For the construction of the normal likelihood function, let  $\hat{x} = \theta(x)$  be the predicted output based on the postulated value  $\theta$ . Thus, the normal likelihood function is defined as

$$\begin{aligned} L(\theta|\mathbf{x}) &= \prod_{i=1}^n f(x_i|\theta_1, \dots, \theta_k) \\ &= \prod_{i=1}^n \left[ \frac{1}{2\pi|R|} \right]^{1/2} e^{-\frac{1}{2}[(\hat{x}_i - x_i)^T R^{-1}(\hat{x}_i - x_i)]} \\ &= \left[ \frac{1}{2\pi|R|} \right]^{n/2} e^{-\frac{1}{2} \sum_{i=1}^n [(\hat{x}_i - x_i)^T R^{-1}(\hat{x}_i - x_i)]} . \end{aligned} \quad (6.2)$$

where  $R$  denotes the *prediction error covariance matrix* ( $R$ ) and  $T$  denotes the transpose operator. As a note, the prediction error covariance matrix plays a major part in the Cramer-Rao bound and is covered in more detail in Section 6.5. Reference [34] indicates that if the prediction error covariance matrix is known, the term multiplying the exponential in Equation 6.2 is a constant and therefore can be discarded as it does not effect the maximization. The normal likelihood Equation, 6.2, is commonly modified by taking the negative of the logarithm to create the *logarithmic likelihood function*, as seen in as seen in Equation 6.3. By using the log likelihood function as

a cost functional,  $J(\theta)$ , the MLE can be obtained through direct minimization.

$$J(\theta) = \frac{1}{2} \sum_{i=1}^n [(\hat{x}_i - x_i)^T R^{-1} (\hat{x}_i - x_i)] \quad (6.3)$$

The cost functional stated in Equation 6.3 provides a direct link to the Cramer-Rao inequality, as will be seen in Equation 6.19. While the MLE provides the most likely estimate of a system parameter, it provides no method to validate the accuracy of that estimate. This will be addressed in the next Section regarding the *Cramer-Rao inequality*.

## 6.4 The Cramer-Rao Inequality

The Cramer-Rao inequality is a statistical method which provides a means to evaluate the accuracy of a given parameter estimate. As stated by reference [34], the Cramer-Rao inequality gives a theoretical limit for the accuracy that is possible for the estimate regardless of the estimator used. Before the Cramer-Rao inequality is described, the concept of *Expected Values* ( $E_X$ ,  $\mu_X$ ), *Variance* ( $Var X$ ,  $\sigma_X^2$ ), and *Covariance* ( $Cov(X, Y)$ ) must first be defined as they are used extensively in this Section. As a note, the definitions listed below are adapted from reference [10].

**6.4.1 Statistical Methods Defined.** The *expected value* or *mean* of a random variable is simply the average value that would be expected from a random sample of a probability distribution. The expected value is also known as the *first moment* of a distribution, and is defined below.

**Definition 6.4.1** (Expected Value). *The expected value,  $E[x(t)]$ , of a random variable  $x(t)$  of the probability distribution  $f_x(x; t)$  is defined as*

$$E[x(t)] = \begin{bmatrix} \int_{-\infty}^{\infty} x(t) f_x(x; t) dx & \text{for continuous distributions} \\ \sum_{x \in \mathcal{X}} x(t) f_x(x; t) & \text{for discrete distributions} \end{bmatrix}$$

The expected value is generally denoted by  $E_x$  or  $\mu_x$ , as will be seen throughout this work.

The *second moment* of a distribution is known as the *variance*, and is described as in definition 6.4.2

**Definition 6.4.2** (Variance). *The variance of a random variable  $x(t)$  is defined as*

$$\begin{aligned} \text{Var}[x(t)] &= E[x(t) - E(x(t))]^2 \\ &= E[x(t) - \mu_x]^2 . \end{aligned}$$

The variance of a random variable  $x$  is also denoted as  $\sigma_x^2$ . The variance defines the spread of a distribution about the mean of the random variable,  $\mu_x$ . The spread about the mean is also commonly measured by the square root of the variance, known as the *standard deviation*,  $\sigma_x$ .

When considering two random variables,  $x(t)$  and  $y(t)$ , the relationship between the two can be evaluated by use of the *covariance*, as defined below in definition 6.4.3

**Definition 6.4.3** (Covariance). *The covariance of two random variables  $x(t)$  and  $y(t)$  is defined as*

$$\begin{aligned} \text{Cov}[x(t), y(t)] &= E[(x(t) - E(x(t)))(y(t) - E(y(t)))] \\ &= E[(x(t) - \mu_x)(y(t) - \mu_y)] . \end{aligned}$$

The sign of the covariance relates the relationship between the two random variables. Thus, if large values of the random variable  $x$  are observed with small values of the random variable  $y$ , the sign of  $\text{Cov}[x(t), y(t)]$  will be negative. Likewise, if large values of the random variable  $x$  are observed with large values of the random variable  $y$ , the sign of  $\text{Cov}[x(t), y(t)]$  will be positive.

6.4.2 *The Cramer-Rao Inequality.* Using the statical methods described in Section 6.4.1, the Cramer-Rao lower bound will now be defined based on the presentation in [10].

**Definition 6.4.4** (The Cramer-Rao Inequality). *Let  $X_1, \dots, X_n$  be a sample with the probability distribution,  $f(x|\theta)$ , and let  $W(X) = W(X_1, \dots, X_n)$  be any estimator satisfying*

$$\frac{d}{d\theta} E_{\theta} W(X) = \int_{\mathcal{X}} \frac{\partial}{\partial \theta} [W(x) f(x|\theta)] dx \quad (6.4)$$

and

$$\text{Var}_{\theta} W(X) < \infty \quad (6.5)$$

Then

$$\text{Var}_{\theta} W(X) \geq \frac{I}{E_{\theta}((\frac{d}{d\theta} \log f(X|\theta))^2)} . \quad (6.6)$$

**Proof:** The proof of the Cramer-Rao inequality is provided by *Casella and Berger* [10] and is stated below. The proof starts by using the Cauchy-Schwartz Inequality, which is stated in Equation 6.7 for any two random variables  $x(t) = X$ ,  $y(t) = Y$

$$[\text{Cov}(X, Y)]^2 \leq (\text{Var } X)(\text{Var } Y) . \quad (6.7)$$

Equation 6.7 can be rearranged to define a lower bound on the variance of the random variable,  $X$ , as stated in Equation 6.8.

$$(\text{Var } X) \geq \frac{[\text{Cov}(X, Y)]^2}{(\text{Var } Y)} \quad (6.8)$$

Before expanding on Equation 6.8 by assigning  $X$  to be the estimator  $W(X)$  and  $Y$  to be the quantity  $\frac{\partial}{\partial\theta}\log f(X|\theta)$ , we first note on the covariance between  $W(X)$  and  $\frac{\partial}{\partial\theta}\log f(X|\theta)$  below:

$$\frac{d}{d\theta}E_{\theta}W(X) = \int_{\mathcal{X}} W(X) \left[ \frac{\partial}{\partial\theta}f(X|\theta) \right] dx \quad (6.9)$$

Equation 6.9 is modified by multiplying through by  $\frac{f(X|\theta)}{f(X|\theta)}$ , which results in

$$\frac{d}{d\theta}E_{\theta}W(X) = E_{\theta} \left[ W(X) \frac{\frac{\partial}{\partial\theta}f(X|\theta)}{f(X|\theta)} \right]. \quad (6.10)$$

Next, Equation 6.10 is transformed by the *property of logs* to reveal Equation 6.11

$$\frac{d}{d\theta}E_{\theta}W(X) = E_{\theta} \left[ W(X) \frac{\partial}{\partial\theta}\log f(X|\theta) \right] \quad (6.11)$$

To declare Equation 6.11 as a covariance between  $W(X)$  and  $\frac{\partial}{\partial\theta}\log f(X|\theta)$  the product of the expected values must be subtracted. By applying  $W(x) = [1]$  to the Equation 6.11 the expectation of  $\frac{\partial}{\partial\theta}\log f(X|\theta)$  can be calculated as

$$E_{\theta} \left[ \frac{\partial}{\partial\theta}\log f(X|\theta) \right] = \frac{d}{d\theta}E_{\theta}[1] = 0. \quad (6.12)$$

Thus, the expectations above are null, and therefore the covariance,  $Cov_{\theta}(W(X), \frac{\partial}{\partial\theta}\log f(X|\theta))$ , is equal to the expectation seen in Equation 6.11. This relationship is depicted in Equation 6.13.

$$Cov_{\theta}(W(X), \frac{\partial}{\partial\theta}\log f(X|\theta)) = E_{\theta} \left[ W(X) \frac{\partial}{\partial\theta}\log f(X|\theta) \right] = \frac{d}{d\theta}E_{\theta}W(X) \quad (6.13)$$

Noting that

$$\frac{d}{d\theta}E_{\theta}W(X) = I \quad (6.14)$$

where  $I$  is the *identity matrix*(I). Additionally, as  $E_\theta \left[ \frac{\partial}{\partial \theta} \log f(X|\theta) \right] = 0$  the variance of  $\frac{\partial}{\partial \theta} \log f(X|\theta)$  is described as seen in Equation 6.15.

$$Var_\theta \left( \frac{\partial}{\partial \theta} \log f(X|\theta) \right) = E_\theta \left[ \left( \frac{\partial}{\partial \theta} \log f(X|\theta) \right)^2 \right] \quad (6.15)$$

Finally, substituting Equations 6.13 and 6.15 into the covariance and variance on the right hand Equation 6.8, the Cramer-Rao inequality is defined in Equation 6.16.

$$\begin{aligned} Var_\theta(W(X)) &\geq \frac{\left( \frac{\partial}{\partial \theta} E_\theta W(X) \right)^2}{E_\theta \left[ \left( \frac{\partial}{\partial \theta} \log f(X|\theta) \right)^2 \right]} \\ &\geq \frac{I}{E_\theta \left[ \left( \frac{\partial}{\partial \theta} \log f(X|\theta) \right)^2 \right]} \end{aligned} \quad (6.16)$$

It is important to note that while this derivation of the Cramer-Rao inequality is presented for continuous time random variables it is also valid for discrete time random variables. This is due to Equation 6.4, in which the integration can be substituted for summation in the discrete time case.

Two important facts can now be discussed concerning the Cramer-Rao inequality. The first is that Equation 6.16 presents the lower bound for the variance of *any* estimator. Furthermore, any unbiased estimator that attains the equality of Equation 6.16 is deemed an *efficient estimator*. In the case of this work, the estimator of interest will be the maximum likelihood estimator. This condition is met based on definition 6.4.5

**Definition 6.4.5** (Existence of an Efficient Estimator). *If an efficient estimator exists for a problem, that estimator is a maximum likelihood estimator*

**Proof:** See reference [34]

The second fact of importance from Equation 6.16 is the existence of the *Fisher Information Matrix*(M) in the Cramer-Rao inequality. The Fisher information ma-

trix,  $M$ , is defined as

$$M_{\theta}(X) = \left[ \left( \frac{\partial}{\partial \theta} \log f(X|\theta) \right)^2 \right] . \quad (6.17)$$

Reference [10] notes the Fisher information matrix is referred to as the *Fisher information* of the sample, as the Fisher information value defines the bound of the variance of the estimator of  $\theta$ . Thus, as the information number gets bigger, more information is available about the  $\theta$ . As a result, a large Fisher number results in a smaller bound on the variance and therefore indicates a more accurate estimate of  $\theta$ . Now, the Cramer-Rao inequality can be restated in terms of the the Fisher Information Matrix as

$$\text{Var}_{\theta}(W(X)) \geq M_{\theta}(X)^{-1} . \quad (6.18)$$

These results of the Cramer-Rao inequality indicate that the lower bound of the variance is a close approximation of the variance of the estimates from a maximum likelihood estimator. This presents an ideal form to used to evaluate the performance of parameter estimates, however, the form of the Fisher information matrix can be cumbersome to compute. Reference [34] presents a close approximate for the Fisher information matrix by way of the *Hessian*,  $H$ , of the cost function,  $J$ , of Equation 6.3, presented as

$$H = \nabla_{\theta}^2 J . \quad (6.19)$$

This approximation is used in the computation of the Cramer-Rao lower bound in Section 6.5.

### **6.5 Cramer-Rao Lower Bound for LTI Systems**

The following is an adaptation from Ref. 3 that describes how the Cramer-Rao bound is calculated for a LTI system in state space form. For LTI systems, the first

step in generating the Cramer-Rao bound is to generate the frequency response of the linear system represented by Eq. 6.20, which is in state space form.

$$\begin{aligned}\dot{x} &= Ax(t) + Bu(t) \\ y &= Cx(t) + Du(t)\end{aligned}\tag{6.20}$$

Here, the frequency response of the linear system is defined as

$$G(\iota\omega_f) = C(\iota\omega_f I - A)^{-1}B + D\tag{6.21}$$

where it is assumed that the matrix  $D$  is zero, since no feed forward signal is assumed in this model. Next, we define in Eq. 6.22 the error between the estimated model frequency responses,  $G_{j,k}(\iota\omega_f)$ , and the test frequency responses,  $G_{j,k}(\iota\omega_f)_{Test}$ , from the real system.

$$\varepsilon_{j,k}(\iota\omega_f) = G_{j,k}(\iota\omega_f) - G_{j,k}(\iota\omega_f)_{test}\tag{6.22}$$

Here the indices  $j$  and  $k$  represent the number of frequency response outputs and frequency response inputs, respectively, to the frequency response,  $G_{j,k}(\iota\omega_f)$ . The response error,  $\varepsilon_{j,k}$  is required to establish a cost function defining the fitness of the estimated frequency response as compared to the actual system response,  $J$ , as defined in Equation 6.23. Note that  $n_o$  is the number of response outputs,  $n_i$  is the number of control inputs, and  $n_{\omega_f}$  represents the number of test frequency points.

$$J = \sum_{j=1}^{n_o} \sum_{k=1}^{n_i} \sum_{l=1}^{n_{\omega_f}} W_{j,k}(\omega_{f_l}) [\varepsilon_{j,k}(\iota\omega_{f_l})]^2\tag{6.23}$$

The cost function of Equation 6.23 is based upon the negative of the logarithm of the *maximum likelihood functional*, as developed in *Maine and Iliff* [34]. This is due to the fact that the Cramer-Rao bound produces the theoretical lower limit of the accuracy of an optimal estimator. In the case of the Cramer-Rao bound, the optimal

estimator is the maximum likelihood estimator. As in the case of the maximum likelihood estimator, the cost functional of Equation 6.23 assumes a Gaussian white noise measurement disturbance having zero mean. The intensity of the measurement noise vector is described by the *prediction error covariance matrix*,  $R$ , which is formed by setting  $R$  equal to the power spectral density of the measurement noise,  $S_v$ . The cost functional of Equation 6.23 provides input for the prediction error covariance matrix by the weighting matrix  $W$ . The matrix  $W$  represents a weighting of the inverse of input noise strength, which is formed by  $W = R^{-1}$ .

The frequency response fitness function  $J$ , defined in Eq. 6.23 forms the core of the Cramer-Rao bound by providing the necessary elements for the Hessian,  $H$ . The Hessian of  $J$  with respect to a selected model parameter  $p$  is defined in Eq. 6.24.

$$H = \nabla_p^2 J \quad (6.24)$$

Thus, the Cramer-Rao bound,  $CR_j$ , is approximated in terms of the Hessian for each identified system parameter of Eq. 6.21,  $p_j$  as

$$CR_j \approx \sqrt{(H^{-1})_{j,j}} . \quad (6.25)$$

In order to form the Hessian, the second partial derivative with respect to  $p$  of Eq. 6.23 must be calculated. The process of calculating the Hessian begins by first calculating the first partial derivative of  $J$  with respect to  $p$ . The result is seen in Eq. 6.26.

$$\frac{\partial J}{\partial p} = \sum_{j=1}^{n_o} \sum_{k=1}^{n_i} \sum_{l=1}^{n_{\omega_f}} \left[ \varepsilon_{j,k}(\omega_{f_l}) W_{j,k}(\omega_{f_l}) \frac{\partial \varepsilon_{j,k}(\omega_{f_l})}{\partial p} \right] \quad (6.26)$$

Note that the real frequency response,  $G_{j,k}(\omega_{f_l})_{Test}$  is not affected by varying model parameters. Thus, the partial derivative of the frequency response error  $\varepsilon_{j,k}$  in Eq. 6.26

can be represented simply as

$$\frac{\partial \varepsilon_{j,k}(\iota\omega_{f_l})}{\partial p} = \frac{\partial G_{j,k}(\iota\omega_{f_l})}{\partial p} . \quad (6.27)$$

It is important to define that  $\frac{\partial G_{j,k}(\iota\omega_{f_l})}{\partial p}$  is the  $j^{th}$  row and  $k^{th}$  column of the frequency response sensitivity matrix in Eq. 6.29.

$$\frac{\partial G(\iota\omega_f)}{\partial p} = \frac{\partial}{\partial p} [C(\iota\omega_f I - A)^{-1}B + D] \quad (6.28)$$

$$= C(\iota\omega_f I - A)^{-1} \frac{\partial A}{\partial p} (\iota\omega_f I - A)^{-1}B + C(\iota\omega_f I - A)^{-1} \frac{\partial B}{\partial p} \quad (6.29)$$

Now, in light of Eq. 6.27, the first partial derivative of  $J$  as represented in Eq. 6.26 can be represented as

$$\frac{\partial J}{\partial p} = \sum_{j=1}^{n_o} \sum_{k=1}^{n_\iota} \sum_{l=1}^{n_{\omega_f}} \left[ \varepsilon_{j,k}(\iota\omega_{f_l}) W_{j,k}(\omega_{f_l}) \frac{\partial G_{j,k}(\iota\omega_{f_l})}{\partial p} \right] . \quad (6.30)$$

Taking the partial of Eq. 6.30 with respect to  $p$ , the Hessian  $H_{j,k}$  is formed, as seen in Eq. 6.31.

$$H_{j,k} = \sum_{l=1}^{n_{\omega_f}} W_{j,k}(\omega_{f_l}) \left[ \frac{\partial G_{j,k}(\iota\omega_{f_l})}{\partial p} \right]^2 \quad (6.31)$$

Having now defined Eq. 6.31, the definition of the Cramer-Rao bound originally stated in Eq. 6.25 is complete.

Once again, the preceding discussion is strictly applicable only to an LTI system, and is not applicable to LTP models such as a helicopter in forward flight. Thus, any parameter identification for the purpose of developing a controllable linear model for such an LTP system will not be verifiable. Furthermore, any controller based on a model developed using those parameters may therefore be inaccurate, since the parameters may not accurately represent the system dynamics.

## 6.6 Cramer-Rao Methodology for LTP Systems

The previous Section described the Cramer-Rao methodology for an LTI system. However, this approach is not applicable to LTP systems, such as a helicopter rotor in forward flight, which exhibits periodic behavior. This is because the state space representation of the Cramer-Rao bound has only been derived for an LTI system. For this approach to work for a LTP system a new approach must be created, as this has not been done to date.

To derive the Cramer-Rao bound for a LTP system in state space the following procedure will be taken. First, following the approach in Section 6.5, the linear system must be described in state space form. Wereley [42] has developed the continuous time Harmonic Balance State Space Model (HBSSM), which provides the ability to analyze linear, time periodic system characteristics using techniques developed originally for linear time periodic systems. Then, following a brief description of the Harmonic Balance State Space Model, the Cramer-Rao bound for an LTP system will be derived in a manner similar to the state space LTI approach.

**6.6.1 LTP State Space Operator.** A linear, time periodic system is said to be *T-periodic* because it oscillates with period *T*. LTP systems are *T-periodic* due to either system dynamics or an input signal modulated at  $\omega_p$ , which is the system *pumping frequency*, or *fundamental frequency*. The pumping frequency defines the amplitude and period at which the system modulation takes place. This concept is illustrated in Figure 6.2, where a simple LTP system is represented as a time varying gain,  $1 - 2\beta \cos\omega_p t$  that modulates the output at the pumping frequency  $\omega_p$ .

The plant dynamics matrix,  $A(t)$ , being *T-periodic* has the property

$$A(t + T) = A(t) \quad \forall t \in (-\infty, \infty). \quad (6.32)$$

If the portion of the matrix defined over the fundamental interval is only considered, then  $A(t)$  is considered bounded such that  $A(t) \in L_2[0, T]$ . Considering this property,

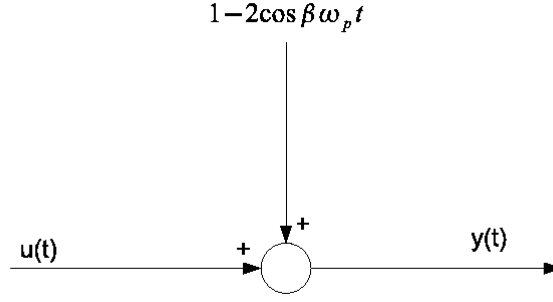


Figure 6.2: Example of a simple LTP system represented by a modulating gain. [42]

the state space model of a  $T$ -periodic system is described as

$$\begin{aligned}\dot{x}(t) &= A(t)x(t) + B(t)u(t) \\ y(t) &= C(t)x(t) + D(t)u(t)\end{aligned}\tag{6.33}$$

noting the matrices  $B(\cdot)$ ,  $C(\cdot)$ ,  $D(\cdot)$  are also  $T$ -periodic. Now, the LTP system represented by Eq. 6.33 can be excited using an exponentially modulated periodic (EMP) signal of the form

$$u(t) = \sum_{m=-\infty}^{\infty} u_m e^{s_m t} \quad t \geq 0\tag{6.34}$$

noting that  $s_m = s + jm\omega_p$ . The steady state response to an EMP signal is represented by the complex Fourier series

$$x(t) = \sum_{m=-\infty}^{\infty} x_m e^{s_m t}\tag{6.35}$$

$$\dot{x}(t) = \sum_{m=-\infty}^{\infty} s_m x_m e^{s_m t}.\tag{6.36}$$

The output signal,  $y(t)$ , is represented by a similar expansion, as seen in Eq. 6.36. Likewise, the  $T$ -periodic state space matrices of Eq. 6.33 can be represented as a

complex Fourier series, as seen in Eq. 6.37.

$$A(t) = \sum_{m=-\infty}^{\infty} A_m e^{jm\omega_p t} \quad (6.37)$$

where  $\omega_p$  is the LTP system *pumping frequency*, or *fundamental frequency*. The matrix expansion shown in Eq. 6.37 is applied identically for  $B(t)$ ,  $C(t)$ , and  $D(t)$  of Eq. 6.33. Now, rewriting the state space representation in Eq. 6.33 with Eqs. 6.36 and 6.37, results in the Fourier series LTP system seen in Eq. 6.38.

$$\begin{aligned} \sum_{n=-\infty}^{\infty} s_n x_n e^{s_n t} &= \sum_{m=-\infty}^{\infty} A_m e^{jm\omega_p t} \sum_{m=-\infty}^{\infty} x_m e^{s_m t} + \sum_{m=-\infty}^{\infty} B_m e^{jm\omega_p t} \sum_{m=-\infty}^{\infty} u_m e^{s_m t} \\ &= \sum_{n,m=-\infty}^{\infty} A_n x_m e^{s_n + m t} + \sum_{n,m=-\infty}^{\infty} B_n u_m e^{s_n + m t} \\ &= \sum_{n,m=-\infty}^{\infty} A_{n-m} x_m e^{s_n t} + \sum_{n,m=-\infty}^{\infty} B_{n-m} u_m e^{s_n t} \end{aligned} \quad (6.38)$$

Note once again that  $s_n = s + jn\omega_p$  and  $s_m$  are represented likewise. Using the same technique, the measurement equation,  $y(t)$  of Eq. 6.33 can be represented in a manner similar to that of Eq. 6.38, as seen in Eq. 6.39.

$$\sum_{n=-\infty}^{\infty} y_n e^{s_n t} = \sum_{n,m=-\infty}^{\infty} C_{n-m} x_m e^{s_n t} + \sum_{n,m=-\infty}^{\infty} D_{n-m} u_m e^{s_n t} \quad (6.39)$$

The principle of *harmonic balance* [12, 42] can be applied to Eqs. 6.38 and 6.39 by moving all terms on the right-hand side of the equations, and then multiplying through both equations by  $e^{-st}$ . The resulting equations generate the modified state space representation of the LTP system as seen in Eq. 6.40.

$$\begin{aligned} s_n x_n &= \sum_{m=-\infty}^{\infty} A_{n-m} x_m + \sum_{m=-\infty}^{\infty} B_{n-m} u_m \\ y_n &= \sum_{m=-\infty}^{\infty} C_{n-m} x_m + \sum_{m=-\infty}^{\infty} D_{n-m} u_m \end{aligned} \quad (6.40)$$

The harmonic state space system in Eq. 6.40 can be simplified into the Toeplitz form, shown in Eq. 6.41. This result is defined as the Harmonic Balance State Space Model (HBSSM).

$$\begin{aligned} s\mathcal{x} &= (\mathcal{A} - \mathcal{N})\mathcal{x} + \mathcal{B}u \\ y &= \mathcal{C}\mathcal{x} + \mathcal{D}u \end{aligned} \quad (6.41)$$

where  $\mathcal{x}$ ,  $u$ , and  $y$  represent the doubly infinite state, control, and output vectors, respectively, defined in terms of modulated complex Fourier series coefficients, as shown in Eq. 6.42.

$$\mathcal{x} = \begin{bmatrix} \vdots \\ \mathbf{x}_{-2} \\ \mathbf{x}_{-1} \\ \mathbf{x}_0 \\ \mathbf{x}_1 \\ \mathbf{x}_2 \\ \vdots \end{bmatrix}, \quad u = \begin{bmatrix} \vdots \\ \mathbf{u}_{-2} \\ \mathbf{u}_{-1} \\ \mathbf{u}_0 \\ \mathbf{u}_1 \\ \mathbf{u}_2 \\ \vdots \end{bmatrix}, \quad y = \begin{bmatrix} \vdots \\ \mathbf{y}_{-2} \\ \mathbf{y}_{-1} \\ \mathbf{y}_0 \\ \mathbf{y}_1 \\ \mathbf{y}_2 \\ \vdots \end{bmatrix}. \quad (6.42)$$

The Toeplitz form of each of the state space matrices  $\mathcal{A}$ ,  $\mathcal{B}$ ,  $\mathcal{C}$ , and  $\mathcal{D}$  represented in Eq. 6.41 is expressed as a doubly infinite block of the complex Fourier coefficients,  $A_n | n \in \mathbb{Z}$ . Eq. 6.43 represents the  $T$ -periodic dynamics matrix,  $A(t)$ , of Eq. 6.40 in

Toeplitz form.

$$\mathcal{A} = \begin{bmatrix} \ddots & \vdots & \vdots & \vdots & \vdots & \vdots & \\ \cdots & \mathbf{A}_0 & \mathbf{A}_{-1} & \mathbf{A}_{-2} & \mathbf{A}_{-3} & \mathbf{A}_{-4} & \cdots \\ \cdots & \mathbf{A}_1 & \mathbf{A}_0 & \mathbf{A}_{-1} & \mathbf{A}_{-2} & \mathbf{A}_{-3} & \cdots \\ \cdots & \mathbf{A}_2 & \mathbf{A}_1 & \mathbf{A}_0 & \mathbf{A}_{-1} & \mathbf{A}_{-2} & \cdots \\ \cdots & \mathbf{A}_3 & \mathbf{A}_2 & \mathbf{A}_1 & \mathbf{A}_0 & \mathbf{A}_{-1} & \cdots \\ \cdots & \mathbf{A}_4 & \mathbf{A}_3 & \mathbf{A}_2 & \mathbf{A}_1 & \mathbf{A}_0 & \cdots \\ & \vdots & \vdots & \vdots & \vdots & \vdots & \ddots \end{bmatrix} \quad (6.43)$$

The matrix  $\mathcal{N}$  in Eq. 6.41 is a doubly infinite block diagonal containing multiples of the pumping frequency, which is defined as

$$\mathcal{N} = \text{blkdiag}\{jn\omega_p \mathbf{I}\} \quad \forall n \in \mathbb{Z} . \quad (6.44)$$

Using the definition of the Toeplitz form of the harmonic state space model in Eq. 6.41, the linear operator  $\mathcal{G}$ , which relates input to output, can be defined as

$$y = \mathcal{G}(s)u \quad (6.45)$$

where

$$\mathcal{G}(s) = \mathcal{C} [s\mathcal{I} - (\mathcal{A} - \mathcal{N})]^{-1} \mathcal{B} + \mathcal{D} . \quad (6.46)$$

*6.6.2 Cramer-Rao Definition for LTP Systems.* In this Section, the Cramer-Rao methodology analogous to that described in Section 6.5 will be developed for a LTP system using the Harmonic Balance State Space Model, Eq. 6.41. This methodology provides a convenient method to quickly construct the bound for the individual model parameters, but has been restricted to LTI systems. This restriction is primarily due to the inability to accurately describe a LTP system as a true linear operator having input and output *signal spaces* of the same dimension. To accurately under-

stand how the linear operator theoretic description in Section 6.5 is applied to a LTP system, it is important to first describe the differences in the signal spaces of LTI vs. LTP systems.

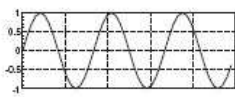
A LTI system having a *sinusoidal input signal* of frequency  $\omega_f$  will map an output signal of  $\omega_n$  but with different magnitude and phase than the input signal. Thus, the signal spaces are identical, as the input and output are both complex exponential sinusoids of frequency  $\omega_f$ . This response for a LTI system is clearly seen in a Bode plot, as phase and magnitude of the system are plotted over the entire range of input frequencies,  $\omega_f = 0 \dots \infty$ .

A LTP system differs from a LTI system in that the system parameters vary periodically rather than remain constant, or *time invariant*. Consider a LTP system defined as such by having a time periodic input matrix,  $B$ . In this case the steady state forced response signal of a LTP system will be composed of the sinusoidal input signal  $\omega_f$  and the pumping frequency input signal  $\omega_p$ , as seen in Figure 6.2. In this Figure an input signal,  $u(t)$ , is convoluted with a time periodic gain  $1 - 2\beta\cos\omega_p t$ . Thus, the output signal,  $y(t)$ , is a convolution of signals best described by the Fourier series containing the frequencies  $\omega_f \pm n\omega_p | \omega_f \in \mathbb{C}, n \in \mathbb{Z}$ , which is an infinite dimension signal space. This is depicted in Figure 6.3. Clearly, the input and output spaces are not the same dimension as in the case of the LTI system spaces. This difference in signal spaces differentiates the LTP system from LTI systems, as the mapping of signal spaces from input to output is not an *isomorphism*, being *one-to-one* and *onto*, but rather a *one-to-many* mapping. It is for this reason that in this form, the LTP system is not considered a true linear operator.

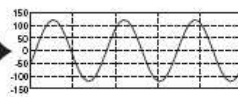
Wereley [42] developed the concepts of *Exponentially modulated periodic signal*, as seen in Equation 6.34, to rectify the signal space imbalance in LTP systems. The EMP signal created an input space of equal dimension to the output signal space, which formed the foundation for the LTP operator described in section 6.6.1. By using the LTP harmonic state space model from definition 6.45 the input-output relationship

**Linear Time-Constant System:**

Sinusoidal Input

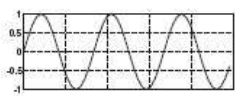


Sinusoidal Response



**Linear Time-Periodic System:**

Sinusoidal Input



Multiharmonic Response

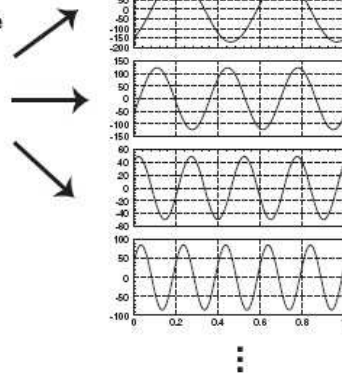
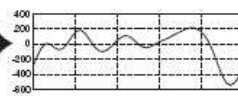


Figure 6.3: Multiharmonic Response of an LTP System [20].

between the input harmonics,  $u_n|n \in \mathbb{Z}$ , and the output harmonics,  $y_n|n \in \mathbb{Z}$ . Thus, a true linear operator for LTP systems is defined.

As the HBSSM is a true linear operator, the Cramer-Rao lower bound can be described using the state space matrices  $\mathcal{A}$ ,  $\mathcal{B}$ ,  $\mathcal{C}$ , and  $\mathcal{D}$  from Eq. 6.41 in a modified form of Equation 6.29, as seen below.

$$\frac{\partial \mathcal{G}(\omega_f)}{\partial p} = \frac{\partial}{\partial p} [\mathcal{C}(\omega_f I - \mathcal{A}\mathcal{H}\mathcal{N})^{-1}\mathcal{B} + \mathcal{D}] \quad (6.47)$$

$$\begin{aligned} &= \mathcal{C}(\omega_f I - \mathcal{A}\mathcal{H}\mathcal{N})^{-1} \frac{\partial \mathcal{A}}{\partial p} (\omega_f I - \mathcal{A}\mathcal{H}\mathcal{N})^{-1} \mathcal{B} \\ &\quad + \mathcal{C}(\omega_f I - \mathcal{A}\mathcal{H}\mathcal{N})^{-1} \frac{\partial \mathcal{B}}{\partial p} \end{aligned} \quad (6.48)$$

where the matrix  $\mathcal{A}\mathcal{H}\mathcal{N}$  is defined as

$$\mathcal{A}\mathcal{H}\mathcal{N} = \mathcal{A} - \mathcal{N} \quad (6.49)$$

The above Equations 6.48 and 6.49 redefine the partial derivative of the response error from Equation 6.27 to an expression containing a doubly infinite block of complex Fourier coefficients in Toeplitz form. To complete the computation of the Cramer-Rao lower bound for LTP systems defined in block Toeplitz form, Equation 6.48 is used to in Equation 6.50 to define the Hessian,  $\mathcal{H}$ , in a manner analogous to Equation 6.31.

$$\mathcal{H}_{j,k} = \sum_{l=1}^{n_{\omega_f}} W_{j,k}(\omega_l) \left[ \frac{\partial \mathcal{G}_{j,k}(\omega_{f_l})}{\partial p} \right]^2 \quad (6.50)$$

Having defined the Hessian for the LTP system in block Toeplitz form in Equation 6.50, the Cramer-Rao lower bound,  $\mathcal{CR}$ , is now defined for LTP systems as

$$\mathcal{CR}_j \approx \sqrt{(\mathcal{H}^{-1})_{j,j}}. \quad (6.51)$$

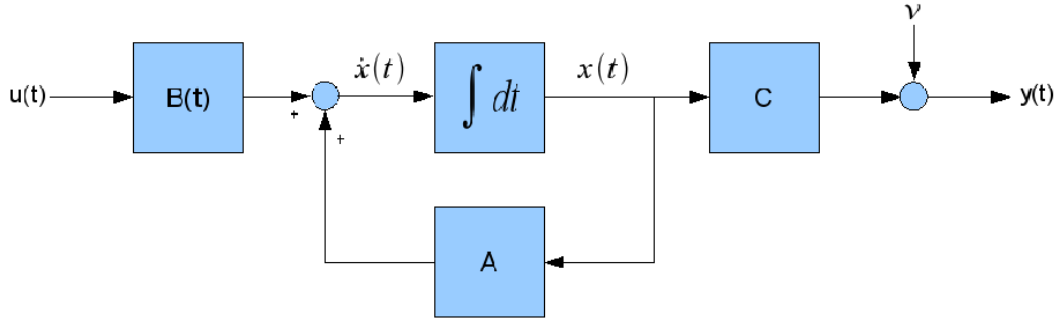


Figure 6.4: Example LTP system with time invariant A,C matrices and time periodic B(t) matrix.

### 6.7 Illustrative Example

Having defined the Cramer-Rao lower bound for LTP systems in Equation 6.51, an example will now show how the method can be applied to LTP systems to validate identified system parameters. For this example, the simple LTP system described in Figure 6.4 will be used to evaluate the validity of the system parameter  $\zeta$ .

For the example, the system depicted in Figure 6.4 is considered with time invariant plant and output matrices  $A_o$  and  $C_o$  and a  $T$ -periodic control matrix  $B(t)$ . The system matrices are defined as seen in Equation in 6.52

$$A_o = \begin{bmatrix} 0 & 1 \\ -\omega_n^2 & -2\zeta\omega_n \end{bmatrix} \quad B(t) = \begin{bmatrix} 0 \\ 1 - 2\beta\cos\omega_p t \end{bmatrix} \quad C_o = \left(\frac{\omega_n^2}{|a|}\right) \begin{bmatrix} 1 & -a \end{bmatrix} \quad (6.52)$$

where the values of the system are defined as  $\omega_p = 1$ ,  $\omega_n = .5$ ,  $\zeta = .3$ ,  $a = -1$ , and  $\beta = 1$ . As the  $B(t)$  matrix is to be described by way of the Fourier series for

use in the Toeplitz transform, it is therefore expressed as in Equation 6.53.

$$\begin{aligned}
B(t) &= \left[ \cdots, 0, B_{-1}, B_0, B_1, 0, \cdots \right] \\
&= \left[ \cdots, 0, \begin{bmatrix} 0 \\ -\beta \end{bmatrix}, B_0, \begin{bmatrix} 0 \\ -\beta \end{bmatrix}, 0, \cdots \right]
\end{aligned} \tag{6.53}$$

These matrices are used to create the HBSSM of this model in the manner described in Section 6.6.1. It is important to note that while the number of harmonics of the HBSSM is doubly infinite, for use in a digital computer, the system is truncated to include only  $n$  positive harmonics with an equal number of negative harmonics along with the zero harmonic. To ensure accurate results in this example,  $n=10$  positive harmonics are used. The rationale for this selection is discussed below.

The Toeplitz block form of Fourier coefficients is key to developing a state space form of the system matrices that define a model. These matrices, as described previously, are considered doubly infinite as they contain a doubly infinite representation of the Fourier series. This, however is untenable for application in code development on a digital computer. For code development to take place, the representative Fourier series of the Toeplitz transform must be truncated to contain  $N$  harmonics. To determine the value of  $N$ , the number of harmonics was increased in the system as to identify convergence in the compared system responses. Based on the experience of Hwang [12],  $n=10$  was determined to produce adequate convergence in system output response.

By creating the HBSSM for this example, the block Toeplitz matrices  $\mathcal{A}$ ,  $\mathcal{B}$ ,  $\mathcal{C}$ , and  $\mathcal{D}$  along with the partial derivatives  $\frac{\partial \mathcal{A}}{\partial p}$  and  $\frac{\partial \mathcal{B}}{\partial p}$  are then used in Equation 6.48 to generate the Hessian of Equation 6.50. The weighting matrix,  $W$  in Equation 6.50 is formed by using an input noise spectral density,  $S_v = 1$ , for the input noise covariance matrix,  $R$ . Thus, for this example, the weighting matrix is unitary as  $W = R^{-1} = 1$ . As this example is determining the Cramer-Rao bound for the system parameter  $\zeta$ ,

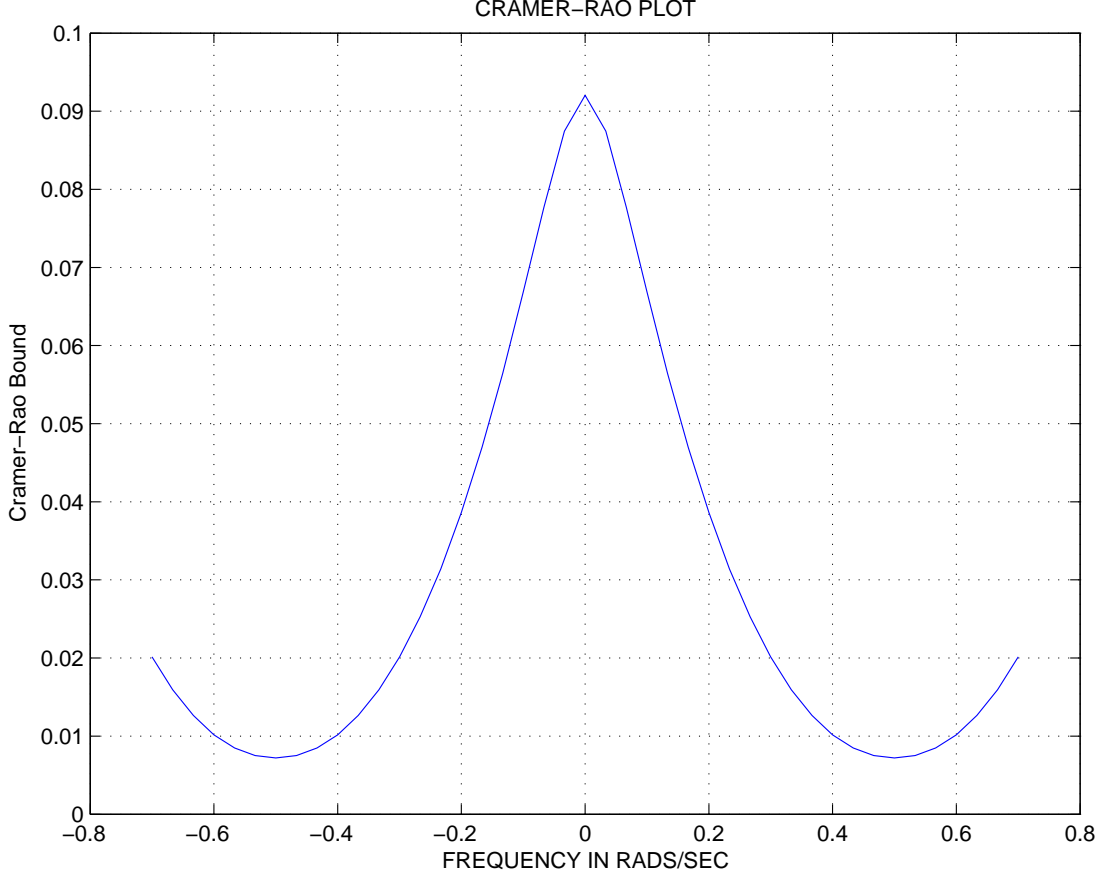


Figure 6.5: Cramer-Rao bound of the system in Equation 6.52 with respect to the parameter  $\zeta$ .

the partial derivatives are taken with respect to  $\zeta$ . After determining the Hessian, the Cramer-Rao bound for  $\zeta$  is determined by use of Equation 6.51. A plot of the Cramer-Rao bound for  $\zeta$  is presented over a frequency range  $\omega_f \in \left(-\frac{\omega_p}{2}, \frac{\omega_p}{2}\right]$ . The Cramer-Rao bound presented in Figure 6.5 is based solely on the first system harmonic, which is the dominant mode of the system. The results of this plot indicate that the lowest Cramer-Rao bound about the parameter,  $\zeta$  is a standard deviation of  $\pm 0.004$ , representing a total bound of 0.008. Additionally, this value occurs at an input frequency of  $\omega_f = 0.5$ . In terms of validating the test parameter by way of the Cramer-Rao bound, any value of  $\zeta$  derived empirically that has a Cramer-Rao bound significantly larger than the smallest Cramer-Rao bound may be invalid and warrants further investigation.

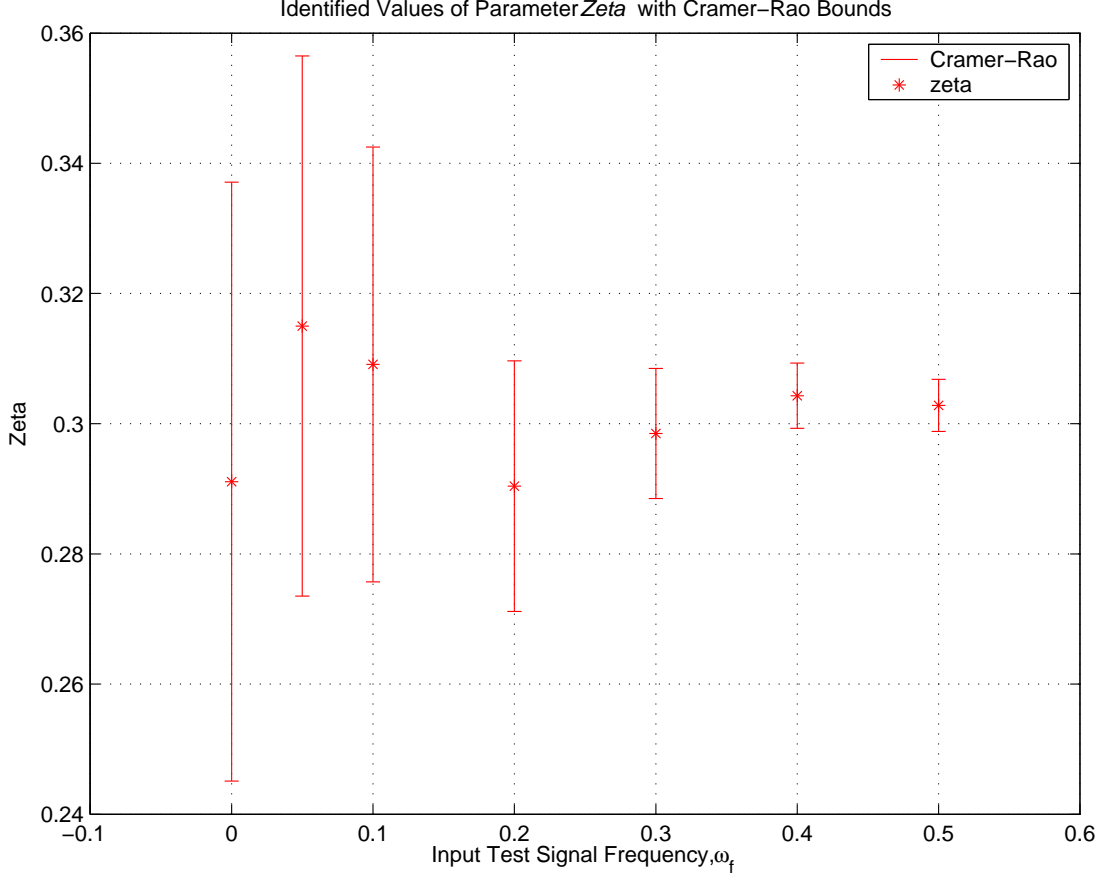


Figure 6.6: Values of  $\zeta$  derived by system identification at input frequency  $\omega_f$  with superimposed Cramer-Rao bounds.

An example of using the Cramer-Rao bound to validate parameter estimates is presented in Figure 6.6. Here parameter estimates of  $\zeta$  are presented at select input frequencies,  $\omega_f = 0, 0.05, 0.1, 0.2, 0.3, 0.4, 0.5 \text{ rad/s}$ . As a note, the parameter estimates of  $\zeta$  were performed by using a frequency domain parameter identification method for LTP systems developed by Hwang [12]. The output data used for these parameter estimates was corrupted by the zero mean Gaussian white measurement noise,  $\nu$ , of Figure 6.4 having spectral density  $S_v = 1$ . This spectral density for the input noise was chosen to match the value used to define the weighting matrix  $W$  of the Cramer-Rao bound. The parameter estimates of  $\zeta$  are presented with their corresponding Cramer-Rao bound from the data presented in Figure 6.5. The values of  $\zeta$  are presented at each frequency used for system identification to compare their

accuracy to the true value of  $\zeta = 0.3$  in addition to showing the size of the corresponding Cramer-Rao bound. As stated in Section 6.5, a large Cramer-Rao bound indicates poor parameter estimation performance, and thus by reviewing Figure 6.6 one can identify accurately and inaccurately identified values of  $\zeta$ . Thus, the values of  $\zeta$  in Figure 6.6 that fall in the input frequency range of  $0.3 \leq \omega_f \leq 0.5$  have both identified values of  $\zeta$  near to the true value of 0.3, and demonstrate small Cramer-Rao bounds, indicating a small standard deviation of the identified value. These values are therefore accurate and should be considered for use in the parametric system model. Likewise, the identified values of  $\zeta$  that fall in the input range of  $0 \leq \omega_f < 0.3$  have excessively large bounds, indicating poor identification of  $\zeta$ , which is evident by their values straying from the true value of  $\zeta = 0.3$ . The data in this range should therefore not be used. If the bound of this parameter grows, it can indicate poor data correlation and thus warrants investigation of the test data used for parameter identification. Finally, it is important to note that this plot presents not only the best identified value of  $\zeta$  based on the Cramer-Rao bound, but also the value of the input frequency,  $\omega_f$  at which this occurs. This can be used to specify the ideal input frequency range to use when performing system identification that will ensure accurate parameter results.

## 6.8 *Concluding Remarks*

A derivation of the theory and methodology required to generate the Cramer-Rao lower bound for a specified parameter in a linear, time periodic (LTP) system in state space form has been presented. This development now makes it possible to determine the bounded standard deviation of a system parameter which has been estimated using any system identification technique. The Cramer-Rao lower bound represents the standard deviation based on using an optimal estimator, thus providing a true measure of the accuracy of the estimate.

Through an illustrative example, it has been shown that in a LTP system, the frequency at which the parameter estimation is performed is critical to the confidence

that one can attribute to the estimate. Therefore, knowledge of the Cramer-Rao lower bound provides those performing the system identification with valuable insights on how best to obtain estimates of system parameters. The importance of this knowledge has also been shown to be particularly important when there is noise in the data used to perform the parameter estimates.

As noted in the Introduction, minimizing the one-per-rev vibrations of helicopter rotors is important to the safe, efficient operation of helicopters. The development of a methodology for determining the Cramer-Rao lower bound for LTP systems provides a means for assessing the quality of parameterized models developed for rotor smoothing. Further research along this line will focus on using the Cramer-Rao methodology to improve the efficiency of rotor smoothing methods. One possibility for reducing the number of flights and manual adjustments is to introduce actuators in the rotor system. These actuators would be controlled by an on-line system which performs continuous system identification, thereby providing verifiably accurate control. Such a system would alleviate the repetitiveness of the current rotor vibration adjustment process by providing continuous adjustments for vibration reduction during flight.

## VII. Rotor Vibration Smoothing Using Cramer-Rao Parameter Validation

The overall intent of this research, as stated in chapter II, is to develop an optimal rotor smoothing approach to reduce out of plane vibrations generated by asymmetrical aerodynamic lift of individual blades. The proposed rotor smoothing method is based upon an framework containing the following three tenets:

1. Perform system identification to populate the rotor system parametric model.
2. Validate the accuracy of the identified parameters of the rotor system model.
3. Produce a vibration control solution using linear optimal methods based upon the validated rotor parameters to reduce out of plane vibrations to an acceptable level.

The previous chapters have provided the necessary tools to accomplish this approach, with an emphasis on the Cramer-Rao bound LTP systems to provide system parameter validation. This chapter will culminate the works of the previous chapter to produce a LTP *Linear Quadratic Regulator* (LQR) based upon Cramer-Rao validated system parameters. Through this approach, the utility of the Cramer-Rao bound will be evident, as it can detect poorly identified system parameters, which ultimately lead to a poorly performing LQR vibration controller.

### 7.1 *Needed Improvements in Rotor Smoothing Algorithms*

Rotor smoothing algorithms for rotors are not in short supply, as outlined in chapter II. However an accurate approach is still elusive. This is due in large part to a smoothing approach based upon a flawed internal model of the rotor system. The primary flaw in these rotor smoothing approaches is the use of a linearized model that does not capture the periodic nature of a rotor system in forward flight. While it is evident that a linearized flapping rotor blade model contains periodic terms in the plant and input matrices,  $A(t)$  and  $B(t)$  respectively, the current rotor smoothing approaches using linear models average the periodic terms in order to produce a LTI

system. This approach has been done in order to use existing control, system identification, and parameter validation techniques that are valid for LTI systems. While this simplification has allowed for the development of rotor smoothing algorithms, it has incurred the inaccuracies associated with using a system that does not capture the time periodic nature of the flapping blade in forward flight.

An additional flaw in existing rotor smoothing approaches is the lack of validated parameters in the internal rotor system model used to develop the smoothing solution. Rotor smoothing algorithms that use an internal system model to develop the vibrational smoothing solution rely on the measured response of the actual system. This data is in turn used to construct a representative internal model used to derive the rotor smoothing solution, as seen in chapter II. The representative model can be either a parametric model, usually in State Space representation, or a non-parametric model such as a frequency response function. For a parametric model, the validity of the individual parameters can be evaluated for accuracy before use using existing approaches, such as the Cramer-Rao approach covered in detail in chapter VI. For non-parametric rotor smoothing algorithms, such as the U.S. Army's *AVA*, a parametric validation approach is reduced to validating the single parameter representing the frequency response, which further reduces the ability to detect modeling errors as there are no physical parameters that can be accurately validated. Regardless of modeling approach, parameter validation is rarely ever used in rotor smoothing and thus modeling inaccuracies that could otherwise be detected by a parameter validation approach are introduced into the rotor vibration reduction solution. *Maine and Iliff* [34] note that if highly accurate estimates cannot or are not distinguished from worthless estimates, to be safe all estimates must be considered suspect or moreover, worthless. On that note, if the smoothing algorithm is to be accurate, a model based upon validated parameters is essential to a well performing smoothing algorithm.

The following Section will describe the methodology used to overcome these deficiencies.

## 7.2 *Outline of Cramer-Rao Validated Controller Development*

The work of this chapter is to describe how to smooth main rotor system out of plane vibrations through a LTP LQR controller. In addition to the controller development, this chapter will demonstrate the importance of the Cramer-Rao lower bound for LTP system parameters by comparing the performance of several LQR controllers. Here, each controller is developed based on upon validated parameters having a Cramer-Rao bound different from another. For the controller comparison, the Cramer-Rao bounds will be increased in size for each successive controller. As shown in chapter VI, the validity of system parameters derived from a parameter identification scheme is garnered from the magnitude of the Cramer-Rao bound. This is due to the fact that the Cramer-Rao bound depicts the standard deviation of the identified parameter. As the performance of the LQR is directly related to the model perturbations, which arise from identified system parameters having varying levels of accuracy, a method to quantify the level of parameter perturbations would allow one to determine the controller effectiveness simply by reviewing the magnitude of the bound itself. Thus, the Cramer-Rao bound will demonstrate that poorly identified system parameters will lead to unsuitable controller demands on control inputs.

In order to achieve the above stated goals the following steps will be accomplished in successive order in this chapter:

1. Describe the rotor system LTP equations of motion based upon a rigid blade model, with 4 blades in total.
2. Develop the LTP LQR controller for out of plane vibration reduction
  - (a) Describe the properties of a LTP LQR controller
  - (b) Outline the tracking regulator design used to reduce out of plane vibrations
  - (c) Explain selection of time periodic gain harmonics
3. Outline the computation of each controller based upon increasing Cramer-Rao bounds.

4. Compare the performance of each controller developed in the above step to demonstrate the effects of large Cramer-Rao bounds on controller performance

The following Sections will address the individual goals in succession, beginning with the derivation of the rotor system equations of motion.

### 7.3 *Rotor System LTP Equations of Motion*

As stated in the introduction to this chapter, each rotor smoothing algorithm relies upon an internal rotor model in order to compute the rotor smoothing solution. For this work a simplified four bladed rotor system is used to represent the dynamics of the flapping rotor blades in forward flight. As this work is only considering rotor smoothing and not higher harmonic control, rigid blades are adequate and therefore will be used to represent the individual blades in the rotor system model. Furthermore, for the sake of simplification, each blade will be considered without a flap hinge offset or spring restraint.

The rotor system will be derived by first developing the equations of motion of an individual blade having the characteristics described in the last paragraph. Once the individual blade model is derived a system comprised of four identical blades will be assembled, with each blade phased 90 degrees apart, as in the configuration of the AH-64 as seen in Figure 7.1 or similar 4 bladed rotor. The derivation for a single rigid blade that follows is derived from the work of Johnson [16], and is presented below.

The rigid blade flapping equations of motion are now considered by first taking the equilibrium of the inertial and aerodynamic moments about the flapping hinge, as seen in Figure 7.2. Considering the blade mass element,  $m \, dr$ , at the radial position  $r$  the the three sectional forces acting on the mass are described as follows:

1. The *Inertial* force, described as  $m\ddot{z} = mr\ddot{\beta}$
2. The *Centrifugal* force, described as  $m\Omega^2 r$
3. The *Aerodynamic* force,  $F_z$

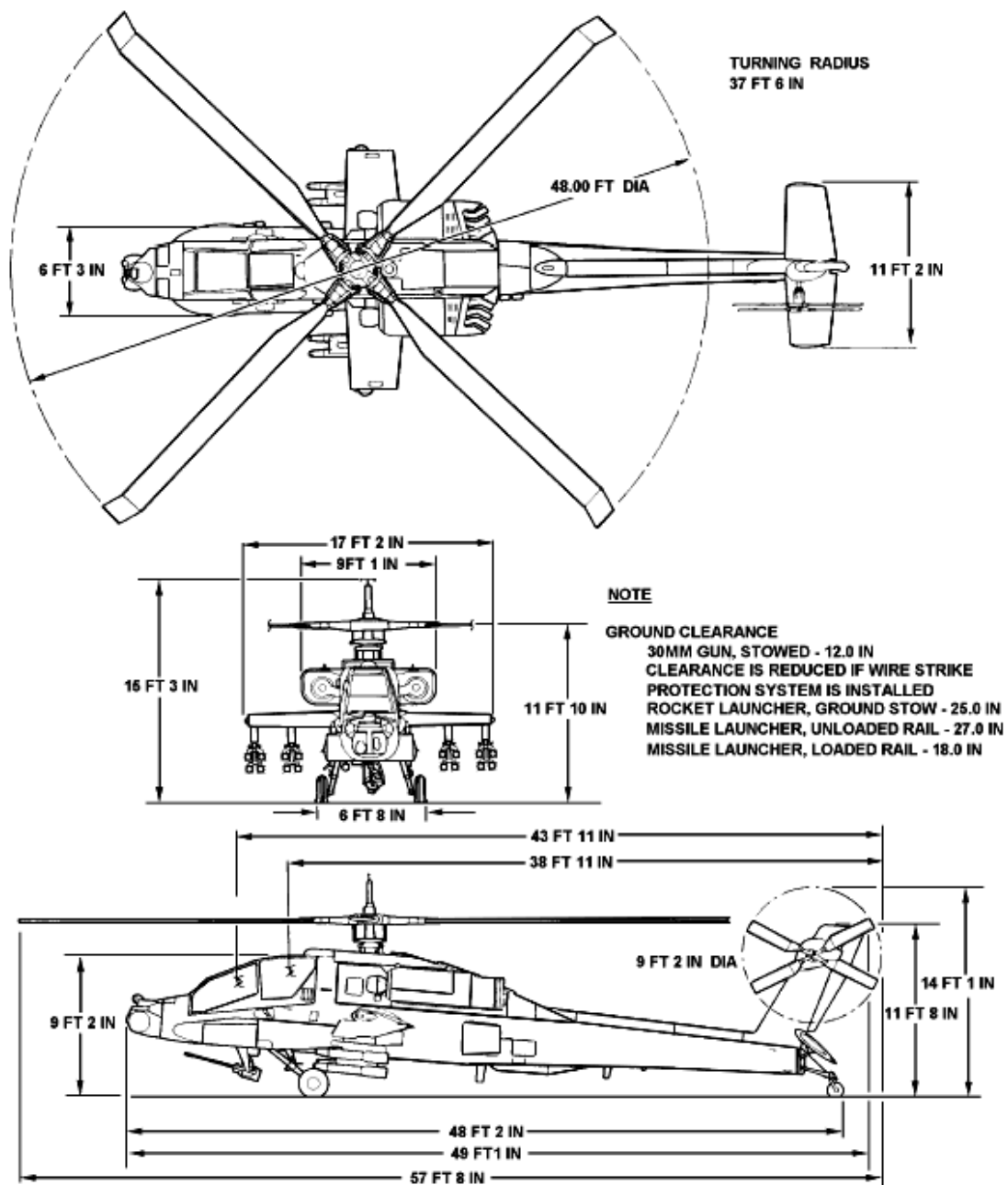


Figure 7.1: Diagram of AH-64 rotor system [14].

where  $z = \beta r$  describes the out of plane deflection of the flapping rotor blade. As each of these forces are considered in terms of moments about the flapping hinge, the radial distances for each force are considered as

1. The *inertial* force has a moment arm  $r$  about the hinge
2. The *centrifugal* force acts radially outward from the blade with moment arm  $z = r\beta$
3. The *Aerodynamic* force  $F_z$  has a moment arm  $r$  about the hinge

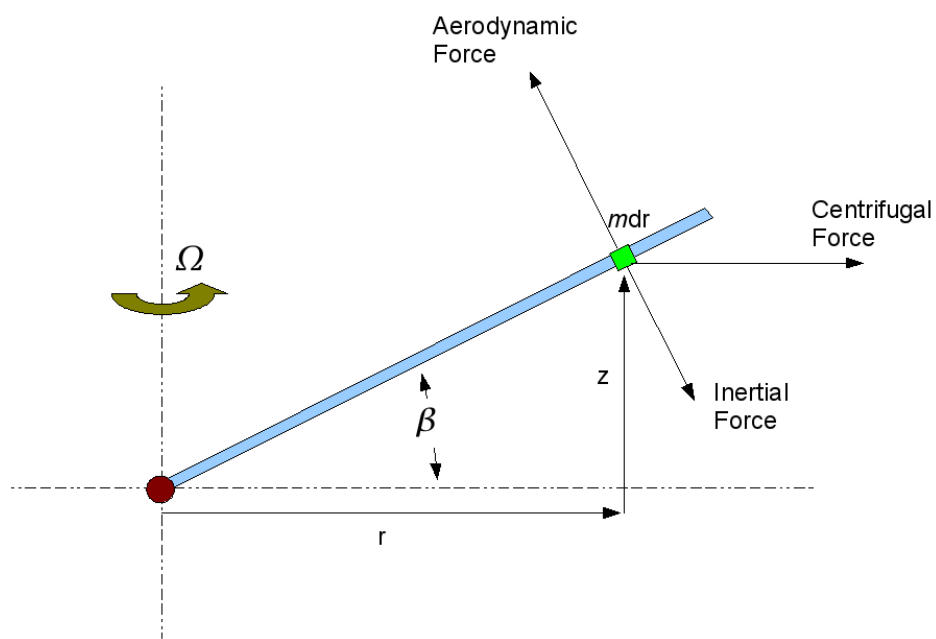
The three forces act to balance the blade in equilibrium when the system rotates with speed  $\Omega$ . Here, the aerodynamic force  $F_z$  is considered as the lift of the individual section of the blade, initiating the upward flap motion registered in terms of the flap angle ( $\beta$ ). The centrifugal force  $m\Omega^2 r$  and inertial force  $mr\ddot{\beta}$  act to oppose the flapping motion caused by the aerodynamic force at each blade section.

The equilibrium condition is generated taking the sum of the moments. The moments in this case will be equal to zero as there is no blade hinge spring considered in this case. The moments are generating by integrating the sectional forces over the entire blade span from root to tip while taking the product with respect to the corresponding moment arm at the location of the sectional force. This operation is represented in Equation 7.1.

$$\int_0^R mr\ddot{\beta}r \, dr + \int_0^R m\Omega^2 r(r\beta) \, dr - \int_0^R F_z r \, dr = 0 \quad (7.1)$$

The representation of the moment equilibrium in Equation 7.1 can be adjusted to put the aerodynamic moments on the right hand side of the equation, as seen in Equation

$$\int_0^R mr\ddot{\beta}r \, dr + \int_0^R m\Omega^2 r(r\beta) \, dr = \int_0^R F_z r \, dr \quad (7.2)$$



1

Figure 7.2: Rigid Rotor Blade Flapping Moments [16].

7.2. The equilibrium equations can be further simplified by defining the blade moment of inertia about the flapping hinge ( $I_b$ ) as represented in Equation 7.3.

$$I_b = \int_0^R r^2 m dr \quad (7.3)$$

Thus, Equation 7.2 reduces to Equation 7.4 by way of Equation 7.3, as seen below.

$$\ddot{\beta} + \beta = \frac{1}{I_b} \int_0^1 r F_z dr \quad (7.4)$$

As a note, the above equation is transformed to use dimensionless quantities for  $\Omega$  and  $R$ . Additionally, the air density coefficient ( $\rho$ ) is normalised for use in the *Lock number* ( $\gamma$  derivation). The Lock number represents the ratio of aerodynamic forces to inertial forces in an dimensionless parameter. It is important to note that the Lock number contains the sole influence on flap motion by way of the air density, as seen in the Lock number definition below. This will play a major part in defining the LTP equations for flapping blade.

$$\gamma = \frac{\rho a c R^4}{I_b} \quad (7.5)$$

As a note, the parameters  $a$  and  $c$  in the Lock number equation above represent the *blade section two dimensional lift curve slope*( $a$ ) and the *blade chord width*( $c$ ) respectively. The Lock number equation can be combined with Equation 7.4 to derive the second order flapping blade equation, as seen in 7.6.

$$\ddot{\beta} + \beta = \gamma \int_0^1 r \frac{F_z}{ac} dr = \gamma M_F \quad (7.6)$$

In order to define the total blade flapping equation the right hand side of Equation 7.6 must be defined. The right hand side of this equation is termed the *aerodynamic flap moment* ( $M_F$ ), which is simply the normalised aerodynamic force,  $\frac{F_z}{ac}$  acting normal to the blade at the radial position,  $r$ . The normalised aerodynamic

force can be more accurately derived in terms of the *tangential and perpendicular air velocities* at the blade segment, (  $U_T$  ) and (  $U_P$  ) respectively, as seen in Equation 7.7.

$$\frac{F_z}{ac} = \frac{L}{ac} = \frac{1}{2}(U_T^2\Theta - U_P U_T) \quad (7.7)$$

where the blade pitch angle is denoted by (  $\Theta$  ). By using the normalised aerodynamic force of Equation 7.7 the aerodynamic flap moment can be described as

$$M_F = \int_0^1 r \frac{F_z}{ac} dr \quad (7.8)$$

$$= \int_0^1 r \frac{1}{2}(U_T^2\Theta - U_P U_T) \quad (7.9)$$

$$= r \frac{1}{2} \left[ (r + \mu \sin\psi)^2 \Theta - (\lambda + r\dot{\beta} + \mu \beta \cos\psi)(r + \mu \sin\psi) \right] dr \quad (7.10)$$

The term  $\psi$  in the above equation refers to the dimensionless time variable for the rotor azimuth(  $\psi$  ), which is related to the rotational velocity  $\Omega$  by  $\psi = \Omega t$  . Also, the terms  $\mu$  and  $\lambda$  refer to the *rotor advance ratio*(  $\mu$  ) and *rotor inflow ratio* (  $\lambda$  ) respectively. These terms are used to describe the forward speed of the rotor system and the ratio of the tangential air inflow due to forward velocity,  $V$ , versus the inflow due to the rotating blades of the rotor system, respectively. As a note, this model assumes linear blade twist and uniform inflow. Performing the integration of Equation

7.10 results in the following expression for the flapping moment

$$M_F = M_\Theta \Theta_{con} + M_{\Theta_{tw}} \Theta_{tw} + M_\lambda \lambda + M_{\dot{\beta}} \dot{\beta} + M_\beta \beta \quad (7.11)$$

$$\begin{aligned} &= \Theta_{con} \left[ \frac{1}{8} + \frac{\mu}{3} \sin \psi + \frac{\mu^2}{4} \sin^2 \psi \right] \\ &+ \Theta_{tw} \left[ \frac{1}{10} + \frac{\mu}{4} \sin \psi + \frac{\mu^2}{6} \sin^2 \psi \right] \\ &- \lambda \left[ \frac{1}{6} + \frac{\mu}{4} \sin \psi \right] \\ &- \dot{\beta} \left[ \frac{1}{8} + \frac{\mu}{6} \sin \psi \right] \\ &- \beta \mu \cos \psi \left[ \frac{1}{6} + \frac{\mu}{4} \sin \psi \right] \end{aligned} \quad (7.12)$$

where  $\Theta_{con}$  is the control input for blade pitch(  $\Theta_{con}$  ) and  $\Theta_{tw}$  is the blade twist (  $\Theta_{tw}$  ). Therefore , by using the above defined representation of the flapping moment,  $M_F$ , Equation 7.6 can be revised as

$$\ddot{\beta} + \beta = \gamma M_F \quad (7.13)$$

$$\ddot{\beta} + \beta = \gamma \left[ M_\Theta \Theta_{con} + M_{\Theta_{tw}} \Theta_{tw} + M_\lambda \lambda + M_{\dot{\beta}} \dot{\beta} + M_\beta \beta \right] .$$

By reviewing Equation 7.14 with consideration of the coefficients making up the flapping moment  $M_F$  in Equation 7.13 it is clear that the second order flapping equations of motion are time periodic. This is due to the *sin* and *cosine* terms in the individual coefficient that make up  $M_F$ . Equation 7.14 can be further simplified by linearising the terms of  $M_F$  and combining like terms to result in

$$\ddot{\beta} + \frac{\gamma}{8} \left( 1 + \frac{4}{3} \mu \sin \psi \right) \dot{\beta} + \left[ 1 + \frac{\gamma}{8} \left( \frac{4}{3} \mu \cos \psi + \mu^2 \sin 2\psi \right) \right] \beta = f(\psi) . \quad (7.14)$$

It is noted with balancing of terms that the terms of  $M_F$  that are left on the right hand side define a periodic forcing function,  $f(\psi)$  as seen in Equation 7.15.

$$f(\psi) = \frac{\gamma}{8} \left( 1 + \mu^2 + \frac{8}{3} \mu \sin \psi - \mu^2 \cos 2\psi \right) \theta_{con} + \gamma \left( \frac{1}{10} + \frac{\mu^2}{12} + \frac{\mu}{4} \sin \psi - \frac{\mu^2}{12} \cos 2\psi \right) \theta_{tw} - \gamma \left( \frac{1}{6} + \frac{\mu}{4} \sin \psi \right) \lambda \quad (7.15)$$

Further simplifications can be made by assuming zero blade twist,  $\Theta_{tw}$ , and neglecting  $\lambda$  as it can be assumed as a plant disturbance in this case.

The linearized equations of motion represented in Equation 7.14 can be transformed into state space form represented in 7.16 having states  $\beta, \dot{\beta}$  and having control input  $\Theta_{con}$ .

$$\begin{aligned} \dot{x}(\psi) &= A(\psi)x(\psi) + B(\psi)u(\psi) \\ y(\psi) &= C(\psi)x(\psi) \end{aligned} \quad (7.16)$$

where the feedforward matrix  $D(\psi)$  is omitted as there is no feedforward in this system. As noted above, the system is linear time periodic, and is described in state space form in term of the time periodic matrices  $A(\psi)$  and  $B(\psi)$  as

$$A(\psi) = \begin{bmatrix} 0 & 1 \\ -\left\{1 + \frac{\gamma}{8} \left( \frac{4}{3} \mu \cos \psi + \mu^2 \sin 2\psi \right) \right\} & -\frac{\gamma}{8} \left( 1 + \frac{4}{3} \mu \sin \psi \right) \end{bmatrix} \quad (7.17)$$

$$B(\psi) = \begin{bmatrix} 0 \\ \frac{\gamma}{8} \left( 1 + \mu^2 + \frac{8}{3} \mu \sin \psi - \mu^2 \cos 2\psi \right) \end{bmatrix}. \quad (7.18)$$

The output of this system is only the state  $\beta$ , which is represented by the output matrix,  $C(\psi)$

$$C(\psi) = \begin{bmatrix} 1 & 0 \end{bmatrix}. \quad (7.19)$$

In order to transform the linear time periodic system in to harmonic balance state space form, the Fourier series coefficients of the time periodic matrices in Equations 7.18 and 7.18 must first be identified. This is seen in Equations 7.20 and 7.21 , for  $A$  and  $B$  respectively. As the output matrix  $C$  has no periodic terms, it will have only the zero harmonic term,  $C_0$ .

$$\begin{aligned}
A_0 &= \begin{bmatrix} 0 & 1 \\ -1 & -\frac{\gamma}{8} \end{bmatrix} \\
A_1 &= \begin{bmatrix} 0 & 0 \\ -\frac{\gamma\mu}{12} & j\frac{\gamma\mu}{12} \end{bmatrix} & A_{-1} = A_1^* \\
A_2 &= \begin{bmatrix} 0 & 0 \\ j\frac{\gamma\mu^2}{16} & 0 \end{bmatrix} & A_{-2} = A_2^* .
\end{aligned} \tag{7.20}$$

$$\begin{aligned}
B_0 &= \begin{bmatrix} 0 \\ \frac{\gamma}{8} (1 + \mu^2) \end{bmatrix} \\
B_1 &= \begin{bmatrix} 0 \\ -j\frac{\gamma\mu}{6} \end{bmatrix} & B_{-1} = B_1^* \\
B_2 &= \begin{bmatrix} 0 \\ -\frac{\gamma\mu^2}{16} \end{bmatrix} & B_{-2} = B_2^* \\
C_0 &= \begin{bmatrix} 1 & 0 \end{bmatrix}
\end{aligned} \tag{7.21}$$

It is important to note that the terms denoted by an asterix in Equations 7.20 and 7.21 are the complex conjugates of the respective matrix. In light of the above comments, the output matrix  $C$  is represented as

$$C_0 = \begin{bmatrix} 1 & 0 \end{bmatrix} . \tag{7.22}$$

Now, by way of Equations 7.20, 7.21, and 7.22, the *HBSSM* presented in Equation 5.43 can now be created for the linear time periodic flapping blade model of the form presented in Equation 7.23

$$\begin{aligned}\dot{x} &= (\mathcal{A} - \mathcal{N})x + \mathcal{B}u \\ y &= \mathcal{C}x + \mathcal{D}u\end{aligned}\tag{7.23}$$

where the matrix  $(\mathcal{A} - \mathcal{N}), \mathcal{B}, \mathcal{C}, \mathcal{D}$  of the HBSSM are in block Toeplitz form.

Now that a single flapping blade model is presented in HBSSM, as in Equation 7.23, the entire rotor system can now be modeled by combining multiple blade models as one state space system. As noted in the beginning of this Section, a four bladed rotor system is desired. To begin with, four individual flapping blades represented each in the form of equations 7.16, 7.18, and 7.18 will be used to form the basic rotor model, as seen below.

$$\begin{aligned}\dot{x}(\psi) &= A(\psi)x(\psi) + B(\psi)u(\psi) \\ y(\psi) &= C(\psi)x(\psi)\end{aligned}\tag{7.24}$$

where the plant matrix,  $A(\psi)$  of the combined system is represented as

$$A(\psi) = \begin{bmatrix} [A_1] & & & \\ & [A_2] & & \\ & & [A_3] & \\ & & & [A_4] \end{bmatrix}\tag{7.25}$$

and the control matrix,  $B(\psi)$  of the combined system is represented as

$$B(\psi) = \begin{bmatrix} [B_1] & & & \\ & [B_2] & & \\ & & [B_3] & \\ & & & [B_4] \end{bmatrix} \quad (7.26)$$

where the off diagonal terms in the above Equations are null. As a note, the submatrices  $A_n$ ,  $n = 1 \dots 4$  of Equation 7.25 are identical to each other and are individually equal to  $A(\psi)$  of the single blade Equation 7.18. The same is true for the submatrices  $B_n$ ,  $n = 1 \dots 4$  of Equation 7.26 which are individually equal to  $B(\psi)$  of the single blade Equation 7.18. Since this system contains no blade lag, the flapping motion of each blade is uncoupled from any other blade. As this system now contains four blades, each with states  $\beta, \dot{\beta}$  and having control input  $\Theta_{con}$ , the state and control matrices must now be redescribed as

$$x(\psi) = \begin{bmatrix} \beta_1 \\ \dot{\beta}_1 \\ \beta_2 \\ \dot{\beta}_2 \\ \beta_3 \\ \dot{\beta}_3 \\ \beta_4 \\ \dot{\beta}_4 \end{bmatrix} \quad (7.27)$$

$$u(\psi) = \begin{bmatrix} \Theta_{con \ 1} \\ \Theta_{con \ 2} \\ \Theta_{con \ 3} \\ \Theta_{con \ 4} \end{bmatrix} \quad (7.28)$$

As a note, the subscript indices in Equations 7.27 and 7.28 refer to the individual blade with which they are associated.

In order to reconstruct the HBSSM for a four bladed rotor, the Fourier coefficients represented in Equations 7.20, 7.21, and 7.22 will be expanded to contain all four blades instead of a single blade. For ease of representation, each matrix from the HBSSM that is associated with a specific blade will be denoted by a subscript, numbered by the number of the blade. For example the zero harmonic contribution of the second blade of the  $A$  matrix will be represented as  $A_{0_2}$ . As all of the blades are assumed identical the Fourier series coefficients represented in Equations 7.20, 7.21, and 7.22 for a single blade are simply repeated for every blade. Thus, for the example of the second blade,  $A_{0_2} = A_0$  of Equation 7.20. This procedure is identical for the  $B$  and  $C$  Fourier matrix formulations. Using this rationale, the Fourier series coefficients of the four bladed rotor system are presented in Equations 7.29, 7.30, and 7.31 below. First, for the  $A$  matrix Fourier coefficient representation:

$$\begin{aligned}
 A_0 &= \begin{bmatrix} [A_{0_1}] & \mathbf{0} & \mathbf{0} & \mathbf{0} \\ \mathbf{0} & [A_{0_2}] & \mathbf{0} & \mathbf{0} \\ \mathbf{0} & \mathbf{0} & [A_{0_3}] & \mathbf{0} \\ \mathbf{0} & \mathbf{0} & \mathbf{0} & [A_{0_4}] \end{bmatrix} \\
 A_1 &= \begin{bmatrix} [A_{1_1}] & \mathbf{0} & \mathbf{0} & \mathbf{0} \\ \mathbf{0} & [A_{1_2}] & \mathbf{0} & \mathbf{0} \\ \mathbf{0} & \mathbf{0} & [A_{1_3}] & \mathbf{0} \\ \mathbf{0} & \mathbf{0} & \mathbf{0} & [A_{1_4}] \end{bmatrix} & A_{-1} = A_1^* \\
 A_2 &= \begin{bmatrix} [A_{2_1}] & \mathbf{0} & \mathbf{0} & \mathbf{0} \\ \mathbf{0} & [A_{2_2}] & \mathbf{0} & \mathbf{0} \\ \mathbf{0} & \mathbf{0} & [A_{2_3}] & \mathbf{0} \\ \mathbf{0} & \mathbf{0} & \mathbf{0} & [A_{2_4}] \end{bmatrix} & A_{-2} = A_2^*
 \end{aligned} \tag{7.29}$$

Next, for the  $B$  matrix Fourier coefficient representation:

$$\begin{aligned}
B_0 &= \begin{bmatrix} [B_{0_1}] & \mathbf{0} & \mathbf{0} & \mathbf{0} \\ \mathbf{0} & [B_{0_2}] & \mathbf{0} & \mathbf{0} \\ \mathbf{0} & \mathbf{0} & [B_{0_3}] & \mathbf{0} \\ \mathbf{0} & \mathbf{0} & \mathbf{0} & [B_{0_4}] \end{bmatrix} \\
B_1 &= \begin{bmatrix} [B_{1_1}] & \mathbf{0} & \mathbf{0} & \mathbf{0} \\ \mathbf{0} & [B_{1_2}] & \mathbf{0} & \mathbf{0} \\ \mathbf{0} & \mathbf{0} & [B_{1_3}] & \mathbf{0} \\ \mathbf{0} & \mathbf{0} & \mathbf{0} & [B_{1_4}] \end{bmatrix} & B_{-1} = B_1^* \\
B_2 &= \begin{bmatrix} [B_{2_1}] & \mathbf{0} & \mathbf{0} & \mathbf{0} \\ \mathbf{0} & [B_{2_2}] & \mathbf{0} & \mathbf{0} \\ \mathbf{0} & \mathbf{0} & [B_{2_3}] & \mathbf{0} \\ \mathbf{0} & \mathbf{0} & \mathbf{0} & [B_{2_4}] \end{bmatrix} & B_{-2} = B_2^*
\end{aligned} \tag{7.30}$$

Finally, the  $C$  matrix Fourier coefficient representation contains only the zero harmonic as it is not periodic as stated above.

$$C_0 = \begin{bmatrix} [C_{0_1}] & \mathbf{0} & \mathbf{0} & \mathbf{0} \\ \mathbf{0} & [C_{0_2}] & \mathbf{0} & \mathbf{0} \\ \mathbf{0} & \mathbf{0} & [C_{0_3}] & \mathbf{0} \\ \mathbf{0} & \mathbf{0} & \mathbf{0} & [C_{0_4}] \end{bmatrix} \tag{7.31}$$

Now, using the same approach for the HBSSM as for the single blade, the HBSSM of the four bladed rotor system can now be created. The Fourier coefficient matrices for the four bladed system represented in Equations 7.29, 7.30, and 7.31 are used to form the block Toeplitz matrices  $(\mathcal{A} - \mathcal{N}), \mathcal{B}, \mathcal{C}, \mathcal{D}$  used to create the four bladed HBSSM of the form listed in Equation 7.23.

With the completion of the four bladed rotor system in HBSSM form, we are able to now able to perform Cramer-Rao bound analysis on the individual system pa-

rameters developed from system identification. Furthermore, we can now develop an optimal LQR controller to attenuate the out of plane rotor vibrations. The structure of the controller will first be explained.

#### ***7.4 Design of a Optimal Vibration Attenuation Controller for a Linear Time Periodic Rotor System***

The intent of this research is to reduce to a suitable level the out of plane vibrations of the main rotor system. However, due to the modeling constraints imposed by existing control methods, several prerequisites to controller development must first be addressed before the control development can go forward. The first prerequisite is namely that the model must be represented as LTP for accuracy. The second prerequisite is the formation of a state space representation of the LTP rotor. These prerequisites have been addressed in the previous chapters, and thus an adequate vibration attenuation controller can now be explored and developed.

As stated in chapter III, several control methodologies currently exist in the area of rotorcraft control, however *optimal control* [7,36,40] will be the focus of this research due to the robust characteristics to systems with poor state knowledge. Furthermore, linear optimal methods were selected for use as they inherently use parametric models for the controller development. This is especially attractive as the one of the key aspects of this research is to both identify and verify a the parameters of a parametric linear model. Finally, the guaranteed stability margins of infinite upward and one half downward gain margins are necessary for a system that is subject to poor system parameters. The next Section will briefly cover the development of a LTP linear quadratic regulator followed by a tracking regulator design used to eliminate rotor vibrations.

#### ***7.5 The Linear Time Periodic Linear Quadratic Regulator***

The linear quadratic regulator (LQR) is a well established method for optimal control for a linearized plant model. The LQR method is built upon optimising a

quadratic cost function while assuming perfect state knowledge. As the LQR controller has been adequately described for both LTI [2] and LTP [42] systems, a brief description of the regulator will be presented. The formulation of the linear quadratic regulator is similar for both LTI and LTP systems by the relation of the harmonic balance state space model. As such, the presentation of LQR will begin in terms of the LTI system and then present the LTP dual.

The model representing the linear state equations for the LQR are in state space form, as presented in Equation 7.32.

$$\dot{x}(t) = Ax(t) + B_u u(t) \quad (7.32)$$

where  $B_u$  is the *controllable* input matrix. The *quadratic cost function*  $J$  that forms the core of the LQR is presented in Equation 7.33.

$$J(x(t), u(t)) = \frac{1}{2} x^T(t_f) \mathbf{H} x(t_f) + \frac{1}{2} \int_0^{t_f} [x^T(t) \mathbf{Q} x(t) + u^T(t) \mathbf{R} u(t)] dt \quad (7.33)$$

where the matrices  $\mathbf{Q}, \mathbf{H}$  are positive semidefinite state weighting matrices and the matrix  $\mathbf{R}$  is a positive definite control weighting matrix. The *Riccati* equation is required to provide the optimal control solution, as it provides the minimum to Equation 7.33. A brief review of the Riccati equation will now be presented, as it provides the key link between an LTI and LTP linear quadratic regulator.

*7.5.1 The Riccati Equation.* The most common method of solving the constrained quadratic cost associated with the LQR method is the use of the Riccati equation. The Riccati equation is a nonlinear matrix differential equation which solves for the matrix of proportionality  $\mathbf{P}(t)$  between the constraint costates and system states by direct integration backward in time. This is possible as the Riccati equation has only final conditions.

The solution to the optimal control problem is essentially reduced to a solving for  $\mathbf{P}(t)$ , as the optimal control law is defined as

$$\begin{aligned} u(t) &= K(t)x(t) \\ u(t) &= -R^{-1}B_u^T P(t)x(t) \end{aligned} \quad (7.34)$$

where  $K(t)$  is the time varying gain matrix for LTI systems. Thus,  $-R^{-1}B_u^T P(t) = K(t)$ . Furthermore, the matrices  $\mathbf{Q}$  and  $\mathbf{R}$  are from the cost function of Equation 7.33. Additionally, the state(s)  $x(t)$  are assumed to be from perfect and total state knowledge.

The value of  $\mathbf{P}(t)$  associated with the optimal solution is found by integrating the Riccati equation, represented in Equation 7.35 backward in time from the final condition,  $\mathbf{P}(t_f)$ .

$$\dot{P}(t) = -P(t)A - A^T P(t) - Q + P(t)B_u R^{-1} B_u^T P(t) \quad (7.35)$$

where the final condition is given as

$$\dot{P}(t_f) = H. \quad (7.36)$$

The optimal control law is formed by inserting the result of Equation 7.35 into Equation 7.34.

The formulation of the Riccati equation in Equation 7.35 is valid for a LTI system. This formulation can be expanded for a LTP system of the form presented in Equation 7.23 by the use of the harmonic balance state space transformation. Thus, using the LTP HBSSM state model, the LTP Riccati equation is represented as described in reference [42]

$$0 = \mathcal{P}_2(\mathcal{A}_2 - \mathcal{N}_2) + (\mathcal{A}_2 - \mathcal{N}_2)^T \mathcal{P}_2 + \mathcal{Q}_2 - \mathcal{P}_2 \mathcal{B}_{2_u} \mathcal{R}_2^{-1} \mathcal{B}_2^T \mathcal{P}_2 \quad (7.37)$$

$$(7.38)$$

where the matrices  $\mathcal{A}_2, \mathcal{B}_{2_u}, \mathcal{P}_2, \mathcal{Q}_2$  and  $\mathcal{R}_2$  are represented as

$$\mathcal{A}_2 = \begin{bmatrix} \text{Re}(\mathcal{A}) & \text{Im}(\mathcal{A}) \\ \text{Im}(\mathcal{A}) & \text{Re}(\mathcal{A}) \end{bmatrix}. \quad (7.39)$$

The formulation of the remaining matrices  $\mathcal{B}_2, \mathcal{P}_2, \mathcal{Q}_2$  and  $\mathcal{R}_2$  are performed in an identical manner as that seen in Equation 7.39. The computation of  $\mathcal{N}_2$  is also performed in a similar manner as that of Equation 7.39, with the note that  $\text{Re}(\mathcal{N}) = 0$ . Thus,

$$\mathcal{N}_2 = \begin{bmatrix} 0 & -j\mathcal{A} \\ -j\mathcal{A} & 0 \end{bmatrix}. \quad (7.40)$$

The augmented matrices for the LTP Riccati equation are necessary to transform the equation from a complex algebraic representation to a real algebraic representation. This transformation makes available the many algebraic Riccati equation solvers, which is advantageous as they are both numerically stable and accurate.

The solution to the optimal gain in the LTP case retains the same form to that of the LTI case, with the exception that the LTP matrices are in Toeplitz form. . Thus, by inserting the transformed Toeplitz matrices  $\mathcal{B}_{2_u}, \mathcal{P}_2$ , and  $\mathcal{R}_2$  into Equation 7.34, the LTP gain is presented as

$$\begin{aligned} u(t) &= -\mathcal{K}(t)x(t) \\ u(t) &= -\mathcal{R}_2^{-1}\mathcal{B}_{2_u}^T\mathcal{P}_2(t)x(t) \end{aligned} \quad (7.41)$$

where  $\mathcal{K}(t)$  is the time periodic gain matrix. As with the Toeplitz matrices  $\mathcal{A}, \mathcal{B}, \mathcal{C}$ , and  $\mathcal{D}$  of the HBSSM, the time periodic gain matrix  $\mathcal{K}(t)$  is of doubly infinite dimension. For practical application, the gain matrix must be truncated in order to execute on a digital computer. This will be further covered in Section 7.7.3.

## 7.6 Vibration Reduction via Reference Tracking Control

The linear quadratic regulator, which is designed to drive the states of the system to zero, must be augmented to act as a vibration controller. A controller, as compared to a regulator, can track a reference input by forcing the reference input to match the reference output. Thus, the LQR can be modified to a *Reference Tracking Controller* by way of augmenting the LTP system model with an additional error state, which is simply the error between the reference input and output. This additional state is handled by the reference tracking method, *integral feedback control*.

Integral feedback is a method in which an error state,  $e$  is used to zero out errors between a constant reference input signal and the reference output from the plant. The reference signal, in the case of this controller, will be a blade flapping angle,  $\beta_{ref}$ , and will be covered in greater detail in Section 7.6.1.

The error state is simply the integral of the differential equation, denoted in Equation 7.42

$$\begin{aligned}\dot{e} &= r - y(t) \\ &= r - C_m x(t)\end{aligned}\tag{7.42}$$

where  $r$  is the *reference input* signal and  $C_m$  is the measurement output matrix. As a note,  $C_m = C_y$ , where  $C_y$  is the state output matrix. The error state is added to the rotor system model to form the augmented system seen in Equation 7.43.

$$\tilde{\dot{x}}(t) = \tilde{A}x(t) + \tilde{B}_u u(t) + \tilde{B}_r r\tag{7.43}$$

where the expanded plant,  $\tilde{A}$ , control  $\tilde{B}_u$ , and reference  $\tilde{B}_r$  matrices are expanded as seen in Equation 7.44

$$\begin{bmatrix} \dot{x}(t) \\ \dots \\ \dot{e}(t) \end{bmatrix} = \begin{bmatrix} A & \vdots & \mathbf{0} \\ \dots & & \\ -C_m & \vdots & \mathbf{0} \end{bmatrix} \begin{bmatrix} x(t) \\ \dots \\ e(t) \end{bmatrix} + \begin{bmatrix} B_u \\ \dots \\ \mathbf{0} \end{bmatrix} u(t) + \begin{bmatrix} \mathbf{0} \\ \dots \\ \mathbf{I} \end{bmatrix} r. \quad (7.44)$$

The control law  $u(t) = -\tilde{K}(t)\tilde{x}$  is augmented to reflect the addition of the error state, as seen below.

$$\begin{aligned} u(t) &= -\tilde{\mathbf{K}}(t) \begin{bmatrix} x(t) \\ \dots \\ e(t) \end{bmatrix} \\ &= -\begin{bmatrix} K_x(t) & \vdots & K_e(t) \end{bmatrix} \begin{bmatrix} x(t) \\ \dots \\ e(t) \end{bmatrix} \end{aligned} \quad (7.45)$$

The tracking controller is formed by inserting Equation 7.45 into 7.44, as seen in Equation 7.46.

$$\begin{bmatrix} \dot{x}(t) \\ \dots \\ \dot{e}(t) \end{bmatrix} = \begin{bmatrix} A & \vdots & \mathbf{0} \\ \dots & & \\ -C_m & \vdots & \mathbf{0} \end{bmatrix} \begin{bmatrix} x(t) \\ \dots \\ e(t) \end{bmatrix} + \begin{bmatrix} B_u \\ \dots \\ \mathbf{0} \end{bmatrix} \begin{bmatrix} -K_x(t) & \vdots & -K_e(t) \end{bmatrix} \begin{bmatrix} x(t) \\ \dots \\ e(t) \end{bmatrix} + \begin{bmatrix} \mathbf{0} \\ \dots \\ \mathbf{I} \end{bmatrix} r \quad (7.46)$$

The above representation of the tracking controller is further simplified by multiplying out the gain and control matrices, as seen below.

$$\begin{bmatrix} \dot{x}(t) \\ \dots \\ \dot{e}(t) \end{bmatrix} = \begin{bmatrix} \begin{bmatrix} A & \vdots & \mathbf{0} \\ \dots & & \\ -C_m & \vdots & \mathbf{0} \end{bmatrix} + \begin{bmatrix} -B_u K_x(t) & \vdots & -B_u K_e(t) \\ \dots & & \\ \mathbf{0} & \vdots & \mathbf{0} \end{bmatrix} \end{bmatrix} \begin{bmatrix} x(t) \\ \dots \\ e(t) \end{bmatrix} + \begin{bmatrix} \mathbf{0} \\ \dots \\ \mathbf{I} \end{bmatrix} r \quad (7.47)$$

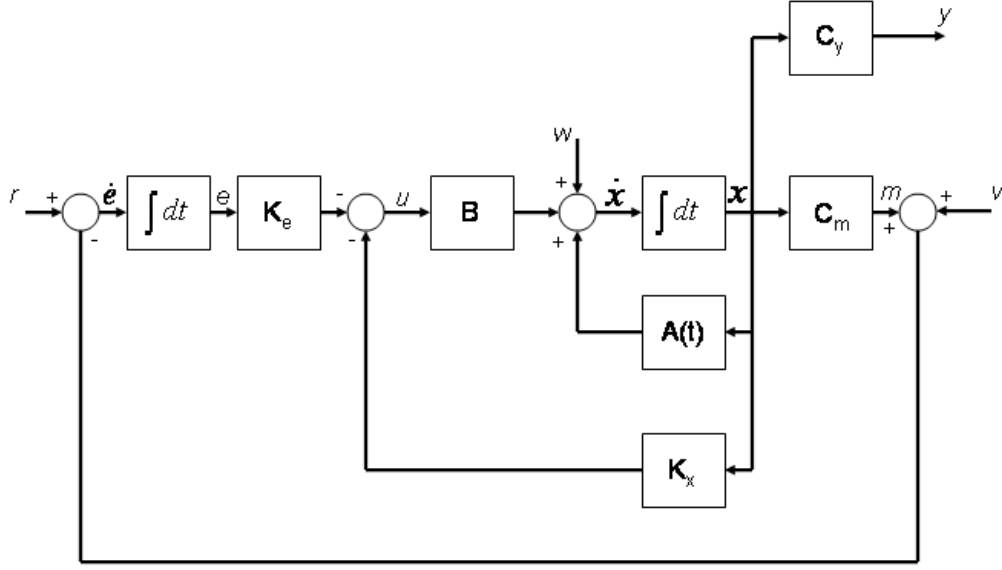


Figure 7.3: Reference Tracking Controller Block Diagram.

The tracking controller is finalised by combining like terms

$$\begin{bmatrix} \dot{x}(t) \\ \dots \\ \dot{e}(t) \end{bmatrix} = \begin{bmatrix} A - B_u K_x(t) & \vdots & -B_u K_e(t) \\ \dots & & \dots \\ -C_m & \vdots & \mathbf{0} \end{bmatrix} \begin{bmatrix} x(t) \\ \dots \\ e(t) \end{bmatrix} + \begin{bmatrix} \mathbf{0} \\ \dots \\ \mathbf{I} \end{bmatrix} r. \quad (7.48)$$

The reference tracking controller described above is seen in Figure 7.3.

The reference tracking controller described so far is applicable to a LTI system. This is easily overcome by using the existing LTP optimal gain calculation method covered in Section 7.5, with the exception of using an augmented system with an error state. Thus, using a process similar to that covered in Equations 7.29 through 7.31 the Fourier series components of the  $A, B$ , and  $C$  matrices can be assembled with the addition of an error state. reference tracking controller can be adapted to a LTP

system. Therefore, the augmented state vector is as follows

$$x(\psi) = \begin{bmatrix} \beta_1 \\ \dot{\beta}_1 \\ \beta_2 \\ \dot{\beta}_2 \\ \beta_3 \\ \dot{\beta}_3 \\ \beta_4 \\ \dot{\beta}_4 \\ e \end{bmatrix} \quad (7.49)$$

which is the same as Equation 7.27 with the exception of the error state. As a note, the control input vector is the same as Equation 7.28. Now, for the augmented matrix  $\tilde{A}$ , the Fourier coefficient representation is presented with the additional error state as

$$\begin{aligned}
\tilde{A}_0 &= \begin{bmatrix} [A_{0_1}] & \mathbf{0} & \mathbf{0} & \mathbf{0} & \mathbf{0} \\ \mathbf{0} & [A_{0_2}] & \mathbf{0} & \mathbf{0} & \mathbf{0} \\ \mathbf{0} & \mathbf{0} & [A_{0_3}] & \mathbf{0} & \mathbf{0} \\ \mathbf{0} & \mathbf{0} & \mathbf{0} & [A_{0_4}] & \mathbf{0} \\ -[C_0] & -[C_0] & -[C_0] & -[C_0] & \mathbf{0} \end{bmatrix} \\
\tilde{A}_1 &= \begin{bmatrix} [A_{1_1}] & \mathbf{0} & \mathbf{0} & \mathbf{0} & \mathbf{0} \\ \mathbf{0} & [A_{1_2}] & \mathbf{0} & \mathbf{0} & \mathbf{0} \\ \mathbf{0} & \mathbf{0} & [A_{1_3}] & \mathbf{0} & \mathbf{0} \\ \mathbf{0} & \mathbf{0} & \mathbf{0} & [A_{1_4}] & \mathbf{0} \\ \mathbf{0} & \mathbf{0} & \mathbf{0} & \mathbf{0} & \mathbf{0} \end{bmatrix} \quad \tilde{A}_{-1} = \tilde{A}_1^* \\
\tilde{A}_2 &= \begin{bmatrix} [A_{2_1}] & \mathbf{0} & \mathbf{0} & \mathbf{0} & \mathbf{0} \\ \mathbf{0} & [A_{2_2}] & \mathbf{0} & \mathbf{0} & \mathbf{0} \\ \mathbf{0} & \mathbf{0} & [A_{2_3}] & \mathbf{0} & \mathbf{0} \\ \mathbf{0} & \mathbf{0} & \mathbf{0} & [A_{2_4}] & \mathbf{0} \\ \mathbf{0} & \mathbf{0} & \mathbf{0} & \mathbf{0} & \mathbf{0} \end{bmatrix} \quad \tilde{A}_{-2} = \tilde{A}_2^*
\end{aligned} \tag{7.50}$$

Next, for the augmented matrix,  $\tilde{B}$  the Fourier coefficient representation is as follows

$$\begin{aligned}
\tilde{B}_0 &= \begin{bmatrix} [B_{01}] & \mathbf{0} & \mathbf{0} & \mathbf{0} \\ \mathbf{0} & [B_{02}] & \mathbf{0} & \mathbf{0} \\ \mathbf{0} & \mathbf{0} & [B_{03}] & \mathbf{0} \\ \mathbf{0} & \mathbf{0} & \mathbf{0} & [B_{04}] \\ \mathbf{0} & \mathbf{0} & \mathbf{0} & \mathbf{0} \end{bmatrix} \\
\tilde{B}_1 &= \begin{bmatrix} [B_{11}] & \mathbf{0} & \mathbf{0} & \mathbf{0} \\ \mathbf{0} & [B_{12}] & \mathbf{0} & \mathbf{0} \\ \mathbf{0} & \mathbf{0} & [B_{13}] & \mathbf{0} \\ \mathbf{0} & \mathbf{0} & \mathbf{0} & [B_{14}] \\ \mathbf{0} & \mathbf{0} & \mathbf{0} & \mathbf{0} \end{bmatrix} & \tilde{B}_{-1} = \tilde{B}_1^* \\
\tilde{B}_2 &= \begin{bmatrix} [B_{21}] & \mathbf{0} & \mathbf{0} & \mathbf{0} \\ \mathbf{0} & [B_{22}] & \mathbf{0} & \mathbf{0} \\ \mathbf{0} & \mathbf{0} & [B_{23}] & \mathbf{0} \\ \mathbf{0} & \mathbf{0} & \mathbf{0} & [B_{24}] \\ \mathbf{0} & \mathbf{0} & \mathbf{0} & \mathbf{0} \end{bmatrix} & \tilde{B}_{-2} = \tilde{B}_2^*
\end{aligned} \tag{7.51}$$

As before, the  $\tilde{C}$  matrix Fourier coefficient representation contains only the zero harmonic as it is not periodic as stated above. It does contain, however, the reference output as the sum of all four blade flapping angles,  $\beta$ . The augmented matrix  $\tilde{C}$  is not required for the gain calculation, however, it will be needed in the development of the reference tracking controller. The selection of the reference output will be covered in Section 7.6.1.

$$\tilde{C}_0 = \begin{bmatrix} [C_{01}] & \mathbf{0} & \mathbf{0} & \mathbf{0} & \mathbf{0} \\ \mathbf{0} & [C_{02}] & \mathbf{0} & \mathbf{0} & \mathbf{0} \\ \mathbf{0} & \mathbf{0} & [C_{03}] & \mathbf{0} & \mathbf{0} \\ \mathbf{0} & \mathbf{0} & \mathbf{0} & [C_{04}] & \mathbf{0} \\ C_{01} & [C_{02}] & [C_{03}] & [C_{04}] & \mathbf{0} \end{bmatrix} \tag{7.52}$$

Now that the Fourier representations of the state and control matrices have been assembled the block Toeplitz forms  $\tilde{\mathcal{A}}$  and  $\tilde{\mathcal{B}}$  can be created using the method covered earlier. From this point, the LQR gains can be computed in an identical fashion as covered in Section 7.5 using these matrices. The remainder of the LTP tracking controller development is identical to that of an LTI system.

*7.6.1 Tracking Control Applied to Out of Plane Rotor Vibrations.* In order to use the tracking controller developed in Section 7.4 an adequate reference input and output must be defined. As noted in chapter II, the out of plane vibrations in a helicopter rotor system are caused by differences in blade lift when each blade in the rotor system is considered. In this work, each blade is considered to have identical profile and thus if each blade has an identical flap track over one period, the lift of each blade is then identical. Thus, an input reference signal is generated by considering the combined blade flapping angles of a perfect rotor. This is represented in Figures 7.4 and 7.5, which is representative of the blade flapping induced by an input of one degree pitch  $\Theta_{con\ 1-4} = 1$  for each blade at an inflow ratio of  $\mu = .3$ . The individual blade flapping angles of all blades in the rotor system are summed at each time step, as presented in Figure 7.5. This value is the optimal reference value, as in this case all the blade lifts are identical, thus having no out of plane vibrations. The output reference value is the summation of each of the blade flapping angles, as seen in the output matrix  $\tilde{C}$  in Equation 7.52. The steady state value presented in Figure 7.5 is the reference input that will be applied to the test rotor system .

The performance of the vibration controller is evaluated in Section 7.8 by inducing a lift imbalance in the rotor system and then reviewing the ability of the system to eliminate the ensuing vibration. To induce the lift imbalance, pitch inputs of one or more of the blade pitch,  $\Theta_{con}$ , differing from the desired setting of one degree will be set. This will generate an imbalance in lifts between the individual blades, which ultimately will cause an out of plane oscillatory vibration. The reference tracking function of the vibration controller will adjust the blade pitches of each blade

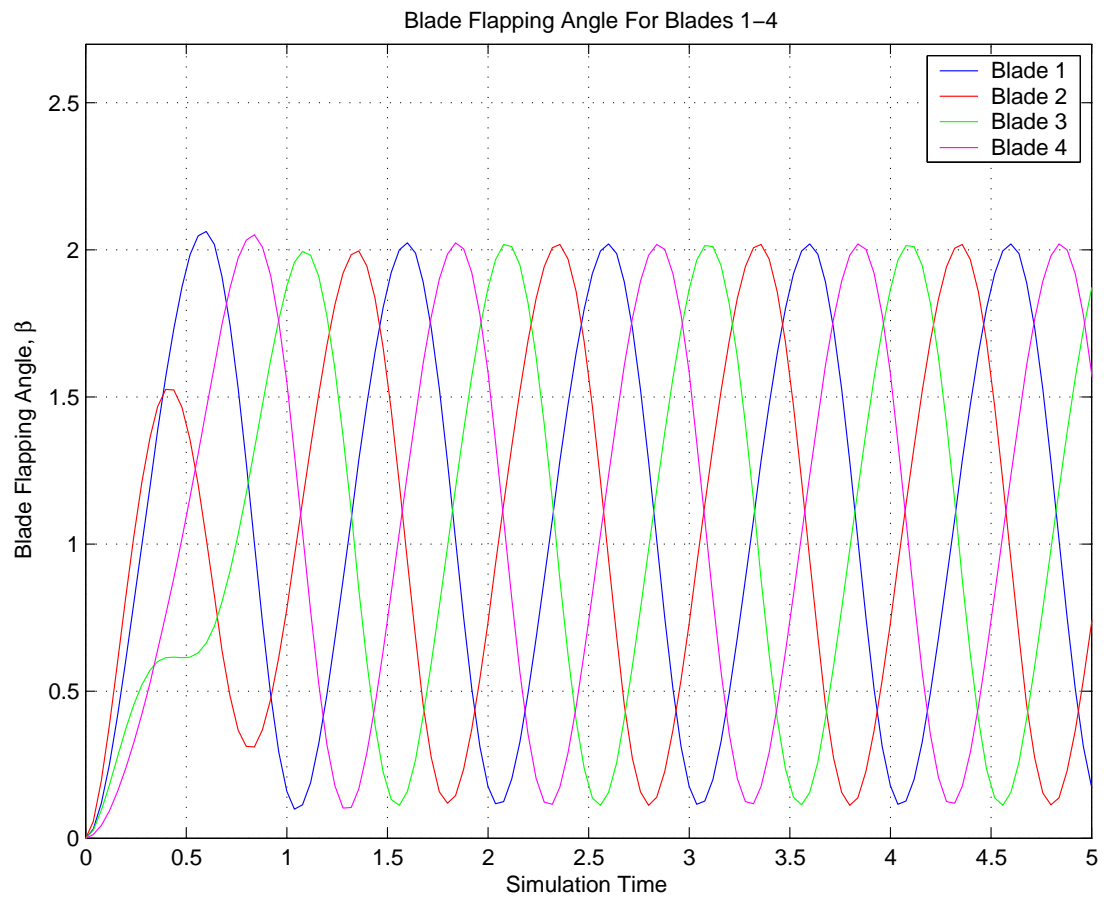


Figure 7.4: Individual Flap Angles of the Four Blades.

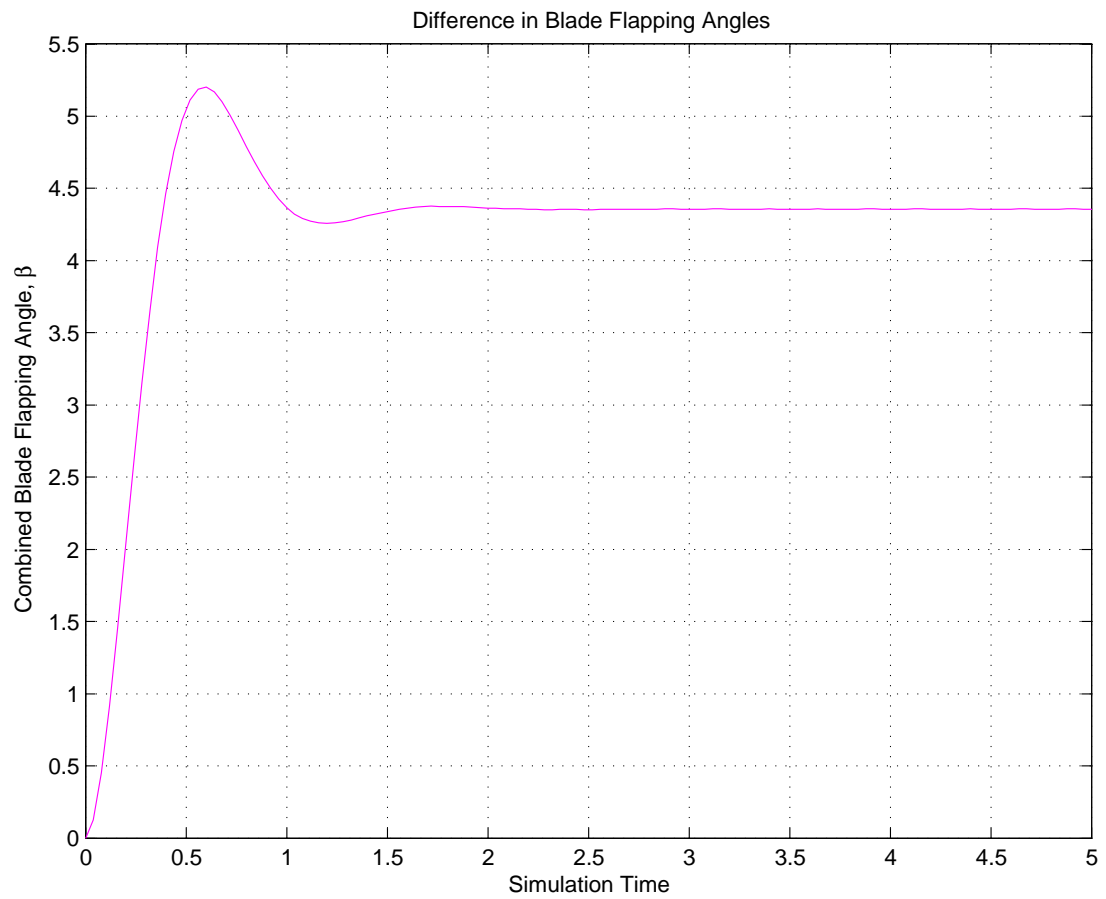


Figure 7.5: Combined Flap Angles of the Four Blades.

until the input and output references are the same, thus eliminating the rotor vibrations. More on this will be covered in Section 7.8, which details an application of this controller on a rotor system that has incorrect pitch input.

The next Section will outline the application of this controller, while demonstrating how the Cramer-Rao bound can validate the control solution.

## ***7.7 Controller Model Parameter Validation via the Cramer-Rao Bound***

An accurate vibration controller has a fundamental underpinning; an accurate model which the controller is based upon. This is important, as the controller will only be as effective as the model is accurate. For an adaptive controller, such as one that identifies the controller's model 'on the fly', a method such as the *Cramer-Rao lower bound* that can validate the model will in turn ensure accurate control. This Section will develop the Cramer-Rao lower bound to validate model parameters which are based upon system identification. The Cramer-Rao bounds will then, in Section 7.8, be used to validate the effectiveness of an adaptive version of the vibration controller described in Section 7.6.

This Section will begin by describing the calculation of the Cramer-Rao bound for parameters of the rotor system model. The Section will conclude by showing the Cramer-Rao bounds for a select model parameter, with the intent to demonstrate the validity of model parameters developed from an online system identification method.

*7.7.1 Cramer-Rao Bound Calculation for a LTP Rotor Model.* As stated in Section 7.7, the accuracy of the individual parameters that make up a model, in this case a HBSSM rotor model, is essential to developing an accurate vibration controller. In the case of poorly identified parameters from system identification, the model developed from those parameters will lead to inaccurate LQR gains. This will ultimately lead to poor controller performance in terms of tracking error or excessive control input to compensate for modeling errors. This Section will develop

the Cramer-Rao bounds needed to detect poorly identified system parameters in an attempt to provide better online controller performance.

The development of the Cramer-Rao lower bound for the LTP rotor model described in Section 7.3 will begin by recalling the work covered in Section 6.6.2. For starters, the Cramer-Rao lower bound can be computed by taking the square root of inverse of the block Toeplitz Hessian,  $\mathcal{H}$ , as seen below in Equation 7.53. As a note, the index  $j$  relates to the parameter for which the Cramer-Rao bound is being developed.

$$\mathcal{CR}_j \approx \sqrt{(\mathcal{H}^{-1})_{j,j}} \quad (7.53)$$

The Hessian is formed by summing the square of the partial derivative of the frequency response function,  $\frac{\partial \mathcal{G}(\iota\omega_f)}{\partial p}$ , with the measurement signal noise weighting matrix,  $W$ , over all input frequencies,  $\omega_f$ . The partial derivative frequency response function is described using the state space matrices  $\mathcal{A}$ ,  $\mathcal{N}$ ,  $\mathcal{B}$ ,  $\mathcal{C}$ , and  $\mathcal{D}$  from Eq. 7.23 in a modified form of Equation 7.55, as seen below.

$$\frac{\partial \mathcal{G}(\iota\omega_f)}{\partial p} = \frac{\partial}{\partial p} [\mathcal{C}(\iota\omega_f I - \mathcal{A}\mathcal{H}\mathcal{N})^{-1}\mathcal{B} + \mathcal{D}] \quad (7.54)$$

$$\begin{aligned} &= \mathcal{C}(\iota\omega_f I - \mathcal{A}\mathcal{H}\mathcal{N})^{-1} \frac{\partial \mathcal{A}}{\partial p} (\iota\omega_f I - \mathcal{A}\mathcal{H}\mathcal{N})^{-1} \mathcal{B} \\ &\quad + \mathcal{C}(\iota\omega_f I - \mathcal{A}\mathcal{H}\mathcal{N})^{-1} \frac{\partial \mathcal{B}}{\partial p} \end{aligned} \quad (7.55)$$

where, as before, the matrix  $\mathcal{A}\mathcal{H}\mathcal{N}$  is defined as

$$\mathcal{A}\mathcal{H}\mathcal{N} = \mathcal{A} - \mathcal{N}. \quad (7.56)$$

The above Equations 7.55 and 7.56 redefine the partial derivative of the response error from Equation 6.27 to an expression containing a doubly infinite block of complex Fourier coefficients in Toeplitz form. To complete the computation of the Cramer-Rao lower bound for LTP systems defined in block Toeplitz form, Equation 6.48 is

used to in Equation 7.57 to define the Hessian,  $\mathcal{H}$ , in a manner analogous to Equation 6.31.

$$\mathcal{H}_{j,k} = \sum_{l=1}^{n_{\omega_f}} W_{j,k}(\omega_l) \left[ \frac{\partial \mathcal{G}_{j,k}(\omega_{f_l})}{\partial p} \right]^2 \quad (7.57)$$

In Equations 7.20 through 7.22 the Fourier series coefficients matrices of an individual rotor blade, Equation 7.18 and 7.18, were presented. As covered previously, these matrices are used to form the block Toeplitz matrices  $\mathcal{A}$  and  $\mathcal{B}$ . The partial derivatives  $\frac{\partial \mathcal{A}}{\partial p}$  and  $\frac{\partial \mathcal{B}}{\partial p}$  are developed for Equation 7.55 in an identical manner by using the definitions for the Fourier coefficients  $\frac{\partial A}{\partial p}$  and  $\frac{\partial B}{\partial p}$  as seen in Equations 7.58 and 7.59. It is important to note that in this case, the parameter  $p$  with which the partial derivative is taken in the *Lock number*,  $\gamma$ . The rationale for this parameter selection will be covered in Section 7.8.

$$\begin{aligned} \frac{\partial A}{\partial \gamma_0} &= \begin{bmatrix} 0 & 1 \\ -1 & -\frac{1}{8} \end{bmatrix} \\ \frac{\partial A}{\partial \gamma_1} &= \begin{bmatrix} 0 & 0 \\ -\frac{\mu}{12} & j\frac{\mu}{12} \end{bmatrix} & \frac{\partial A}{\partial \gamma_{-1}} &= A_1^* \\ \frac{\partial A}{\partial \gamma_2} &= \begin{bmatrix} 0 & 0 \\ j\frac{\mu^2}{16} & 0 \end{bmatrix} & \frac{\partial A}{\partial \gamma_{-2}} &= A_2^* \end{aligned} \quad (7.58)$$

$$\begin{aligned} \frac{\partial B}{\partial \gamma_0} &= \begin{bmatrix} 0 \\ \frac{1}{8}(1 + \mu^2) \end{bmatrix} \\ \frac{\partial B}{\partial \gamma_1} &= \begin{bmatrix} 0 \\ -j\frac{\mu}{6} \end{bmatrix} & \frac{\partial B}{\partial \gamma_{-1}} &= B_1^* \\ \frac{\partial B}{\partial \gamma_2} &= \begin{bmatrix} 0 \\ -\frac{\mu^2}{16} \end{bmatrix} & \frac{\partial B}{\partial \gamma_{-2}} &= B_2^* \end{aligned} \quad (7.59)$$

As before, by developing the Fourier series coefficients, the block Toeplitz forms of the plant and control matrices were then populated. Similarly, the same method is applied to form the partial derivatives  $\frac{\partial A}{\partial p}$  and  $\frac{\partial B}{\partial p}$  by using Equations 7.58 and 7.59 to form Equation 7.60.

$$\frac{\partial A}{\partial \gamma} = \begin{bmatrix} \ddots & \vdots & \vdots & \vdots & \vdots & \vdots & \\ \dots & \frac{\partial A}{\partial \gamma_0} & \frac{\partial A}{\partial \gamma_{-1}} & \frac{\partial A}{\partial \gamma_{-2}} & \mathbf{0} & \mathbf{0} & \dots \\ \dots & \frac{\partial A}{\partial \gamma_1} & \frac{\partial A}{\partial \gamma_0} & \frac{\partial A}{\partial \gamma_{-1}} & \frac{\partial A}{\partial \gamma_{-2}} & \mathbf{0} & \dots \\ \dots & \frac{\partial A}{\partial \gamma_2} & \frac{\partial A}{\partial \gamma_1} & \frac{\partial A}{\partial \gamma_0} & \frac{\partial A}{\partial \gamma_{-1}} & \frac{\partial A}{\partial \gamma_{-2}} & \dots \\ \dots & \mathbf{0} & \frac{\partial A}{\partial \gamma_2} & \frac{\partial A}{\partial \gamma_1} & \frac{\partial A}{\partial \gamma_0} & \frac{\partial A}{\partial \gamma_{-1}} & \dots \\ \dots & \mathbf{0} & \mathbf{0} & \frac{\partial A}{\partial \gamma_2} & \frac{\partial A}{\partial \gamma_1} & \frac{\partial A}{\partial \gamma_0} & \dots \\ & \vdots & \vdots & \vdots & \vdots & \vdots & \ddots \end{bmatrix} \quad (7.60)$$

where  $\frac{\partial B}{\partial p}$  is performed in a likewise manner.

The necessary components of Equation 7.53 are now complete and the Cramer-Rao bound can be calculated for the identified Lock parameter,  $\gamma$ , of the blade model. The next Section will show results of the Cramer-Rao bound for the parameter  $\gamma$ , which is derived from the frequency domain system identification method developed by Hwang [12] for LTP systems.

*7.7.2 Cramer-Rao Bounds of Lock Number,  $\gamma$ .* In this Section the *Lock* number,  $\gamma$ , of the rotor blade model represented by Equations 7.18 and 7.18 will be validated for accuracy by way of the Cramer-Rao bound. The parameters to be validated are first collected by way of a frequency domain system identification method developed by Hwang [12] for LTP systems over a range of input frequency,  $\omega_f$ , and measurement noise,  $S_v$ . Once these values are obtained for all frequency inputs and noise variances, the corresponding Cramer-Rao bound calculated by way of Equation 7.53 is then compared to the identified value.

The system identification process begins by using a blade model consisting of the following parameters, as defined in table 7.61

Advance Ratio, $\mu$	Lock Number, $\gamma$	(7.61)
$\mu = 0.3$	$\gamma = 8$	

The system identification process proceeds by inputting an oscillation of frequency  $\omega_f$  in  $\Theta_{con}$ . Each system identification run is performed at a single input frequency, where the range of  $\omega_f = \omega_p(0, 0.05, 0.1, 0.2, 0.3, 0.4, 0.5)$ , where  $\omega_p = 1$ . As a note, both the system identification method and the Cramer-Rao bound method can accept a range of multiple input frequencies for each run, such as a signal chirp. This method was not selected for this work, however, as the parameter validity was desired at individual frequencies so that a range of acceptable parameters could be identified. This will be addressed as the plots of the Cramer-Rao bounds are discussed.

As each system is stimulated at one of the values of  $\omega_f$ , the system output measurement is corrupted by white noise having spectral density,  $S_v$ . In this work, a range of spectral densities  $S_v = 1, 2, 3, 4$  was considered. For all values in the range of  $S_v$ , a run is made for every input value in the range of  $\omega_f$ . Figures A.1, A.2, A.3, and A.4 of Appendix A are plots of the identified value of  $\gamma$  at each  $\omega_f$  with the corresponding Cramer-Rao bound overlaid. Each plot is representative of the one of the values of  $S_v$  in the defined range above.

By reviewing the comparison plots mentioned above in Appendix A, it is clear that both input frequency,  $\omega_f$ , and the intensity of the measurement noise,  $S_v$ , directly affect the quality of the estimate of the parameter,  $\gamma$ . First, consider the effect of the input frequency,  $\omega_f$ , on the accuracy of the parameter estimate. As was discussed in chapter VI, the Cramer-Rao bound presents a scaled inverse of the frequency response function. Thus, as frequency response falls off the Cramer-Rao bound begins to grow in magnitude. This is seen in Figure 7.6, which plots the Cramer-Rao bound for the blade model for all input frequencies from  $0 \leq \omega_f \leq 0.5\omega_p$ . As an example, this

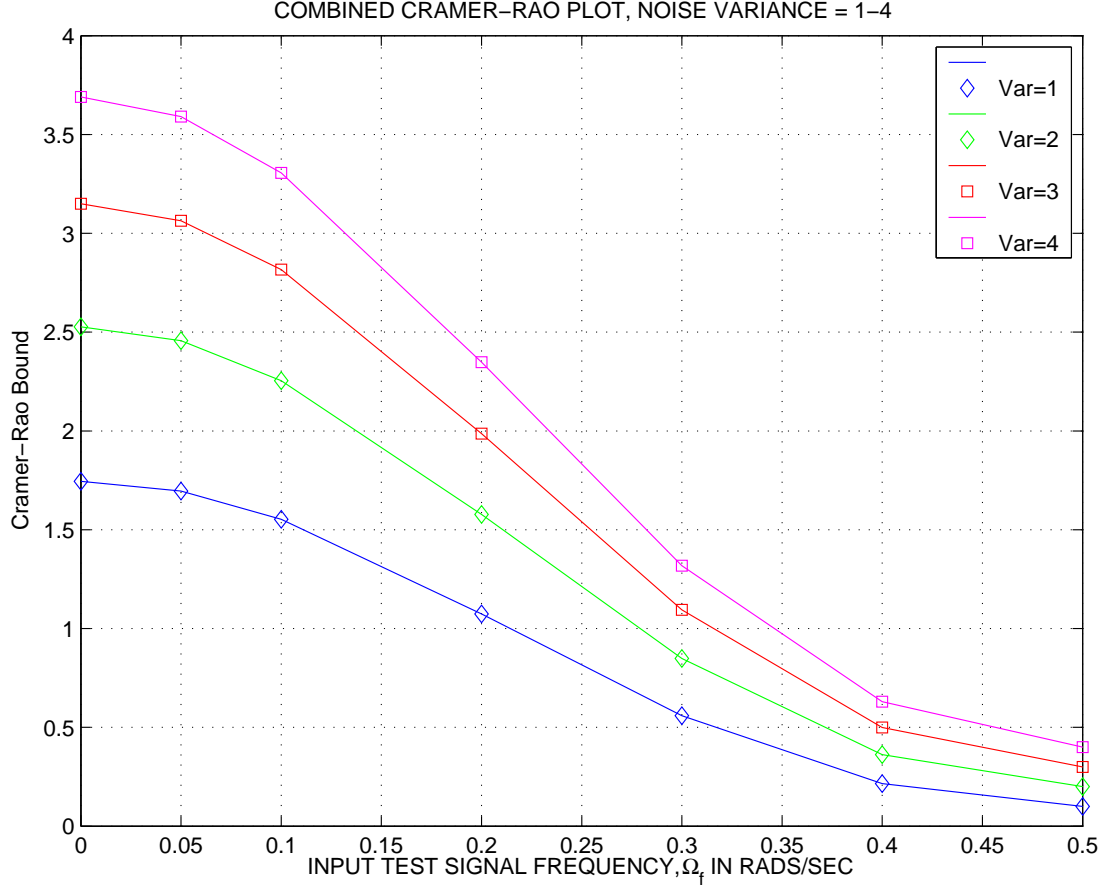


Figure 7.6: Cramer-Rao Bounds for all Frequencies,  $\omega_f$ , all Noise Values,  $S_v$ .

plot reveals that at low input frequencies the corresponding Cramer-Rao bound has a large magnitude. This is due to the poor frequency response of the blade model at low frequency input. Secondly, this plot also presents the Cramer-Rao bound over this range for each value of  $S_v$ , which demonstrates the effect of measurement signal noise on the magnitude of the bound. When considering the computation on the Hessian, as seen in Equation 7.57, a weighting factor  $W$  scales the effect of the partial derivative of the frequency response function. As a reminder, this weighting factor is formed by taking the inverse of the prediction error covariance matrix,  $R$ . As an additional note, the prediction error covariance matrix in this case is simply equal to the power spectral density of the measurement noise,  $S_v$ . Thus,  $W = R^{-1}$  and  $R = S_v$ . With this in mind, as signal noise increases the magnitude of the Hessian

decreases. This ultimately increases the magnitude of the Cramer-Rao bound, as seen in Equation 7.53. This is expected, as any degradation in measurement signal quality will effect the input-output relation of the system. The varying levels of noise are depicted in the plot as  $Var_1$ ,  $Var_2$ ,  $Var_3$ , and  $Var_4$  depict the input noise levels,  $S_v = 1$ ,  $S_v = 2$ ,  $S_v = 3$ , and  $S_v = 4$ , respectively.

The plots of Appendix A depict the relationship between the identified value of  $\gamma$  at each  $\omega_f$  and  $S_v$  with the corresponding Cramer-Rao bound. To demonstrate this relationship, two cases will be discussed. The first, as seen in Figure 7.7 depicts Cramer-Rao bounds for low frequency response and high signal noise. The second case, as seen in Figure 7.8 depicts Cramer-Rao bounds for high frequency response and low signal noise. The analysis will begin with case one.

Case one considers cases of poor measurement signal quality and low signal input frequency, such as the case of Figure 7.7 at  $\omega_f = 0$ . Here, the accuracy of  $\gamma$  is low, as the identified value  $\tilde{\gamma} = 5.2$ , where as the true value of  $\gamma = 8$ . This is expected, however, as the magnitude of the Cramer-Rao bound is almost equal to 9. As the Cramer-Rao bound is simply the standard deviation of the expected value of  $\gamma$ , the bound indicates the expected value of  $\tilde{\gamma}$  to be in the range of  $0.5 \leq \tilde{\gamma} \leq 8.9$ . With a standard deviation this large, it is obvious that this identified value of  $\gamma$  is of low value and needs to be re-evaluated or more importantly, discarded altogether.

The opposite is true for case two, which considers values of  $\gamma$  in Figure 7.8, evaluated at  $\omega_f = 0.5$ . In this case, both the measurement noise is low and the input frequency is high, thus corresponding to a small Cramer-Rao bound. As would be expected, the identified value of  $\gamma$  is nearly perfect, with  $\tilde{\gamma} = 7.99$ . This corresponds to a standard deviation of the expected value of  $\gamma$  to be in the range of  $7.9 \leq \tilde{\gamma} \leq 8.1$ . In this case, it is advisable to accept this identified parameter as accurate as the bounds are small.

As discussed in Chapter III, the Cramer-Rao bound is superior to traditional data scatter analysis to evaluate the validity of the an estimated parameter. This was

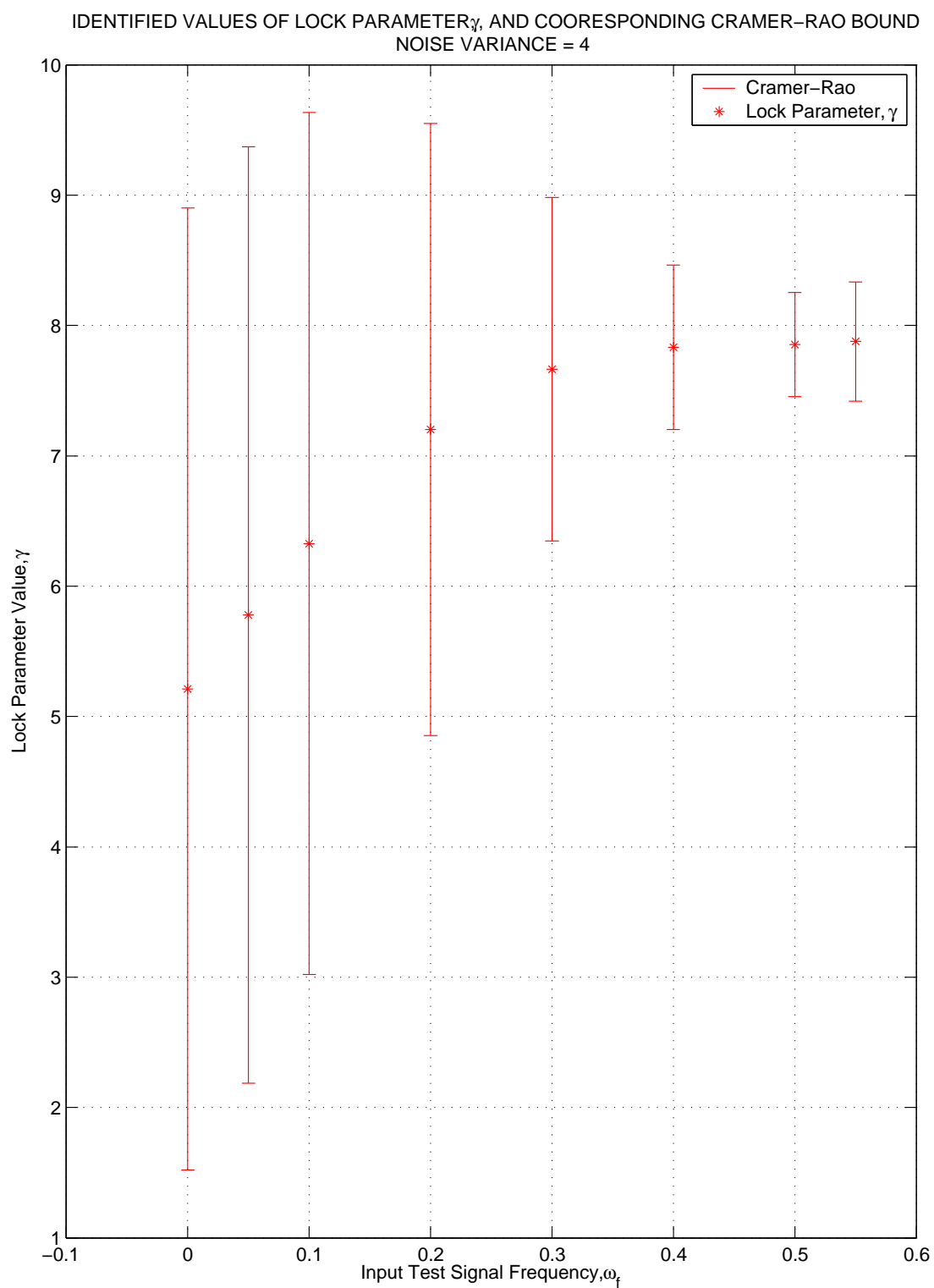


Figure 7.7: Cramer-Rao Bounds for all Frequencies,  $\omega_f$ , at Noise Value,  $S_v = 4$ .

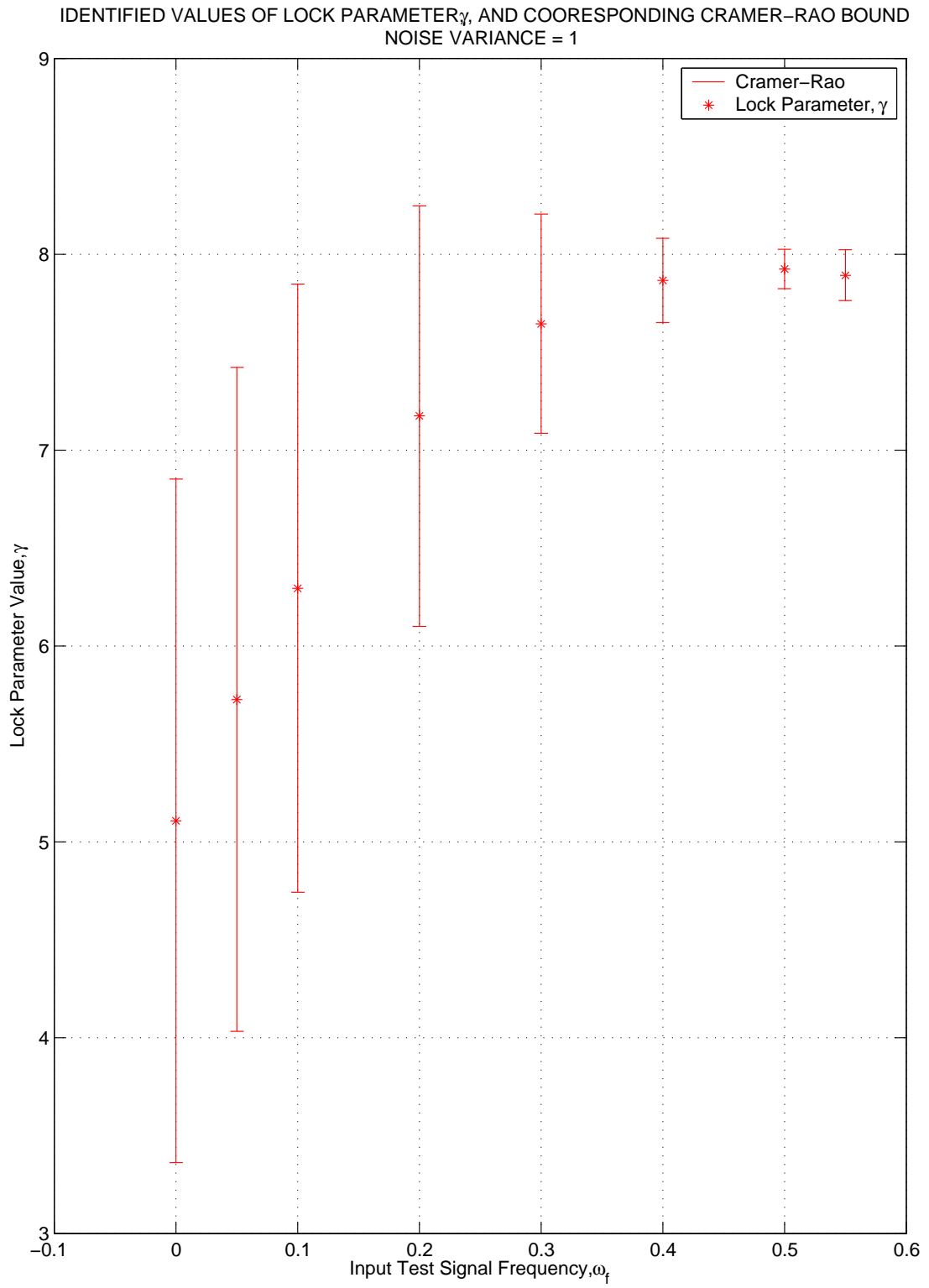


Figure 7.8: Cramer-Rao Bounds for all Frequencies,  $\omega_f$ , at Noise Value,  $S_v = 1$ .

demonstrated in Figure 3.2, which showed that tight data scatter, a common used method to qualify data as accurate, does not directly relate to an accurately estimated parameter. Only by reviewing the magnitude of the Cramer-Rao bound versus the data scatter can the parameter estimates truly be determined as accurate. Therefore, to demonstrate the usefulness of the Cramer-Rao bound to validate parameter estimates, the Cramer-Rao bounds represented in Appendix A were superimposed on estimates of the blade Lock number,  $\gamma$ . The data scatter represents the estimates of the Lock number from 100 individual tests. An example of this analysis is presented in Figures 7.9 and 7.10. These plots present the Cramer-Rao bounds calculated at each the input frequencies,  $\omega_f$ , at two noise levels,  $S_v = 1$  and  $S_v = 4$ . Upon review of both Figures it is clear that data scatter does not directly relate to the validity of parameter estimates. Take Figure 7.9 for example. By review of the values of  $\gamma$  estimated at the optimal frequency response point,  $\omega_f = 0.5$ , both the Cramer-Rao bound and the data scatter agree. However, as the frequency response falls off as  $\omega_f \rightarrow 0$  the Cramer-Rao bound and the corresponding data scatter do not agree. This is most pronounced at  $\omega_f = 0.0$ , where the data scatter is very tight, however the Cramer-Rao bound is large. If one was to evaluate the data scatter alone at this point the tight data scatter may lead to a false determination that the parameter estimate was indeed accurate. Figure 7.10 can be evaluated as previously described, however this plot reveals the effect of greater signal noise on the parameter estimates. While the data scatter is overall less tight than that of the lower noise case of Figure 7.9, the same conclusion can be made regarding the false readings data scatter can produce when determining parameter estimates.

The size of the bound that corresponds to a poor estimate is ultimately left to engineering judgement, as to what is acceptable in the particular application. In the next Section the size of the bound will be evaluated in terms of the accuracy of the vibration suppression controller developed in this chapter. Before this is covered, however, a brief word on the adaptation of the HBSSM for the use in a digital computer will be made.

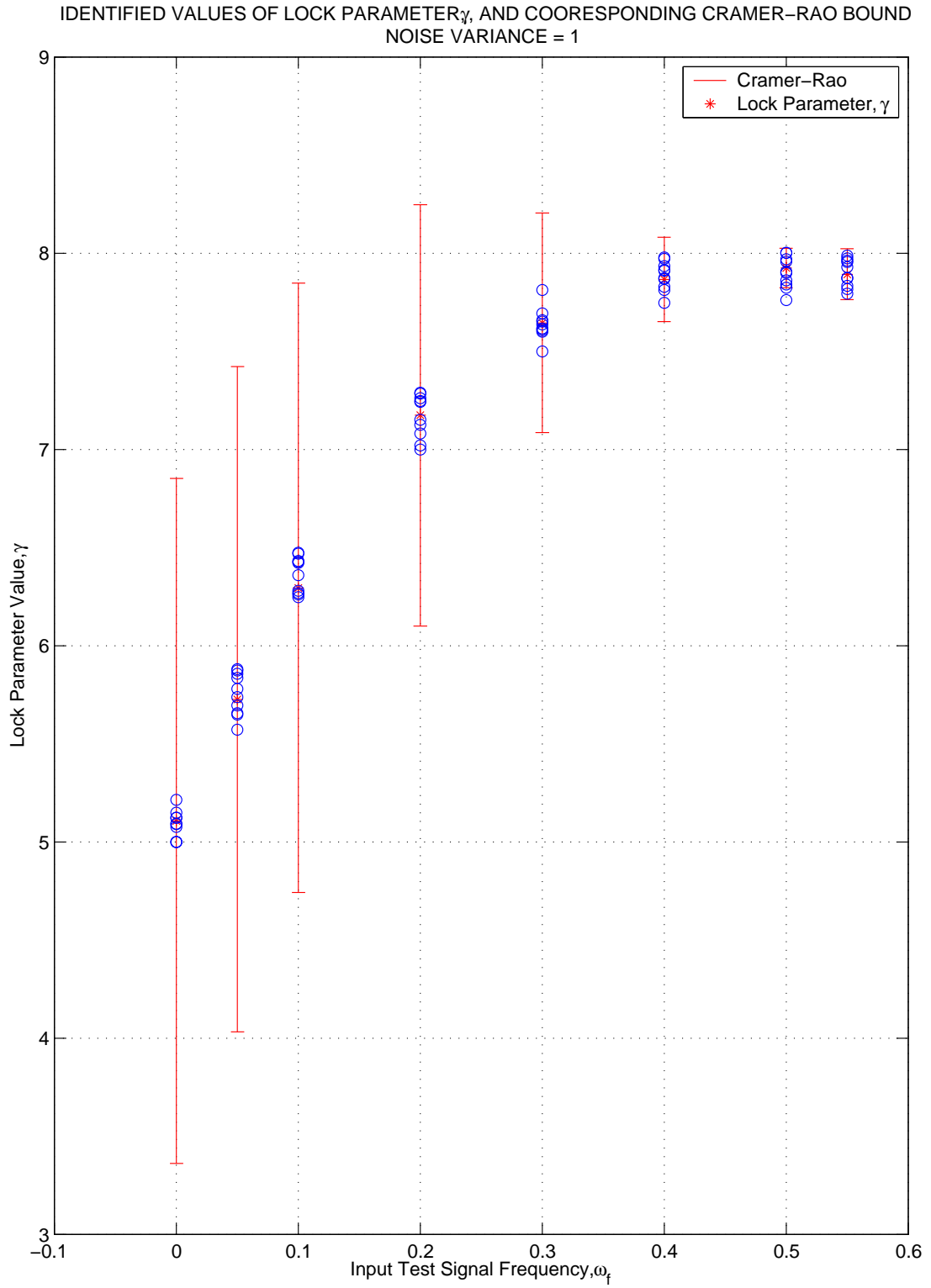


Figure 7.9: Cramer-Rao Bounds vs. Data Scatter of 100 runs for all Frequencies,  $\omega_f$ , at Noise Value,  $S_v = 1$ .

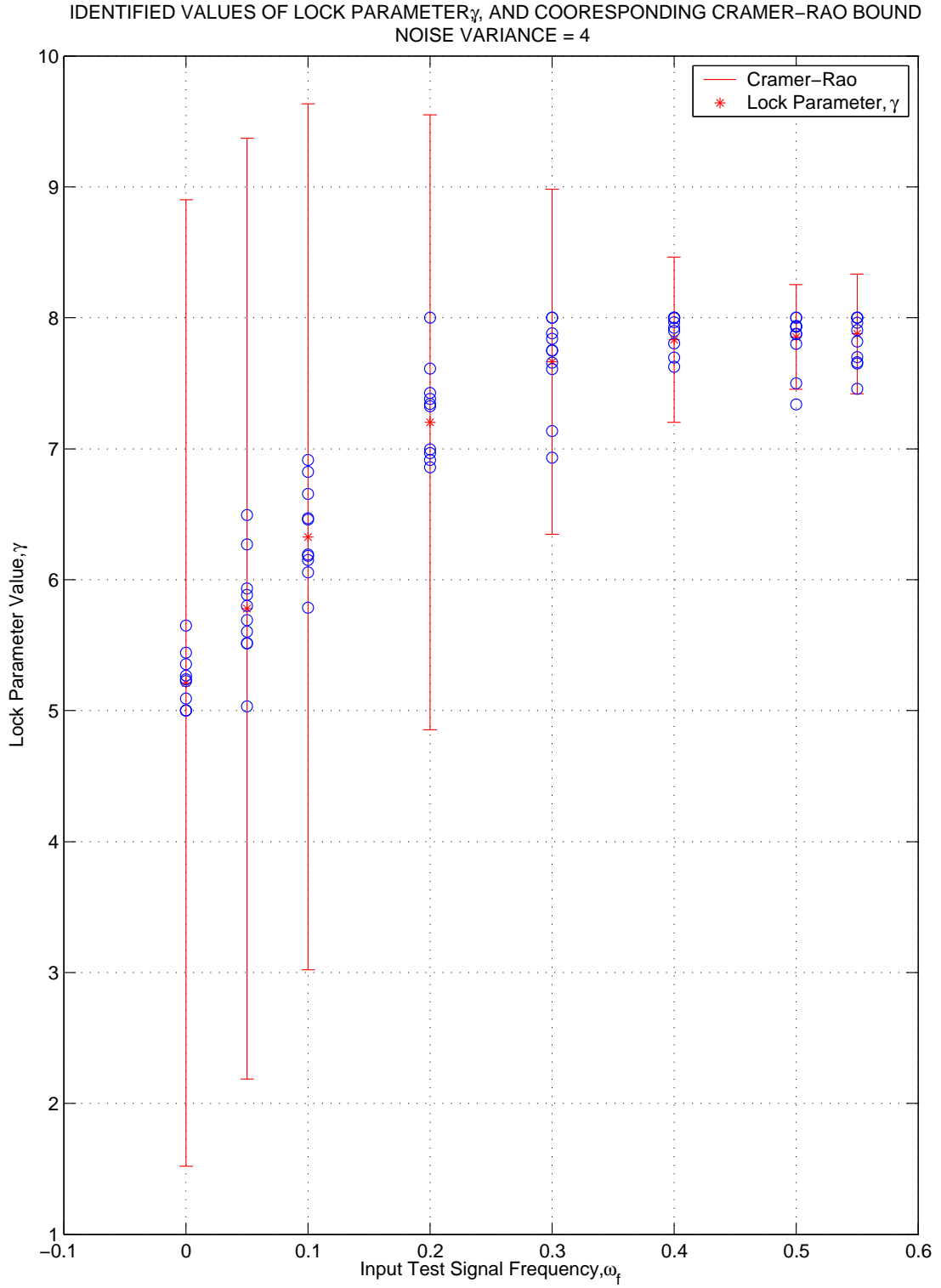


Figure 7.10: Cramer-Rao Bounds vs. Data Scatter of 100 runs for all Frequencies,  $\omega_f$ , at Noise Value,  $S_v = 4$ .

*7.7.3 Determination of Model Dimension.* The Toeplitz block form of Fourier coefficients is key to developing a state space form of the system matrices that define a model. These matrices, as described previously, are considered doubly infinite as they contain a doubly infinite representation of the Fourier series. This, however is untenable for application in code development on a digital computer. For code development to take place, the representative Fourier series of the Toeplitz transform must be truncated to contain  $N$  harmonics. To determine the value of  $N$ , the number of harmonics was increased in the system as to identify convergence in the compared system responses. Based on the experience of Hwang [12],  $N=5$  was determined to produce adequate convergence in system output response. The same procedure was conducted when determining the number of harmonics to include in the LQR gains, as they are also Fourier series dependent. The closed loop system response, as will be seen in Section 7.8, was evaluated for convergence while increasing the number of harmonics in the LQR gains. In this case,  $N=2$  proved adequate for an optimal control solution based on response convergence.

## **7.8 Vibration Controller Validation via the Cramer-Rao Bound**

In this final Section of the chapter the performance of the vibration controller developed in Section 7.6 will be evaluated based on the accuracy of the identified system model parameters, in this case  $\gamma$ . The model of the rotor system will be that of Section 7.3, with the distinction of having three blades with an identical blade pitch input  $\Theta_{con} = 1$  deg, while one blade will differ with  $\Theta_{con} = 1.3$  deg. This difference in blade pitch input will generate asymmetric lift in the rotor system, thus causing an out of plane vibration synonymous with that of the 'track and balance', as mentioned in Section 7.6.1. The intent of this Section is to demonstrate the effect poorly identified system parameters, determined by the Cramer-Rao bound, have on the performance of a controller.

The effect of a parameter variation, of the type discussed in Section 7.8, is that the model in which the parameter resides will differ from the true system it is to

represent. This presents a problem when this model is used in controller synthesis. In this case the optimal control solution is designed based upon an a model that has error due to incorrectly estimated parameters when compared to the true system. For example, Burl [2] states that most control system designers have synthesised a controller with good performance, simulated the controller to verify the performance, then implemented the controller, only to discover that the performance is totally unacceptable. These discrepancies between the mathematical model of the plant and the actual system are denoted as model perturbations. In this case, and moreover in general, Burl [2] notes that uncertainty in the plant is modeled by a set of feedback perturbations. In these cases, a robust control scheme must be used to ensure stable operation to overcome the modeling limitations.

As was described earlier, the LQR control method was selected as the controller synthesis method upon which the vibration reduction system is based upon. This selection was made based on the relevance to the problem; the rotor model used for controller synthesis will contain bounded uncertainty in the plant parameters, in this case the Lock number,  $\gamma$ . The Lock number was selected as it is a key factor in determining the flap response to the blade model used in this study. The linear quadratic regulator is tolerant to feedback perturbations and as such was selected based on these characteristics. This tolerance is due to the guaranteed bound on the smallest destabilising feedback perturbation, which by using the triangle inequality [2,42] provides an guaranteed gain margins of  $GM^+ = \infty, GM^- \leq \frac{1}{2}$ . As this system contains multiple inputs, phase margins are irrelevant. With these stability margins the LQR is recognised as having robust performance for feedback perturbations, as this system is defined as having.

The ability of this type of controller to deliver adequate reference tracking performance while having feedback uncertainty may not necessarily guarantee overall adequate system performance. This is because the controller will generally require greater control input to compensate for the modeling discrepancies mentioned above. While these control inputs will not destabilise the system, they may hinder the ability

of the system to perform other functions. An example of this is control saturation, which would prohibit the pilot of a helicopter from performing other controlled maneuvers if the vibration controller is dominating the available control input to the system. Another example would be that excessive control input may drive the system to points of aerodynamic stall, as in the case of high  $\Theta_{con}$  demands by the control system. The following Section will present an example of this by reviewing the performance of the vibration controller subject to varying cases of model uncertainty, in the case of the varying parameter  $\gamma$ .

#### *7.8.1 Vibration Controller Performance Evaluated By Cramer-Rao Bound.*

This Section will present the performance of the vibration controller developed in this work subject to parameter inaccuracies. The system will be reviewed over the range of  $\gamma$  as defined in Section 7.7 where the Cramer-Rao bound of the parameter was compared to the corresponding system identified parameter value. This range of test conditions will allow for a direct comparison of the controller performance in terms of control demands exhibited by the controller to the validity of the parameter  $\gamma$ . This comparison will reveal that while the vibration controller has adequate tracking performance, the control requirements may be unacceptable by the terms listed above.

The vibration controller test condition is defined by the inflow ratio of  $\mu = .3$  and Lock number  $\gamma = 8$  for the actual rotor system at a pumping frequency of  $\omega_p = 1$ . The  $Q$  and  $R$  matrices which define the LQR controller were selected as such;  $Q = \text{diag}([0 \ 0 \ 0 \ 0 \ 0 \ 0 \ 0 \ 0 \ 2.0])$ ; where the weighting on each blade state is zero and increased weighting on the error state, and  $R$  weights equally the four control

inputs by  $\frac{1}{100}$  on the diagonal, as seen in Equations 7.62 and 7.63.

$$Q = \begin{bmatrix} 0 & 0 & 0 & 0 & 0 & 0 & 0 & 0 & 0 \\ 0 & 0 & 0 & 0 & 0 & 0 & 0 & 0 & 0 \\ 0 & 0 & 0 & 0 & 0 & 0 & 0 & 0 & 0 \\ 0 & 0 & 0 & 0 & 0 & 0 & 0 & 0 & 0 \\ 0 & 0 & 0 & 0 & 0 & 0 & 0 & 0 & 0 \\ 0 & 0 & 0 & 0 & 0 & 0 & 0 & 0 & 0 \\ 0 & 0 & 0 & 0 & 0 & 0 & 0 & 0 & 0 \\ 0 & 0 & 0 & 0 & 0 & 0 & 0 & 0 & 0 \\ 0 & 0 & 0 & 0 & 0 & 0 & 0 & 0 & 2 \end{bmatrix} \quad (7.62)$$

$$R = \begin{bmatrix} \frac{1}{100} & 0 & 0 & 0 \\ 0 & \frac{1}{100} & 0 & 0 \\ 0 & 0 & \frac{1}{100} & 0 \\ 0 & 0 & 0 & \frac{1}{100} \end{bmatrix} \quad (7.63)$$

These selections of weighting matrices were made to demonstrate good vibration reduction while not limiting controller input. The rotor system will produce an out of plane vibration by defining the input to the third blade to have a bias input of 0.3 deg to any commanded input. The remaining blades will have no bias and will produce the desired command input. This bias is designed to replicate an incorrectly adjusted pitch linkage on blade three as compared to the remaining blades of the rotor system. The open loop blade flapping response of the rotor system subject to the defined test conditions is presented in Figure 7.11. This unbalance in flap angles corresponds to a oscillation in the summation of the blade flapping angles as seen in Figure 7.12. The oscillation in the summation of the blade flapping angles seen in Figure 7.12 is indicative of a out of plane rotor vibration caused by asymmetric lift in the rotor system, as discussed in Section 7.6.1. The intent of vibration controller, as outlined in Section 7.6.1 is to smooth the blade individual blade flapping angles such that the

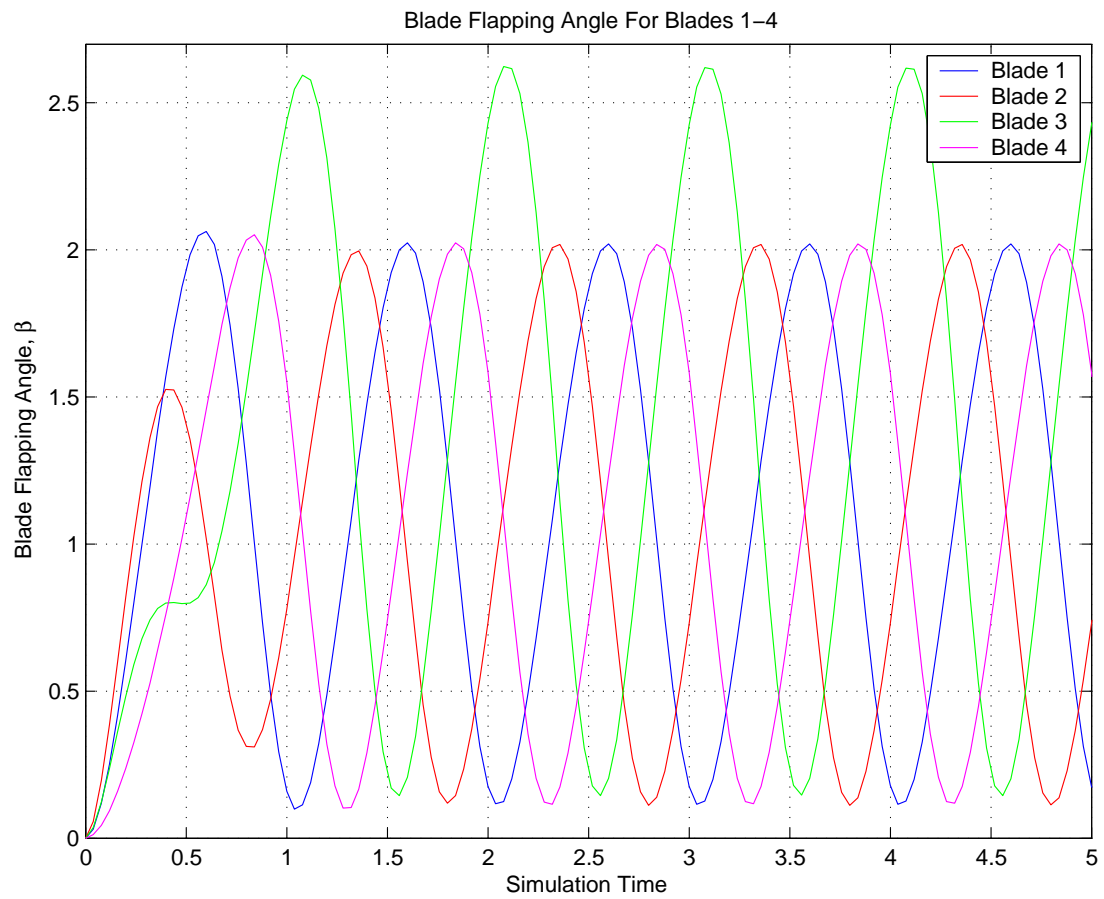


Figure 7.11: Blade Flapping Angles For an Unbalanced Rotor.

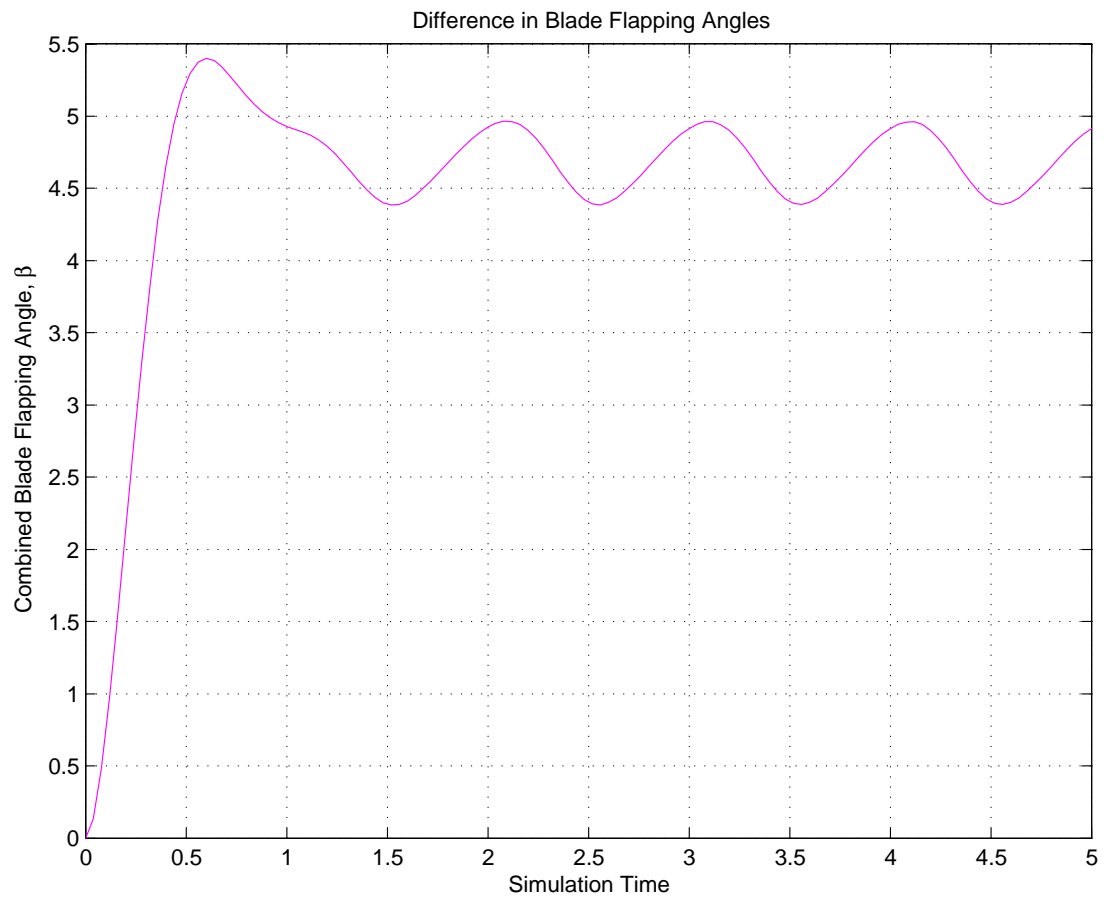


Figure 7.12: Summation of the Blade Flapping Angles For an Unbalanced Rotor.

oscillations present in Figure 7.12 will reduce to match the reference input signal of Figure 7.4. This reference signal is designed to reproduce the flapping response of the four identically bladed rotor system, having parameters  $\gamma = 8, \mu = 0.3$ , with identical pitch inputs,  $\Theta_{con} = 1$  deg, as described in Section 7.6.1.

For this review, the test controller will be reviewed as 28 individual test points, each corresponding to a specific value of the parameter  $\gamma$  identified at a specific value of input frequency  $\omega_f$  and measurement noise  $S_v$ . As a note, these are the same parameters as were reviewed in Section 7.7.2 and thus the analysis of that Section will carry over here. The 28 total test points that correspond to the identified values of  $\gamma$  are defined by the input frequencies,  $\omega_f = \omega_p(0, 0.05, 0.1, 0.2, 0.3, 0.4, 0.5)$ , and measurement noise spectral densities  $S_v = 1, 2, 3, 4$ . Once again, these were the same parameters used to identify the Lock number in Section 7.7.2. The performance of each test point are presented in Appendices C, D, E, and F, each corresponding to a value of  $S_v = 1, 2, 3, 4$ , respectively. A review of the plots of the individual flap angles, calculated LQR gains, control usage, and vibration controller performance in terms of tracking performance for each of the 28 individual test cases is presented in these appendices.

Of these 28 cases, two cases representing the best and worst values of  $\omega_f$  and  $S_v$  used to identify  $\gamma$  will be compared with respect to the Cramer-Rao bound to establish a connection between bound magnitude and controller effectiveness. The first test case is representative of the best identified value of  $\gamma$ , having  $\omega_f = .5\omega_p$  and  $S_v = 1$ . These points are based on analysis of Section 7.7.2 when correlating the Cramer-Rao bound to parameter estimate quality. The second test case is representative of the identified parameter  $\gamma$  having lowest quality, which occurs at  $\omega_f = 0.0\omega_p$  and  $S_v = 4$ .

A quick review of the tracking performance of the vibration controllers in Figures 7.13 and 7.14 for the best and worst cases, respectively, reveals little difference in overall tracking performance of the reference signal. This is to be expected based on the previous discussions on the robustness of the LQR to perturbations. This does

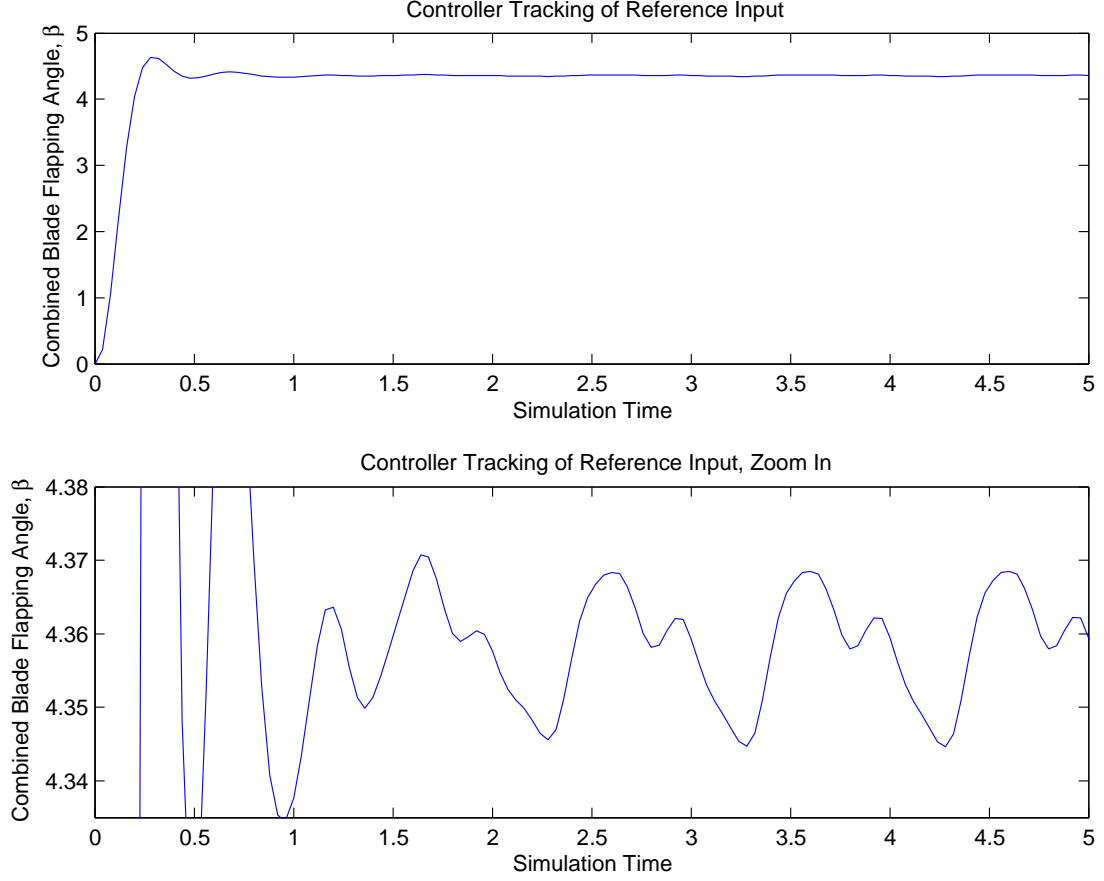


Figure 7.13: Best Case: Tracking Performance of Vibration Controller for case  $\omega_f = 0.5\omega_p$ ,  $S_v = 1$ .

not indicate, however, that both control designs are equivalent, as will be discussed next.

A further review of the input control required to achieve this level of vibration reduction in both test cases is more revealing in term of the differences between the two cases. The required inputs,  $\Theta_{con}$  for blades 1-4 of the best case range from approximately  $-6.8 \leq \Theta_{con} \leq +2.2$  are greatly reduced compared to the worst case, whose corresponding values of range from approximately  $-9.3 \leq \Theta_{con} \leq +3.3$ . These results are seen in Figures 7.15 and 7.16, which once again represent the best and worst cases, respectively. The difference in the control requirements are not surprising, as the increased model perturbation due to poor identification of  $\gamma$  in the case of the worst case require greater control input to compensate for what is essentially an unknown

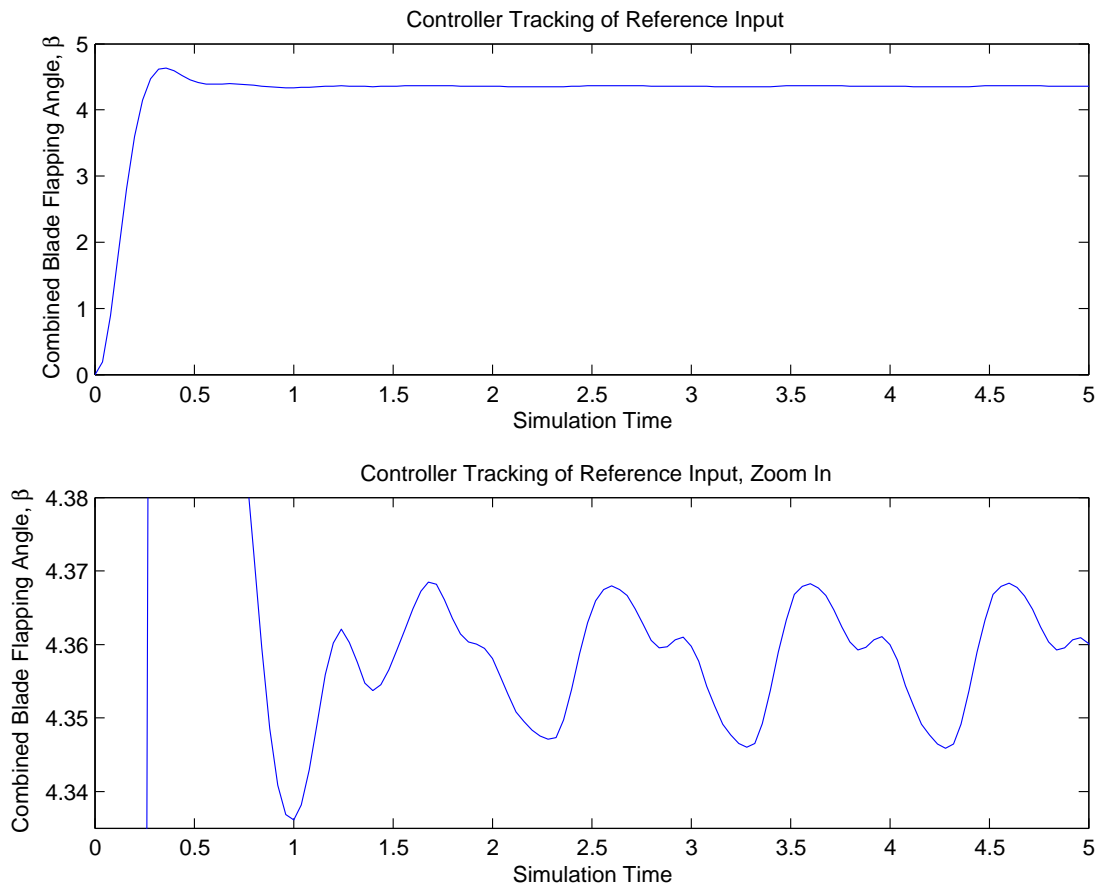


Figure 7.14: Worst Case: Tracking Performance of Vibration Controller for case  $\omega_f = 0.0\omega_p$ ,  $S_v = 4$ .

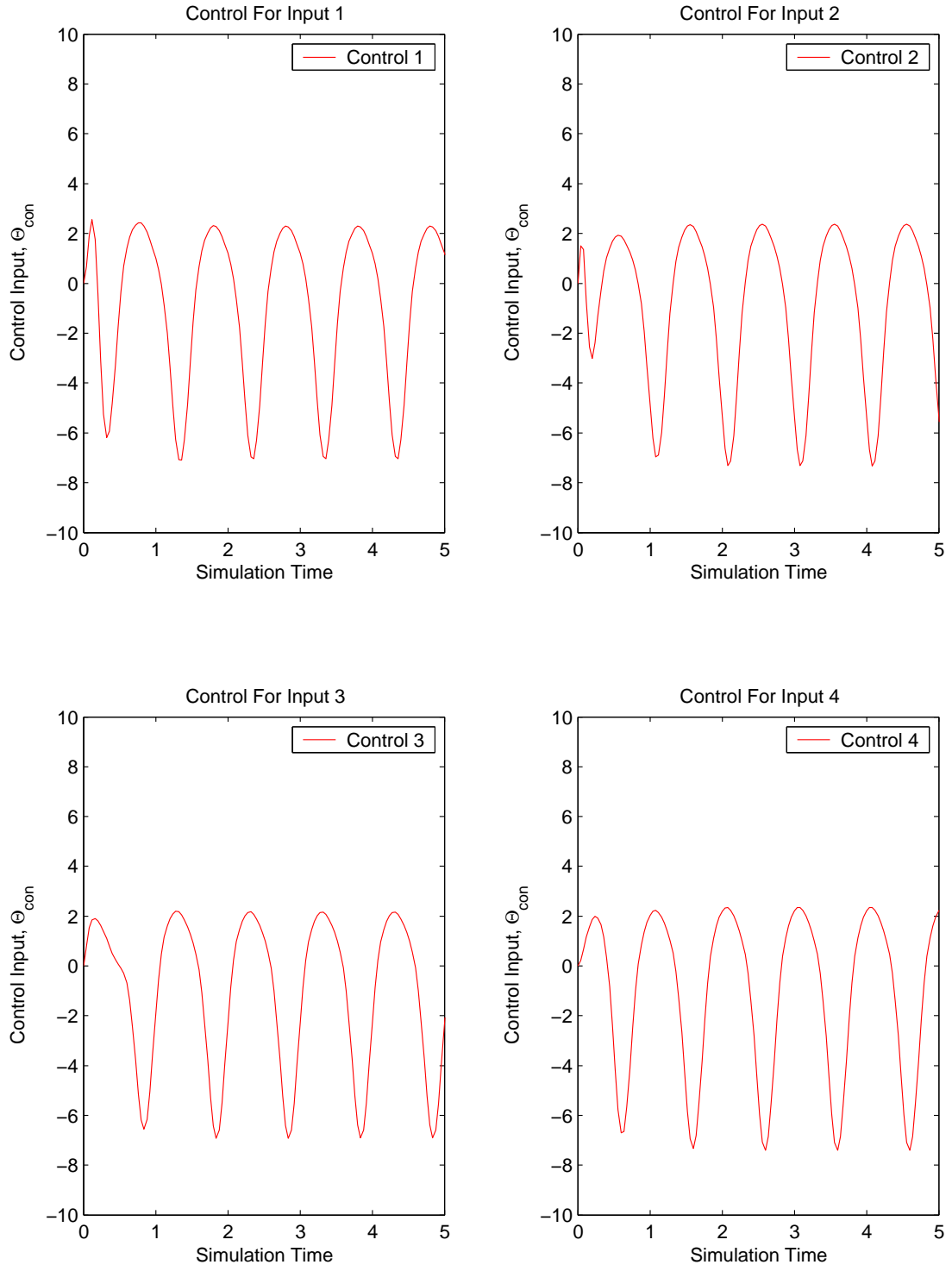


Figure 7.15: Best Case: Control Usage for case  $\omega_f = 0.5\omega_p$ ,  $S_v = 1$ .

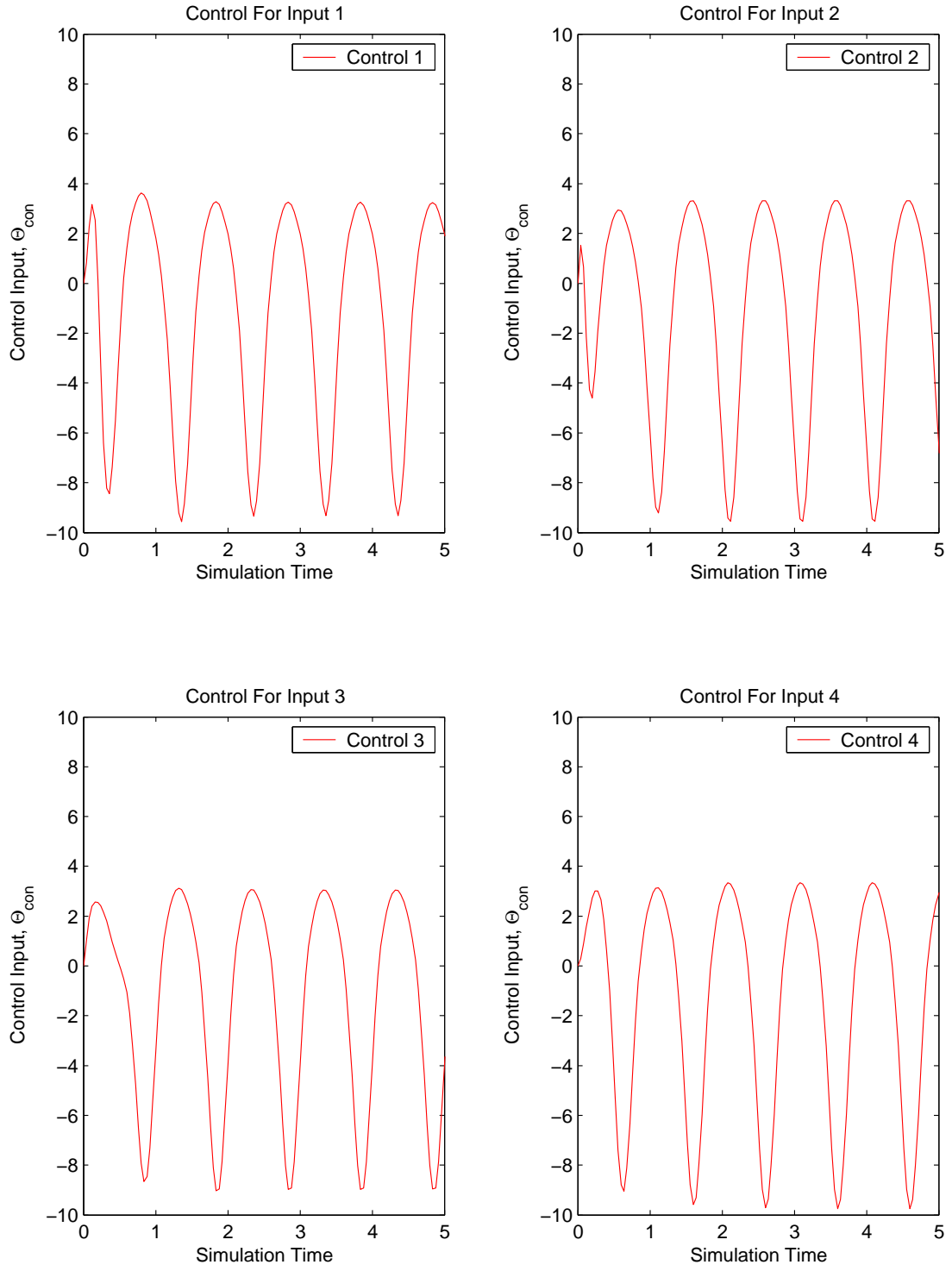


Figure 7.16: Worst Case: Control Usage for case  $\omega_f = 0.0\omega_p$ ,  $S_v = 4$ .

model disturbance, as discussed previously. This disturbance is not destabilising, however it has a tremendous impact on the availability of control input. This test case is not representative of a real system, however if one was to assume that the available control inputs were between a range of  $-10 \leq \Theta_{con} \leq 10$ , the available control authority of the worst case would be almost zero in terms of negative  $\Theta_{con}$ . The best system, by comparison, still has adequate control authority available by the same standards. Thus, by relating the Cramer-Rao bound to the parameter perturbations in a manner similar to that of Section 7.7.2, a direct relationship between controller performance and parameter quality can be made. Simply put, the size of the Cramer-Rao bound is in direct relation to the parameter perturbation of the LQR controller, which ultimately dictates the necessary control authority needed to achieve a desired level of control.

The above discussion reveals the relationship between the Cramer-Rao bound and the corresponding magnitude of control input by way of comparing best and worst cases. Furthermore, it was shown in Section 7.7.2 that the input frequency,  $\omega_f$ , also corresponds to the magnitude of the Cramer-Rao bound. Knowing this, it is then clear the Cramer-Rao bound and the magnitude of the input control are related by way of the input frequency,  $\omega_f$ . Thus, the relationship between the magnitude of the Cramer-Rao bound and control requirements can be further clarified by plotting their respective magnitudes with respect to their input frequencies. This type of plot is presented in Appendix G for each rotor blade at input noise cases of  $S_v = 1$  and  $S_v = 1, 2, 3, \text{ and } 4$ . The individual noise case is presented to demonstrate the relationship in an easy to read format, while the combined noise case is presented to demonstrate the relationship for all cases.

To demonstrate how the above described plots can relate the magnitude of the control input to the magnitude of the Cramer-Rao bound two cases will be considered. The first case, as seen in Figure 7.17, will be for Blade 4 where only the noise case,  $S_v = 1$ , will be considered. The second case will be for Blade 4, but for all noise cases and is presented in Figure 7.18. The plots are 3D representations as there are

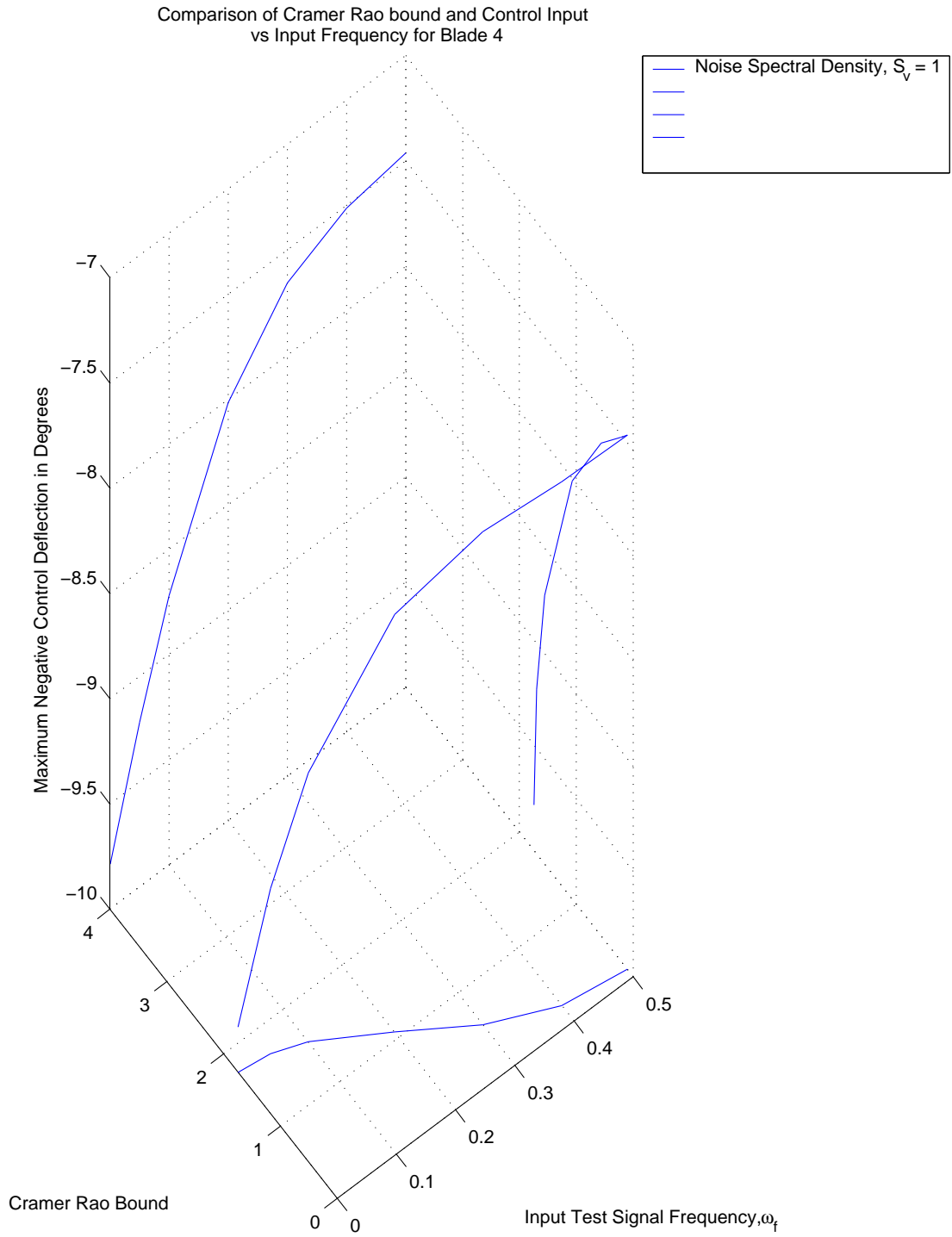


Figure 7.17: Comparison of Cramer-Rao Bound to Maximum Negative Control Deflection For Blade 4:  $\omega_f = \omega_p(0, 0.05, 0.1, 0.2, 0.3, 0.4, 0.5)$ ,  $S_v = 1$ .

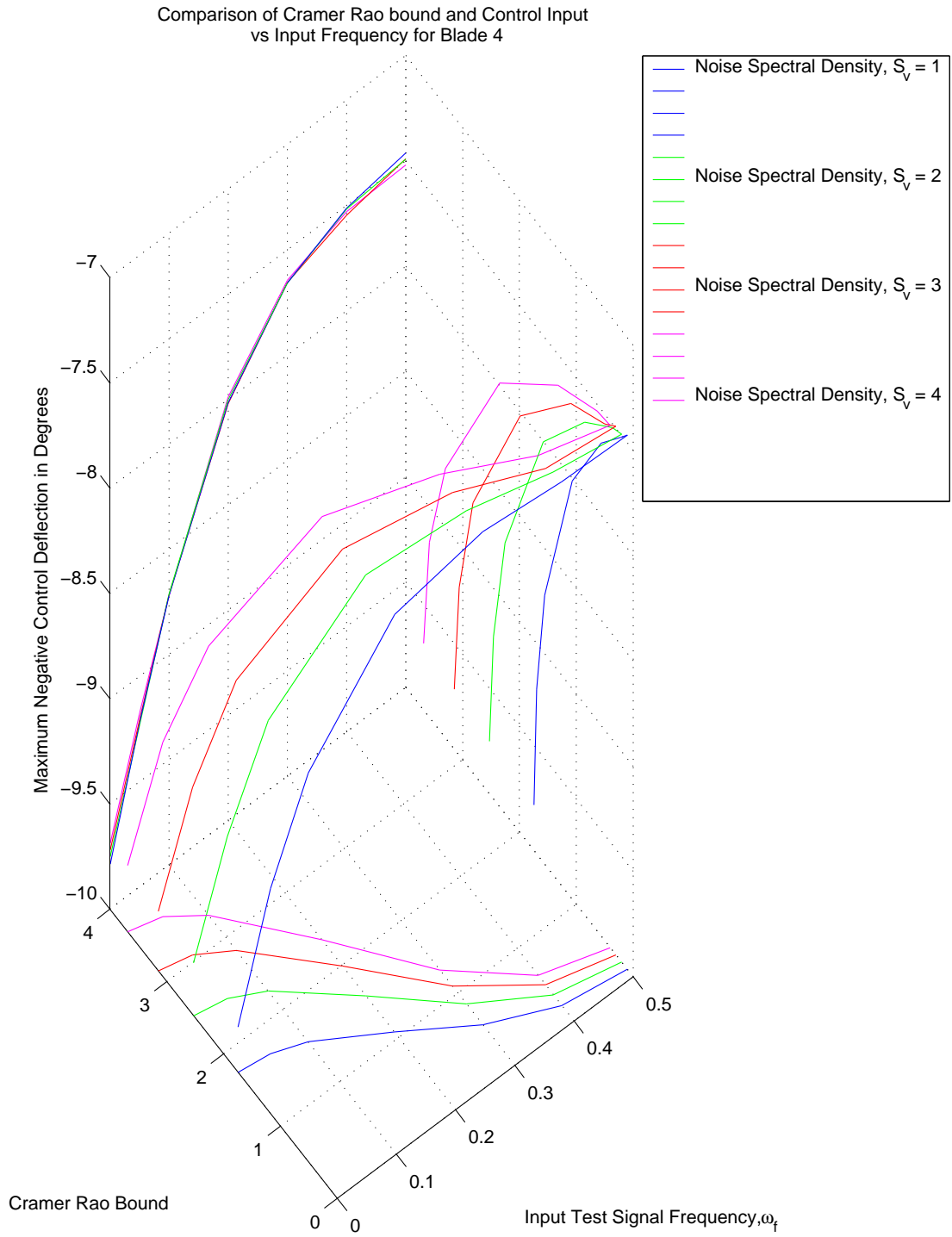


Figure 7.18: Comparison of Cramer-Rao Bound to Maximum Negative Control Deflection For Blade 4:  $\omega_f = \omega_p(0, 0.05, 0.1, 0.2, 0.3, 0.4, 0.5)$ ,  $S_v = 1, 2, 3, 4$ .

three variables presented. The plots are interpreted as a series of 2D reflections of the 3D plot with one 2D plot for each combination of the variables. The combination of Cramer-Rao bound vs input frequency has already been discussed in Section 7.7.2 and therefore the corresponding 2D plot will be familiar. Furthermore, the maximum negative control deflection vs input frequency was discussed in Section 7.8.1 and the 2D reflection on these axis will also be familiar. The new plot will be that of the maximum negative control deflection vs the Cramer-Rao bound. It is this 2D plot that is of greatest importance as it provides the ability to directly compare the Cramer-Rao bound to the maximum negative control deflection. This, afterall, is the ultimate intent of using the Cramer-Rao bound to evaluate the control system performance. By reviewing Case 1 in Figure 7.17 the Cramer-Rao bound vs. Control deflection reveals that as the bound gets large the corresponding control deflection gets large. This is evident as the large Cramer-Rao bound indicates a poor parameter estimate, and with poor parameter estimates a controller based upon that parameter will therefore have poor performance. The poor performance, in this case, is indicated by the controller having to compensate for modeling error by putting in more control. This large control input is seen by a larger negative control deflection. Case 2 in Figure 7.18 can be interpreted as described for Case 1, with the exception that Case 2 is for all noise cases. Case 2 reveals that the control deflection is generally the same despite the increase in signal noise. This is due to the parameter error, described by the increased Cramer-Rao bound, is more due to the frequency response than signal noise.

By the results of the discussions above, the Cramer-Rao bound can be used in control design by estimating controller performance based purely on the bound of the identified parameter. This, in turn, alleviates the necessity of having to construct a controller at that test case. The size of the bound threshold can be determined by engineering judgement to determine the maximum acceptable perturbation allowable in the system.

## 7.9 *Concluding Remarks*

This chapter presented how the Cramer-Rao bound can be used to quantify the performance of an optimal rotor vibration controller. This was accomplished by first determining the magnitude of an identified system parameter variation by way of the direct comparison of the identified parameter value to the corresponding Cramer-Rao bound. The Cramer-Rao bound was then used to relate how model perturbations from the identified parameters effect controller performance.

In order to develop the methods stated above the following steps were first accomplished in successive order in this chapter. For starters, after briefly stating why a vibration controller was needed, the chapter began by outlining the rotor system LTP equations of motion based upon a rigid blade, with 4 blades in total. This was followed by developing the LTP LQR controller for out of plane vibration reduction. The controller development first outlined the properties of a LTP LQR controller including the robust characteristics of guaranteed stability margins. This was followed by outlining the tracking regulator design used to reduce out of plane vibrations, which included an explanation of how the selection of time periodic gain harmonics was performed. The chapter concluded by outlining how the performance of each controller based upon identified parameters having increasing Cramer-Rao bounds was quantified. This was done by first determining the magnitude of Cramer-Rao bounds for the identified system parameter, the Lock number  $\gamma$ . This was followed by relating the performance of the controller based upon the identified parameter  $\gamma$  to the corresponding Cramer-Rao bound. The next two paragraphs will detail these final two steps in greater detail, in the respective order presented above.

The validation of the control system began by evaluation the parameters which define the mathematical model in which it is synthesised upon. This Section evaluated how the variables which define the test space, in this case input frequency  $\omega_f$  and measurement noise  $S_v$  affect the quality of the system identified model parameters, in this case  $\gamma$ . By reviewing the comparison plots in Appendix A, it was shown that both

input frequency,  $\omega_f$ , and the intensity of the measurement noise,  $S_v$ , directly affect the quality of the estimate of the parameter,  $\gamma$ . This was shown by first considering the effect of the input frequency,  $\omega_f$ , on the accuracy of the parameter estimate by evaluation the inverse relationship between the Cramer-Rao bound and system frequency response. Thus, as frequency response falls off the Cramer-Rao bound begins to grow in magnitude. Next, the effect of measurement signal noise on the magnitude of the bound was then evaluated. This was done to demonstrate the relationship  $S_v$  has to the Cramer-Rao bound over the test space for each value of  $\gamma$ . This was done by considering how an increase in measurement noise reduced the value of the Hessian, as seen in Equation 7.57, through a weighting factor  $W$ . This ultimately increases the magnitude of the Cramer-Rao bound, as the square root inverse of the Hessian is the definition of the bound. This analysis provided a method to define where in the test space the Cramer-Rao bound would be large, thus revealing that identified parameters in this region would have large perturbations from the true value.

The effects of the parameter accuracies were then quantified by relating the model perturbation they cause to the control requirements produced by the corresponding controller. This Section outlined that while each controller developed in the test space has guaranteed stability, the control requirements needed to offset the parameter induced modeling inaccuracies may be excessive. Thus, by relating the Cramer-Rao bound to the parameter perturbations in a manner similar to the parameter validation discussed in the previous paragraph, a direct relationship between controller performance and parameter quality was made. This was done by noting that the size of the Cramer-Rao bound is in direct relation to the parameter perturbation of the LQR controller, which ultimately dictates the necessary control authority needed to achieve a desired level of control. Thus, the Cramer-Rao bound can be used in control design by estimating controller performance based purely on the bound of the identified parameter. This ultimately improves the process of control development

by alleviating the necessity of having to construct a controller at every test case to determine how much control authority the vibration controller will demand.

This chapter presented a method to evaluate the performance of a vibration controller based upon the Cramer-Rao bound. The next chapter will present a summary of the overall work presented in this document, and recommend future improvements to related works.

## VIII. Summary

The primary objective of this research was to develop a robust rotor smoothing algorithm based on system parameters determined from a frequency domain system identification methodology. As this work was to be compatible with a helicopter rotor in forward flight, which is best represented as a linear time periodic system [12, 42], all of the system identification, parameter validation, and control methods had to be compatible or developed for LTP systems. The performed research was extended based on the the works of [12, 42] by introducing a theory to validate system parameters of the identified model based on the Cramer-Rao bound [3, 34]. The LTP Cramer-Rao methodology was then used to identify the performance of the LTP optimal vibration controller developed in this work. This chapter will review the content developed in each chapter and make suggestions for future research.

### 8.1 *Summary and Conclusions*

This work began by outlining the problem of out of plane rotor vibrations and how the existing rotor vibration smoothing methods are deficient, as presented in chapters I through III. The historical methods of rotor track and balance and the modern rotor smoothing methods were outlined in terms of the methods they employ to reduce the out of plane rotor vibrations caused by asymmetric lift across the rotor. The key aspect of the review of these methods was that in the case of the modern methods each failed to accurately reduce the rotor vibrations due to an inability to accurately model the rotor. As an accurate rotor model is necessary to develop an accurate control adjustment solution to reduce the vibrations, it was determined that a method to identify a parametric rotor model from actual measurement, validate that model for accuracy, and then apply control to the system based on this developed model was needed. From this assessment the objectives for this work were developed. These objectives were to model the rotor system as a linear time periodic system in state space form, develop the Cramer-Rao bound for a LTP system in state space form for the purpose of parameter validation, and finally develop a LTP optimal control

solution which uses system identified parameters to reduce the out of plane vibrations in an accurate and timely manner.

The basis of the work was the linear time periodic system. As such, chapter IV detailed the mathematical basis for such a system. It was stated that while the principals of linear time invariant models are well understood, many of the mathematical foundations of linear time periodic systems are not. Therefore, this chapter presented several of the required mathematical elements of linear time periodic systems, as they formed the basis of the work covered in later chapters to develop the LTP system model. The work of this chapter began by describing the properties of the Fourier series as this was critical to the development of the time periodic theory. Eigenvector and eigenvalues were briefly described, along with the theory of singular value decomposition. This was used in the following chapter on LTP system theory. The final subject covered was the Toeplitz transformation, which allowed an infinite dimension Fourier series to be recast in a doubly infinite matrix form. This was critical to the LTP theory in the following chapter.

As all of the system theory to be used to meet the objectives of this research had to be cast as a LTP system in state space form, chapter V outlined the basis of this theory. This chapter described the formation of the Linear Time Periodic system in terms of the state space based upon the work of Wereley [42]. The linear time periodic state space representation was essential to later chapters in system parameter validation and control. As In the chapters following this one, linear time periodic analogues of system parameter validation and optimal control methods were build upon existing state space based LTI methods. It is for this reason that a linear time periodic state space operator was developed in this chapter. The fundamental work of this chapter was the harmonic balance state space model, which allowed for the creation of the LTP state space operator. This form was fundamental in the creation of the Cramer-Rao bound and optimal controller of later chapters.

The cornerstone of this research was the development of the Cramer-Rao lower bound for a LTP system, as presented in chapter VI. This work was necessary to accomplish as the intent of this research was to develop a more accurate method of rotor smoothing by way of controlling a verifiably accurate rotor system model. In the last chapter the concept of the linear time periodic model was developed, which provides the foundation for an accurate helicopter rotor in forward flight. The identified parameters that populate that LTP model, however, must be accurate in order to provide a basis for an effective controller. This chapter developed the Cramer-Rao lower bound for a linear periodic system in order to validate the identified system parameters. This chapter developed by first outlining the Cramer-Rao inequality and how it is related to the maximum likelihood estimator. The Cramer-Rao lower bound was then developed and adapted for an LTP system based on an LTI analog. A derivation of the theory and methodology required to generate the Cramer-Rao lower bound for a specified parameter in a linear, time periodic (LTP) system in state space form has been presented. This development made possible the determination of the bounded standard deviation of a system parameter which has been estimated using any system identification technique. The Cramer-Rao lower bound represents the standard deviation based on using an optimal estimator, thus providing a true measure of the accuracy of the estimate. This development of parameter accuracy played a critical part in the final chapter, the development of the optimal vibration controller.

The final aspect of this work was the development of an optimal control solution to reduce out of plane rotor vibrations, as detailed in chapter VII. This chapter culminated the works of the previous chapter to produce a LTP linear quadratic regulator based upon a Cramer-Rao validated system parameter, in this case the Lock number  $\gamma$ . By using the Cramer-Rao bounds of parameters developed from the LTP frequency domain system identification method developed by Hwang [12], a technique to determine the performance of the controller was developed. This chapter first developed the LTP equations of motion for a four bladed rotor loosely based upon

the AH-64 for flap only. This model was then used to develop a unique vibration controller based upon a feedback reference tracking scheme for a LTP LQR system. The chapter culminated by relating the size of the Cramer-Rao bound calculated for the system identified parameter to the controller performance in terms of control usage demanded by the controller. This was done by showing the variation in the identified values of  $\gamma$  as quantified by the Cramer-Rao bound could then be directly related to the perturbations in the model used to calculate the optimal control solution. The perturbations essentially cause additional noise in the control system, that must be handled by using additional control power. Thus, the Cramer-Rao bound allowed for quantification of the controller performance without having to calculate the controller.

## ***8.2 Recommendations for Future Research***

Two recommendations can be made to further the research presented in this work. The first improvement addresses the the measurement of states to feedback in the controller, while the second makes a recommendation to improve the vibration reduction by suggesting a new reference tracking signal. These recommendations are discussed below.

The first improvement is to change the structure of the reference tracking vibration controller by changing the internal structure from a a linear quadratic regulator to a linear quadratic Gaussian controller. This is important to address as the requirement to have perfect measurement of all system states is unrealistic. For this improvement, the Kalman filter should be adapted to a linear time period system by way of the harmonic balance state space operator. Thus, a realistic state estimator would reduce the demand to measure blade flapping angles states required by the current configuration of the vibration controller.

The second improvement is to modify the selection of a reference signal used by the vibration controller. The current reference signal is based upon an assumption that all blades produce the same lift at identical flapping angles. By reducing the assumption that the blades are identical, the summation of the lift from each blade can

be used as the error state feedback to a reference lift that is required for steady state operation. This would improve the applicability of the vibration controller proposed in this research, as the assumption of identical blades is heavily restricting.

*Appendix A. Lock Number Validation Plots via the Cramer-Rao  
Bound*

This appendix holds all of the plots generated by the Lock parameter validation by way of the Cramer-Rao bound in section 7.7.2. Four plots are presented in total, each with a specific value of  $S_v$  specified by the range  $S_v = 1, 2, 3, 4$ .

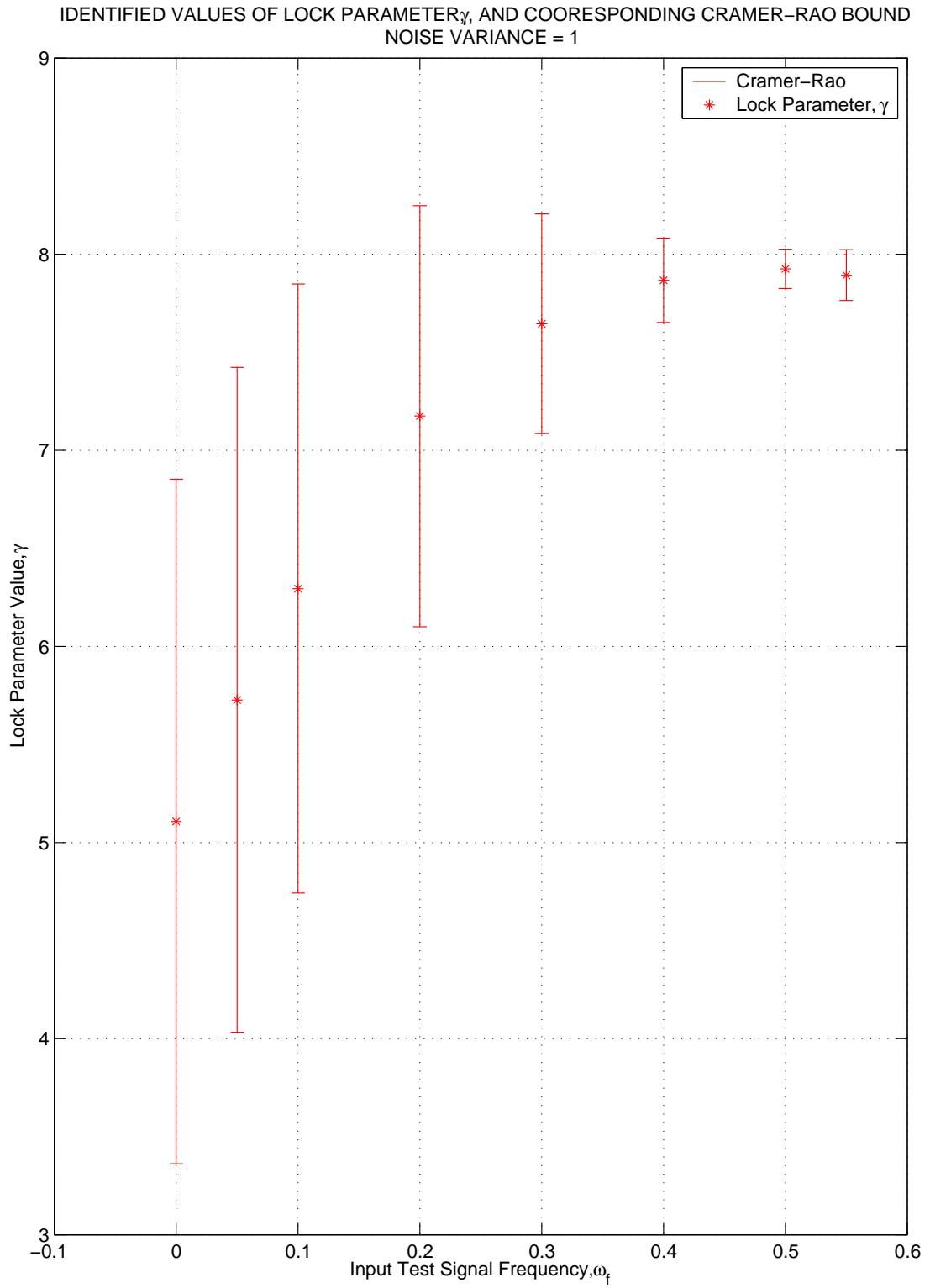


Figure A.1: Comparison of Identified Lock Number to Cramer-Rao Bound,  $S_v = 1$

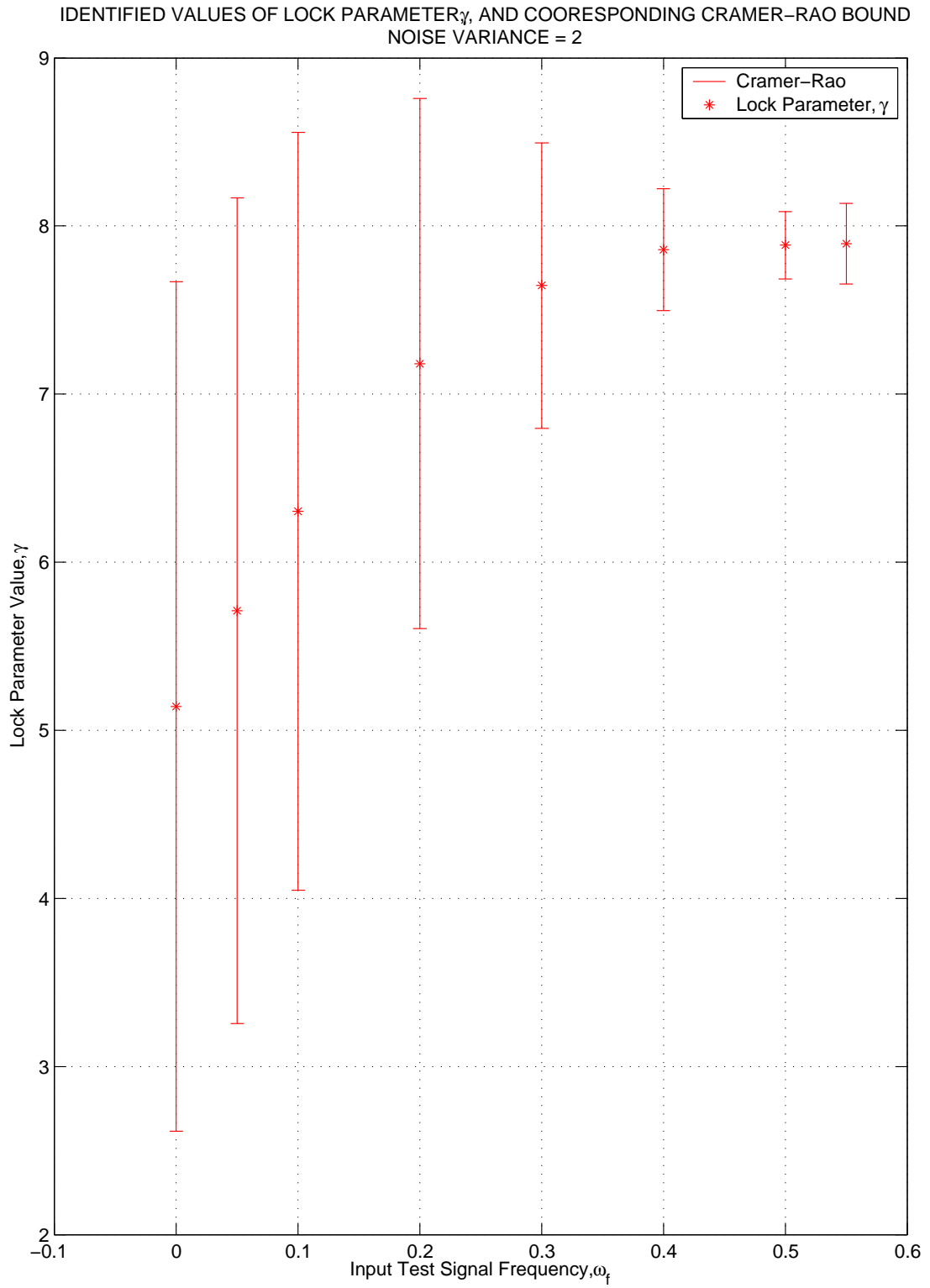


Figure A.2: Comparison of Identified Lock Number to Cramer-Rao Bound,  $S_v = 2$

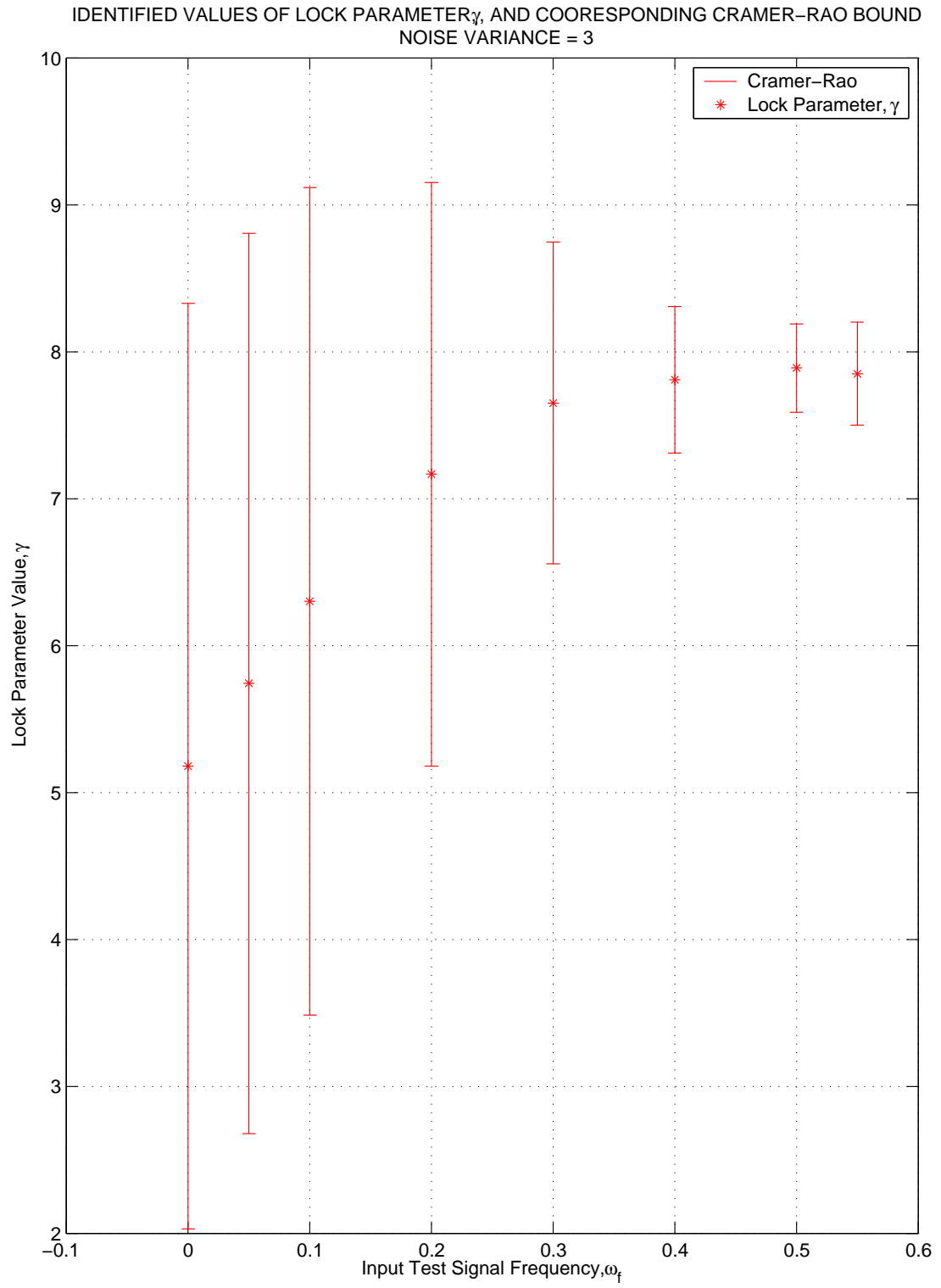


Figure A.3: Comparison of Identified Lock Number to Cramer-Rao Bound,  $S_v = 3$

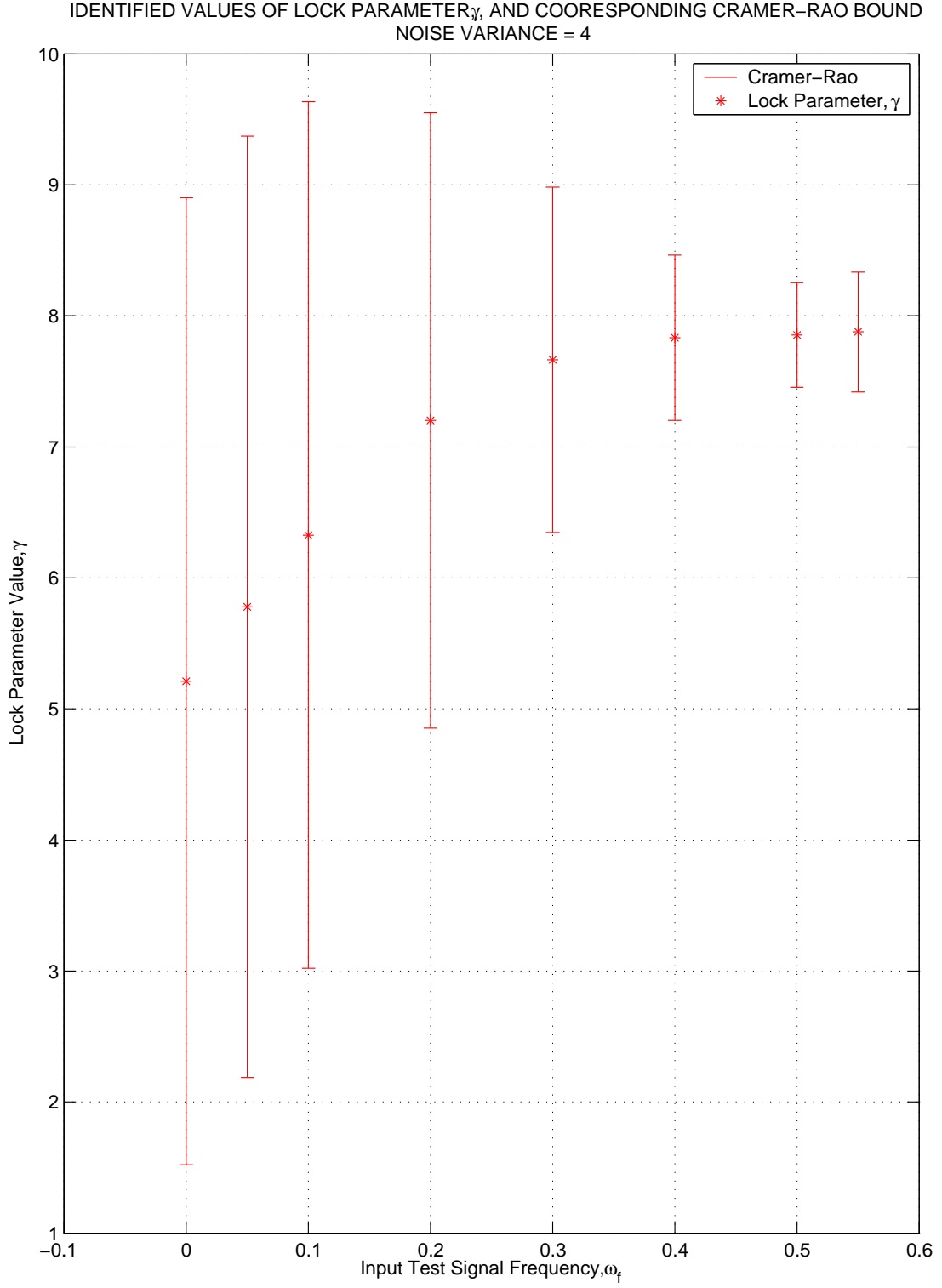


Figure A.4: Comparison of Identified Lock Number to Cramer-Rao Bound,  $S_v = 4$

## Appendix B. Cramer-Rao Bound Plots for an Individual Rotor Blade

This appendix contains the Cramer-Rao plots for an individual blade at a specified measurement signal noise spectral density,  $S_v$ . Four plots are presented in total, each with a specific value of  $S_v$  specified by the range  $S_v = 1, 2, 3, 4$ .

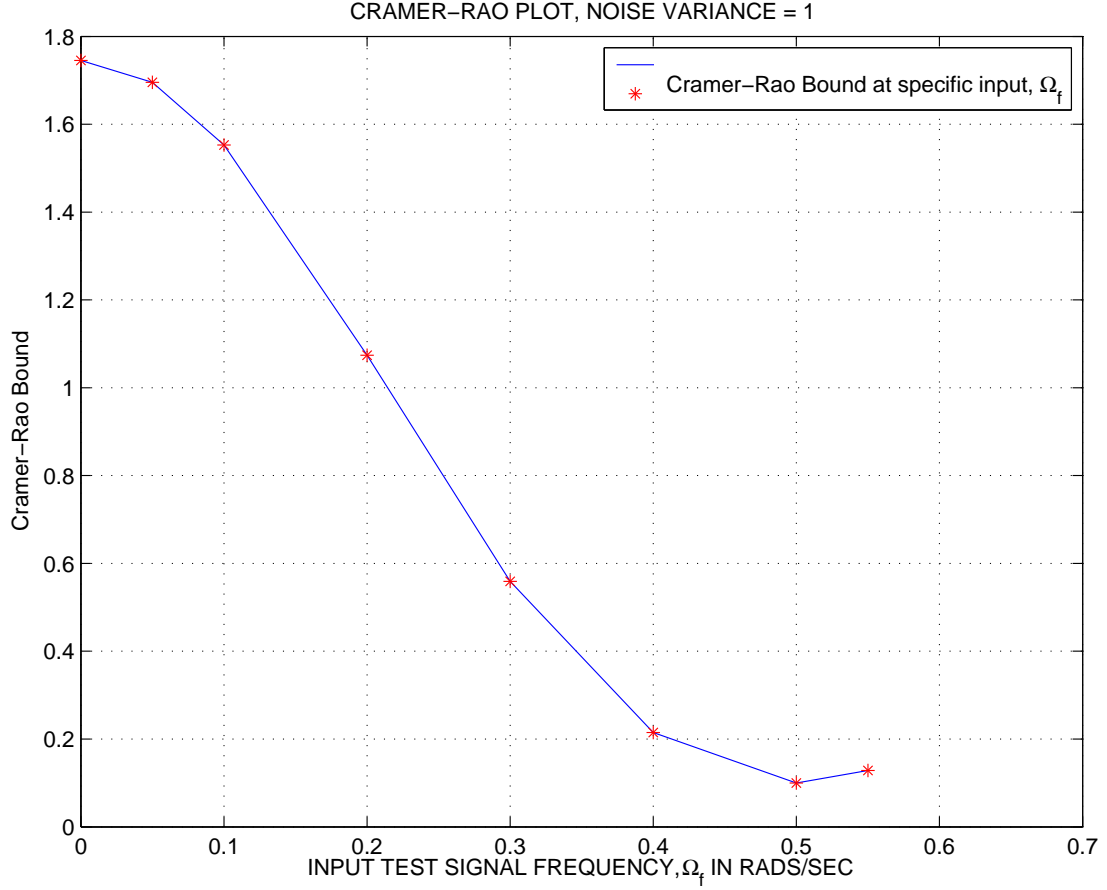


Figure B.1: Cramer-Rao Bound of Blade,  $S_v = 1$

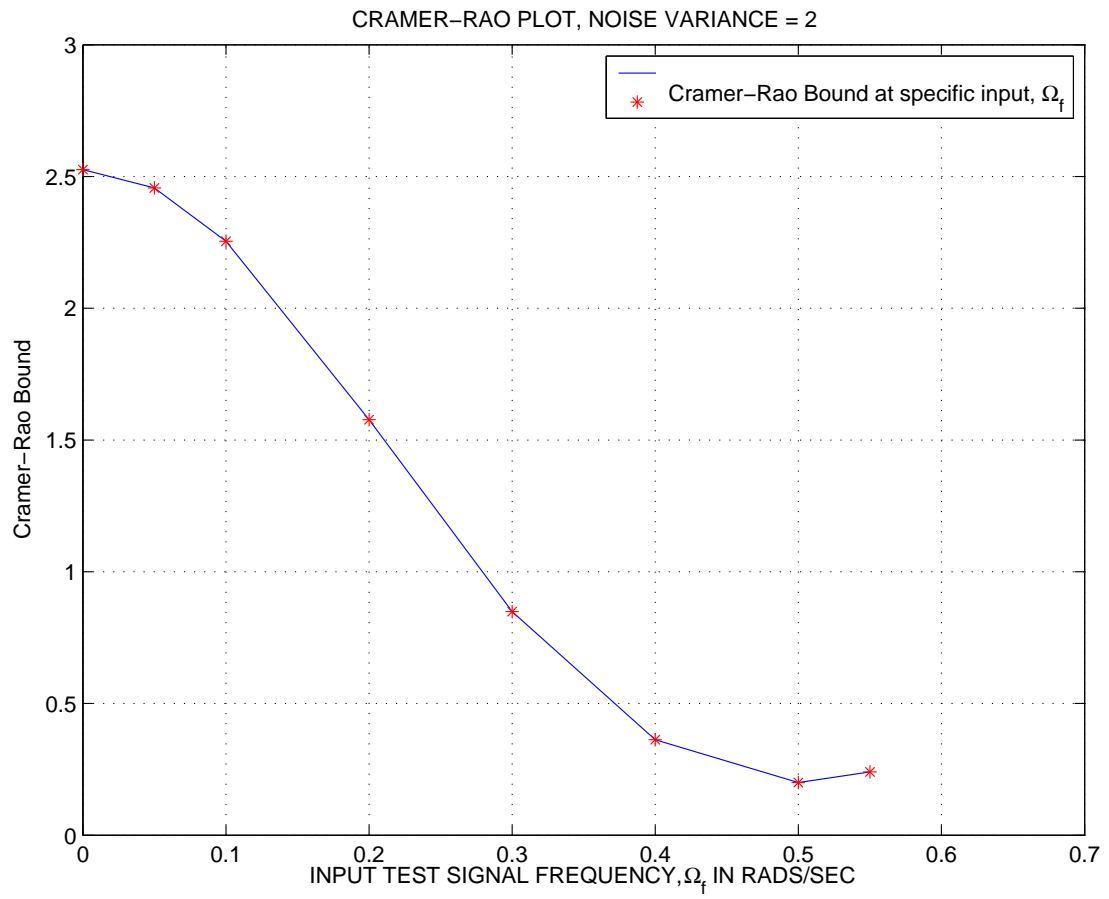


Figure B.2: Cramer-Rao Bound of Blade,  $S_v = 2$

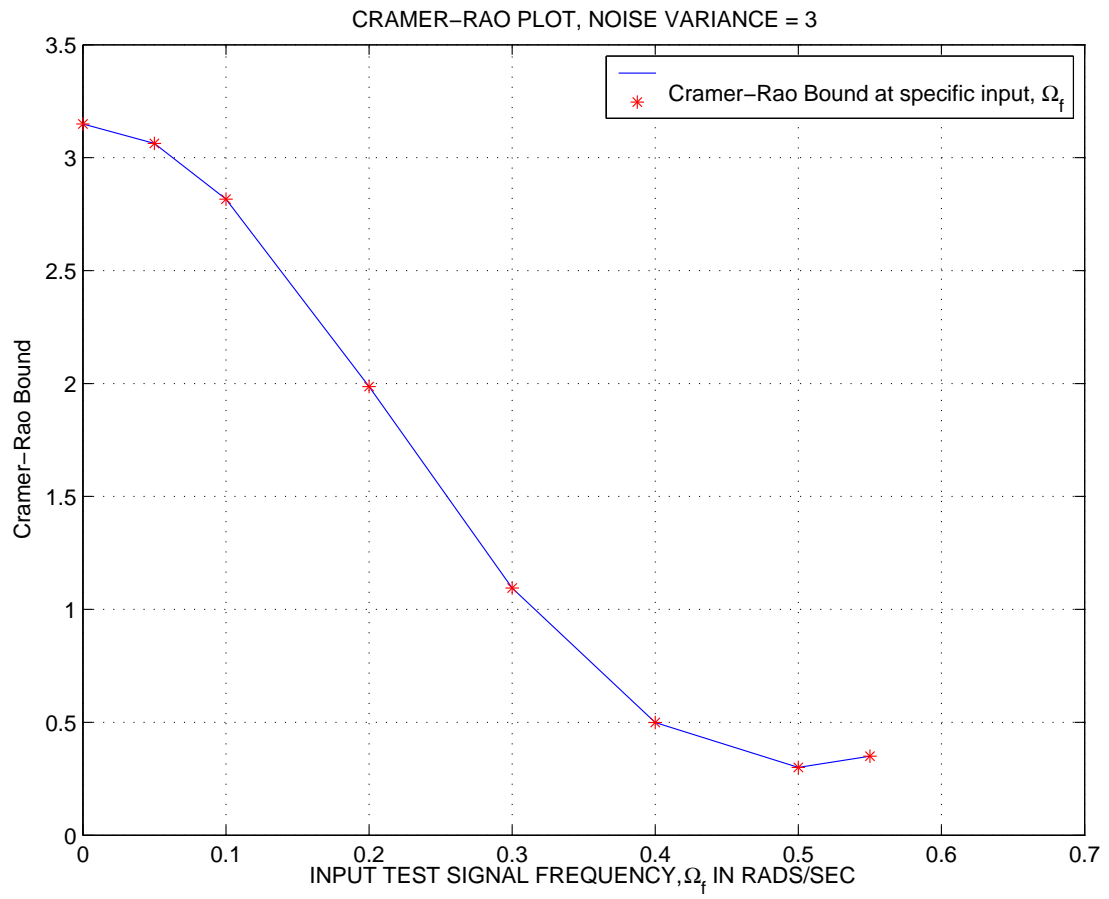


Figure B.3: Cramer-Rao Bound of Blade,  $S_v = 3$

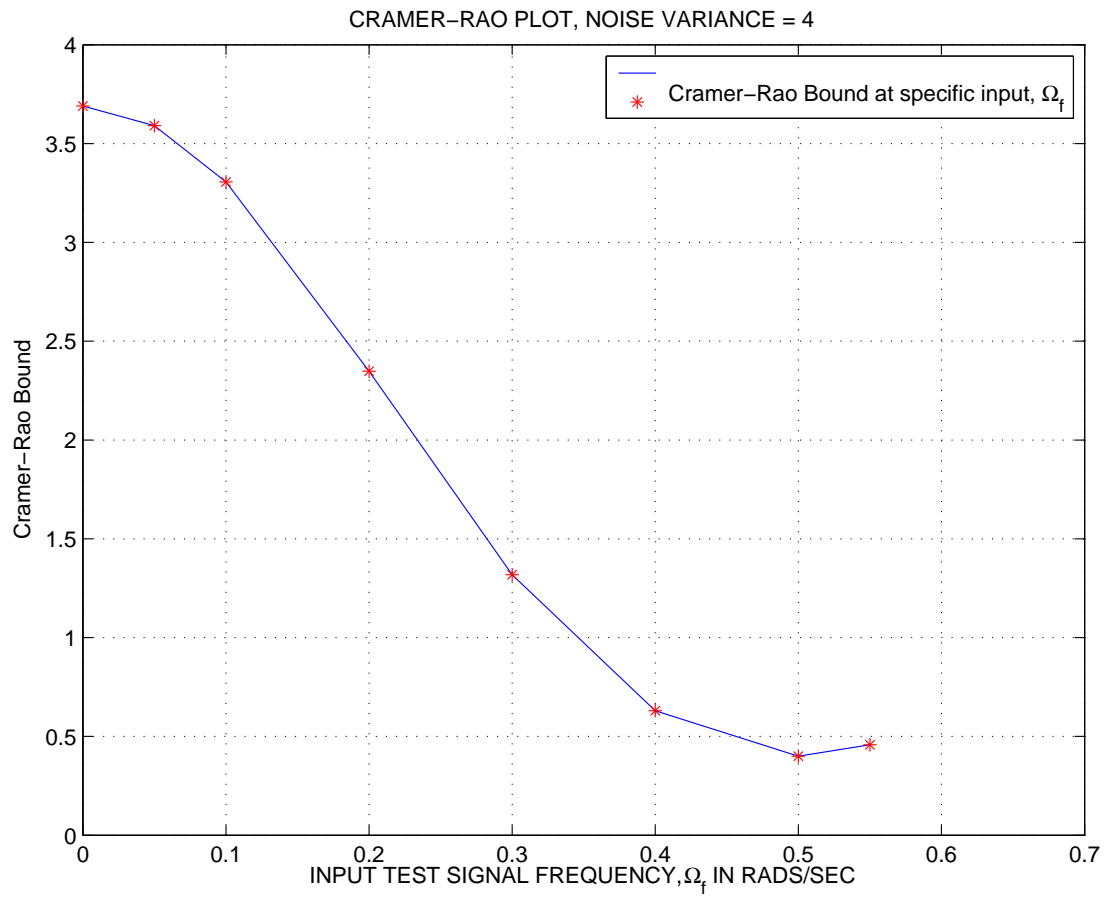


Figure B.4: Cramer-Rao Bound of Blade,  $S_v = 4$

### *Appendix C. Vibration Controller Comparison Plots, Noise Case*

$$S_v = 1$$

This appendix contains the plots of the individual flap angles, calculated LQR gains, control usage, and vibration controller performance as computed at specific cases of input frequency  $\omega_f$  and noise spectral density  $S_v$ . For the cases presented in this appendix, the range of values of input and measurement noise are  $\omega_f = \omega_p(0, 0.05, 0.1, 0.2, 0.3, 0.4, 0.5)$  and  $S_v = 1$  are used, which results in 7 individual cases. Each case will present four plots; one representing the individual flap angles of each blade after control is applied to eliminate the asymmetric lift, one for calculated LQR gains, one for control usage,  $\Theta_{con}$  for each blade, and one depicting the vibration controller performance in terms of matching the reference input.

Case 1	
Controller Design Parameters	
Input Frequency, $\omega_f$	Noise spectral density, $S_v$
$\omega_f = 0.5\omega_p$	$S_v = 1$

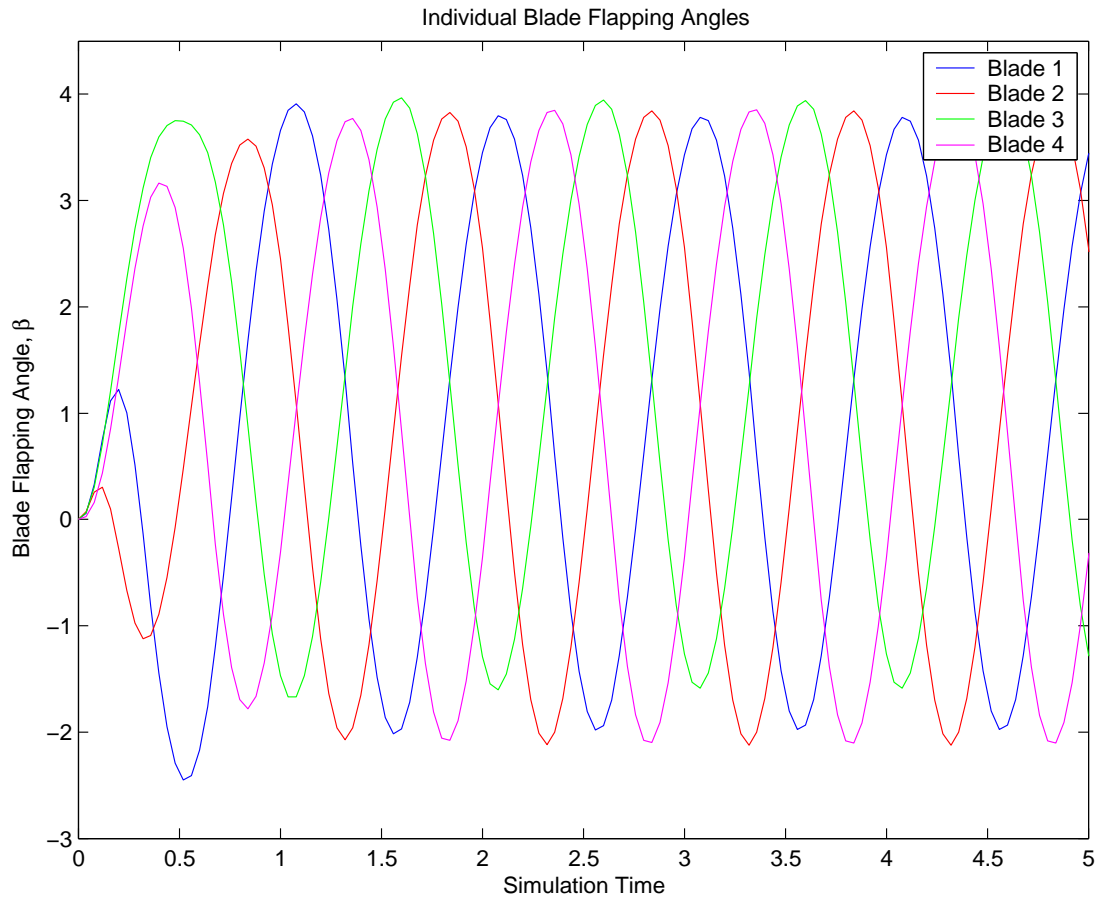


Figure C.1: Individual Flap Angles,  $\beta$ , for case  $\omega_f = 0.5\omega_p$ ,  $S_v = 1$

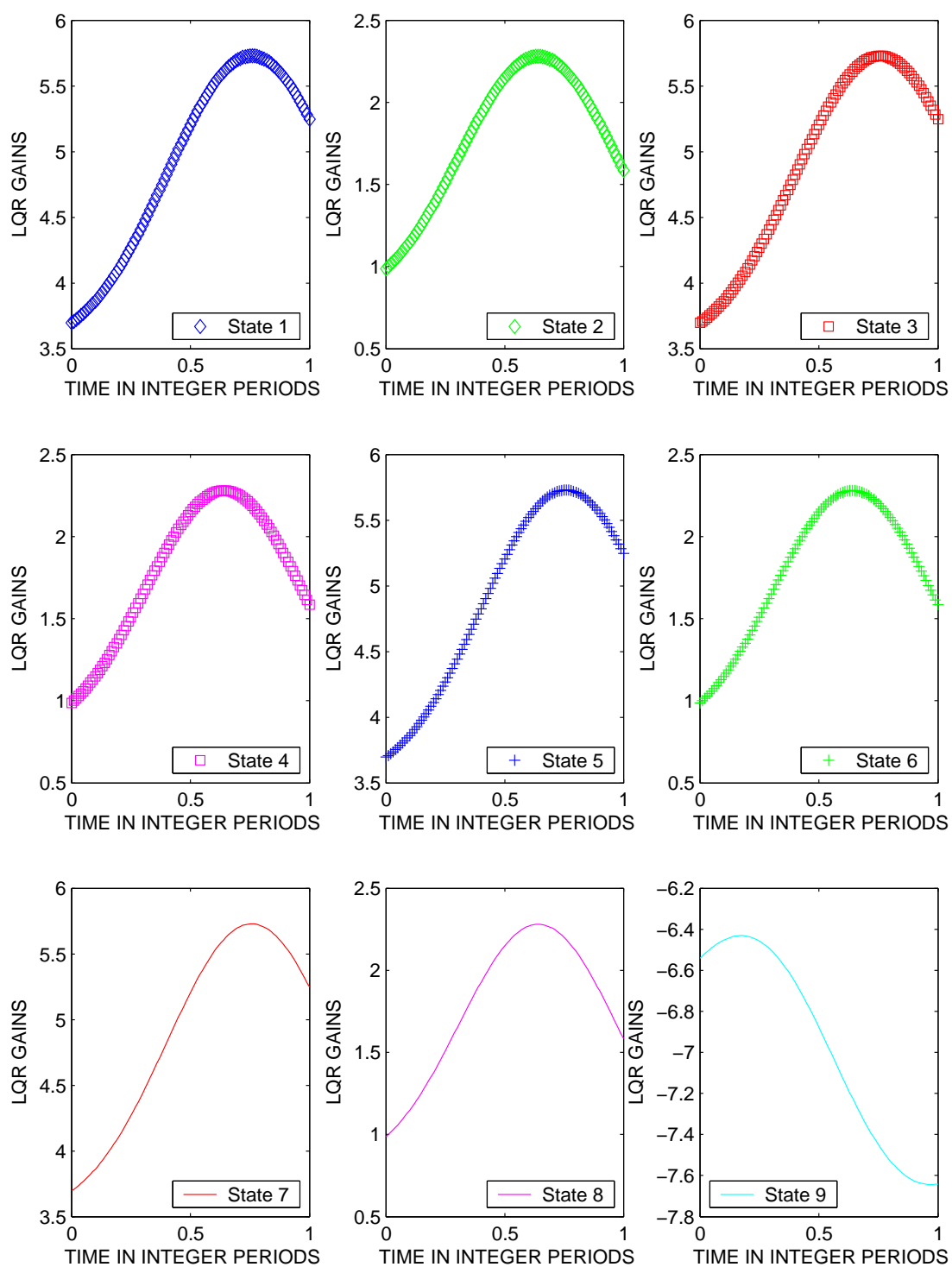


Figure C.2: All LQR Gains for case  $\omega_f = 0.5\omega_p$ ,  $S_v = 1$

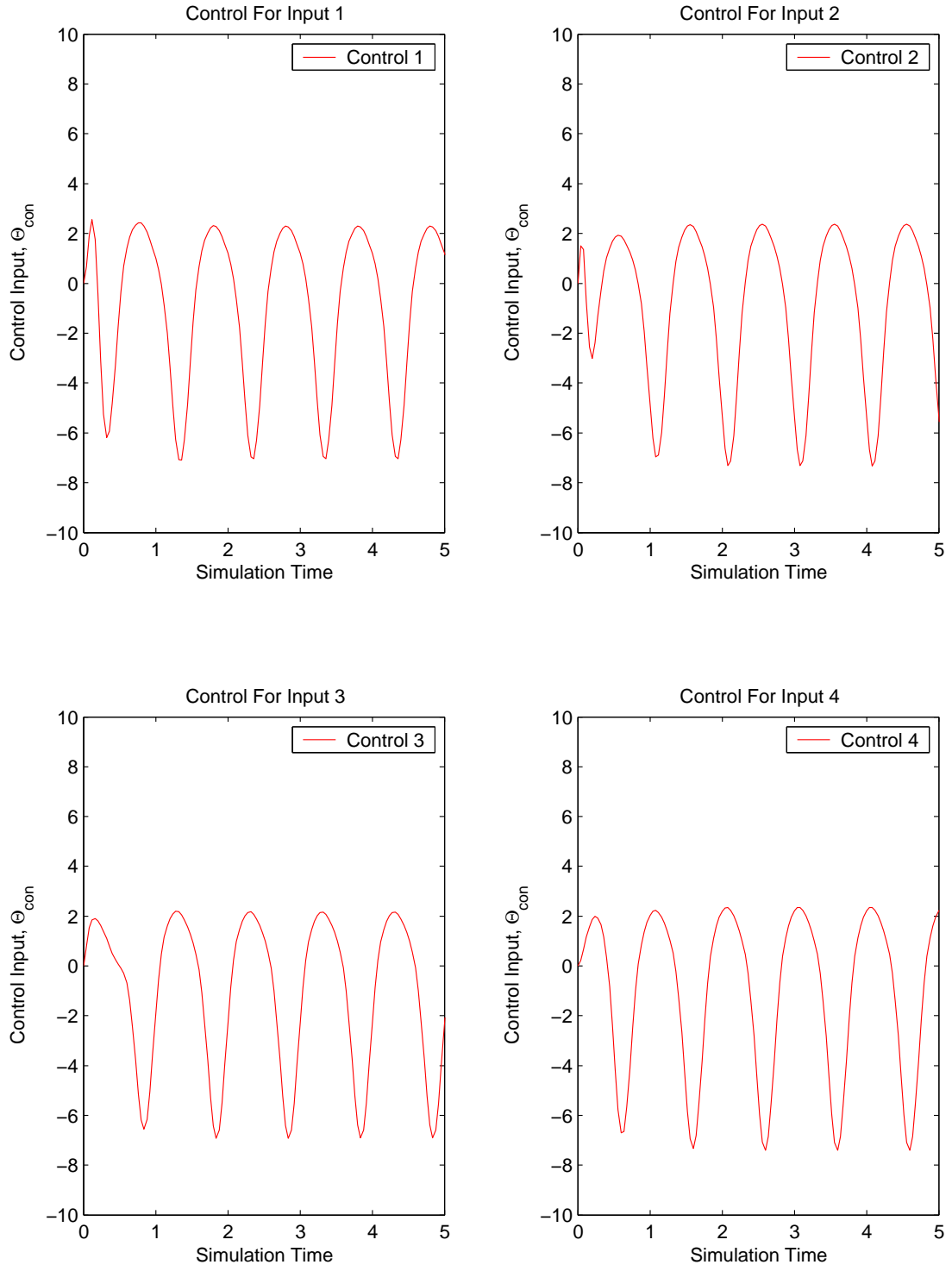


Figure C.3: Control Usage for case  $\omega_f = 0.5\omega_p$ ,  $S_v = 1$

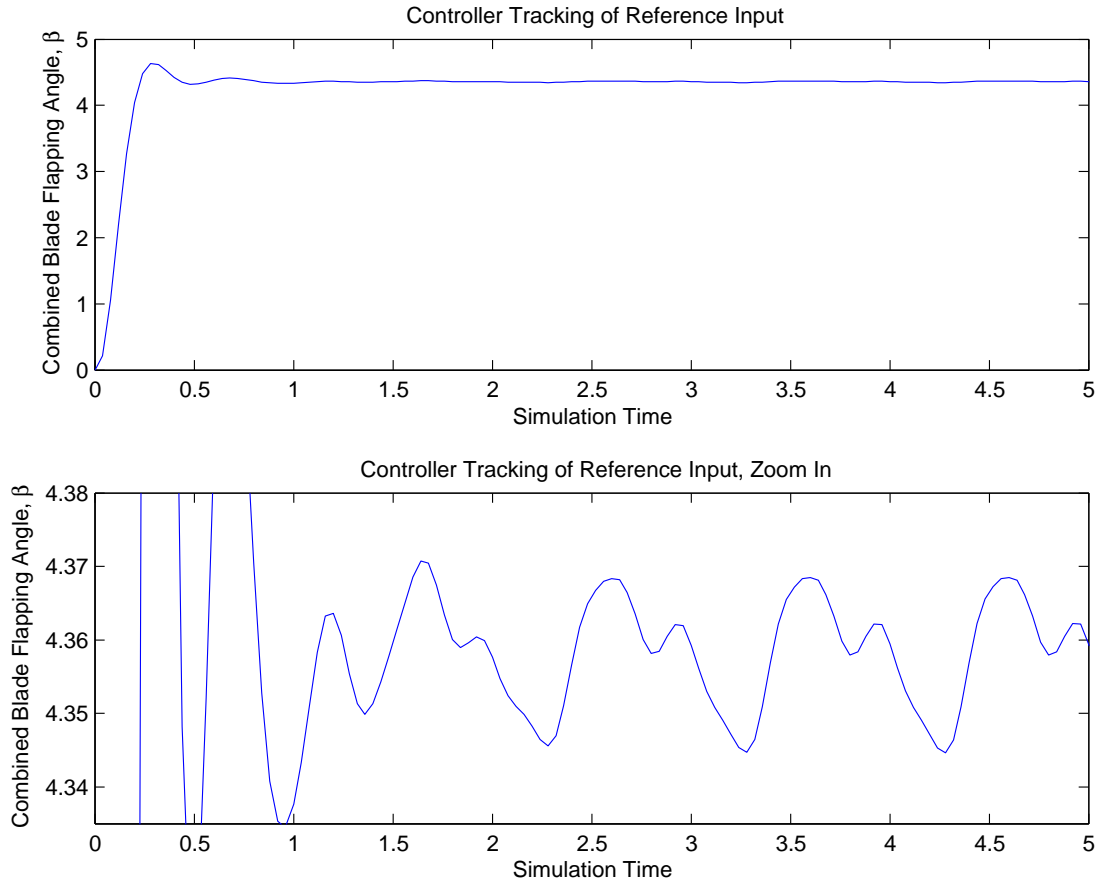


Figure C.4: Tracking Performance of Vibration Controller for case  $\omega_f = 0.5\omega_p$ ,  $S_v = 1$

Case 2	
Controller Design Parameters	
Input Frequency, $\omega_f$	Noise spectral density, $S_v$
$\omega_f = .4\omega_p$	$S_v = 1$

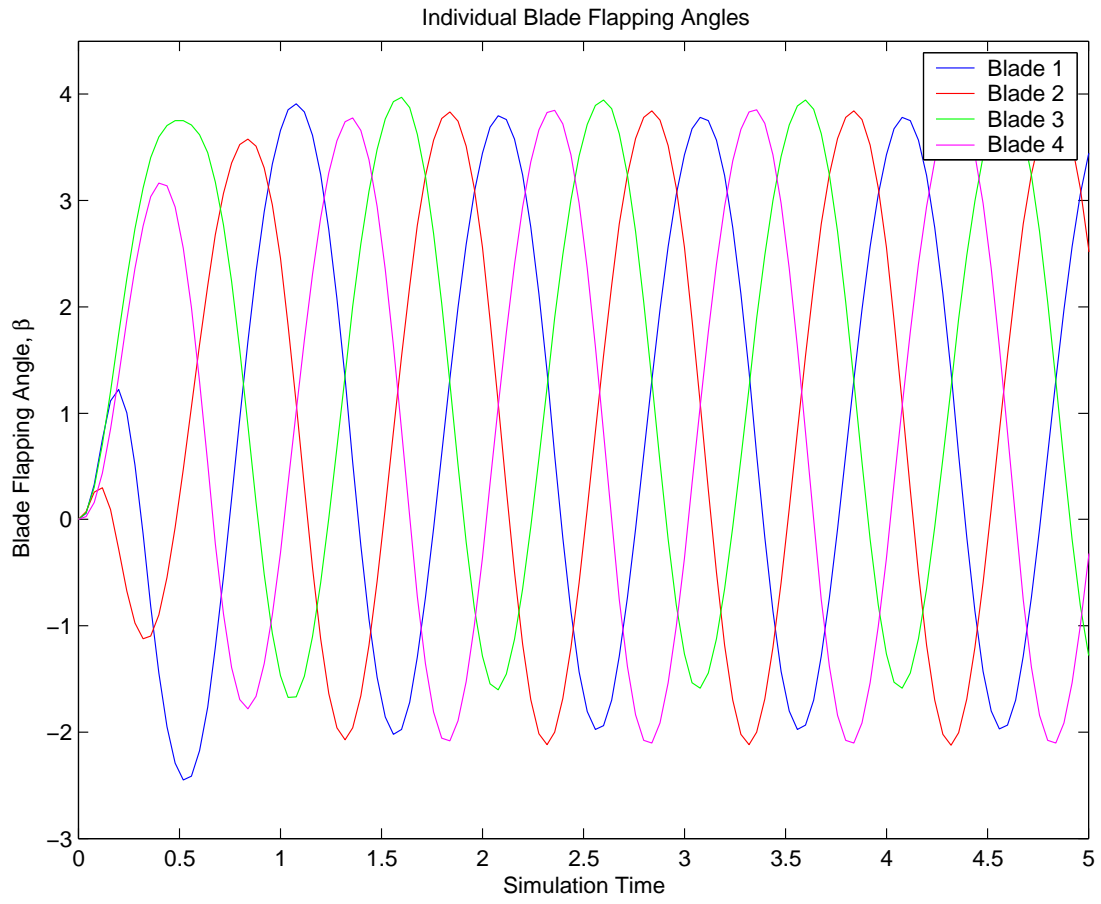


Figure C.5: Individual Flap Angles,  $\beta$ , for case  $\omega_f = 0.4\omega_p$ ,  $S_v = 1$

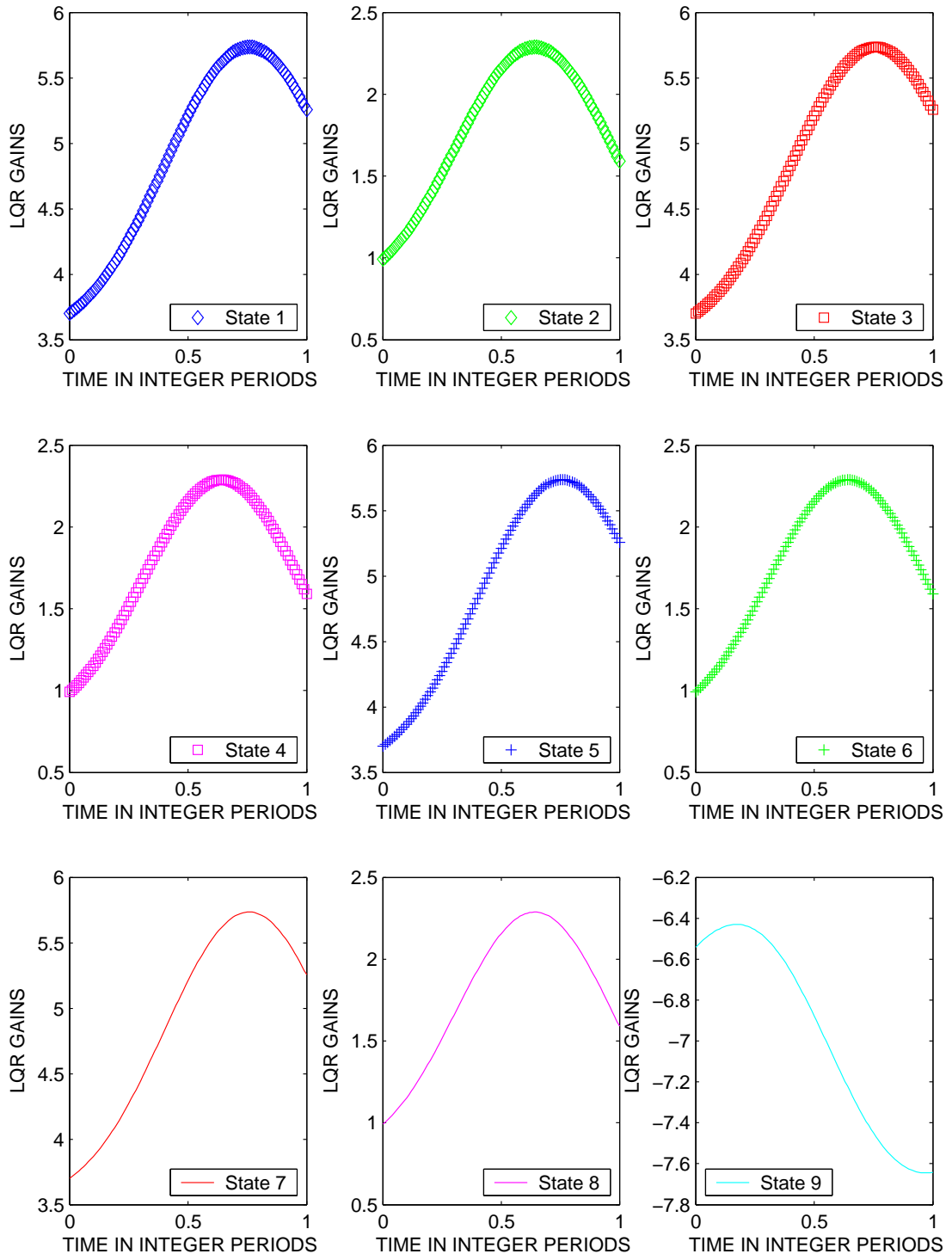


Figure C.6: All LQR Gains for case  $\omega_f = 0.4\omega_p$ ,  $S_v = 1$

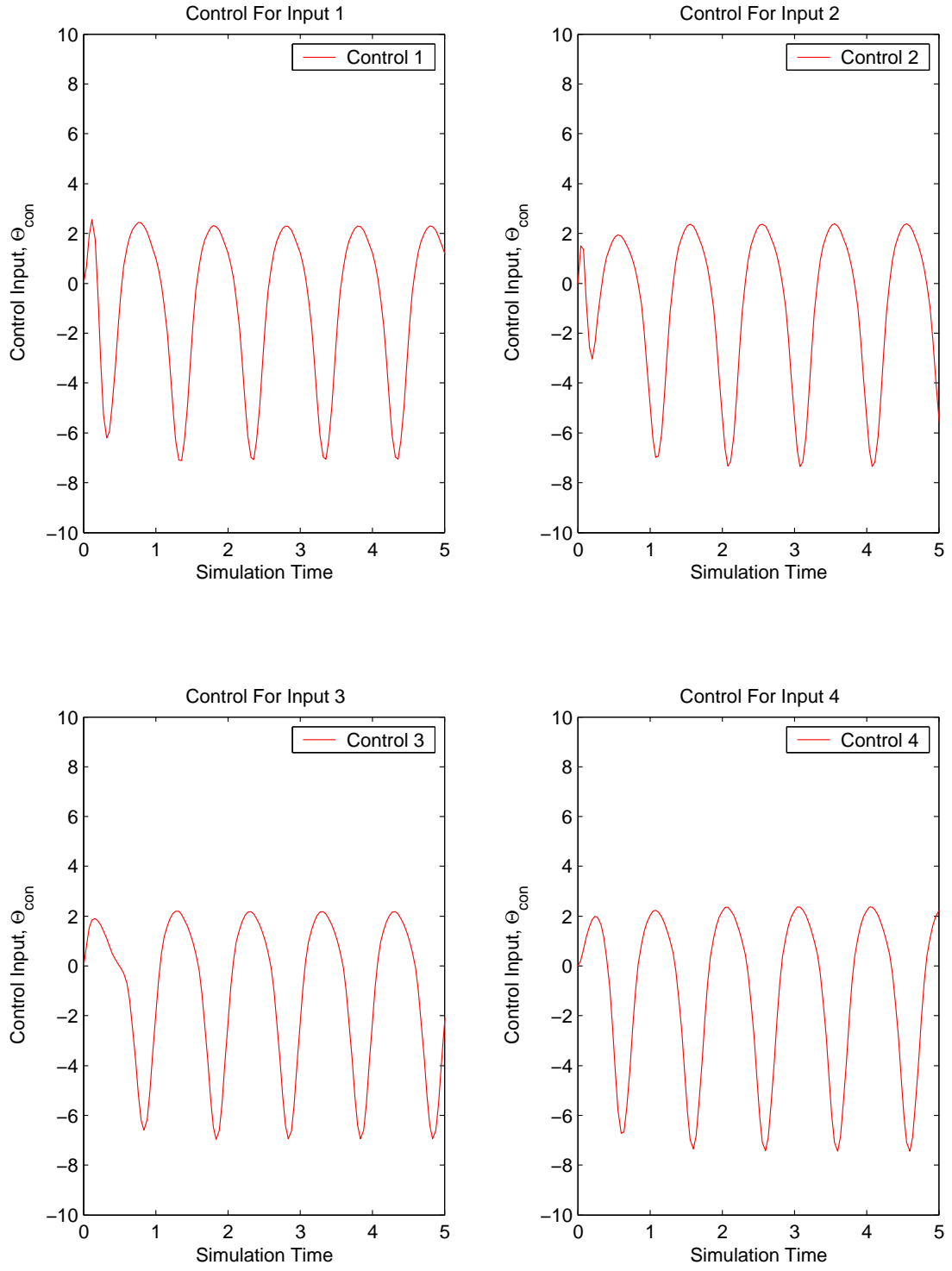


Figure C.7: Control Usage for case  $\omega_f = 0.4\omega_p$ ,  $S_v = 1$

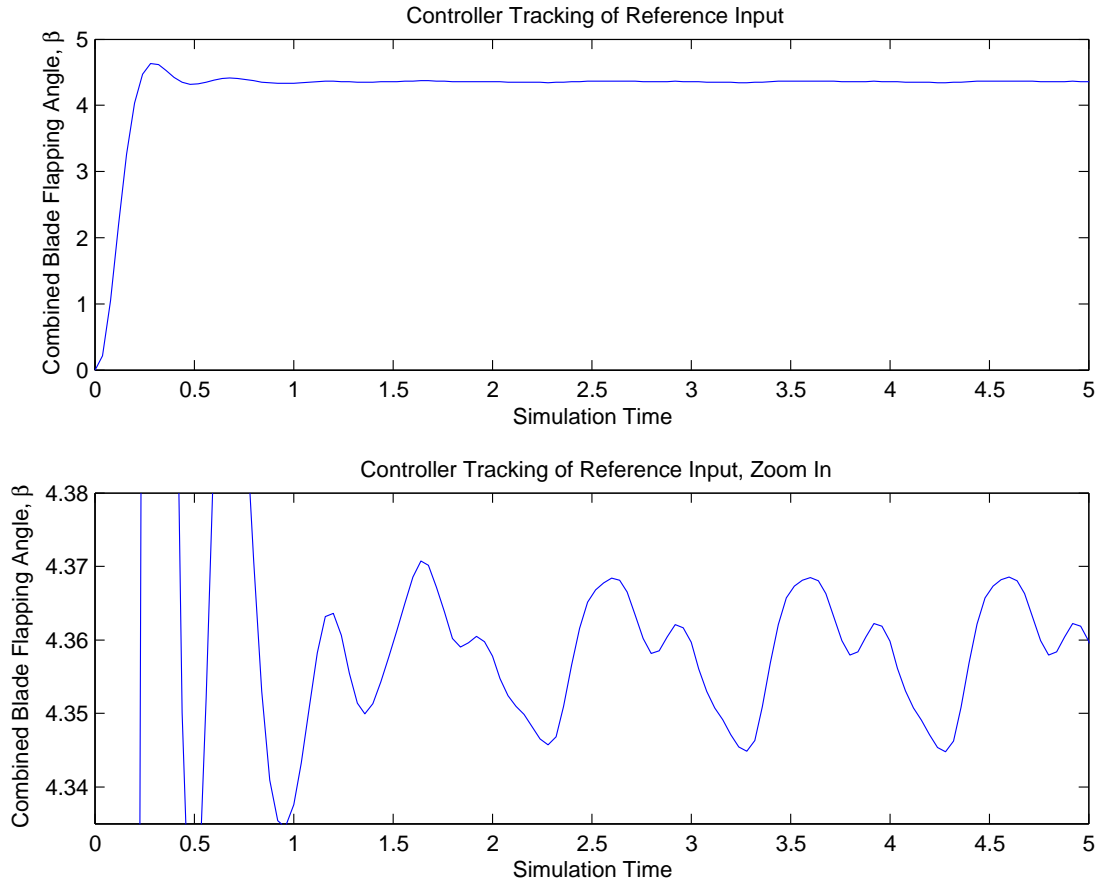


Figure C.8: Tracking Performance of Vibration Controller for case  $\omega_f = 0.4\omega_p$ ,  $S_v = 1$

Case 3	
Controller Design Parameters	
Input Frequency, $\omega_f$	Noise spectral density, $S_v$
$\omega_f = .3\omega_p$	$S_v = 1$

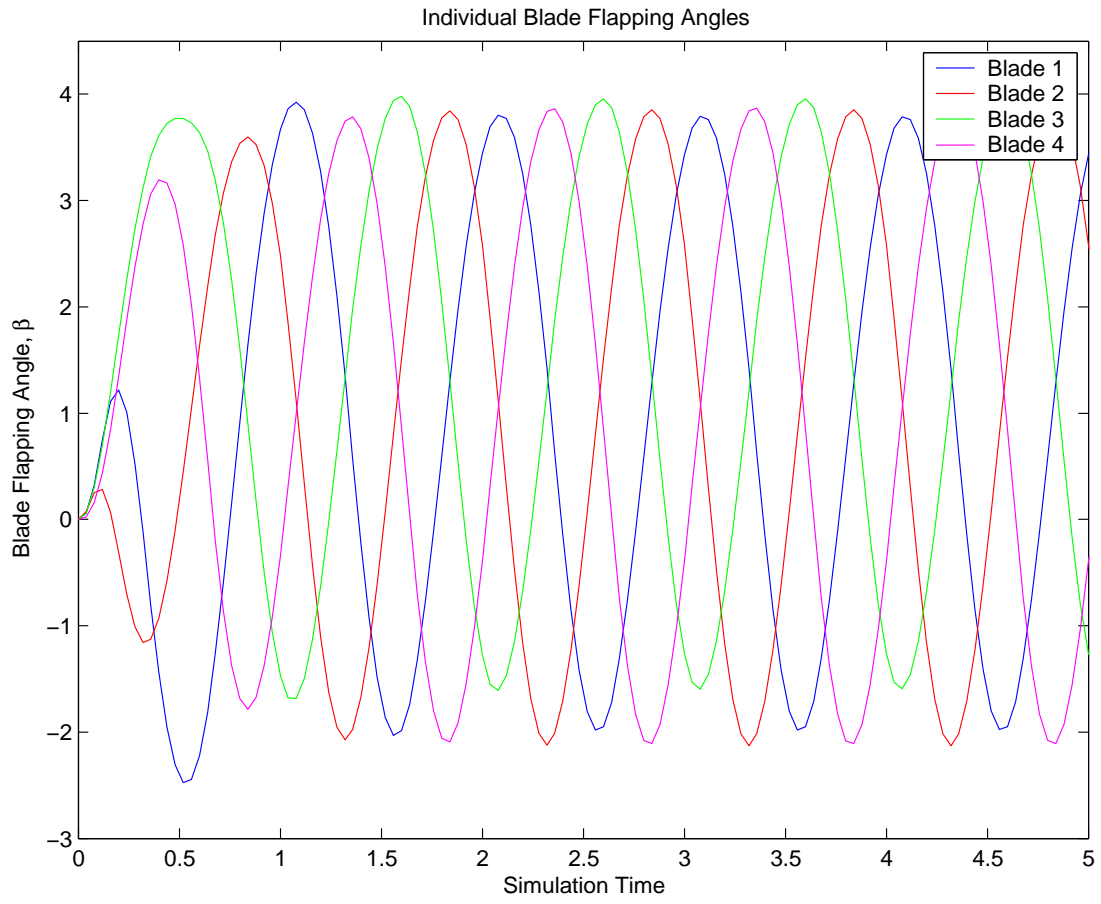


Figure C.9: Individual Flap Angles,  $\beta$ , for case  $\omega_f = 0.3\omega_p$ ,  $S_v = 1$

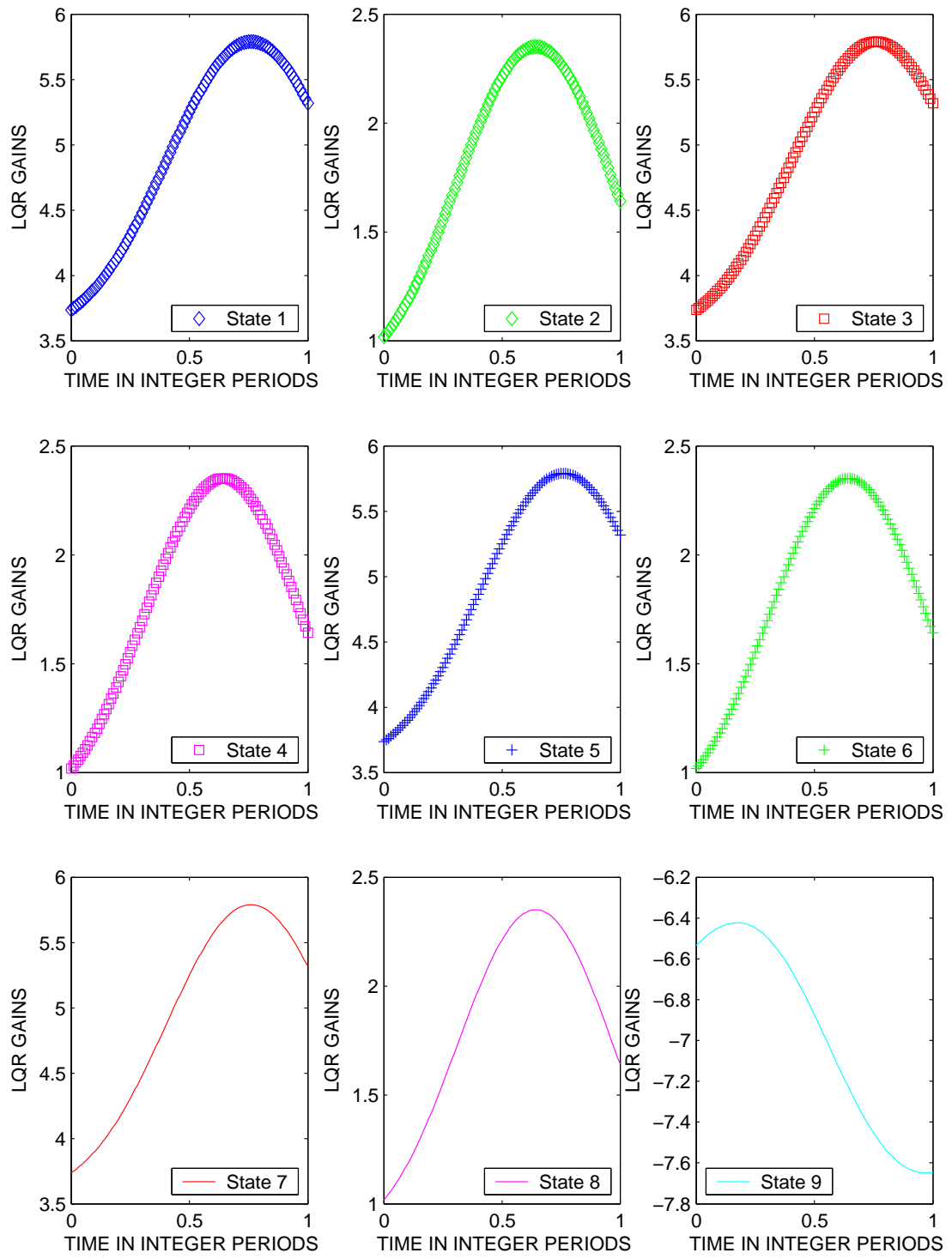


Figure C.10: All LQR Gains for case  $\omega_f = 0.3\omega_p$ ,  $S_v = 1$

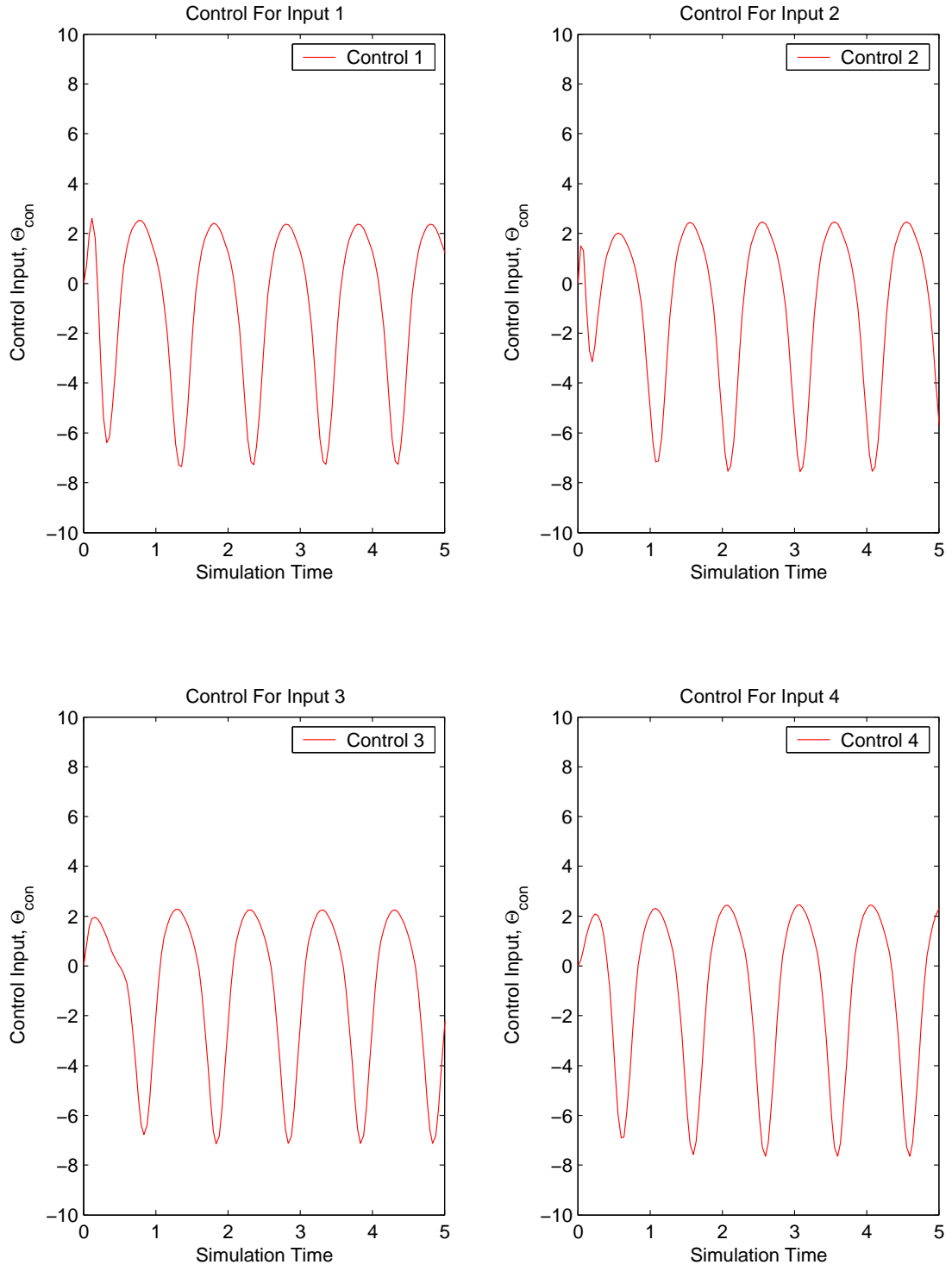


Figure C.11: Control Usage for case  $\omega_f = 0.3\omega_p$ ,  $S_v = 1$

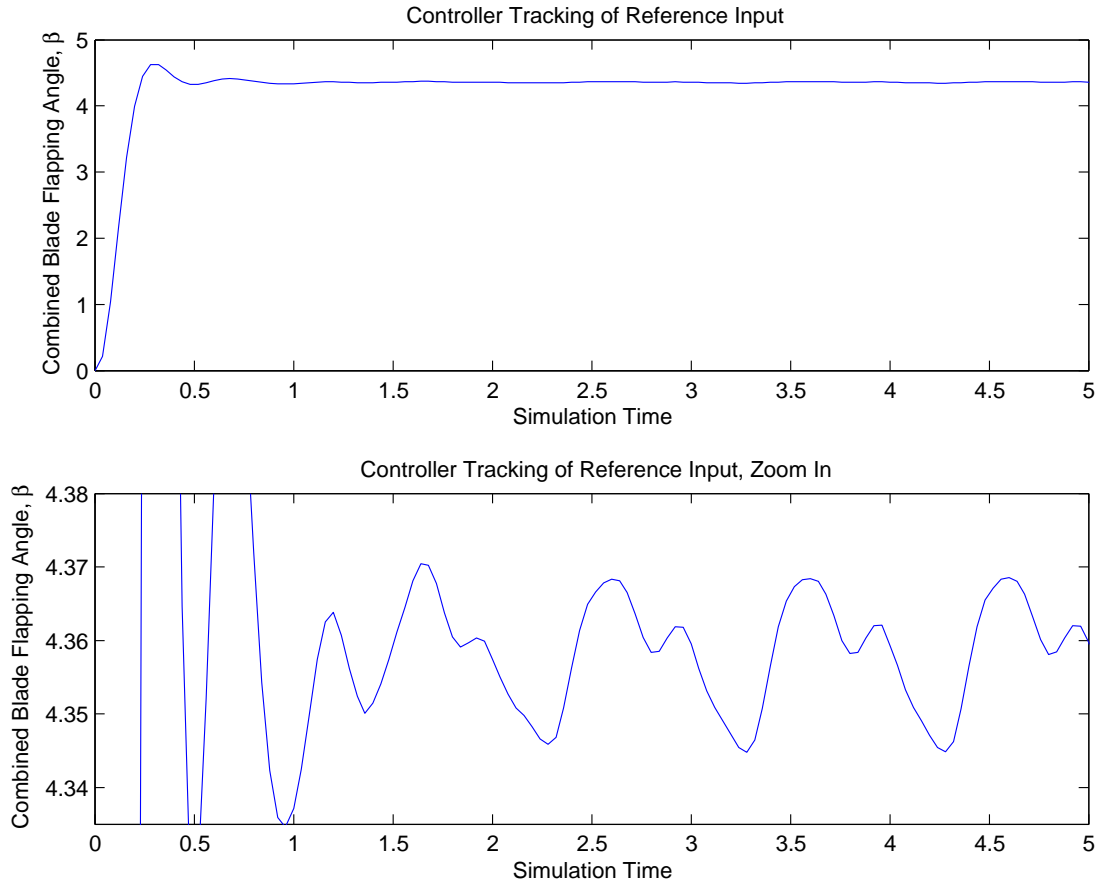


Figure C.12: Tracking Performance of Vibration Controller for case  $\omega_f = 0.3\omega_p$ ,  $S_v = 1$

Case 4	
Controller Design Parameters	
Input Frequency, $\omega_f$	Noise spectral density, $S_v$
$\omega_f = .2\omega_p$	$S_v = 1$

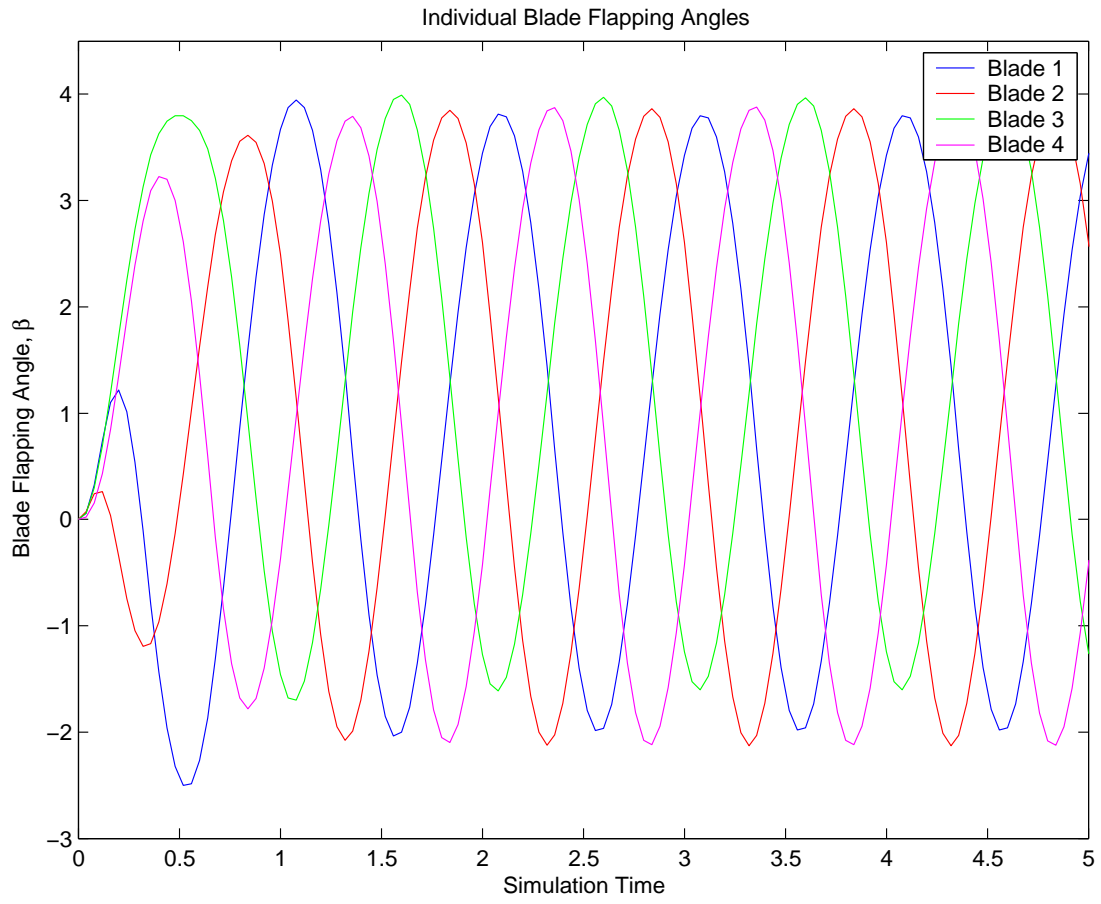


Figure C.13: Individual Flap Angles,  $\beta$ , for case  $\omega_f = 0.2\omega_p$ ,  $S_v = 1$

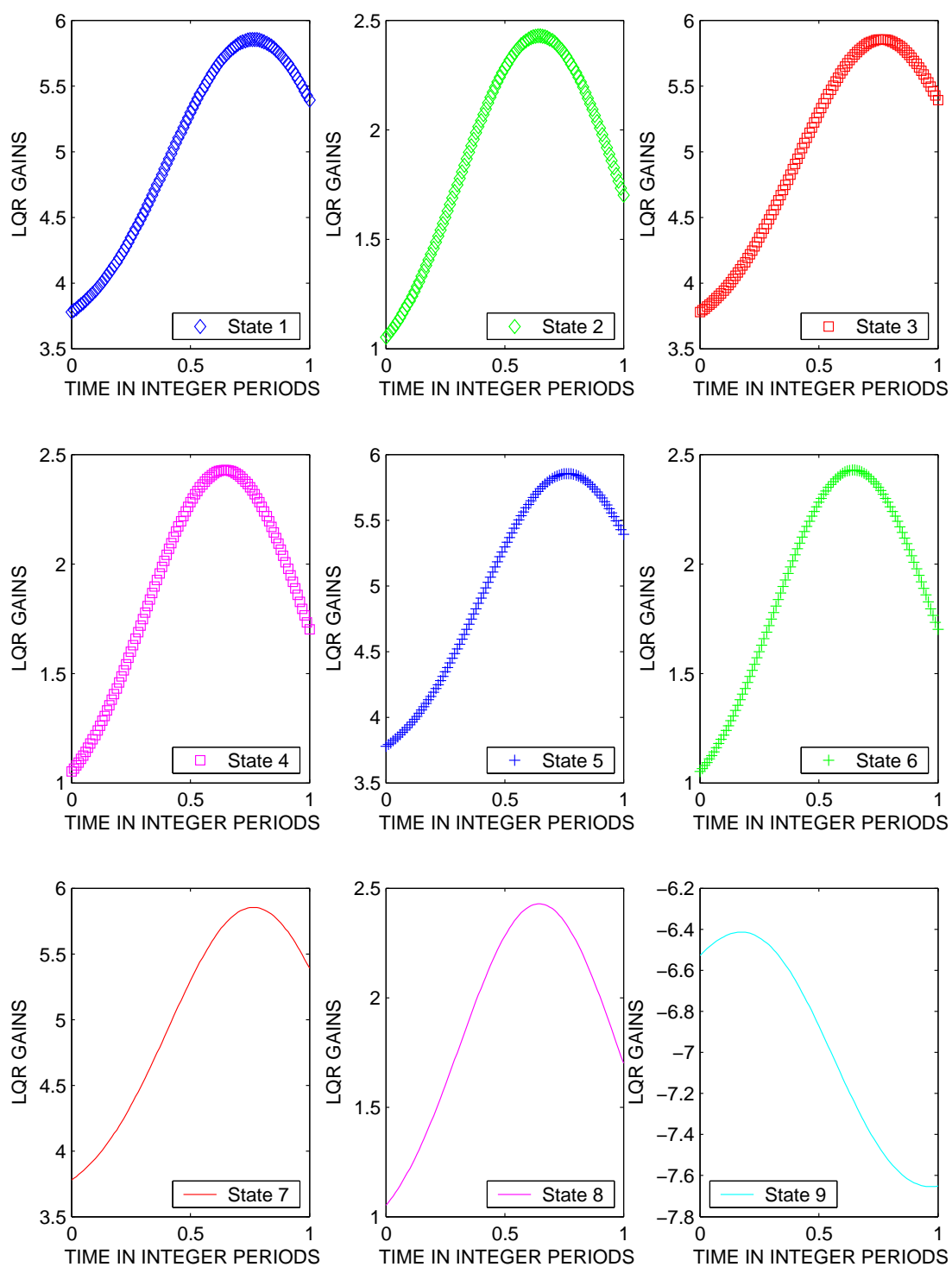


Figure C.14: All LQR Gains for case  $\omega_f = 0.2\omega_p$ ,  $S_v = 1$

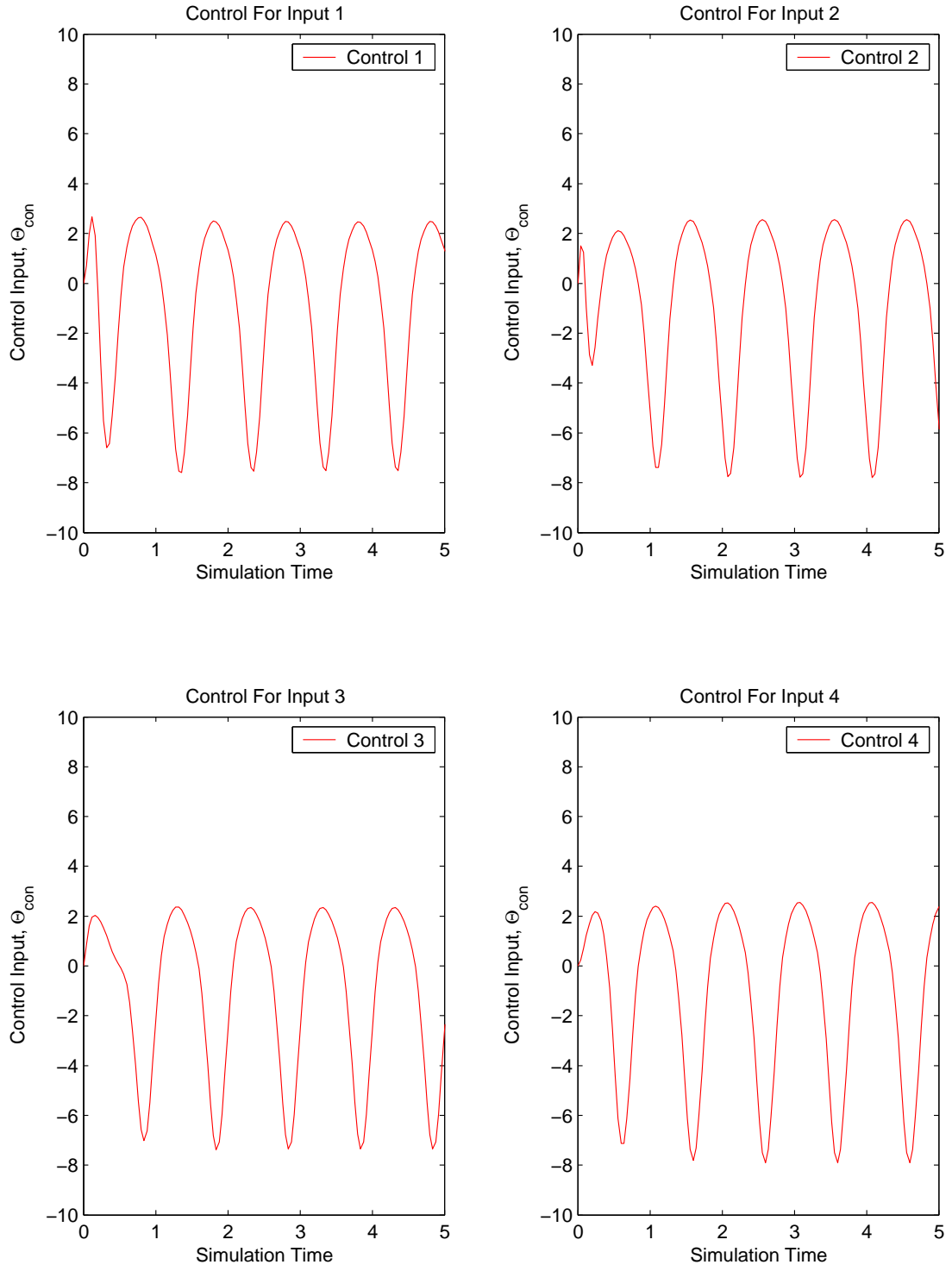


Figure C.15: Control Usage for case  $\omega_f = 0.2\omega_p$ ,  $S_v = 1$

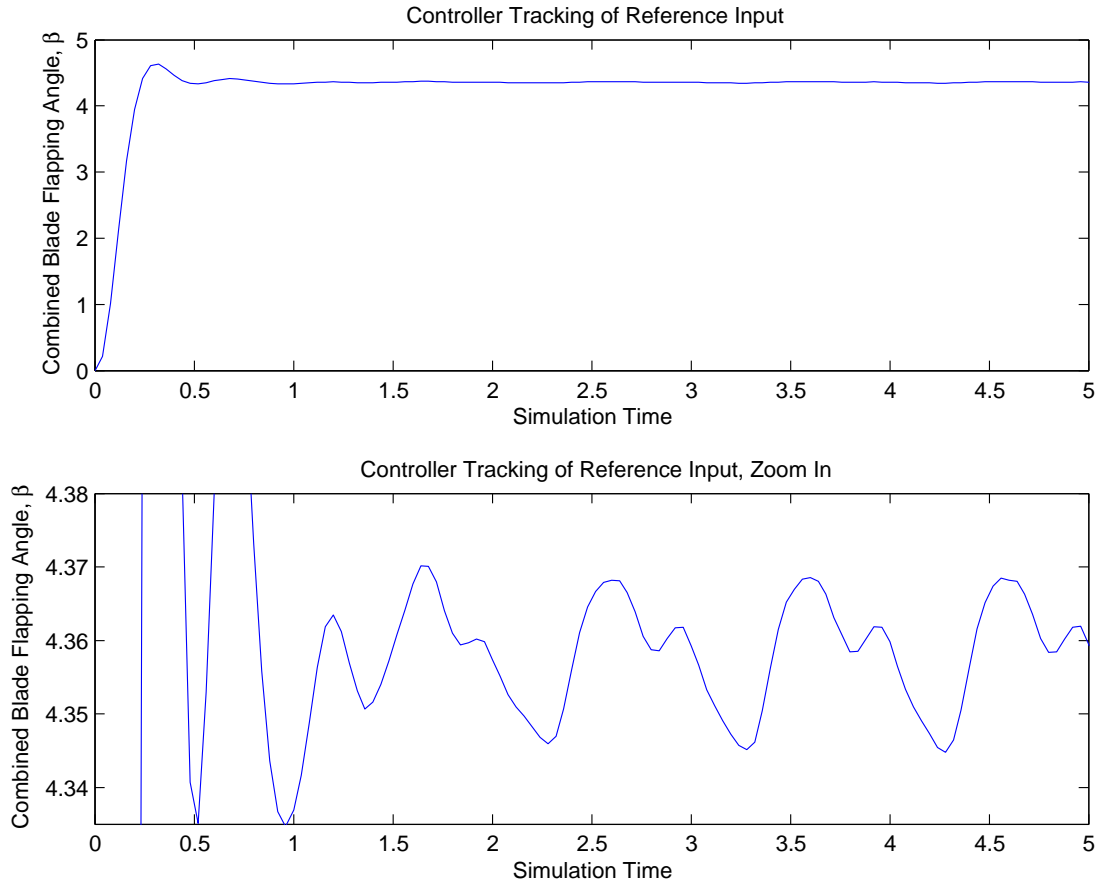


Figure C.16: Tracking Performance of Vibration Controller for case  $\omega_f = 0.2\omega_p$ ,  $S_v = 1$

Case 5	
Controller Design Parameters	
Input Frequency, $\omega_f$	Noise spectral density, $S_v$
$\omega_f = .1\omega_p$	$S_v = 1$

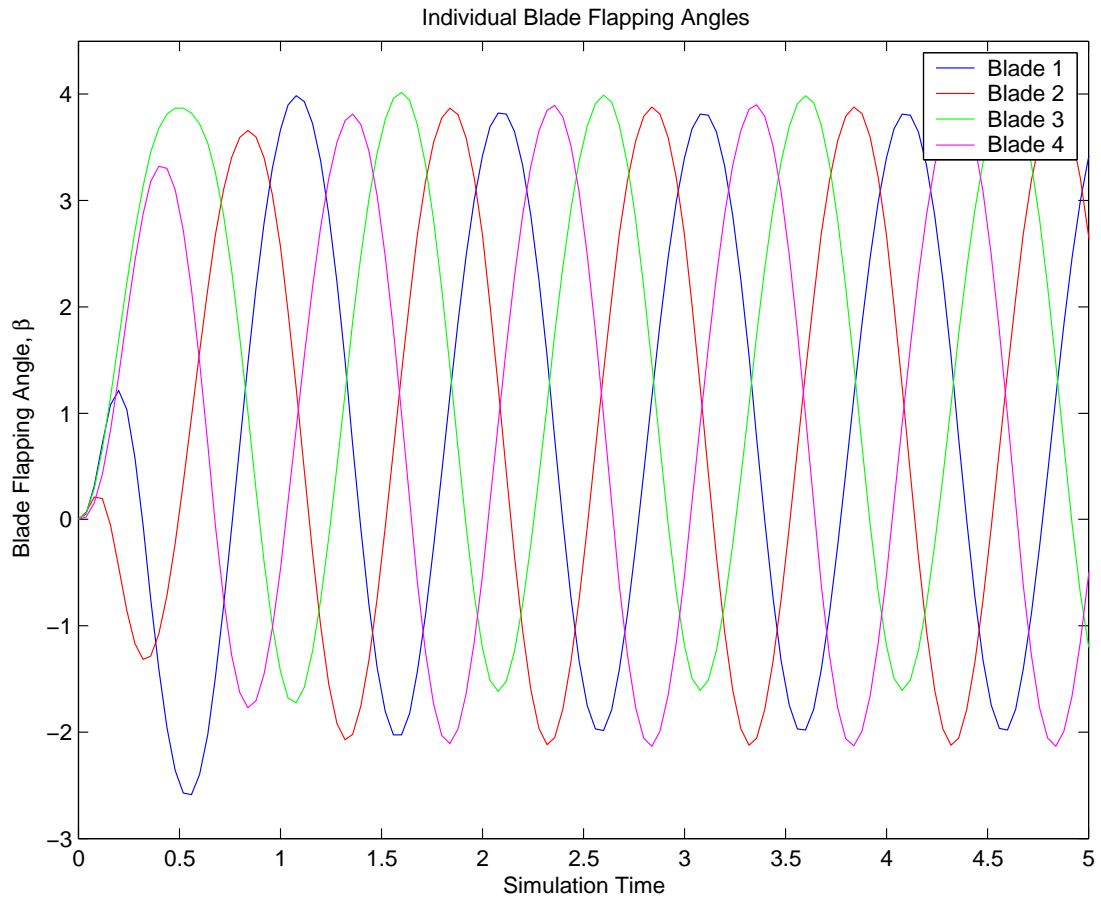


Figure C.17: Individual Flap Angles,  $\beta$ , for case  $\omega_f = 0.1\omega_p$ ,  $S_v = 1$

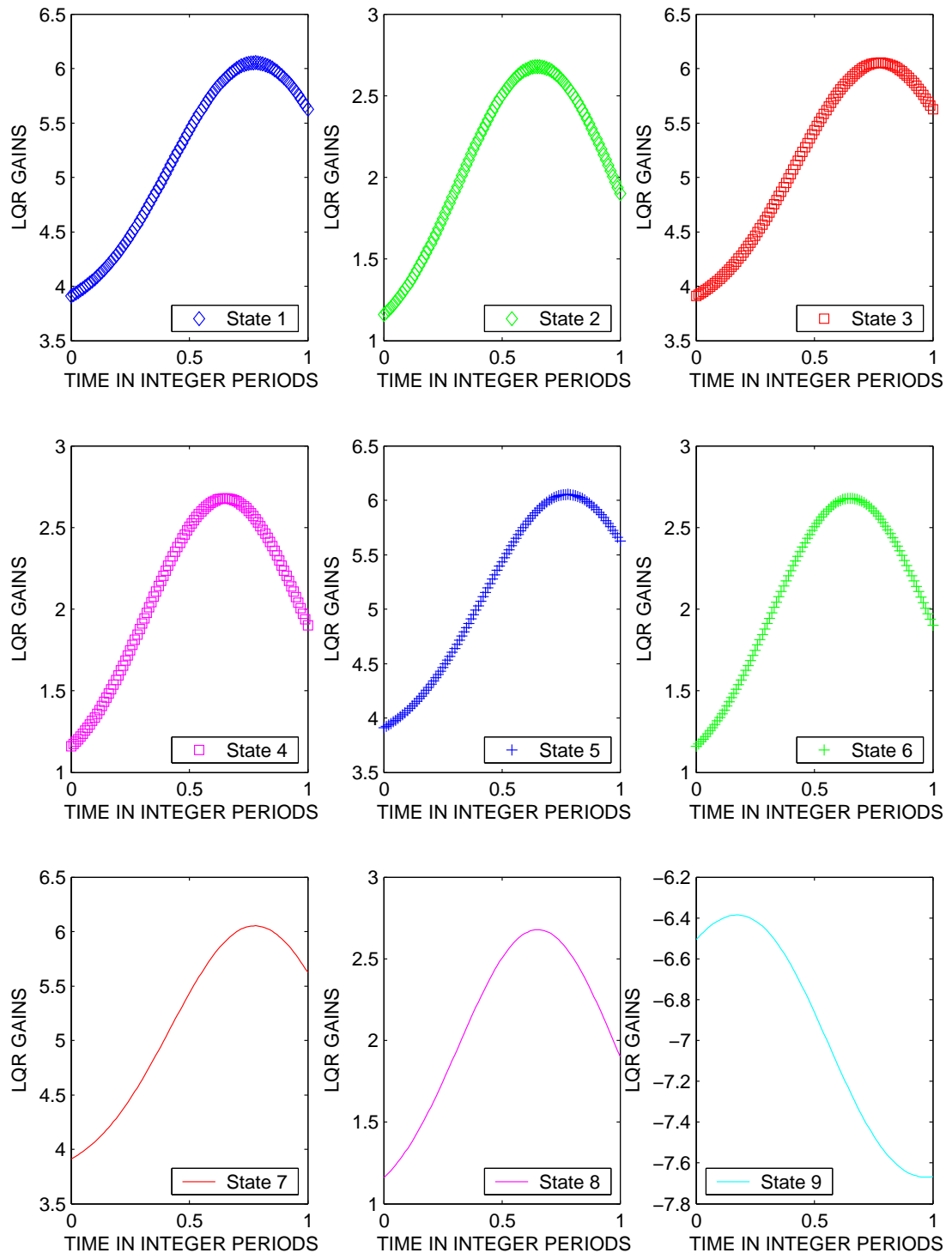


Figure C.18: All LQR Gains for case  $\omega_f = 0.1\omega_p$ ,  $S_v = 1$

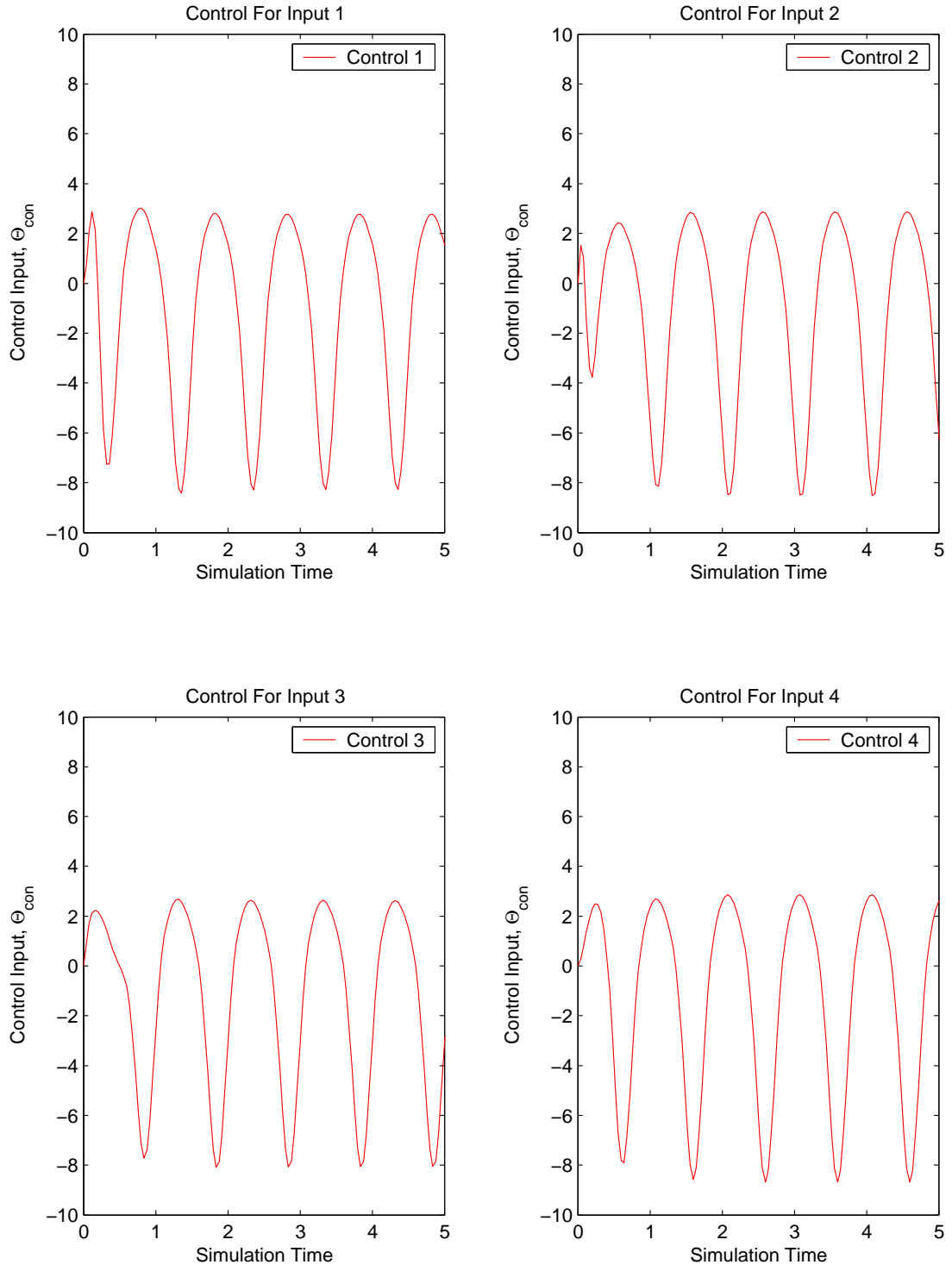


Figure C.19: Control Usage for case  $\omega_f = 0.1\omega_p$ ,  $S_v = 1$

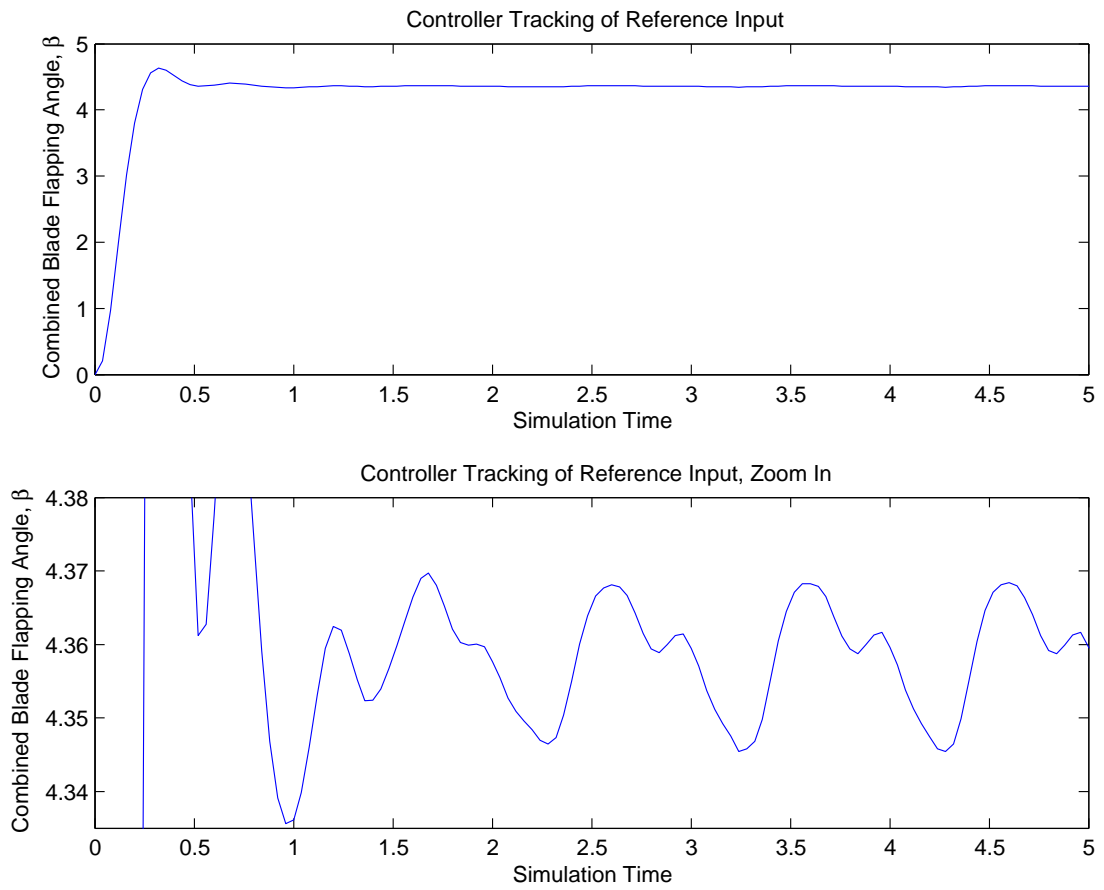


Figure C.20: Tracking Performance of Vibration Controller for case  $\omega_f = 0.1\omega_p$ ,  $S_v = 1$

Case 6	
Controller Design Parameters	
Input Frequency, $\omega_f$	Noise spectral density, $S_v$
$\omega_f = .05\omega_p$	$S_v = 1$

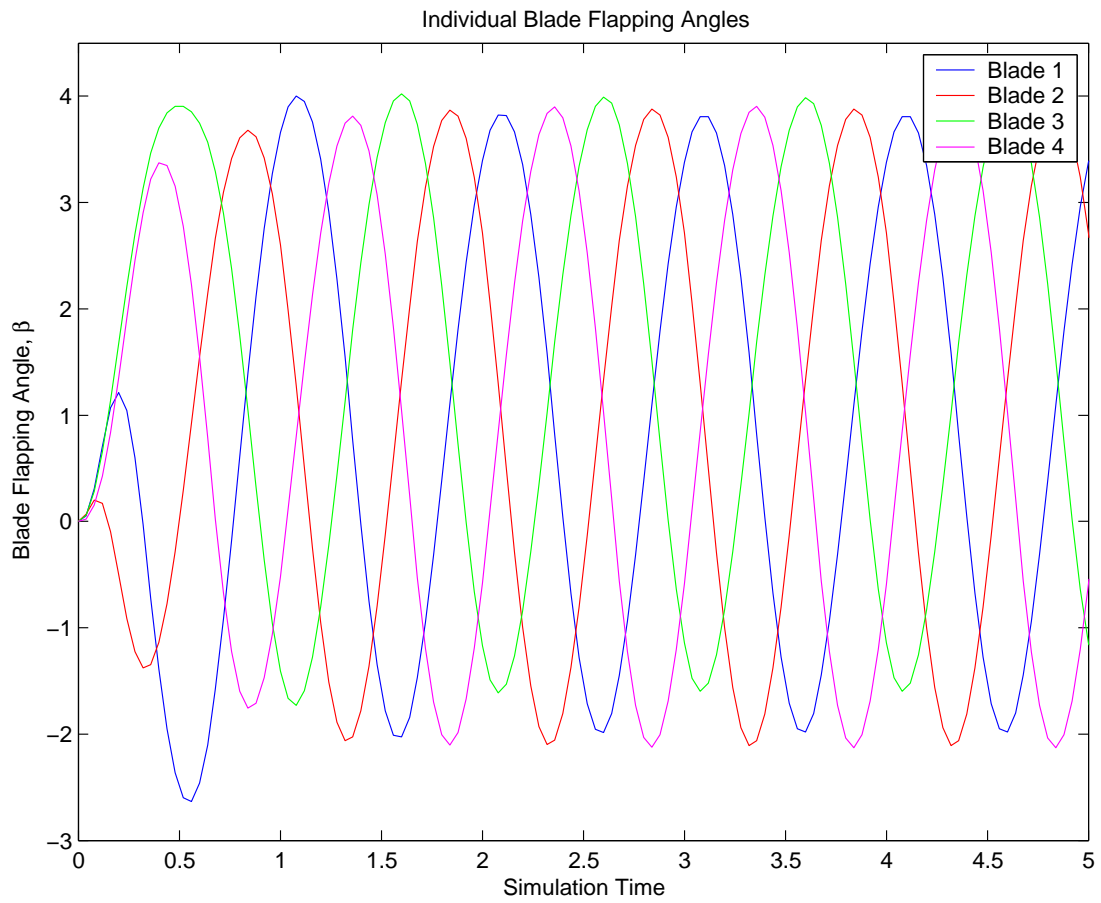


Figure C.21: Individual Flap Angles,  $\beta$ , for case  $\omega_f = 0.05\omega_p$ ,  $S_v = 1$

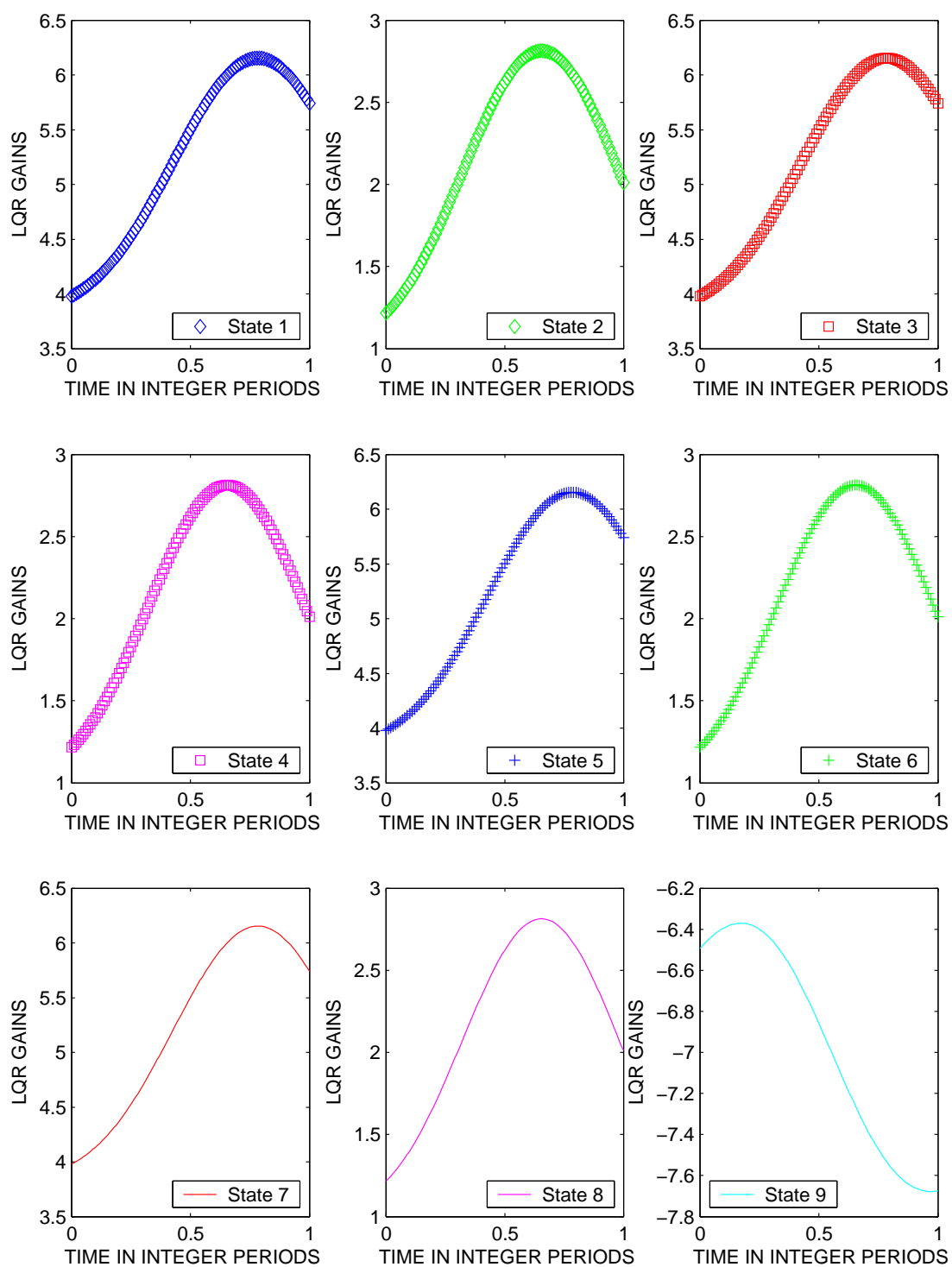


Figure C.22: All LQR Gains for case  $\omega_f = 0.05\omega_p$ ,  $S_v = 1$

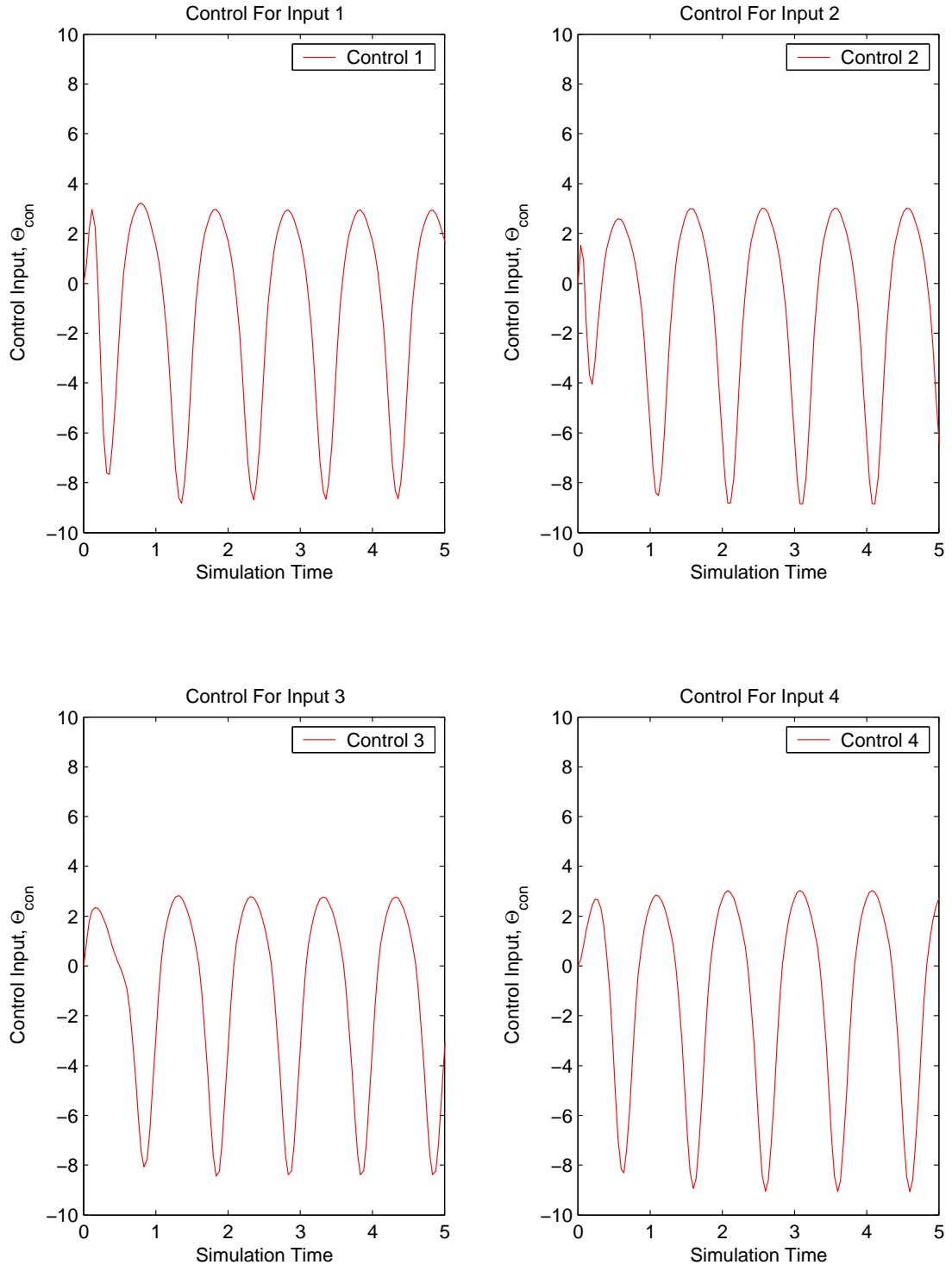


Figure C.23: Control Usage for case  $\omega_f = 0.05\omega_p$ ,  $S_v = 1$

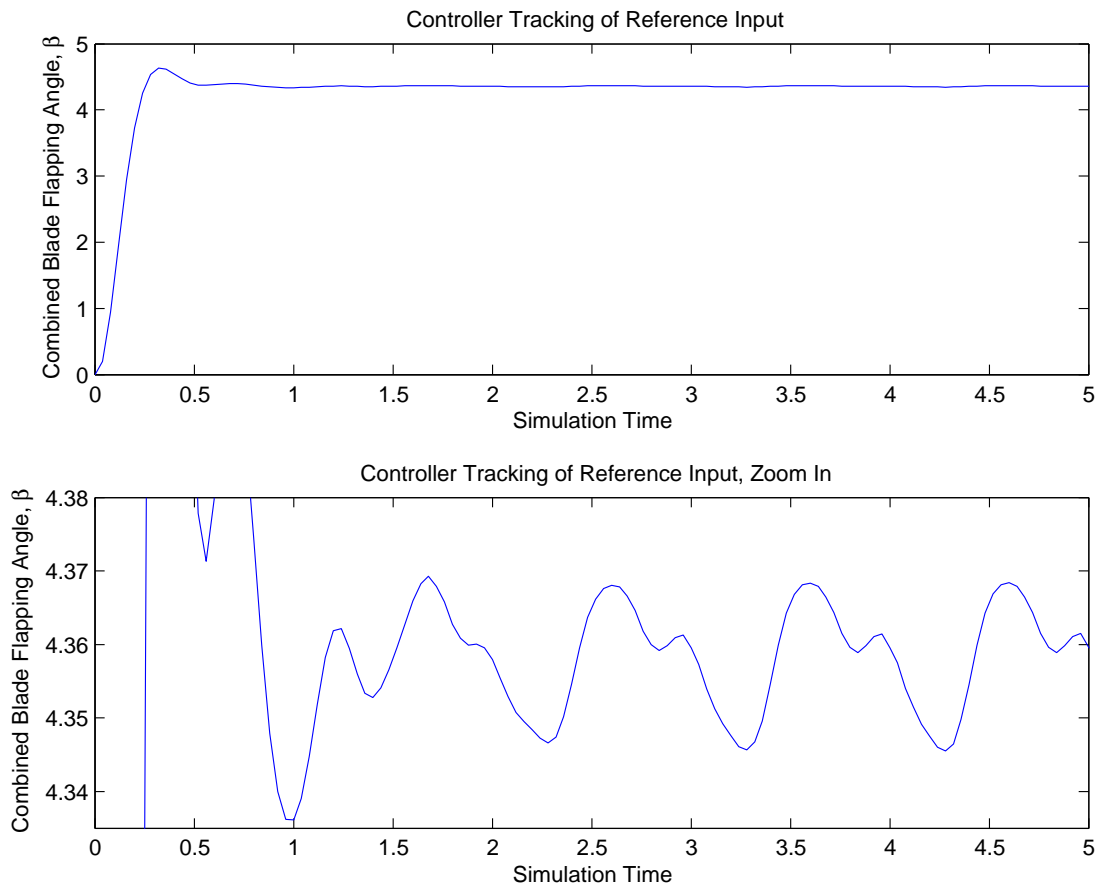


Figure C.24: Tracking Performance of Vibration Controller for case  $\omega_f = 0.05\omega_p$ ,  $S_v = 1$

Case 7	
Controller Design Parameters	
Input Frequency, $\omega_f$	Noise spectral density, $S_v$
$\omega_f = .0\omega_p$	$S_v = 1$

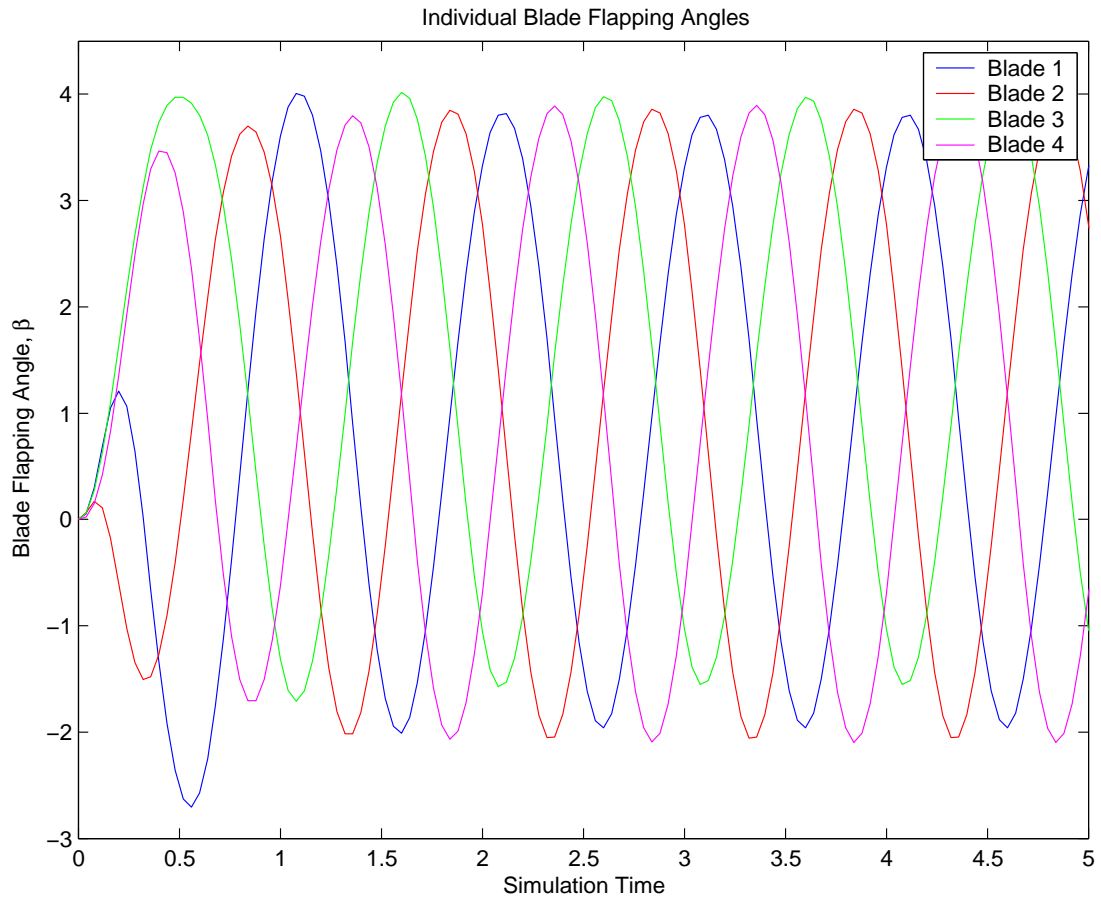


Figure C.25: Individual Flap Angles,  $\beta$ , for case  $\omega_f = 0.0\omega_p$ ,  $S_v = 1$

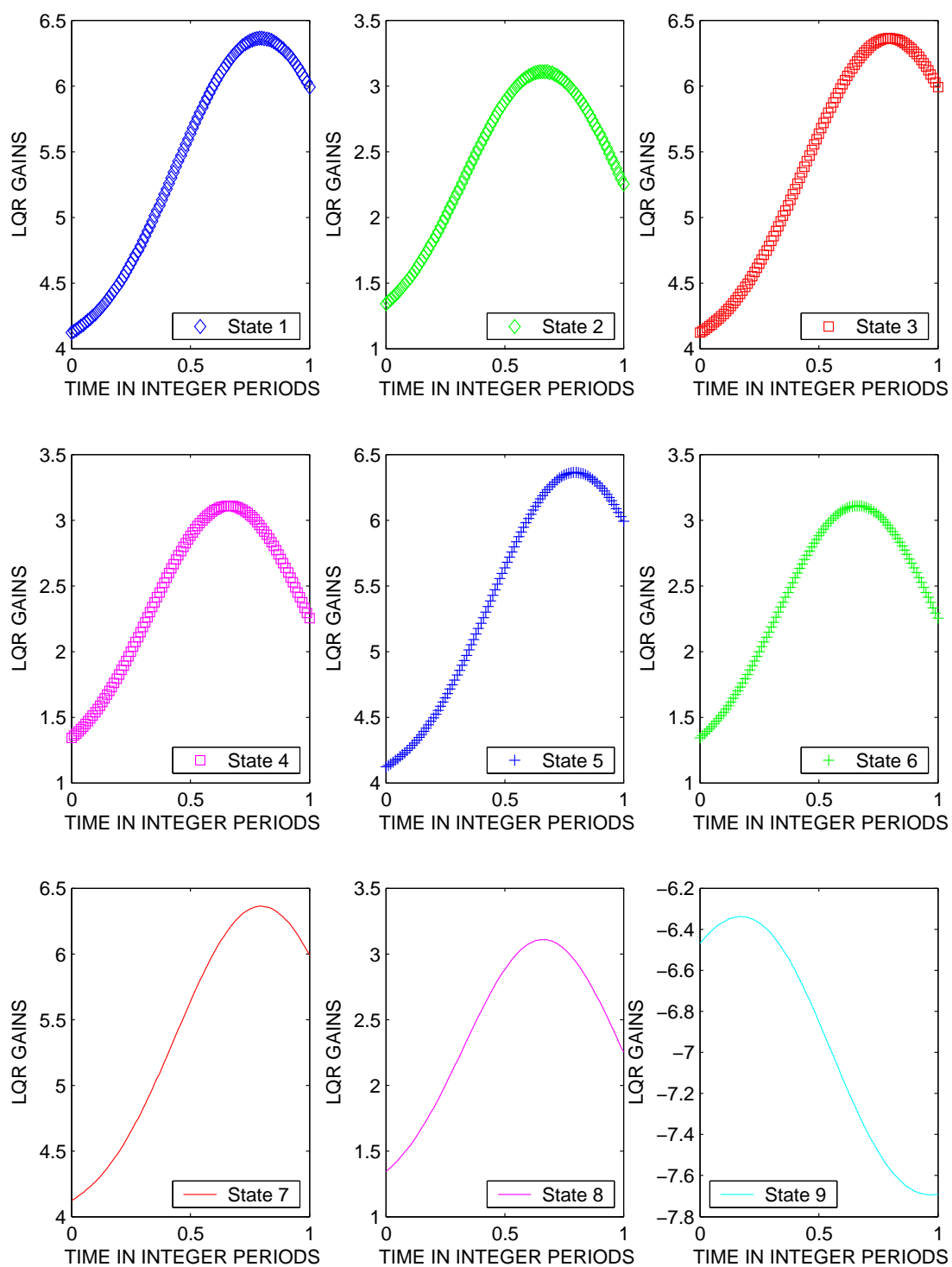


Figure C.26: All LQR Gains for case  $\omega_f = 0.0\omega_p$ ,  $S_v = 1$

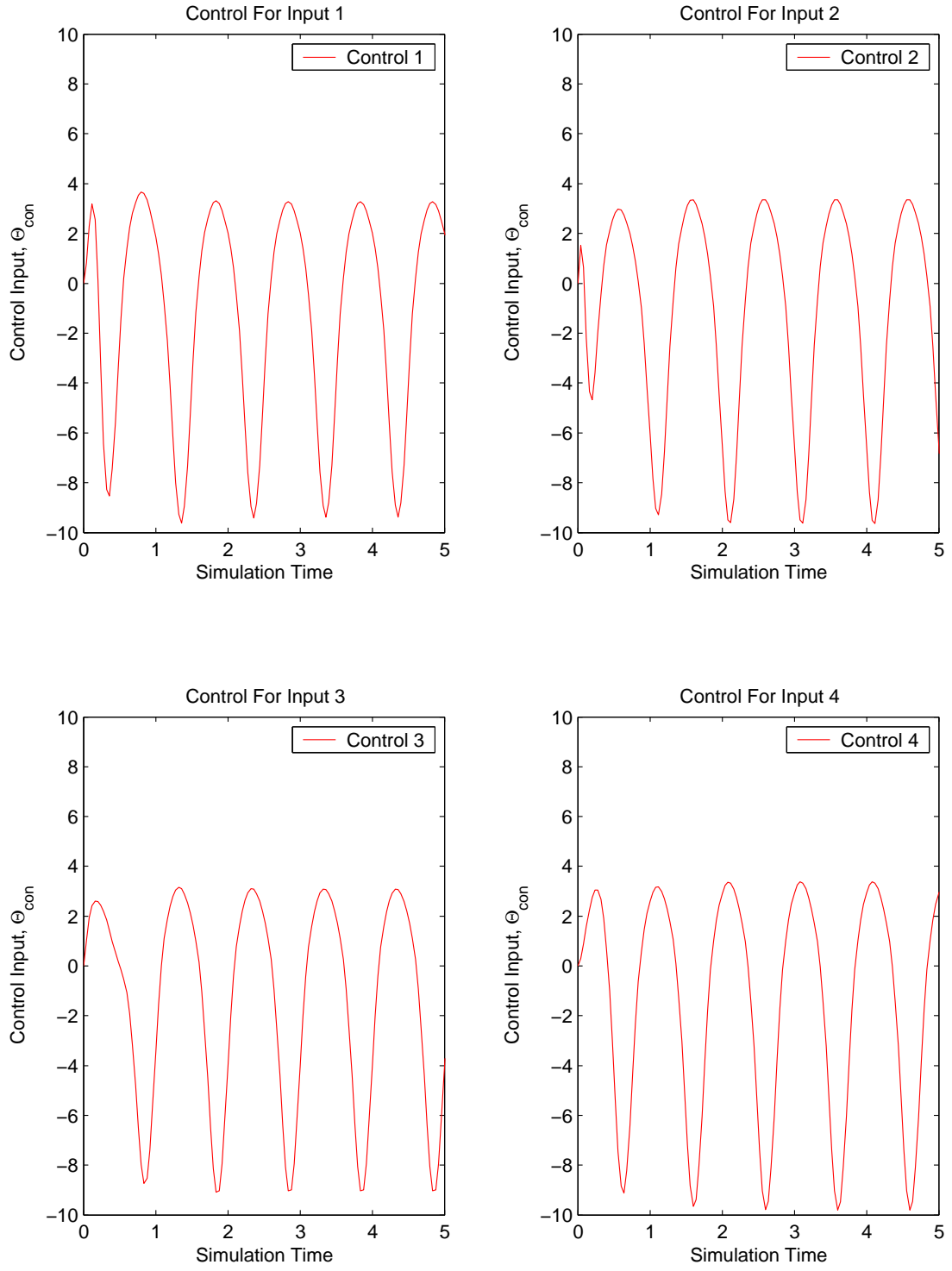


Figure C.27: Control Usage for case  $\omega_f = 0.0\omega_p$ ,  $S_v = 1$

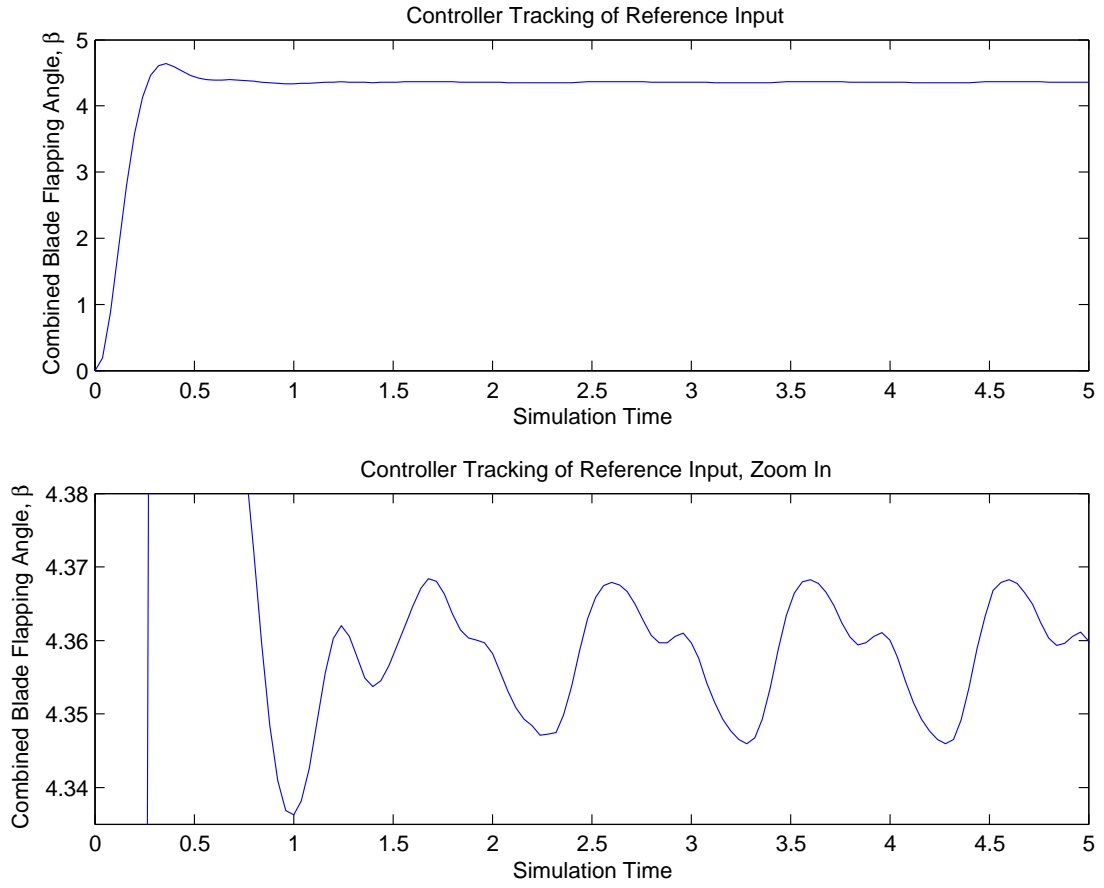


Figure C.28: Tracking Performance of Vibration Controller for case  $\omega_f = 0.0\omega_p$ ,  $S_v = 1$

#### *Appendix D. Vibration Controller Comparison Plots, Noise Case*

$$S_v = 2$$

This appendix contains the plots of the individual flap angles, calculated LQR gains, control usage, and vibration controller performance as computed at specific cases of input frequency  $\omega_f$  and noise spectral density  $S_v$ . For the cases presented in this appendix, the range of values of input and measurement noise are  $\omega_f = \omega_p(0, 0.05, 0.1, 0.2, 0.3, 0.4, 0.5)$  and  $S_v = 2$  are used, which results in 7 individual cases. Each case will present four plots; one representing the individual flap angles of each blade after control is applied to eliminate the asymmetric lift, one for calculated LQR gains, one for control usage,  $\Theta_{con}$  for each blade, and one depicting the vibration controller performance in terms of matching the reference input.

Case 1	
Controller Design Parameters	
Input Frequency, $\omega_f$	Noise spectral density, $S_v$
$\omega_f = 0.5\omega_p$	$S_v = 2$

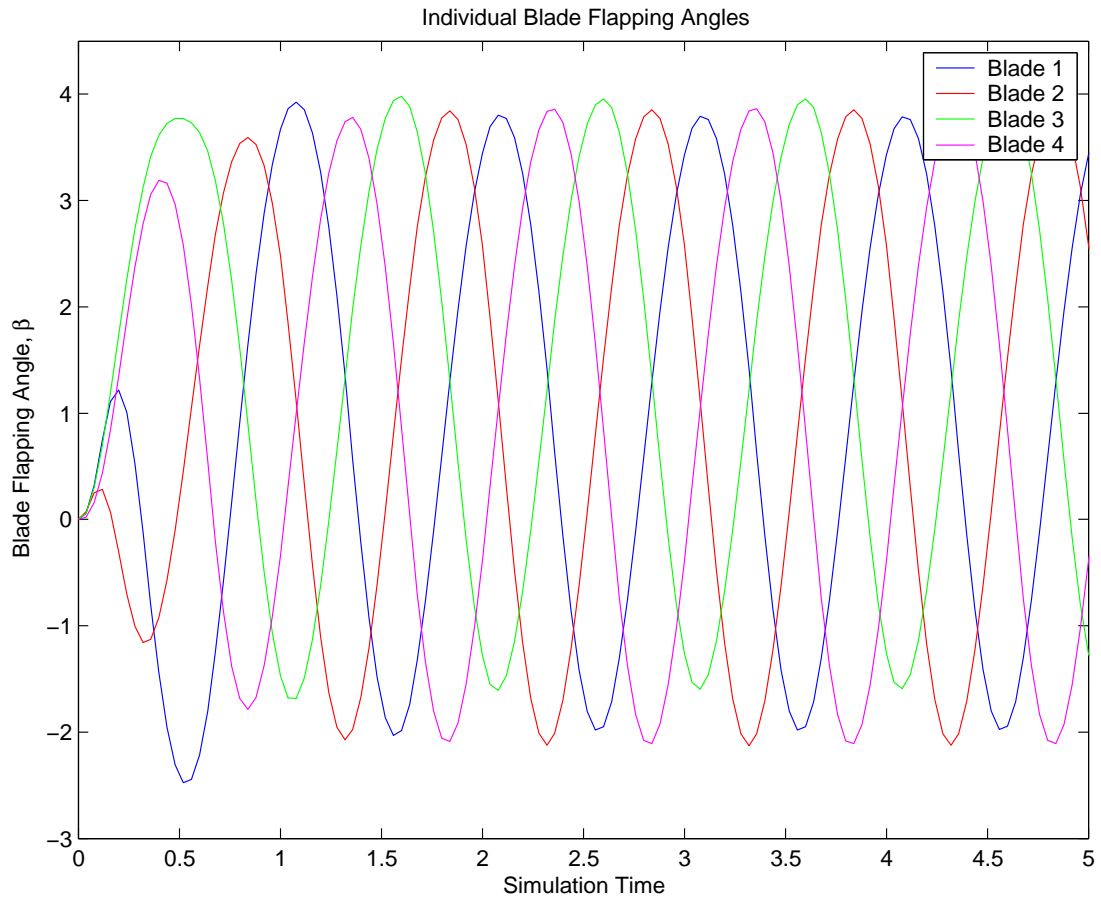


Figure D.1: Individual Flap Angles,  $\beta$ , for case  $\omega_f = 0.5\omega_p$ ,  $S_v = 2$

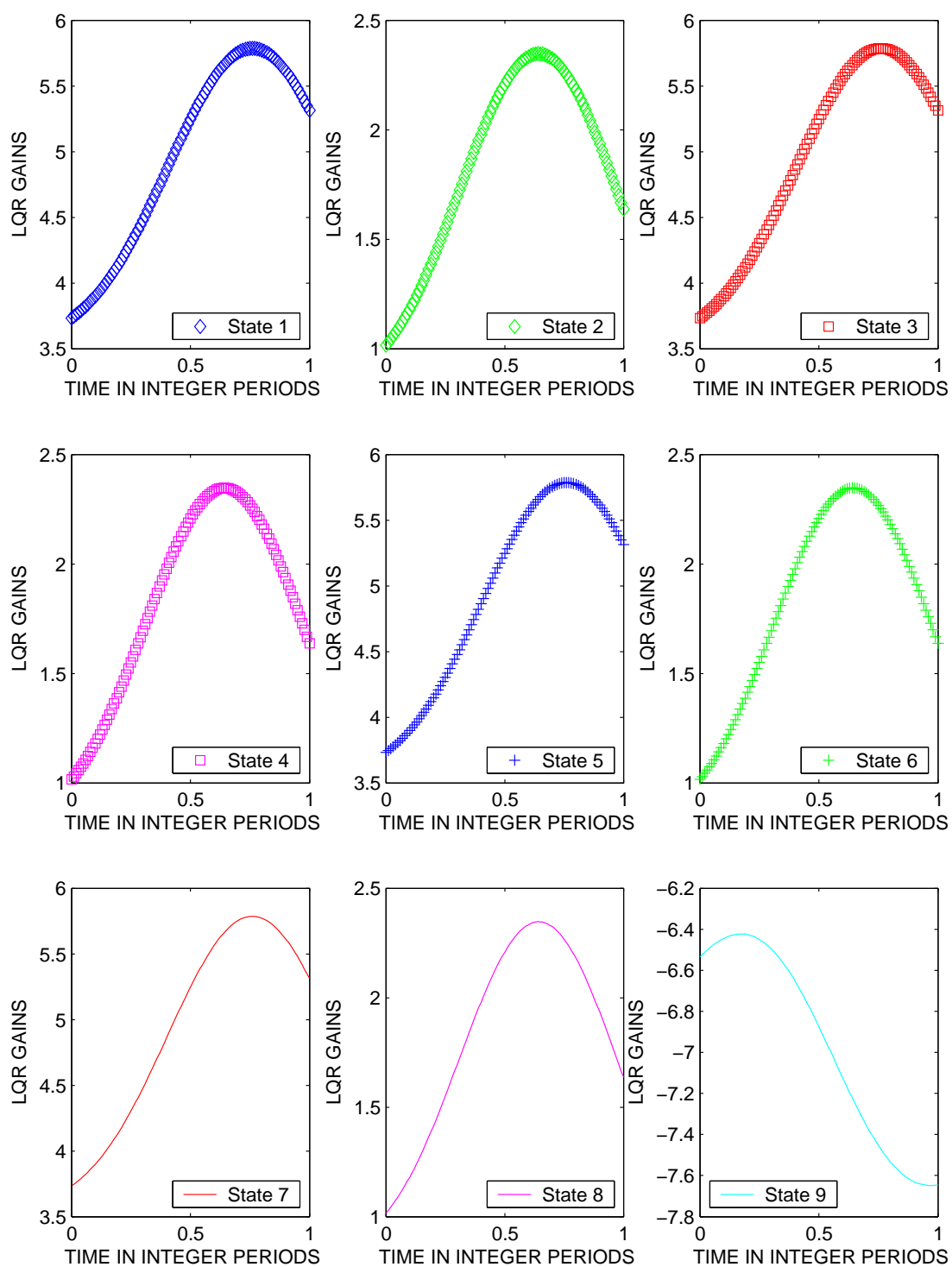


Figure D.2: All LQR Gains for case  $\omega_f = 0.5\omega_p$ ,  $S_v = 2$

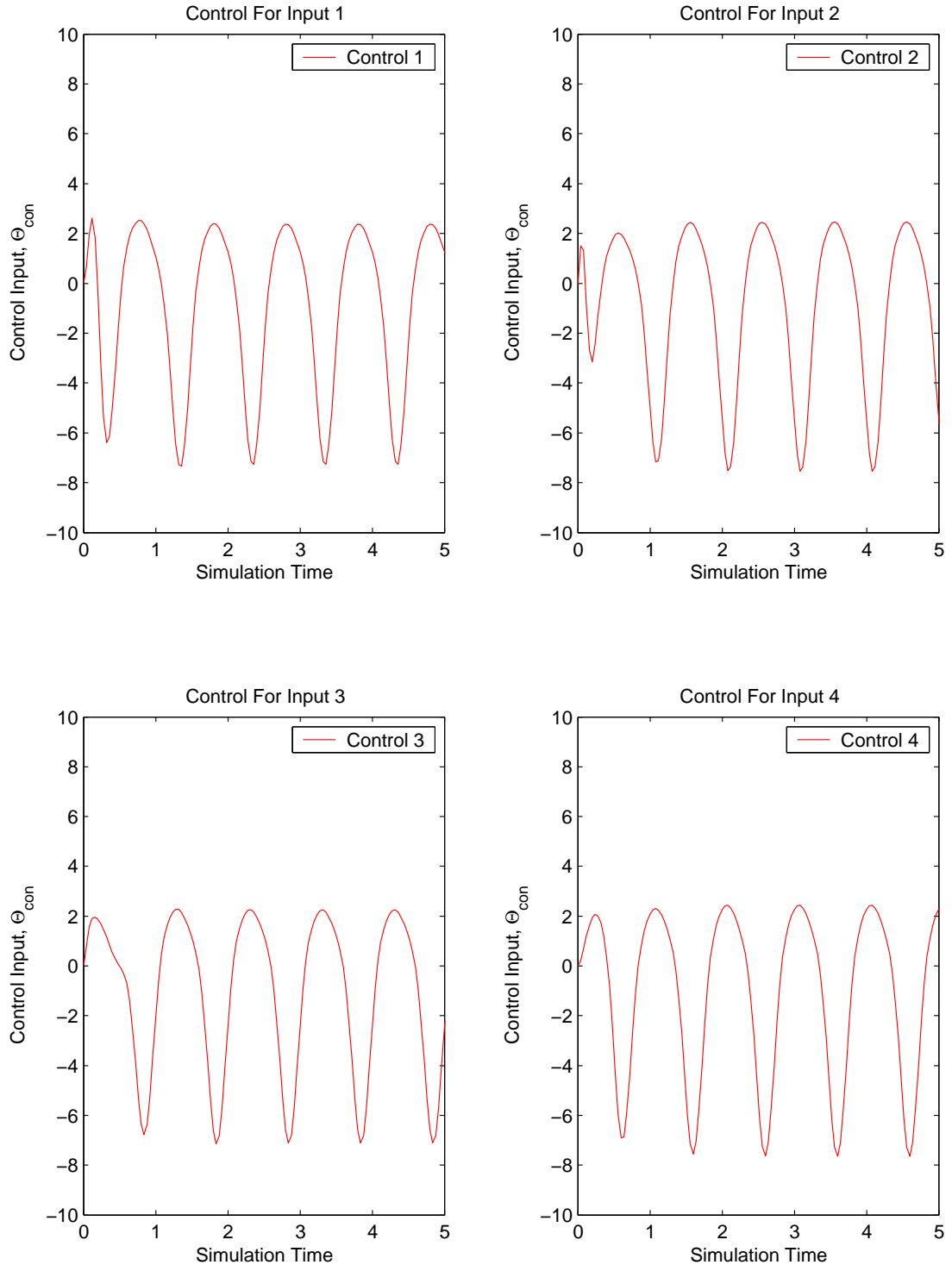


Figure D.3: Control Usage for case  $\omega_f = 0.5\omega_p$ ,  $S_v = 2$

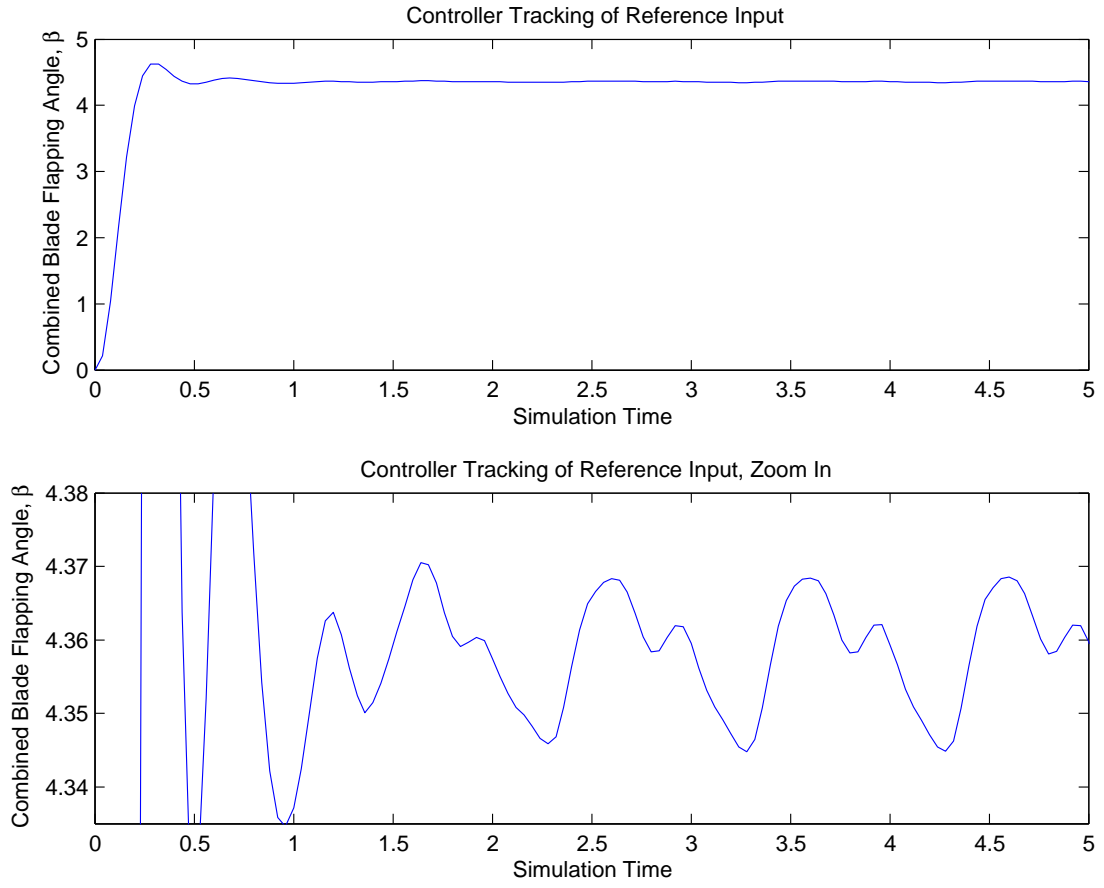


Figure D.4: Tracking Performance of Vibration Controller for case  $\omega_f = 0.5\omega_p$ ,  $S_v = 2$

Case 2	
Controller Design Parameters	
Input Frequency, $\omega_f$	Noise spectral density, $S_v$
$\omega_f = .4\omega_p$	$S_v = 2$

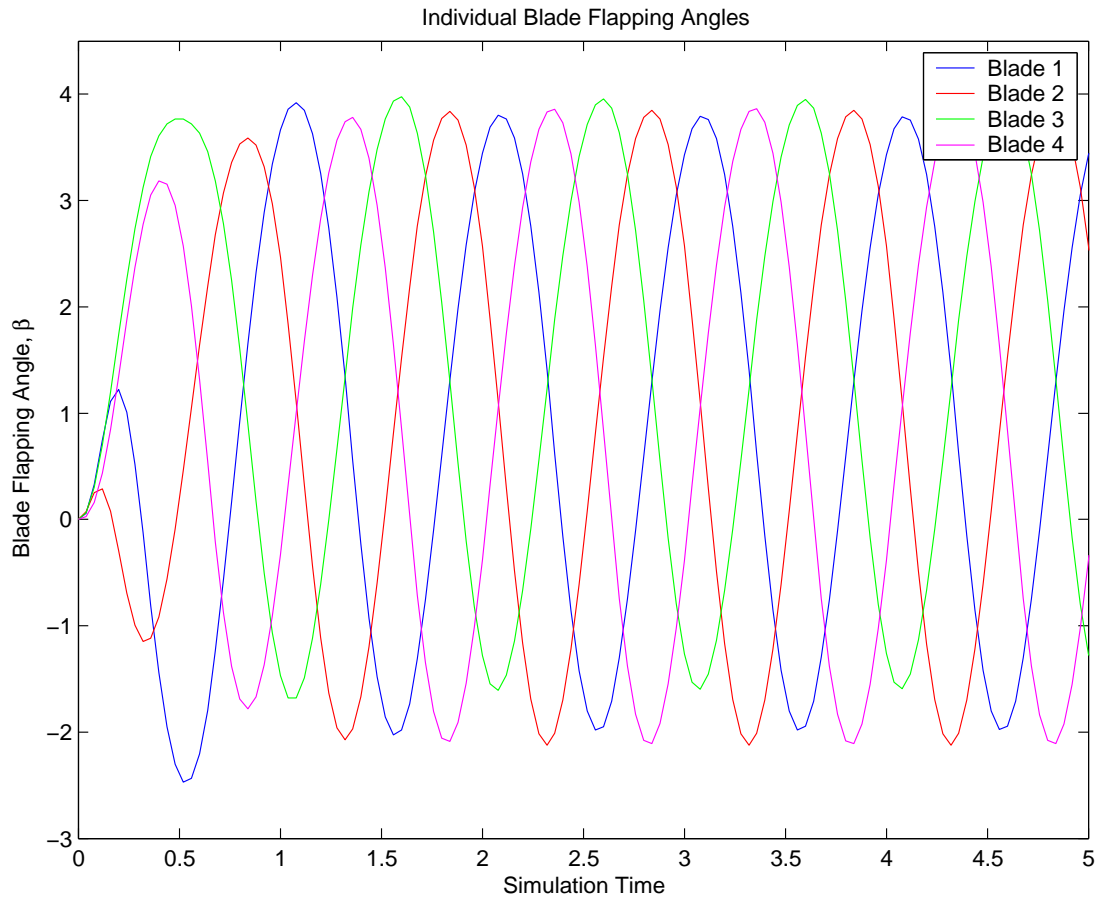


Figure D.5: Individual Flap Angles,  $\beta$ , for case  $\omega_f = 0.4\omega_p$ ,  $S_v = 2$

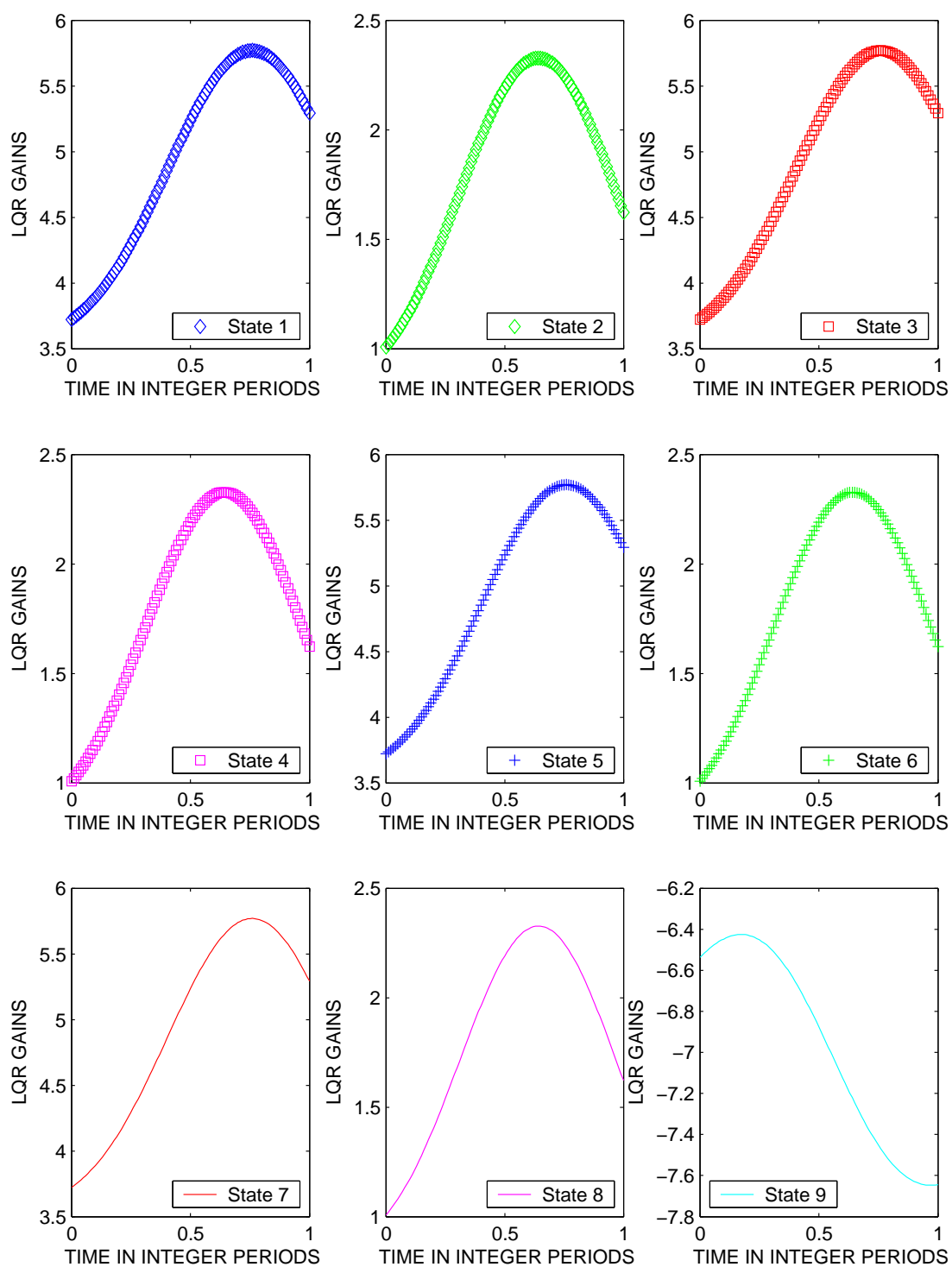


Figure D.6: All LQR Gains for case  $\omega_f = 0.4\omega_p$ ,  $S_v = 2$

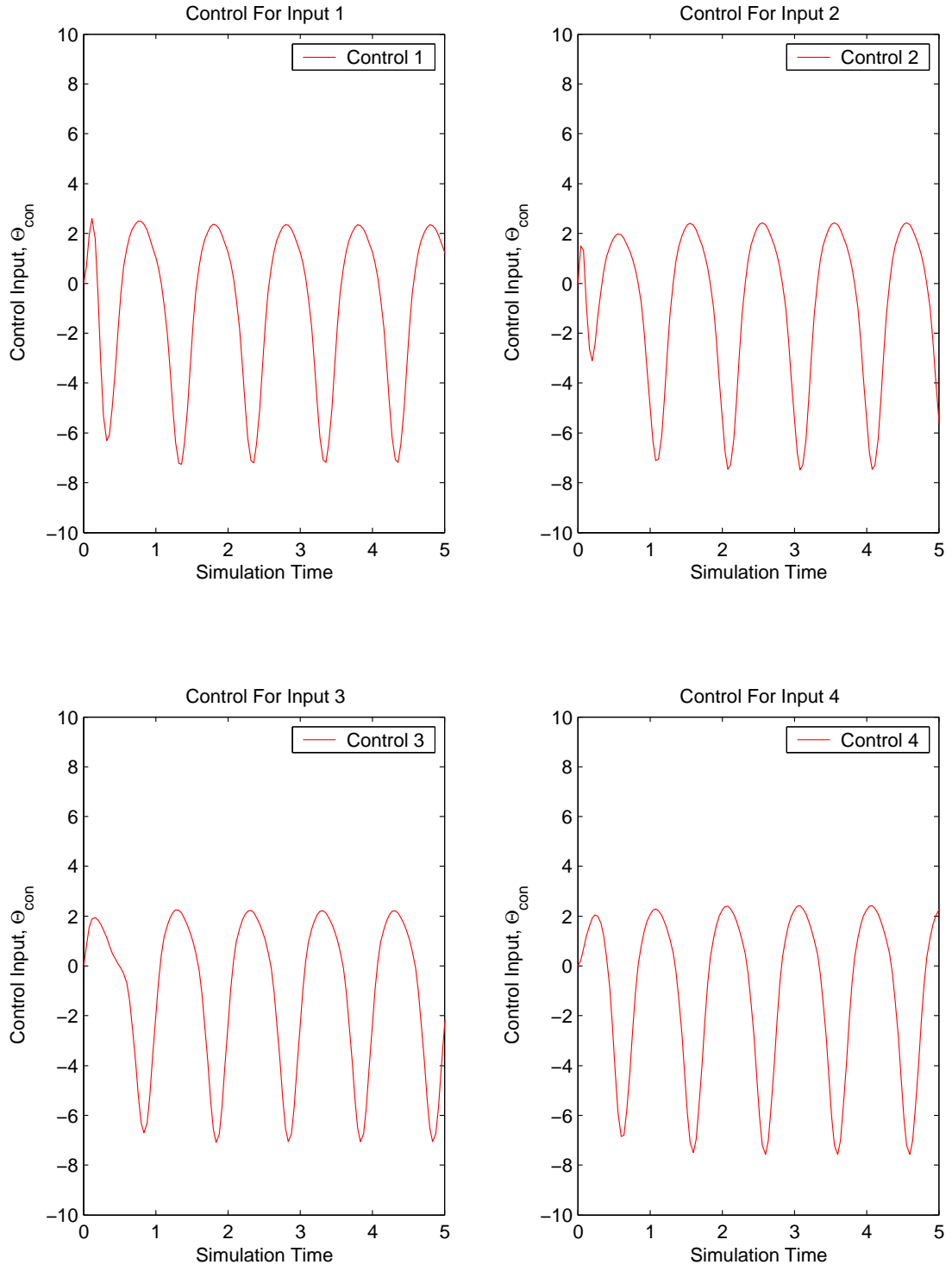


Figure D.7: Control Usage for case  $\omega_f = 0.4\omega_p$ ,  $S_v = 2$

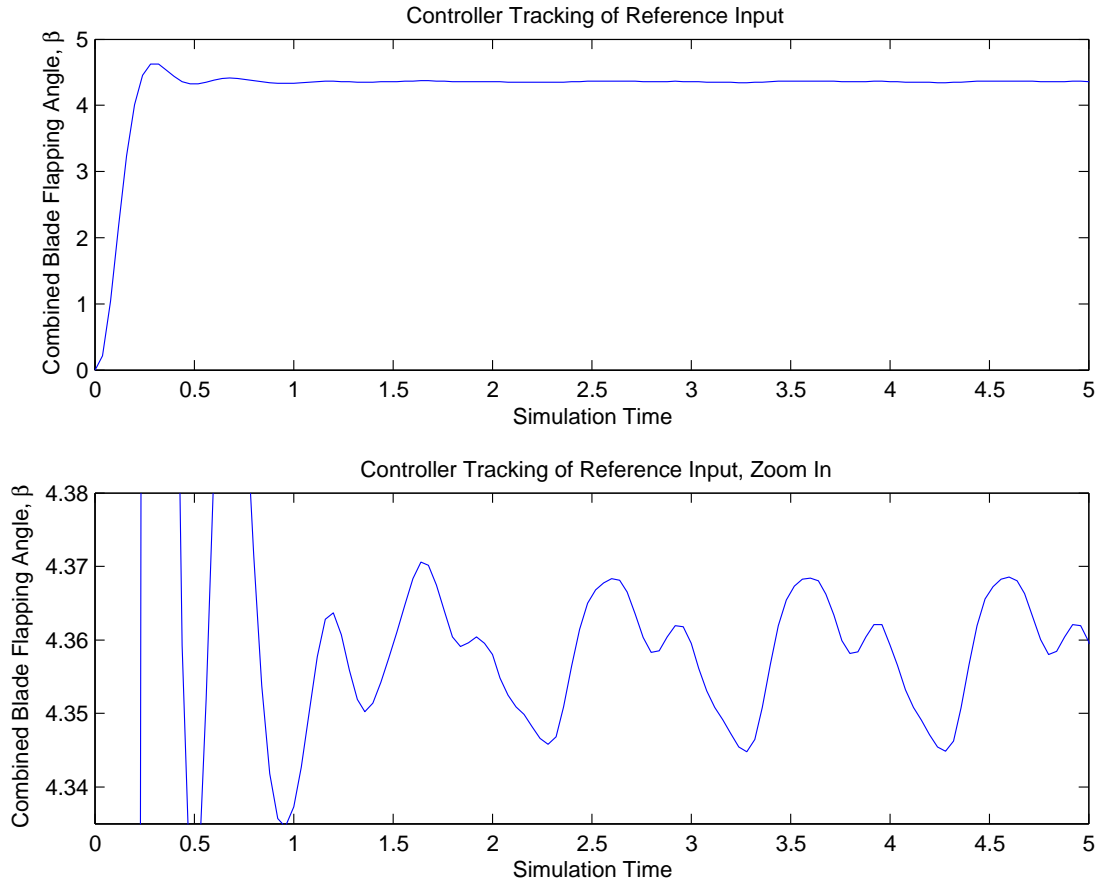


Figure D.8: Tracking Performance of Vibration Controller for case  $\omega_f = 0.4\omega_p$ ,  $S_v = 2$

Case 3	
Controller Design Parameters	
Input Frequency, $\omega_f$	Noise spectral density, $S_v$
$\omega_f = .3\omega_p$	$S_v = 2$

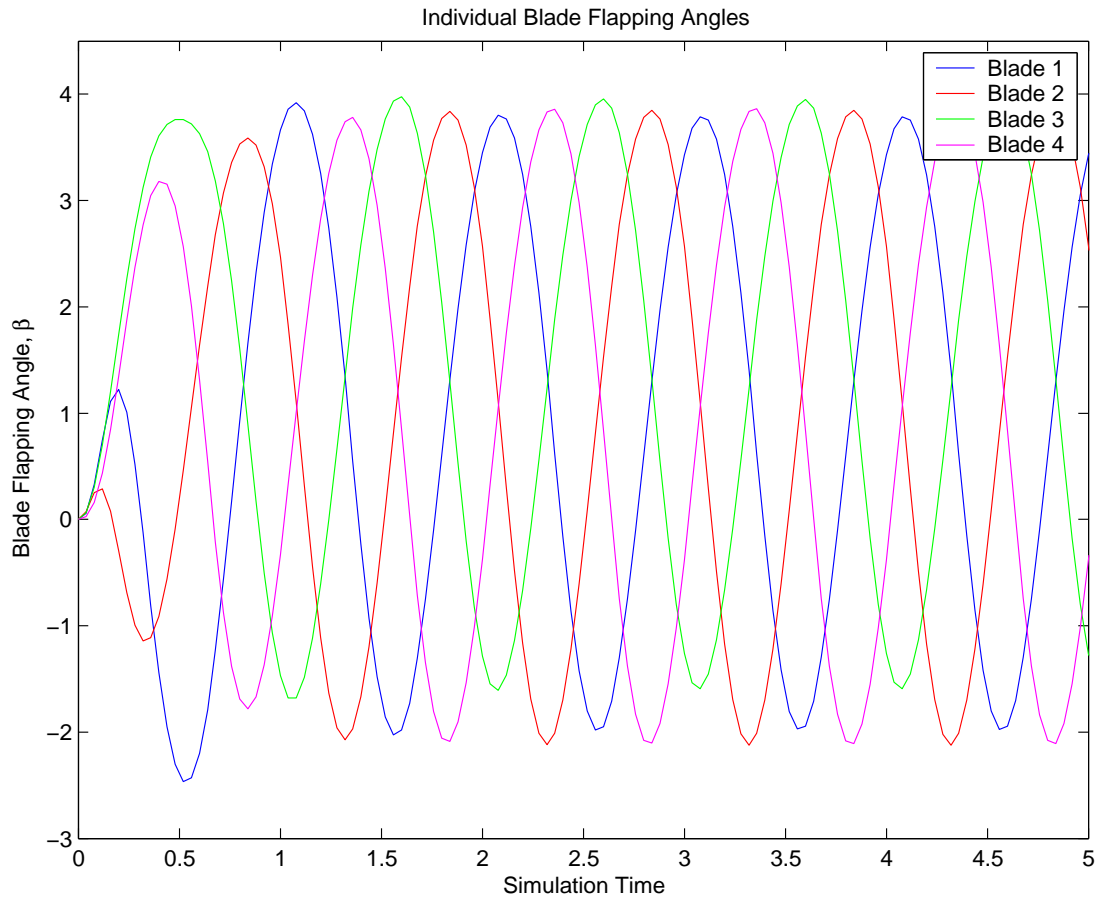


Figure D.9: Individual Flap Angles,  $\beta$ , for case  $\omega_f = 0.3\omega_p$ ,  $S_v = 2$

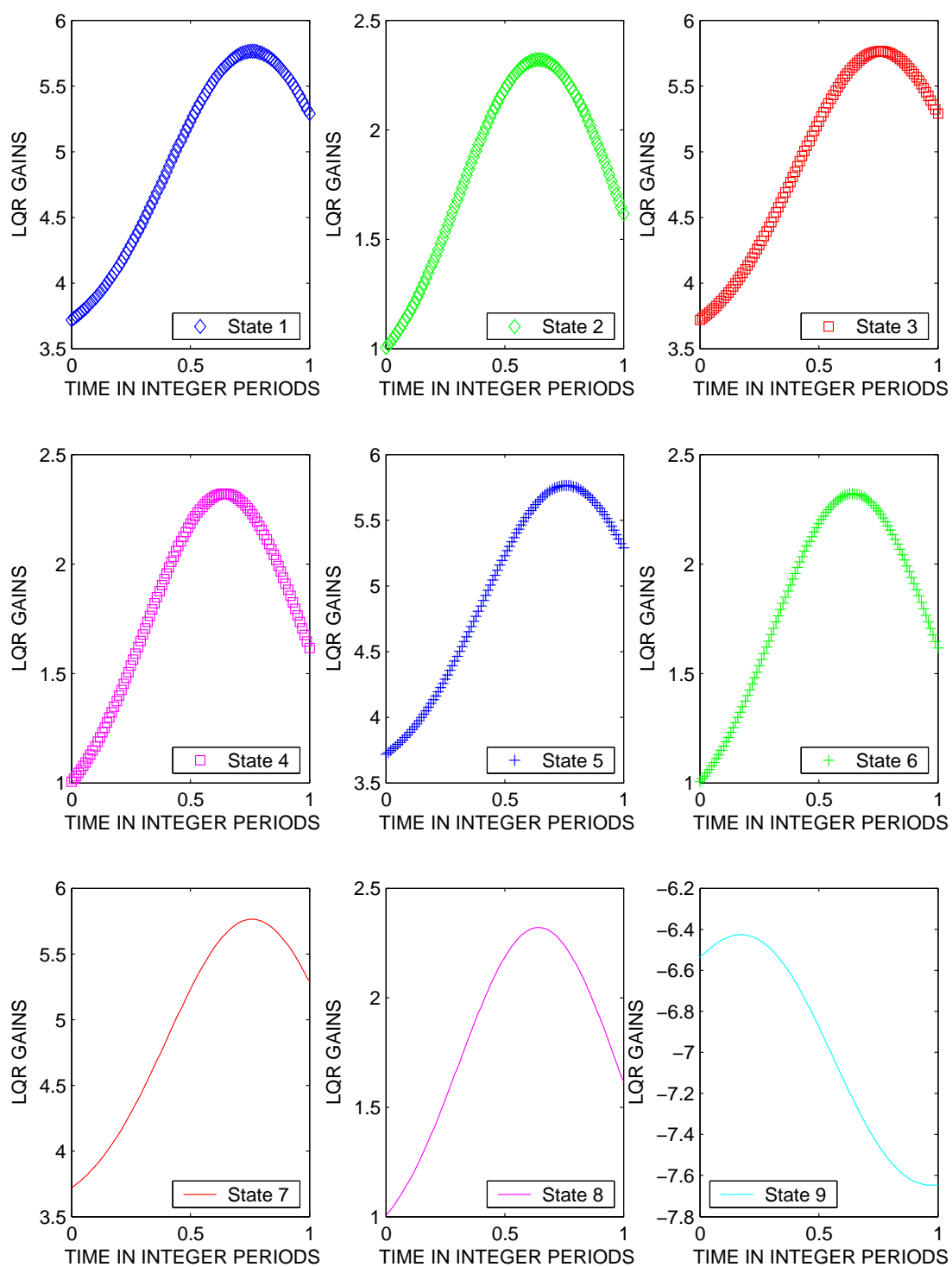


Figure D.10: All LQR Gains for case  $\omega_f = 0.3\omega_p$ ,  $S_v = 2$

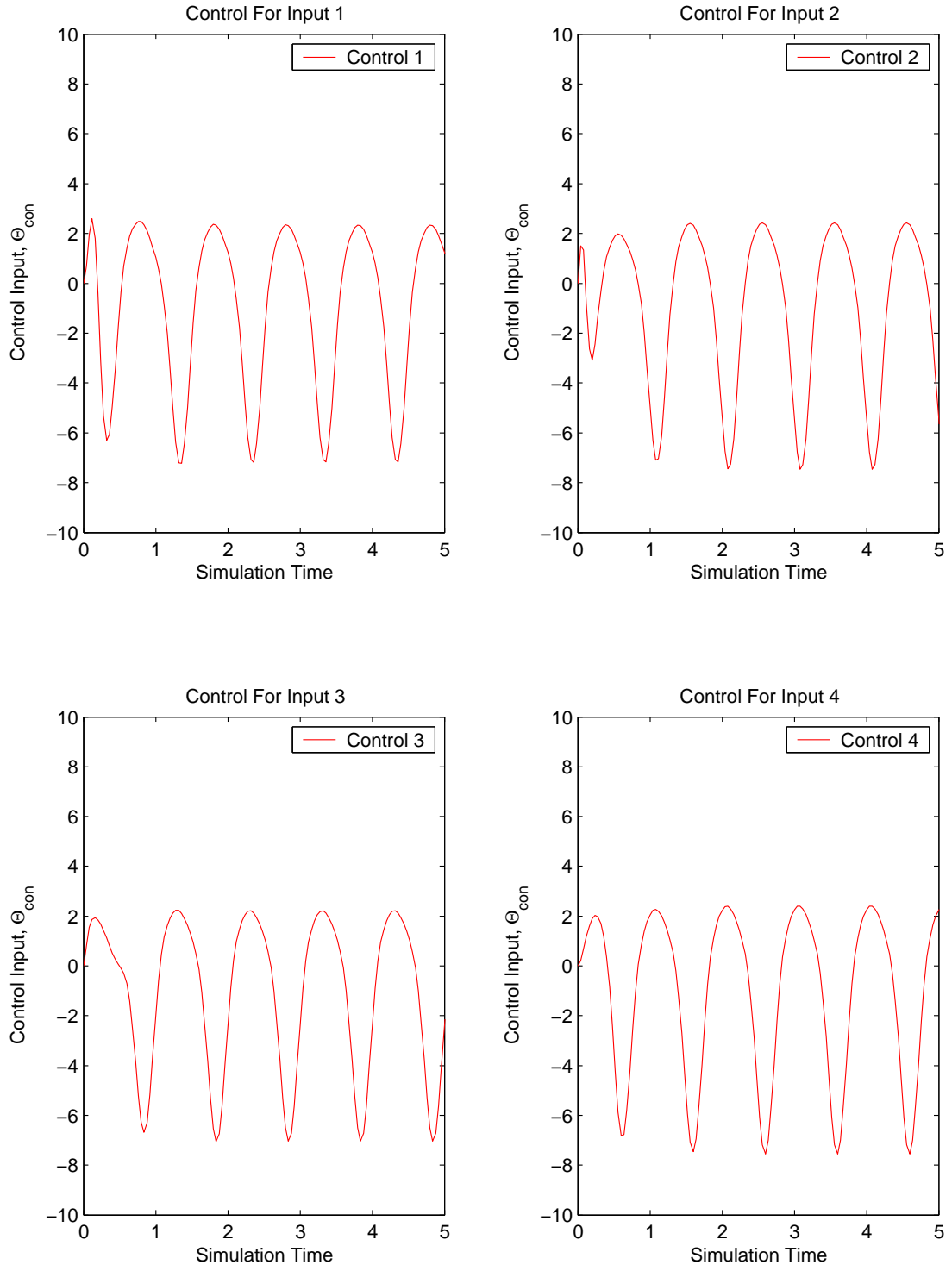


Figure D.11: Control Usage for case  $\omega_f = 0.3\omega_p$ ,  $S_v = 2$

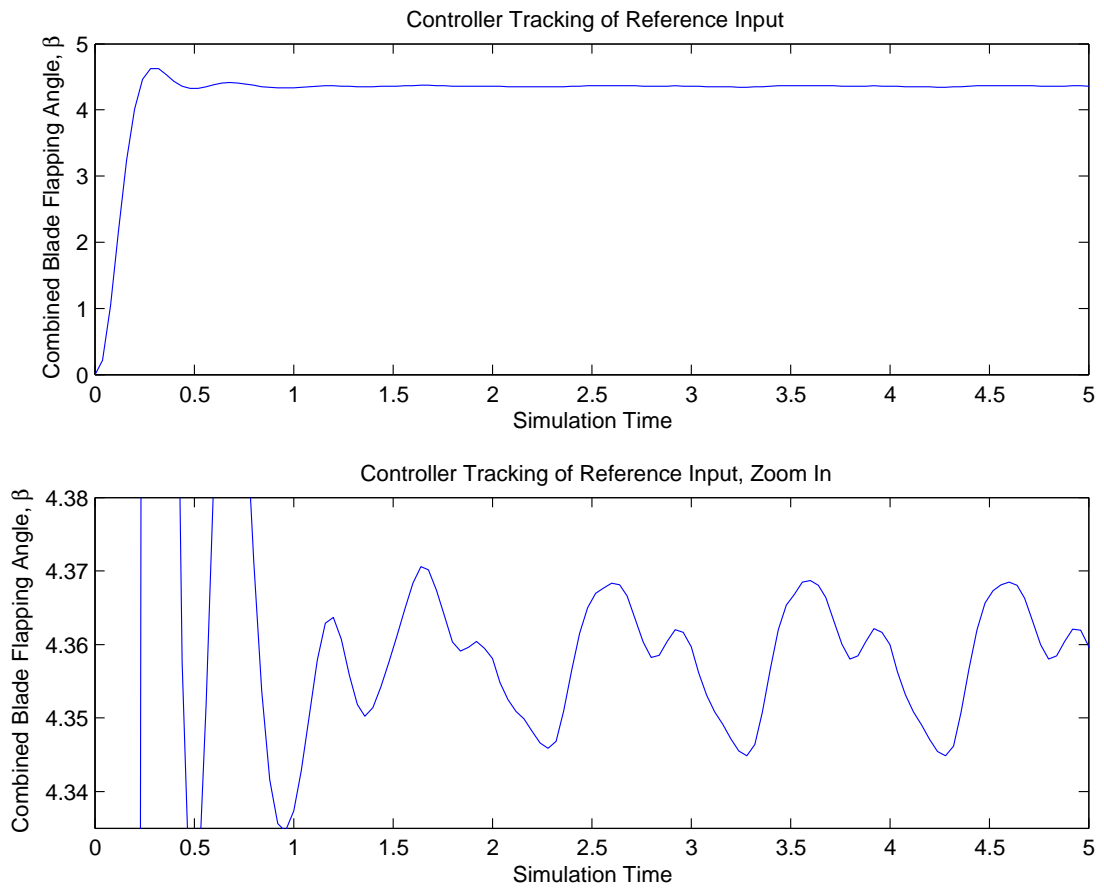


Figure D.12: Tracking Performance of Vibration Controller for case  $\omega_f = 0.3\omega_p$ ,  $S_v = 2$

Case 4	
Controller Design Parameters	
Input Frequency, $\omega_f$	Noise spectral density, $S_v$
$\omega_f = .2\omega_p$	$S_v = 2$

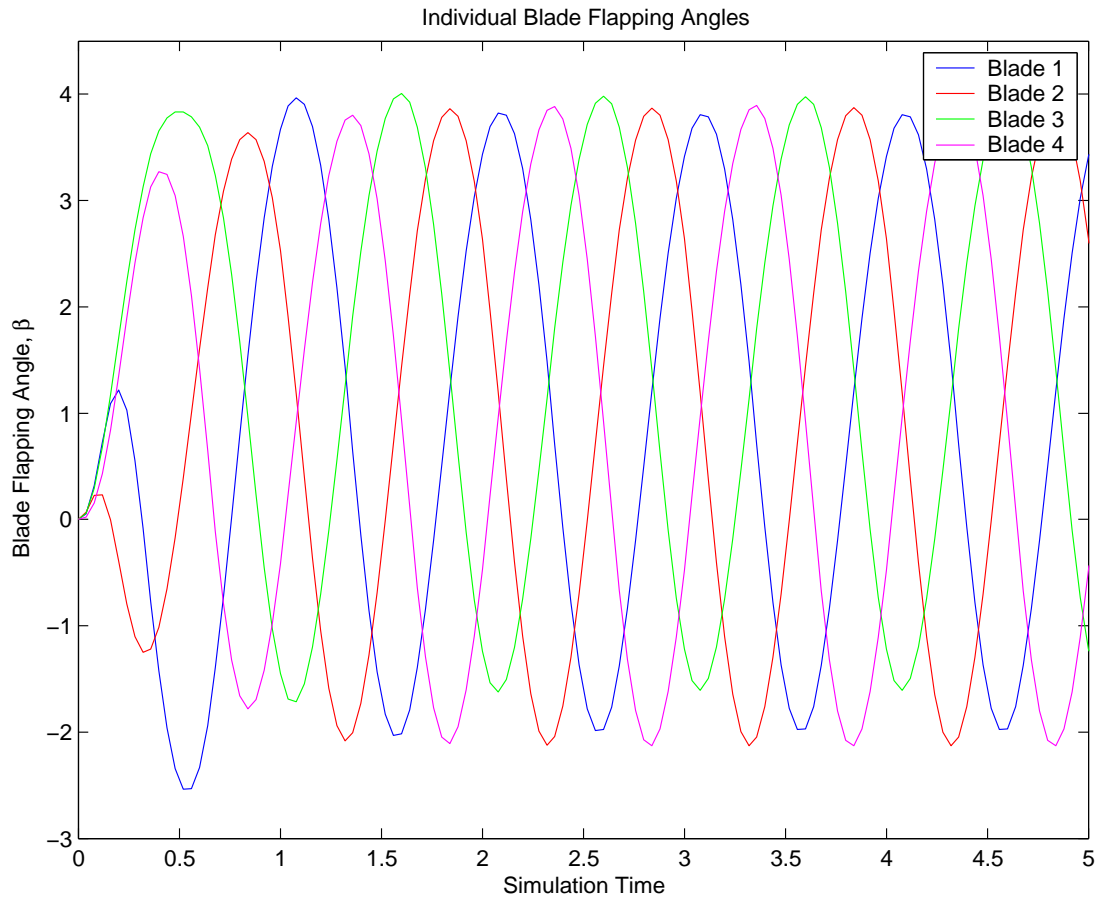


Figure D.13: Individual Flap Angles,  $\beta$ , for case  $\omega_f = 0.2\omega_p$ ,  $S_v = 2$

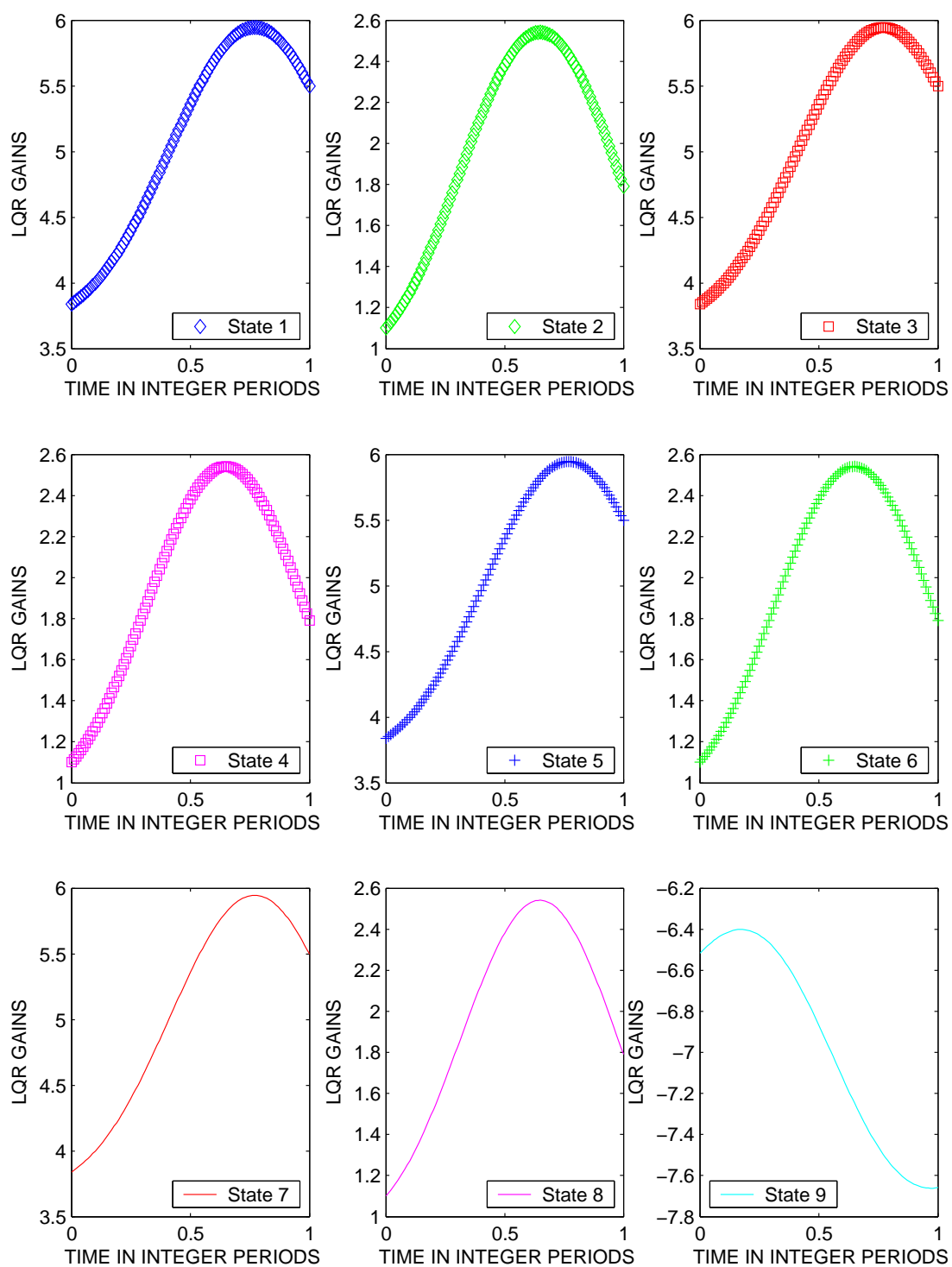


Figure D.14: All LQR Gains for case  $\omega_f = 0.2\omega_p$ ,  $S_v = 2$

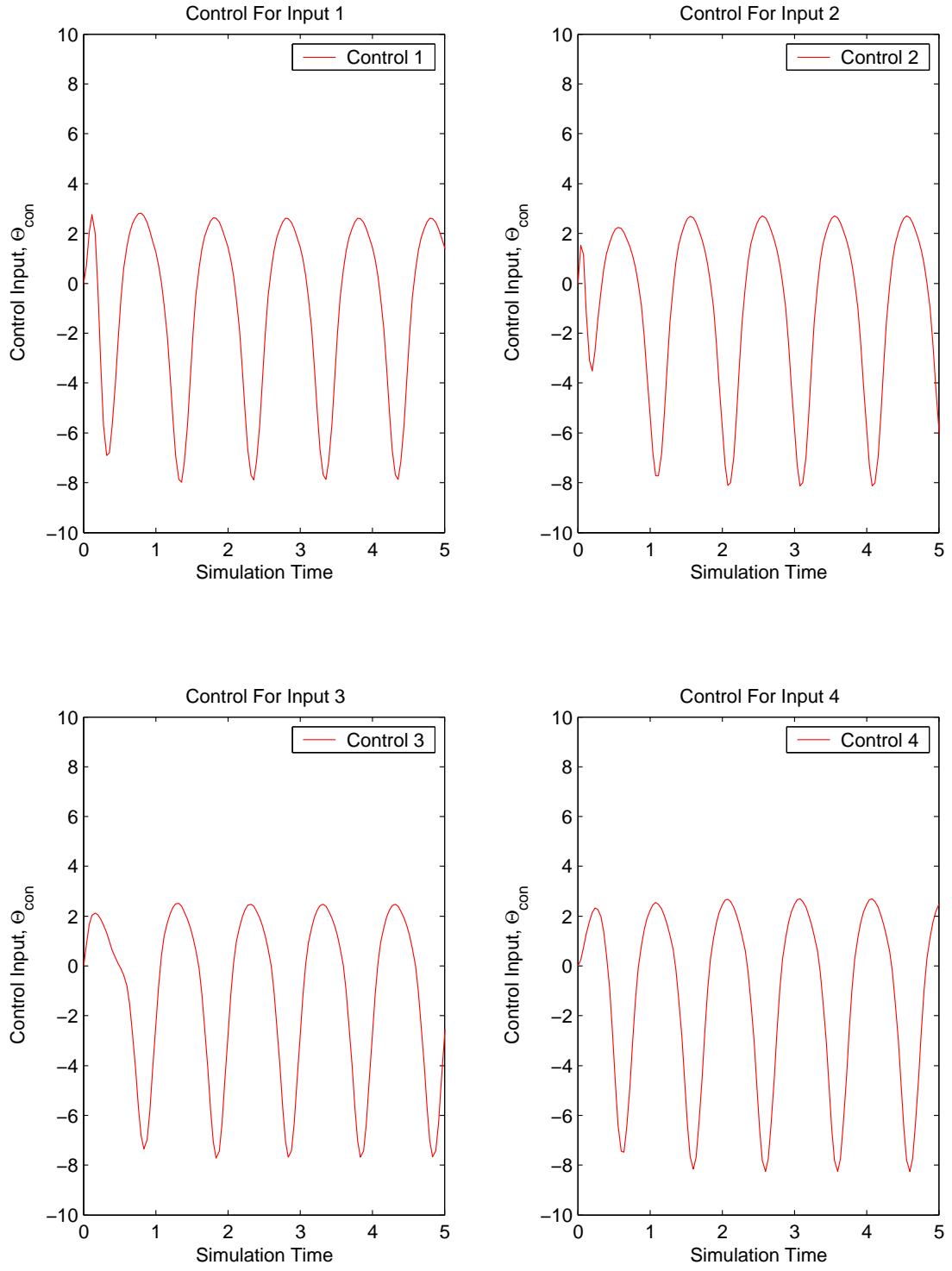


Figure D.15: Control Usage for case  $\omega_f = 0.2\omega_p$ ,  $S_v = 2$

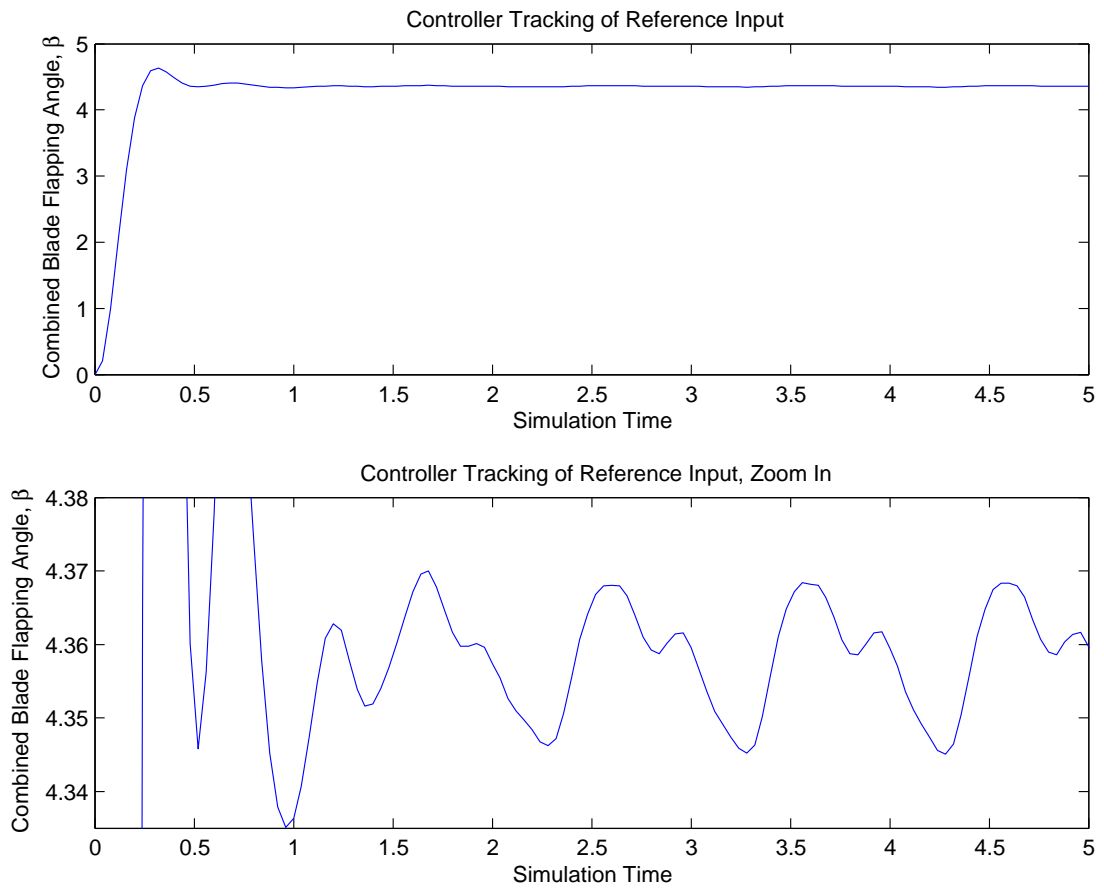


Figure D.16: Tracking Performance of Vibration Controller for case  $\omega_f = 0.2\omega_p$ ,  $S_v = 2$

Case 5	
Controller Design Parameters	
Input Frequency, $\omega_f$	Noise spectral density, $S_v$
$\omega_f = .1\omega_p$	$S_v = 2$

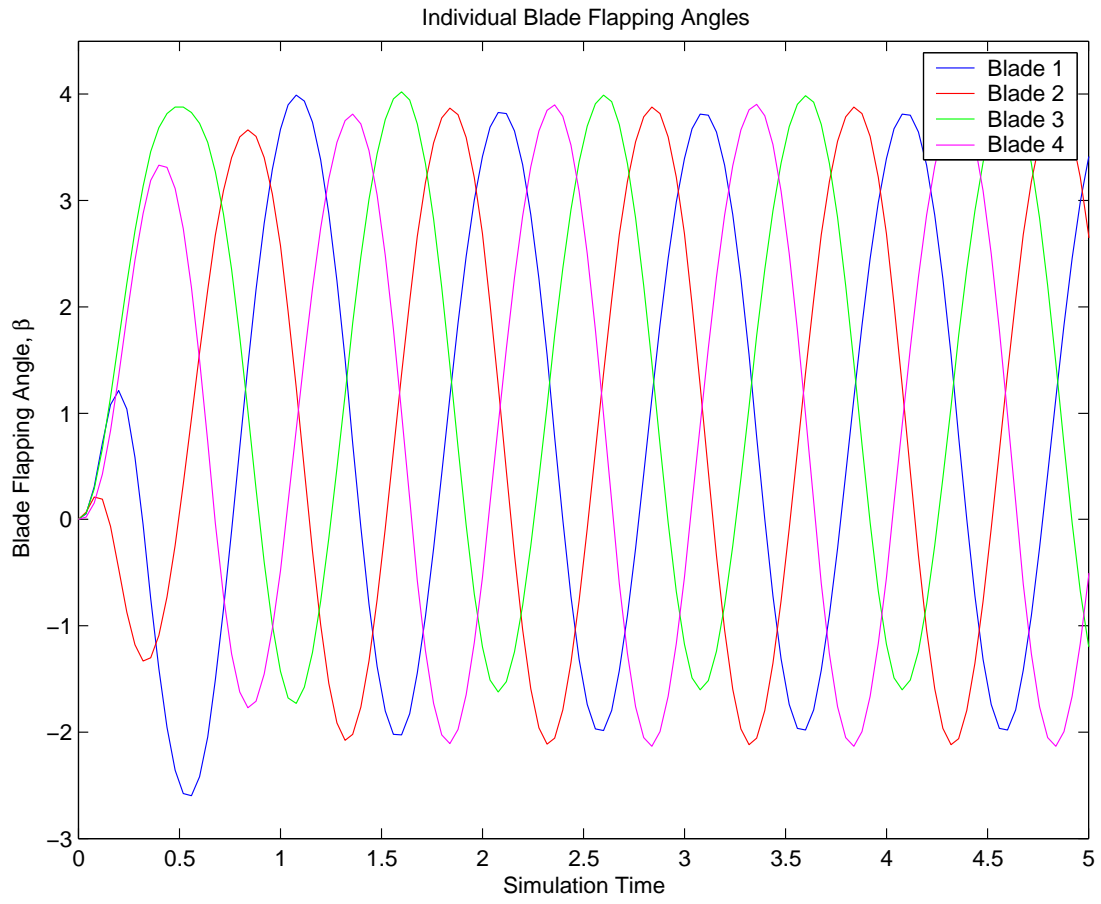


Figure D.17: Individual Flap Angles,  $\beta$ , for case  $\omega_f = 0.1\omega_p$ ,  $S_v = 2$

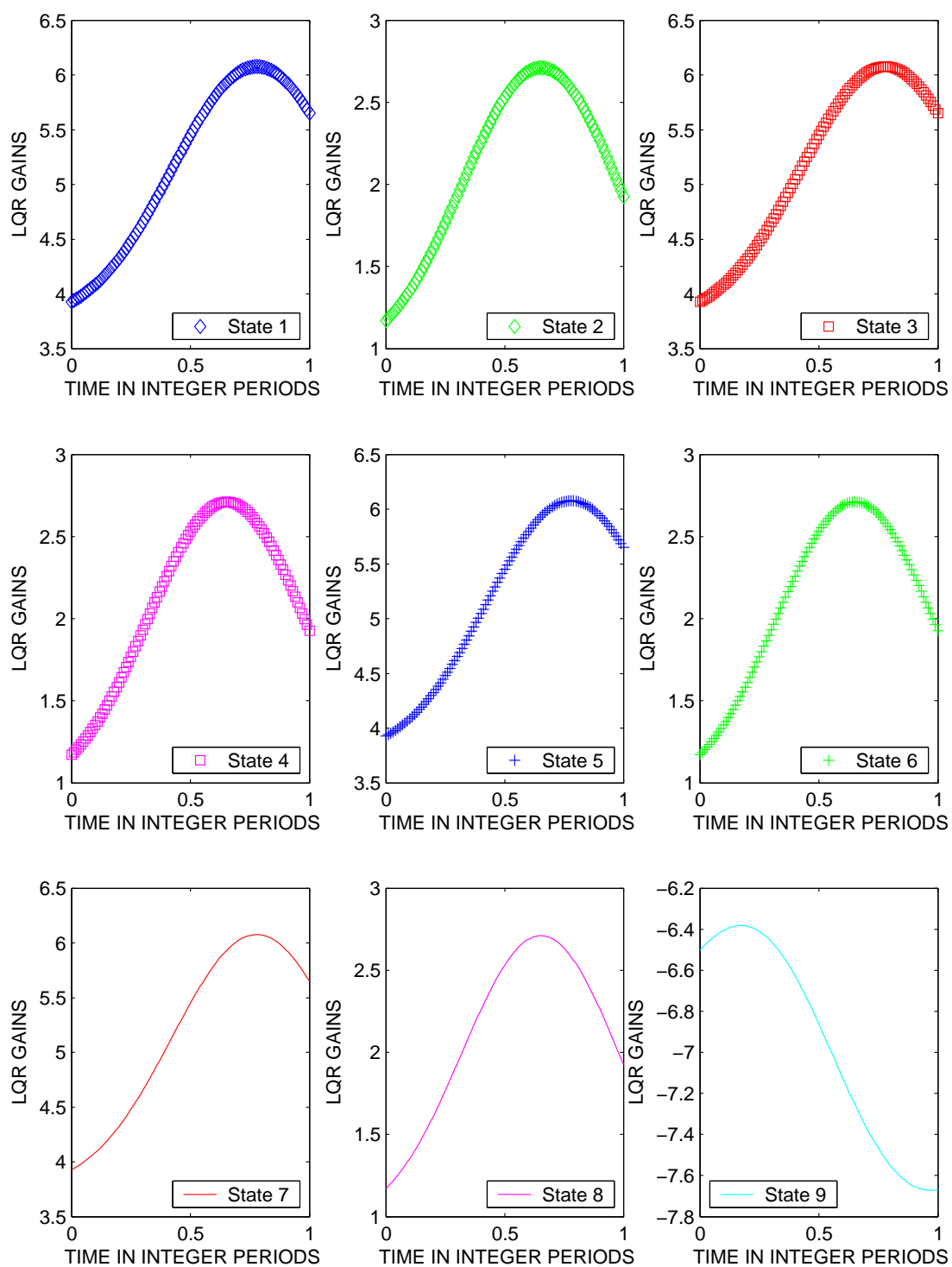


Figure D.18: All LQR Gains for case  $\omega_f = 0.1\omega_p$ ,  $S_v = 2$

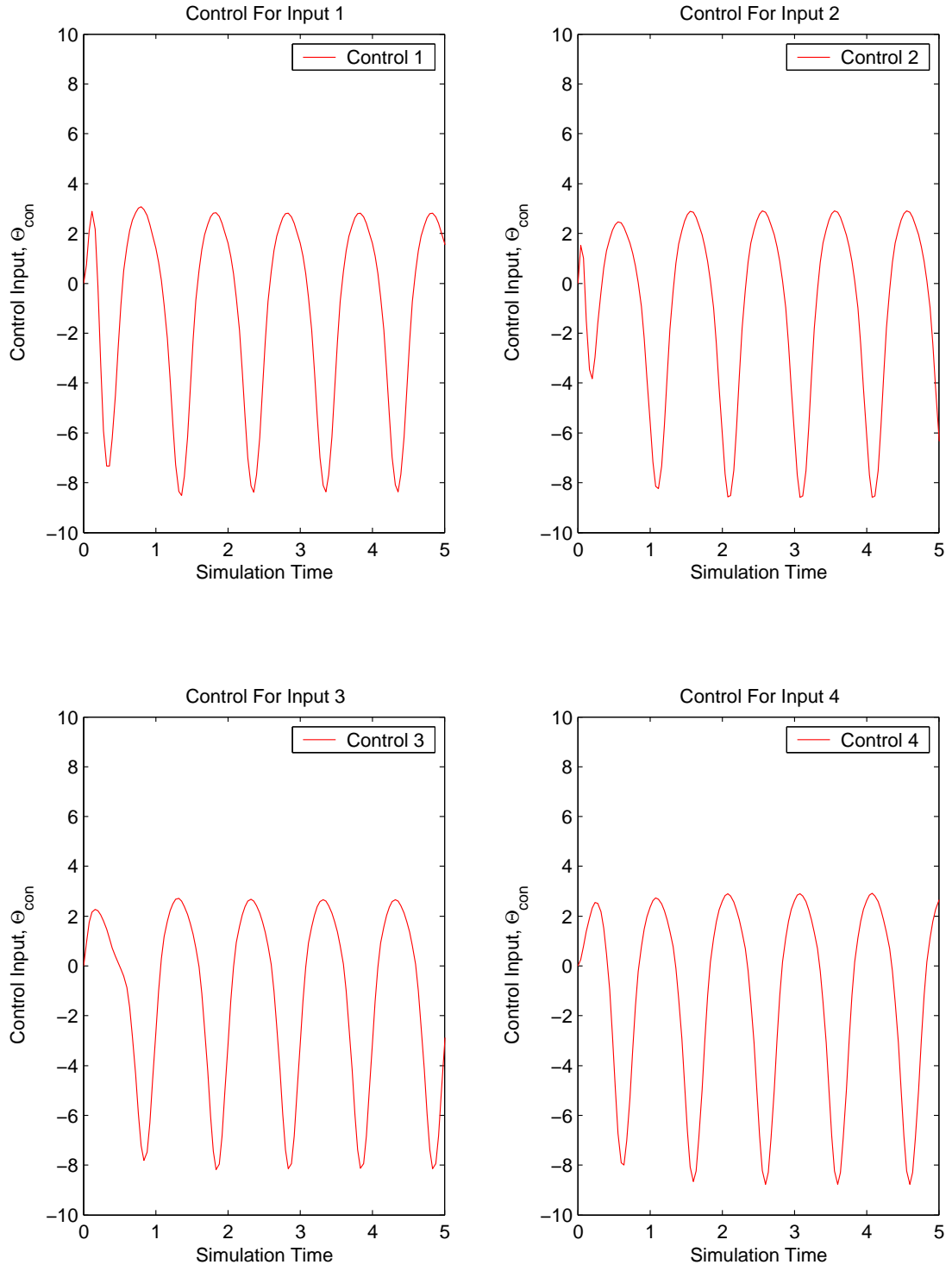


Figure D.19: Control Usage for case  $\omega_f = 0.1\omega_p$ ,  $S_v = 2$

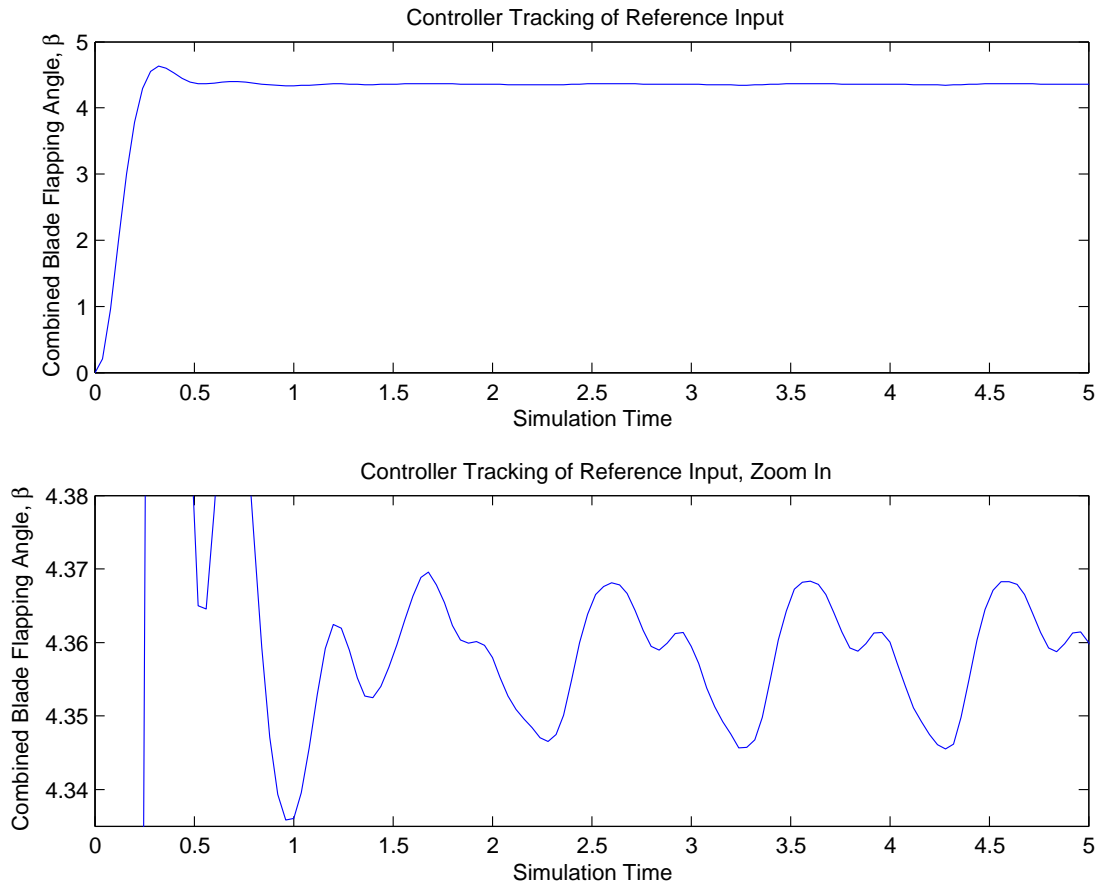


Figure D.20: Tracking Performance of Vibration Controller for case  $\omega_f = 0.1\omega_p$ ,  $S_v = 2$

Case 6	
Controller Design Parameters	
Input Frequency, $\omega_f$	Noise spectral density, $S_v$
$\omega_f = .05\omega_p$	$S_v = 2$

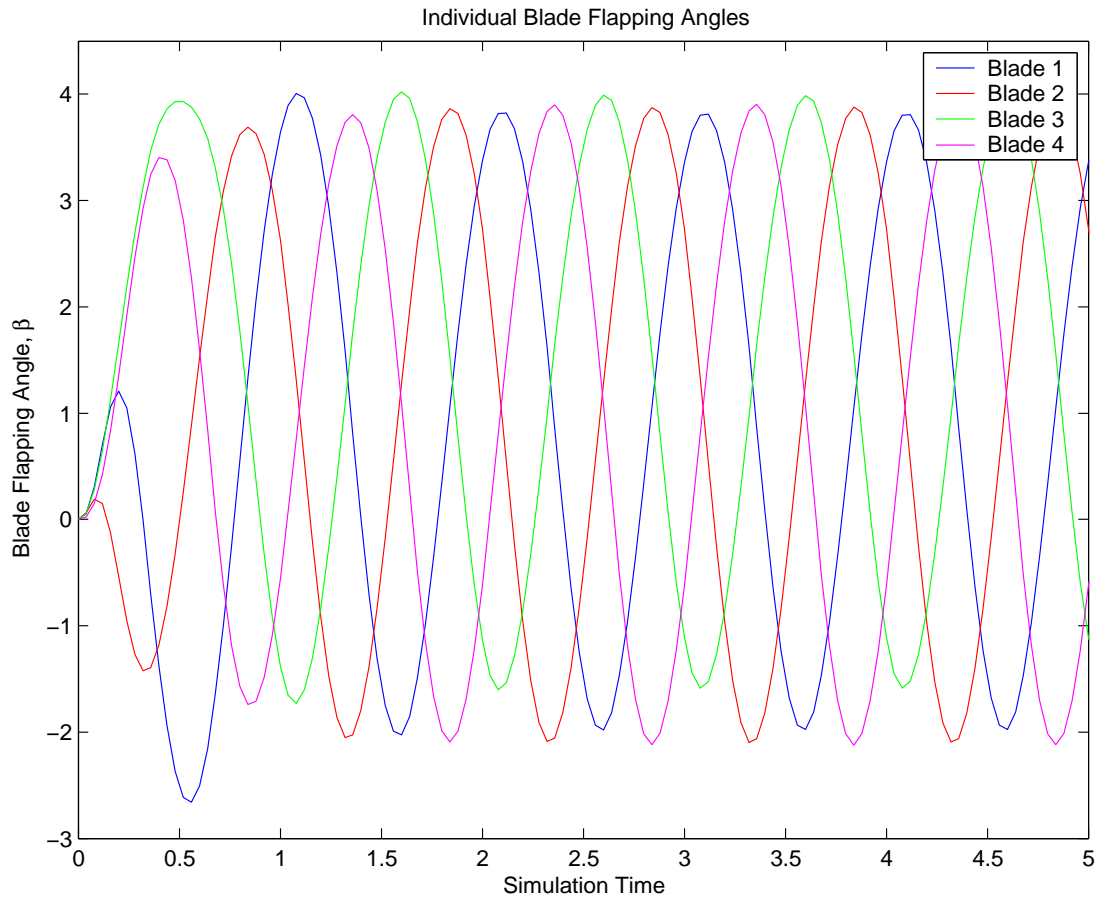


Figure D.21: Individual Flap Angles,  $\beta$ , for case  $\omega_f = 0.05\omega_p$ ,  $S_v = 2$

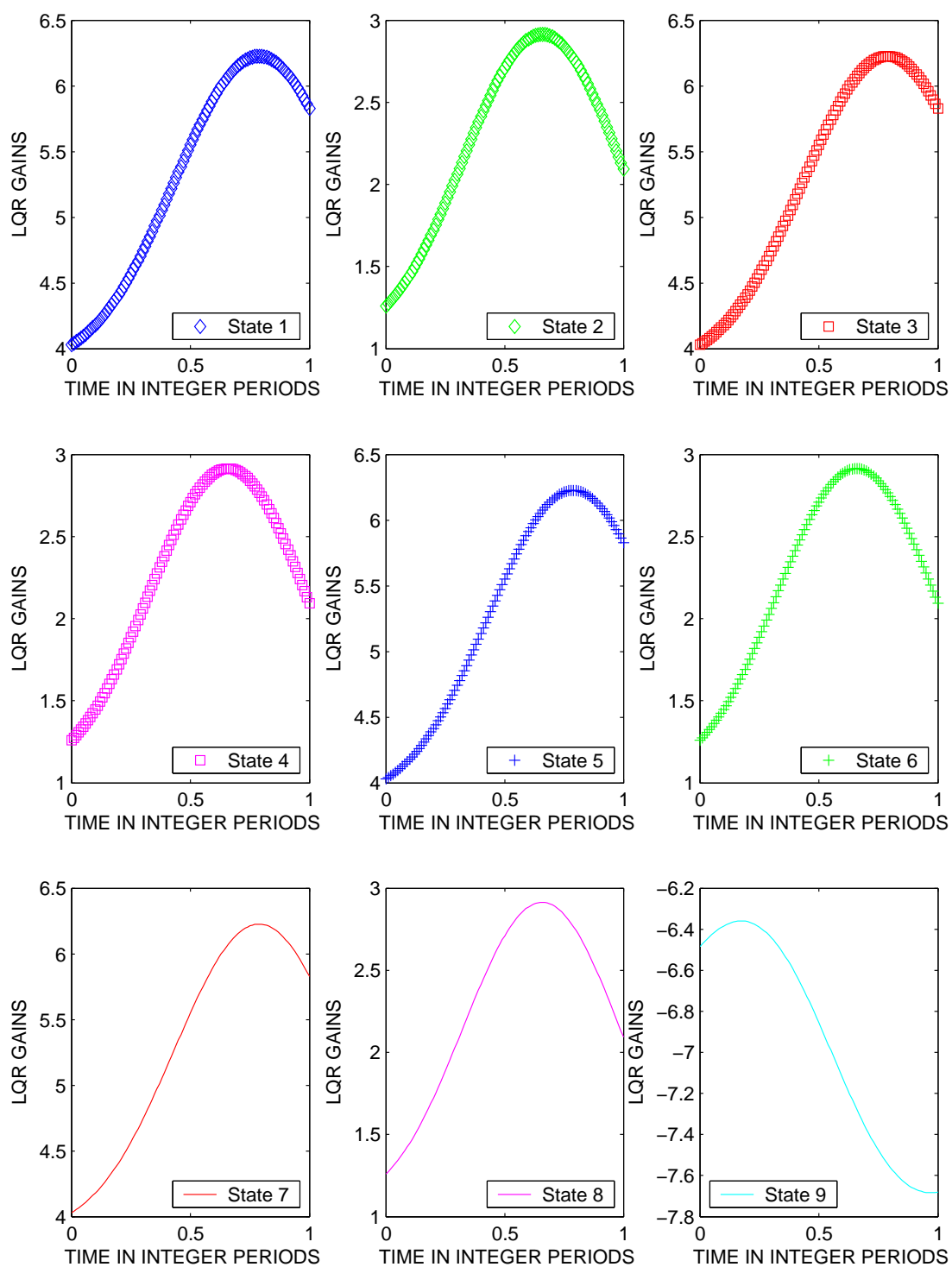


Figure D.22: All LQR Gains for case  $\omega_f = 0.05\omega_p$ ,  $S_v = 2$

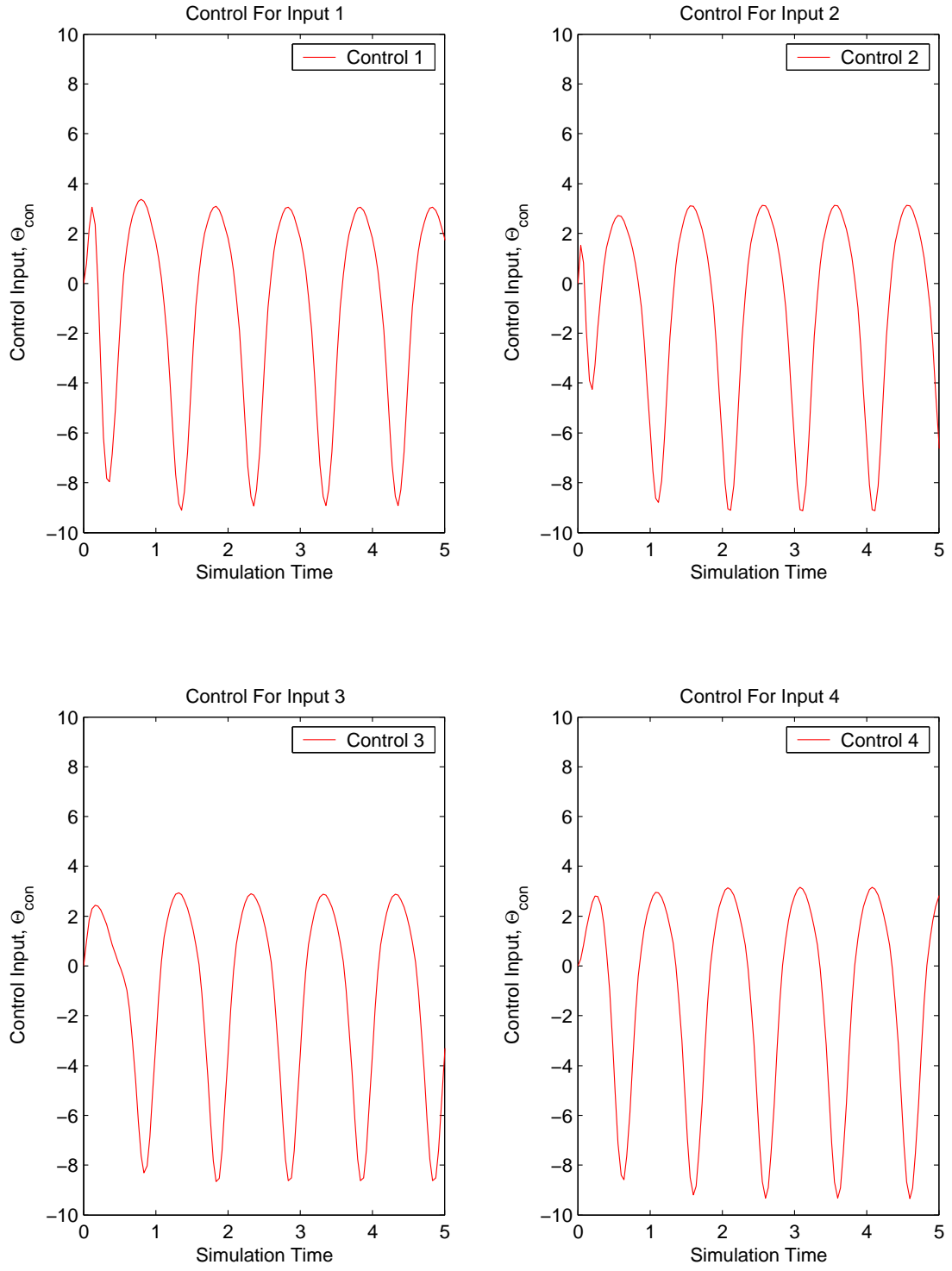


Figure D.23: Control Usage for case  $\omega_f = 0.05\omega_p$ ,  $S_v = 2$

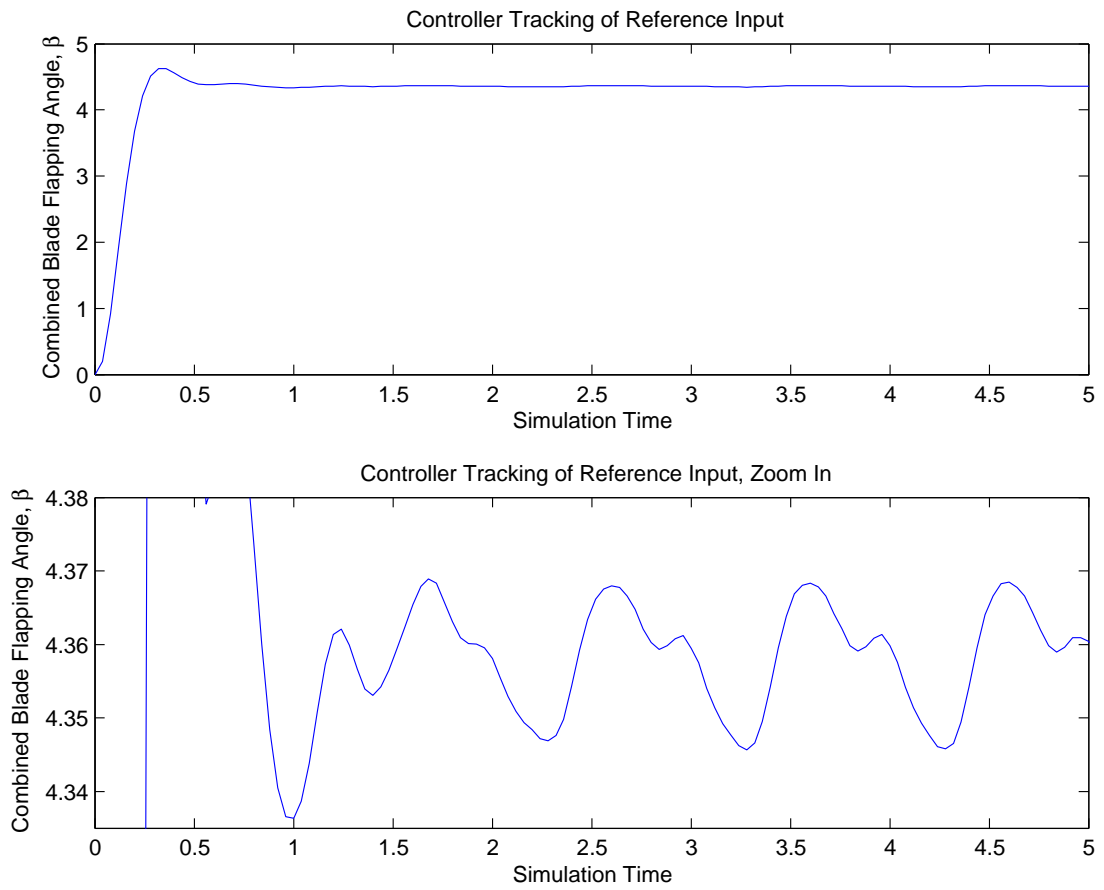


Figure D.24: Tracking Performance of Vibration Controller for case  $\omega_f = 0.05\omega_p$ ,  $S_v = 2$

Case 7	
Controller Design Parameters	
Input Frequency, $\omega_f$	Noise spectral density, $S_v$
$\omega_f = .0\omega_p$	$S_v = 2$

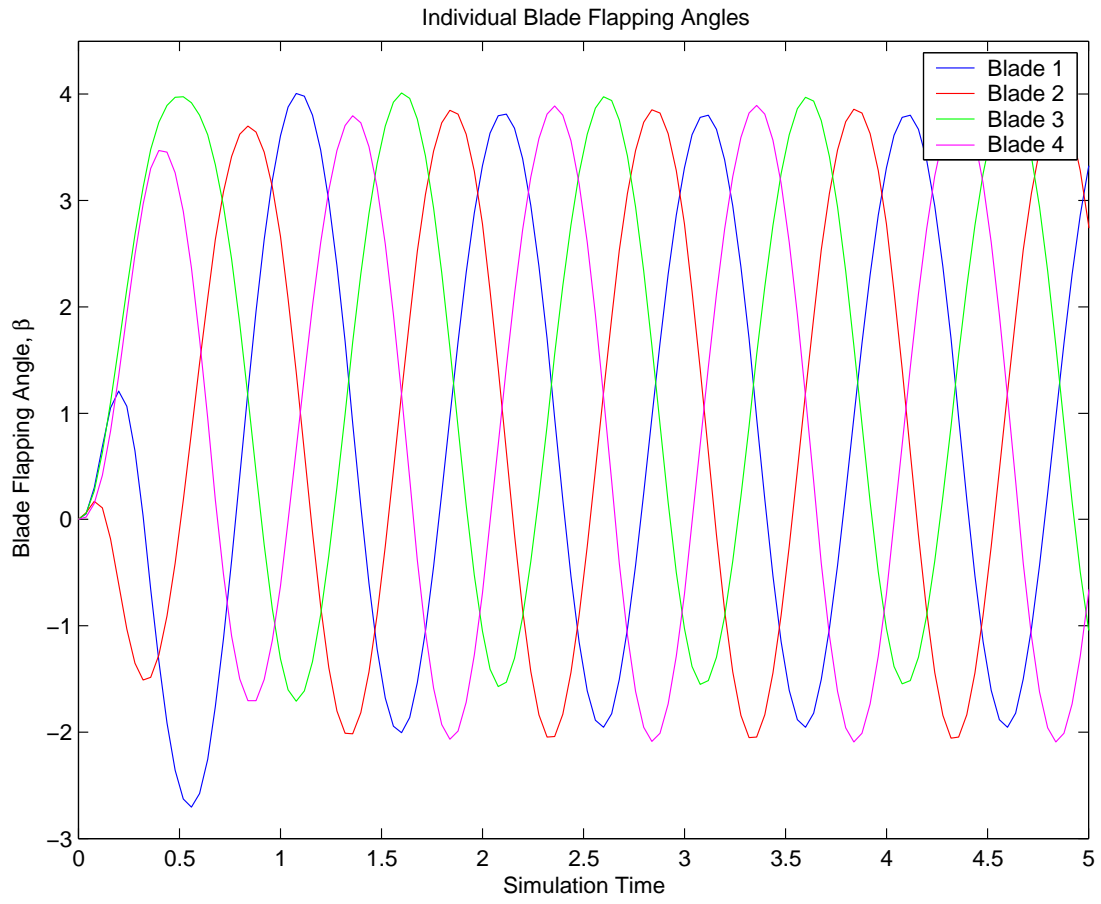


Figure D.25: Individual Flap Angles,  $\beta$ , for case  $\omega_f = 0.0\omega_p$ ,  $S_v = 2$

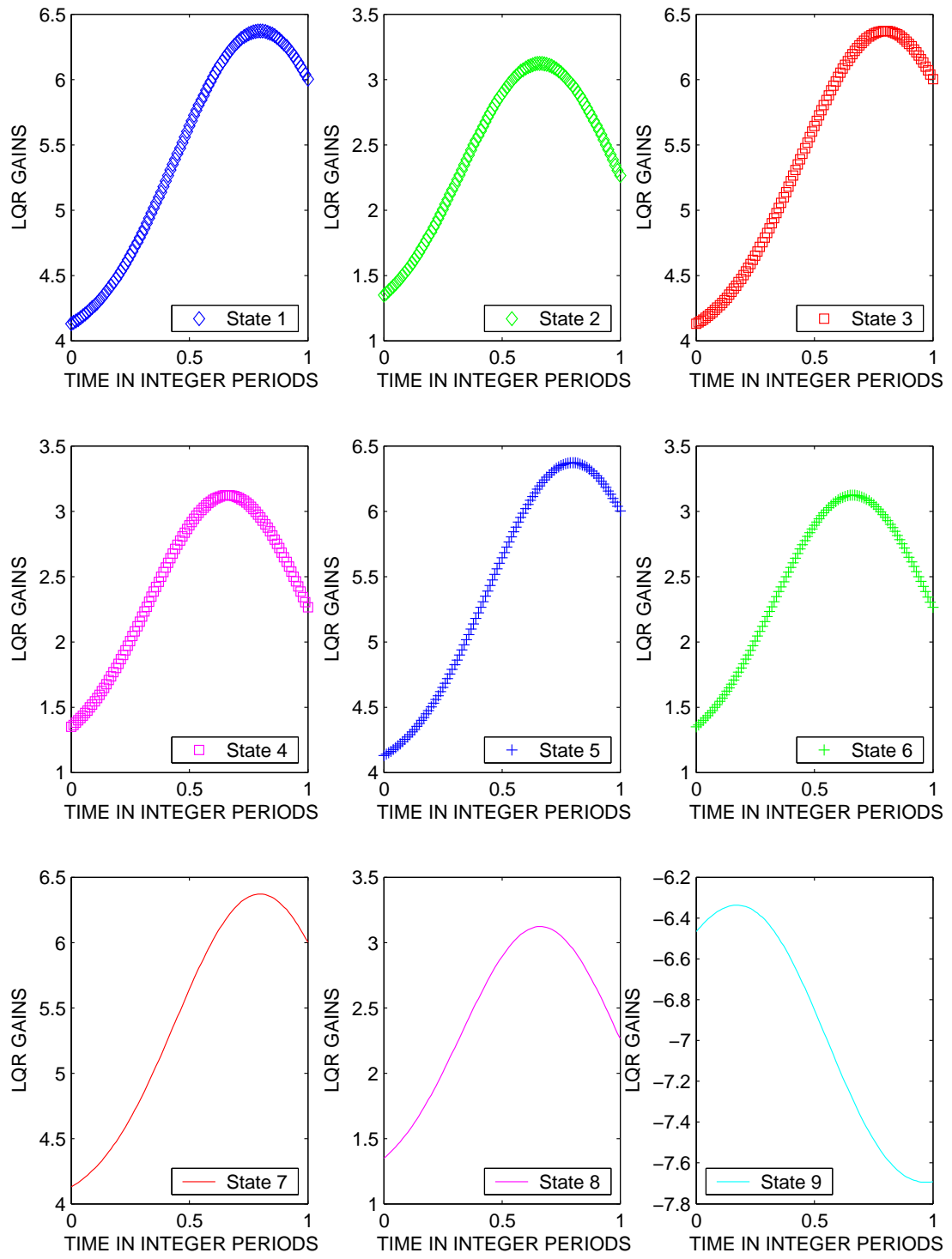


Figure D.26: All LQR Gains for case  $\omega_f = 0.0\omega_p$ ,  $S_v = 2$

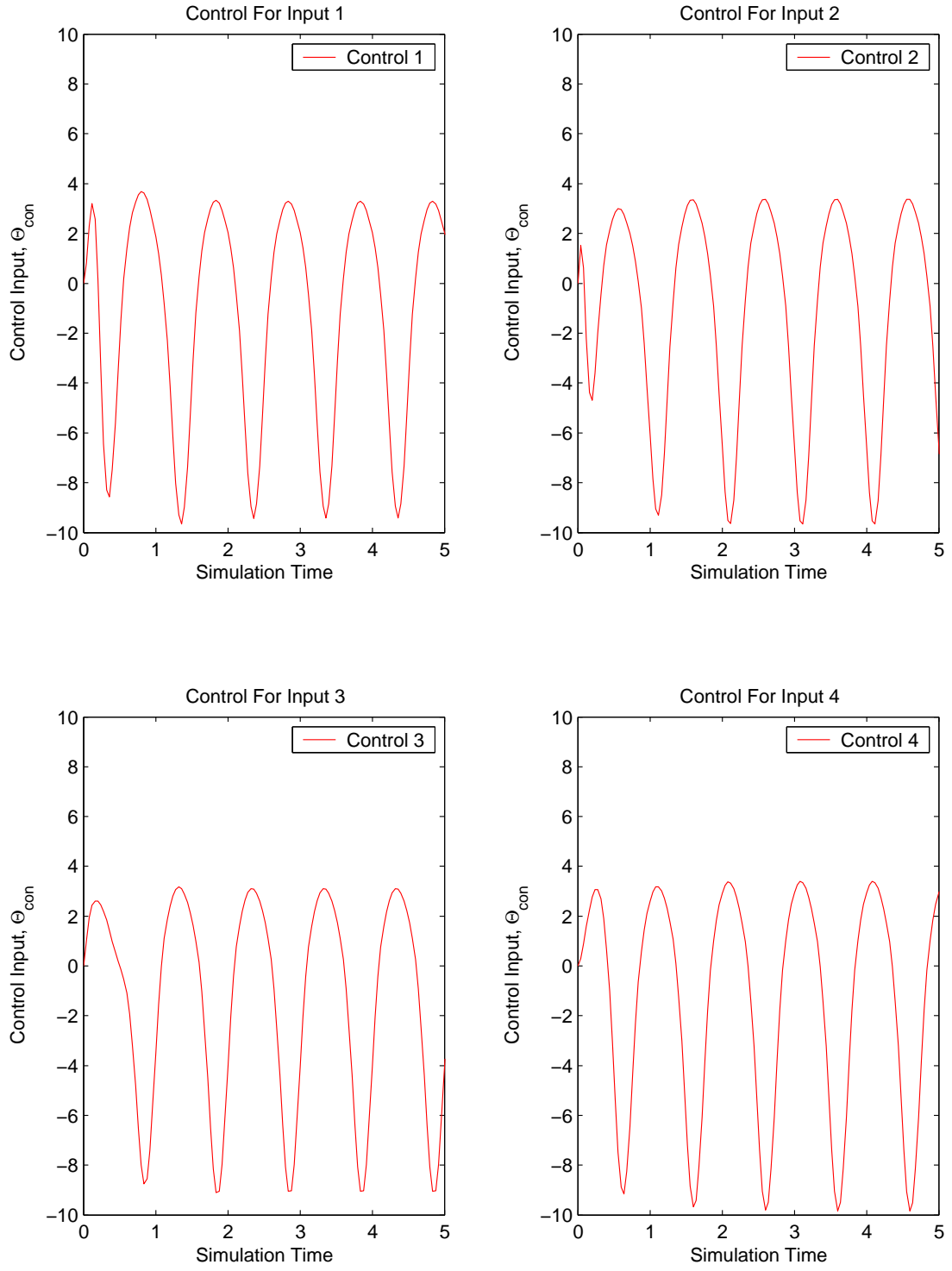


Figure D.27: Control Usage for case  $\omega_f = 0.0\omega_p$ ,  $S_v = 2$

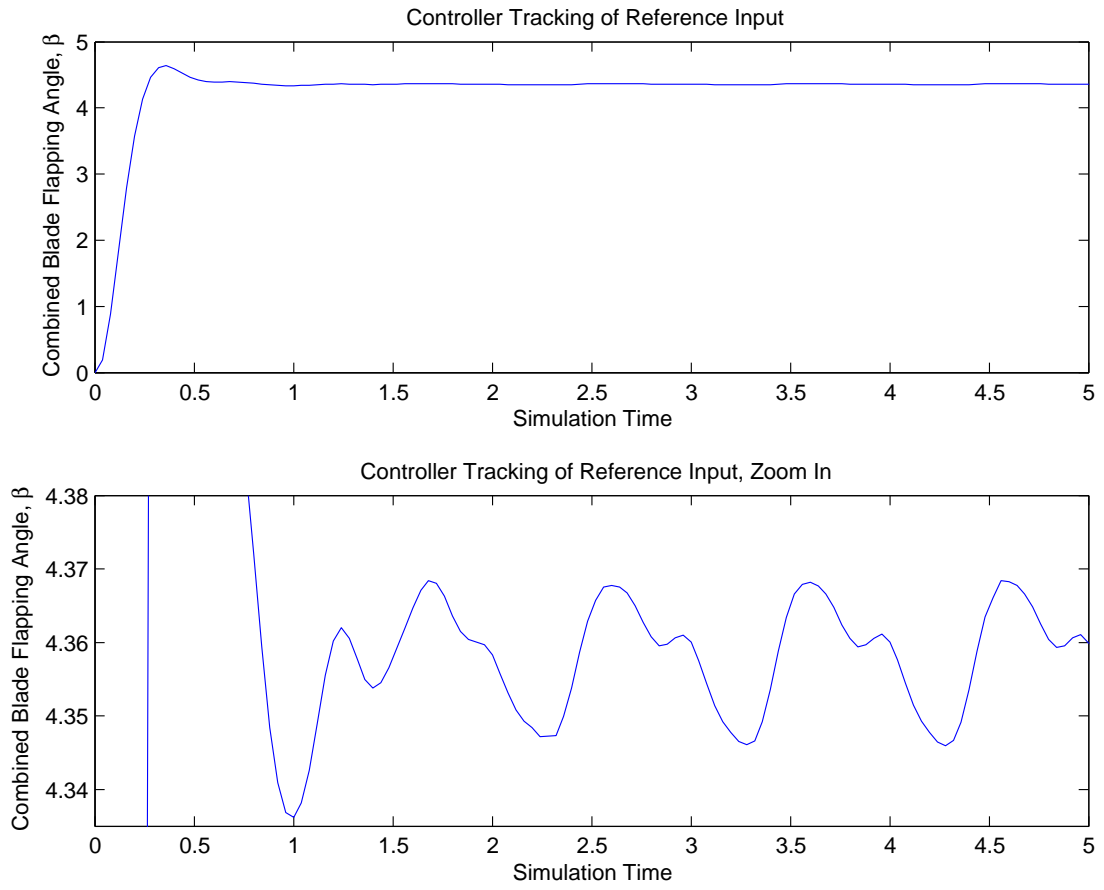


Figure D.28: Tracking Performance of Vibration Controller for case  $\omega_f = 0.0\omega_p$ ,  $S_v = 2$

## *Appendix E. Vibration Controller Comparison Plots, Noise Case*

$$S_v = 3$$

This appendix contains the plots of the individual flap angles, calculated LQR gains, control usage, and vibration controller performance as computed at specific cases of input frequency  $\omega_f$  and noise spectral density  $S_v$ . For the cases presented in this appendix, the range of values of input and measurement noise are  $\omega_f = \omega_p(0, 0.05, 0.1, 0.2, 0.3, 0.4, 0.5)$  and  $S_v = 3$  are used, which results in 7 individual cases. Each case will present four plots; one representing the individual flap angles of each blade after control is applied to eliminate the asymmetric lift, one for calculated LQR gains, one for control usage,  $\Theta_{con}$  for each blade, and one depicting the vibration controller performance in terms of matching the reference input.

Case 1	
Controller Design Parameters	
Input Frequency, $\omega_f$	Noise spectral density, $S_v$
$\omega_f = .5\omega_p$	$S_v = 3$

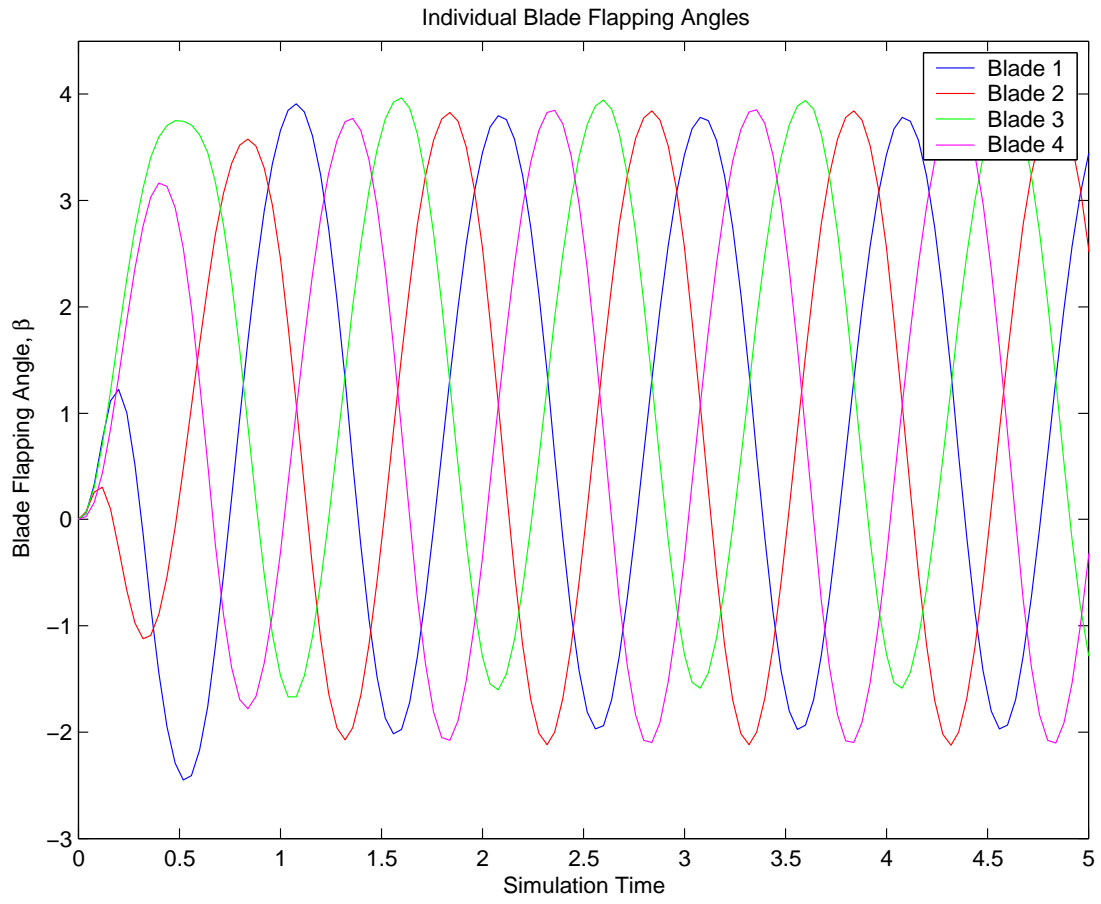


Figure E.1: Individual Flap Angles,  $\beta$ , for case  $\omega_f = 0.5\omega_p$ ,  $S_v = 3$

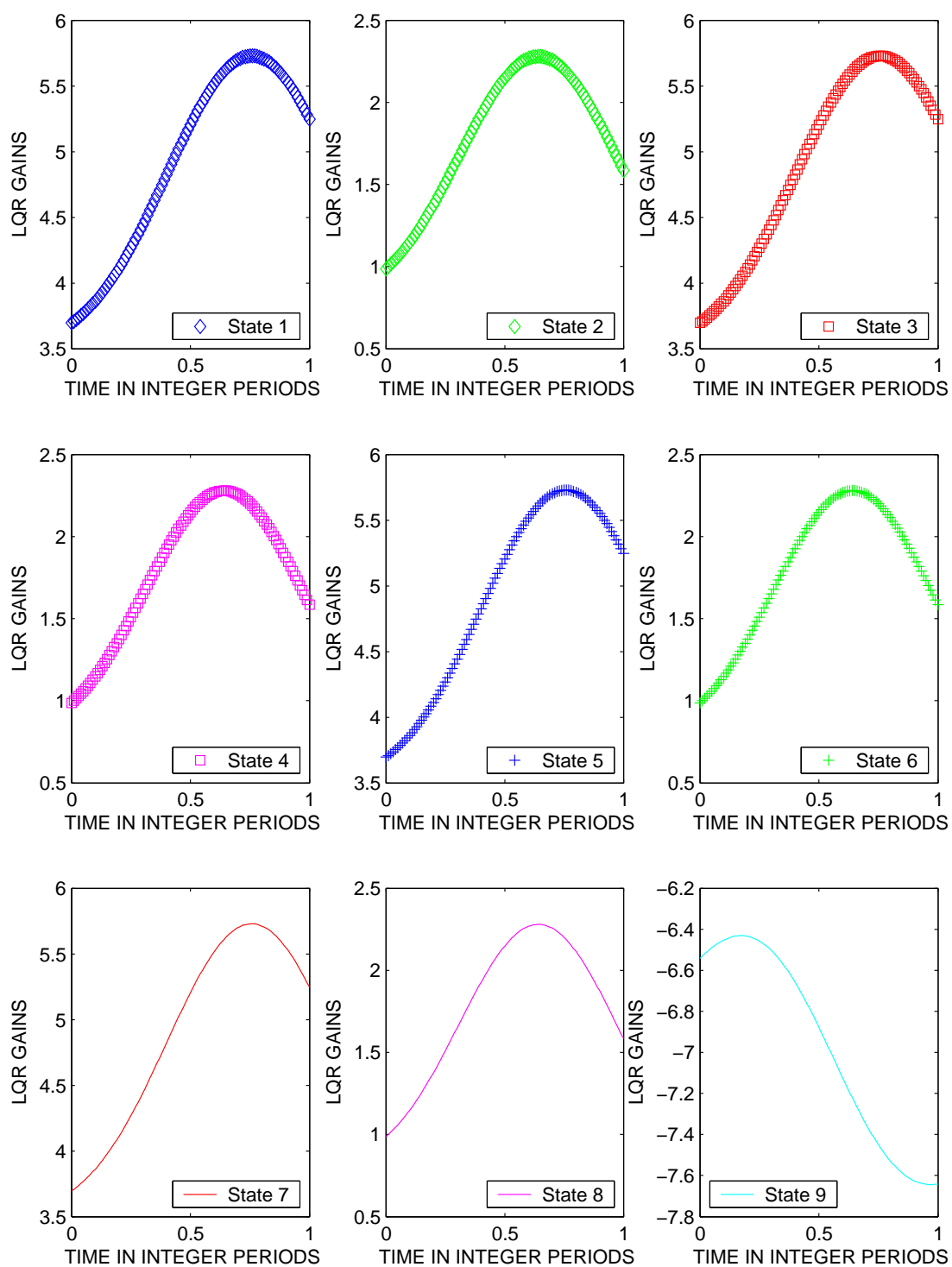


Figure E.2: All LQR Gains for case  $\omega_f = 0.5\omega_p$ ,  $S_v = 3$

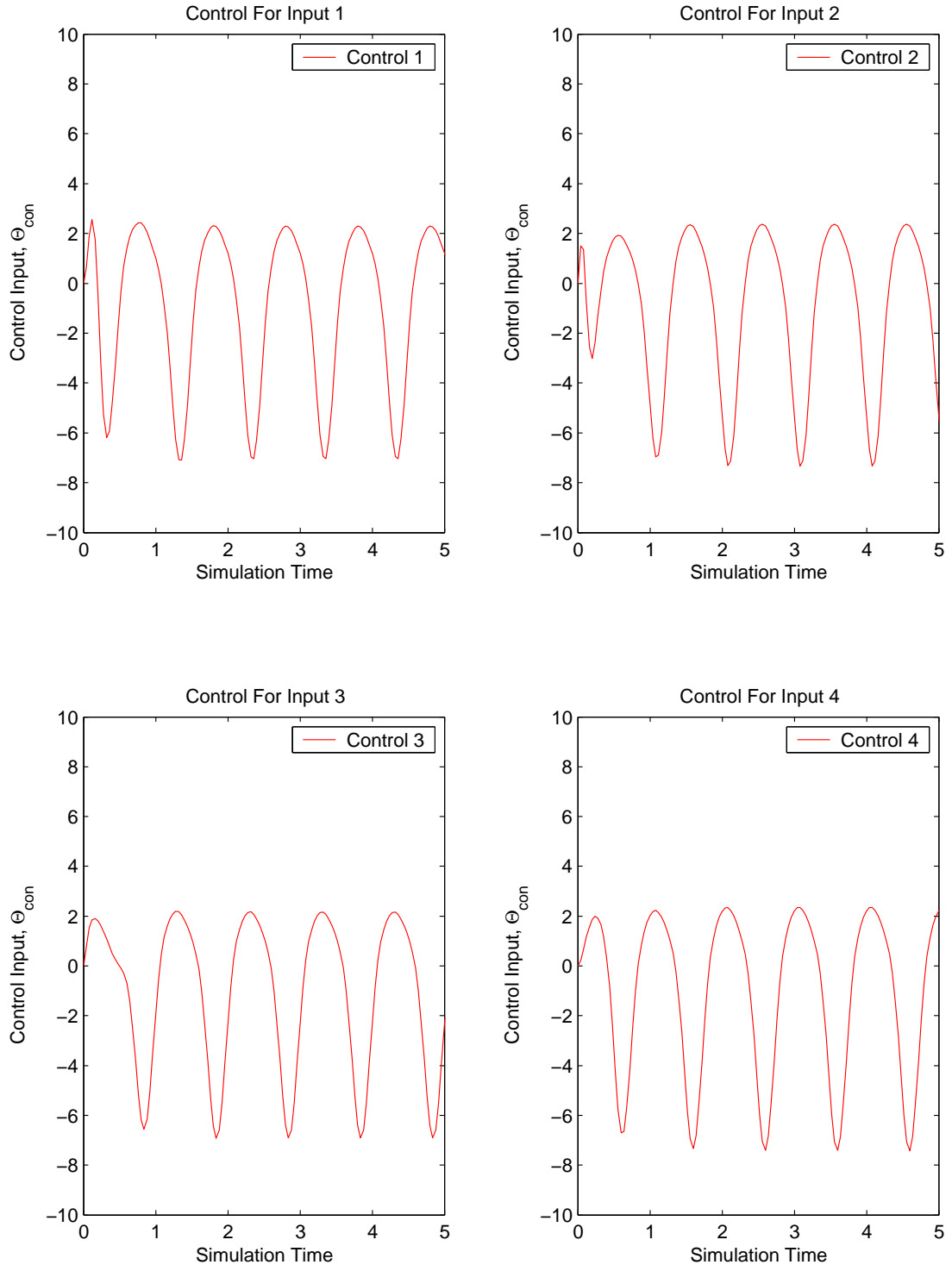


Figure E.3: Control Usage for case  $\omega_f = 0.5\omega_p$ ,  $S_v = 3$

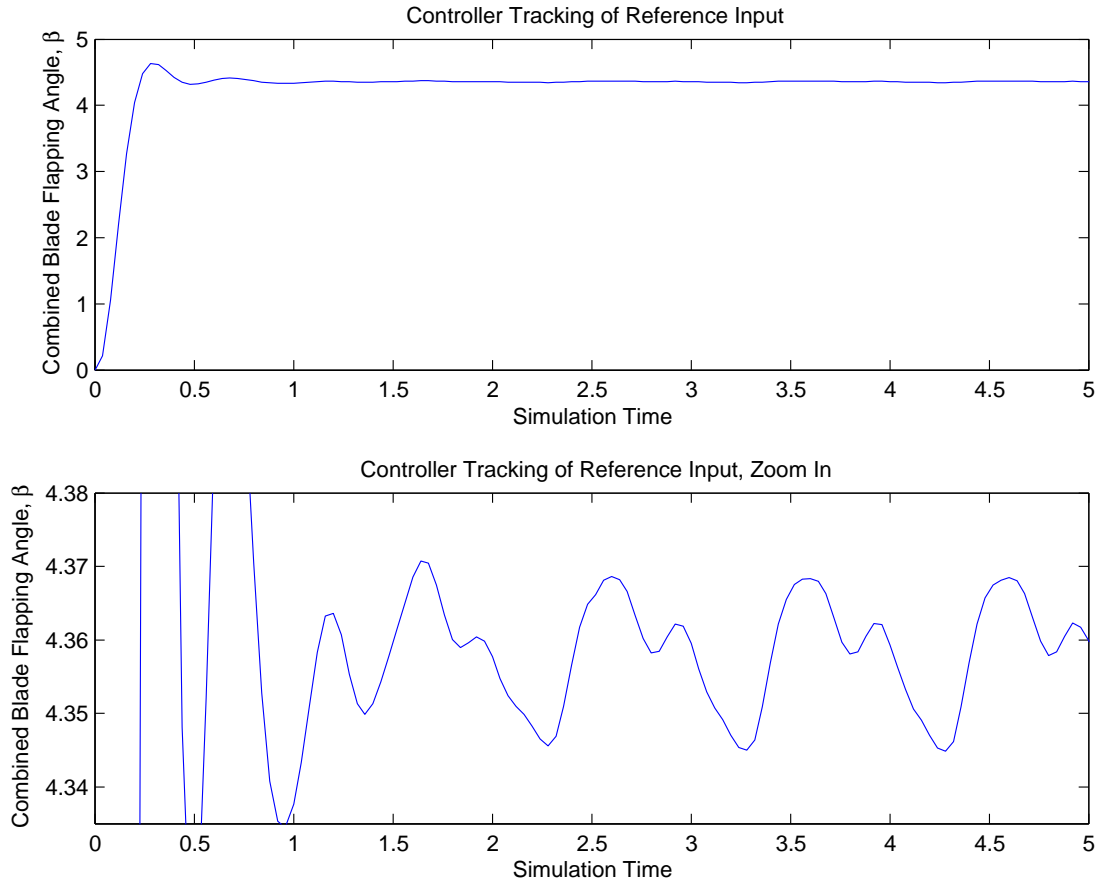


Figure E.4: Tracking Performance of Vibration Controller for case  $\omega_f = 0.5\omega_p$ ,  $S_v = 3$

Case 2	
Controller Design Parameters	
Input Frequency, $\omega_f$	Noise spectral density, $S_v$
$\omega_f = .4\omega_p$	$S_v = 3$

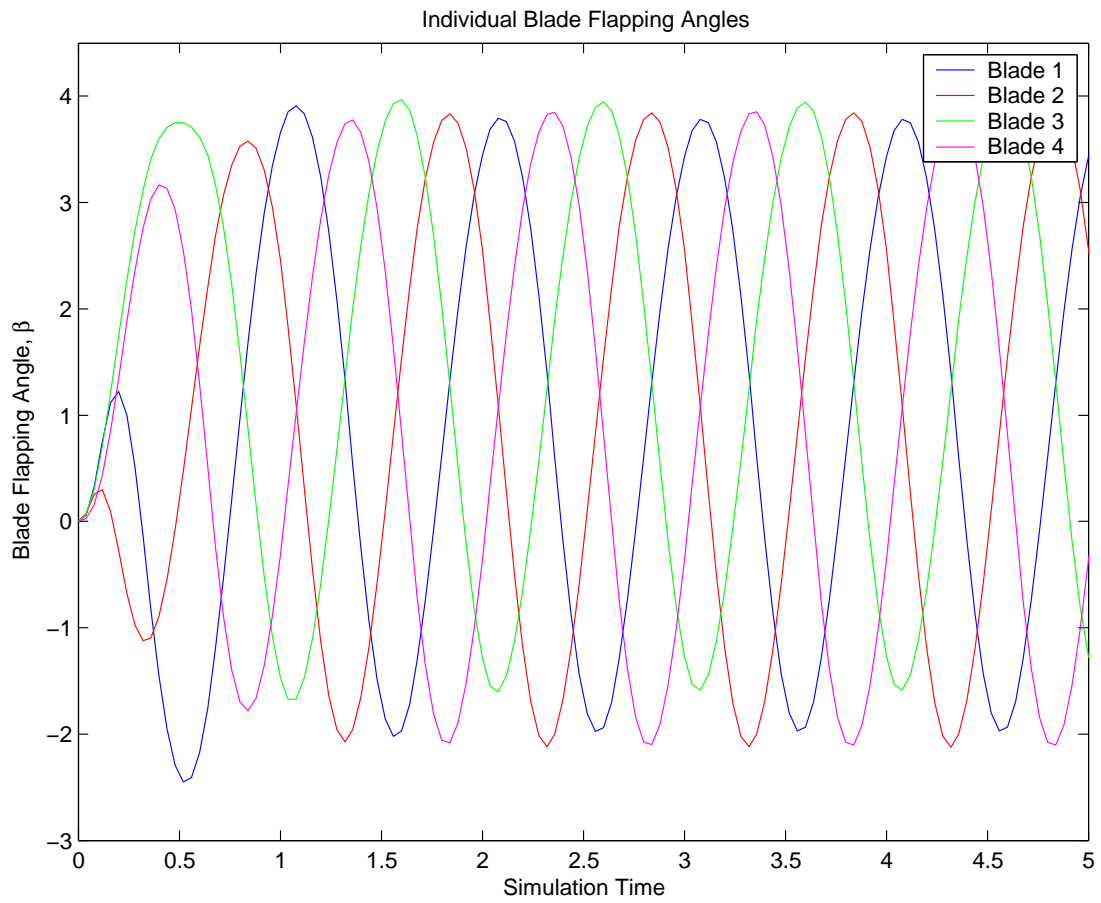


Figure E.5: Individual Flap Angles,  $\beta$ , for case  $\omega_f = 0.4\omega_p$ ,  $S_v = 3$

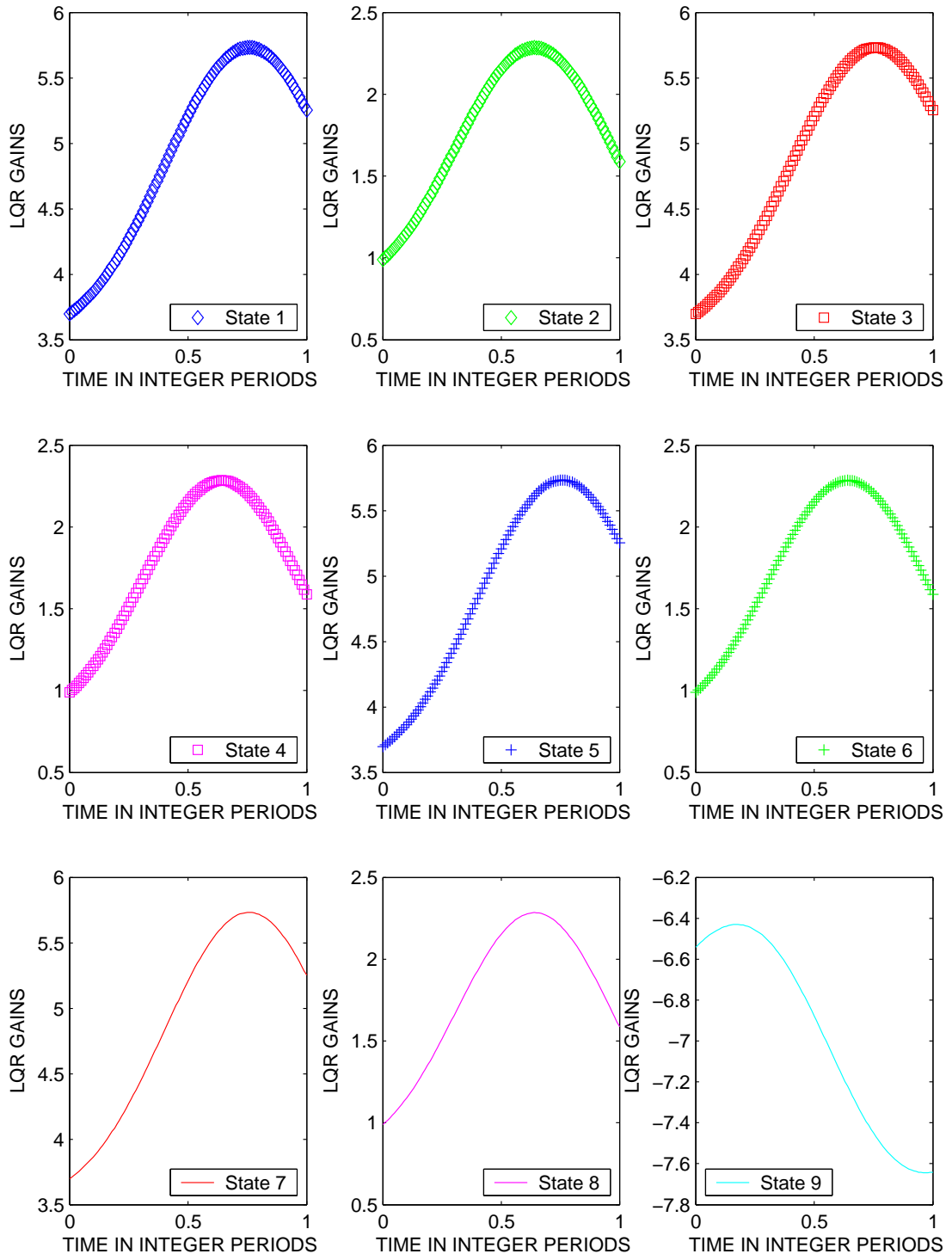


Figure E.6: All LQR Gains for case  $\omega_f = 0.4\omega_p$ ,  $S_v = 3$

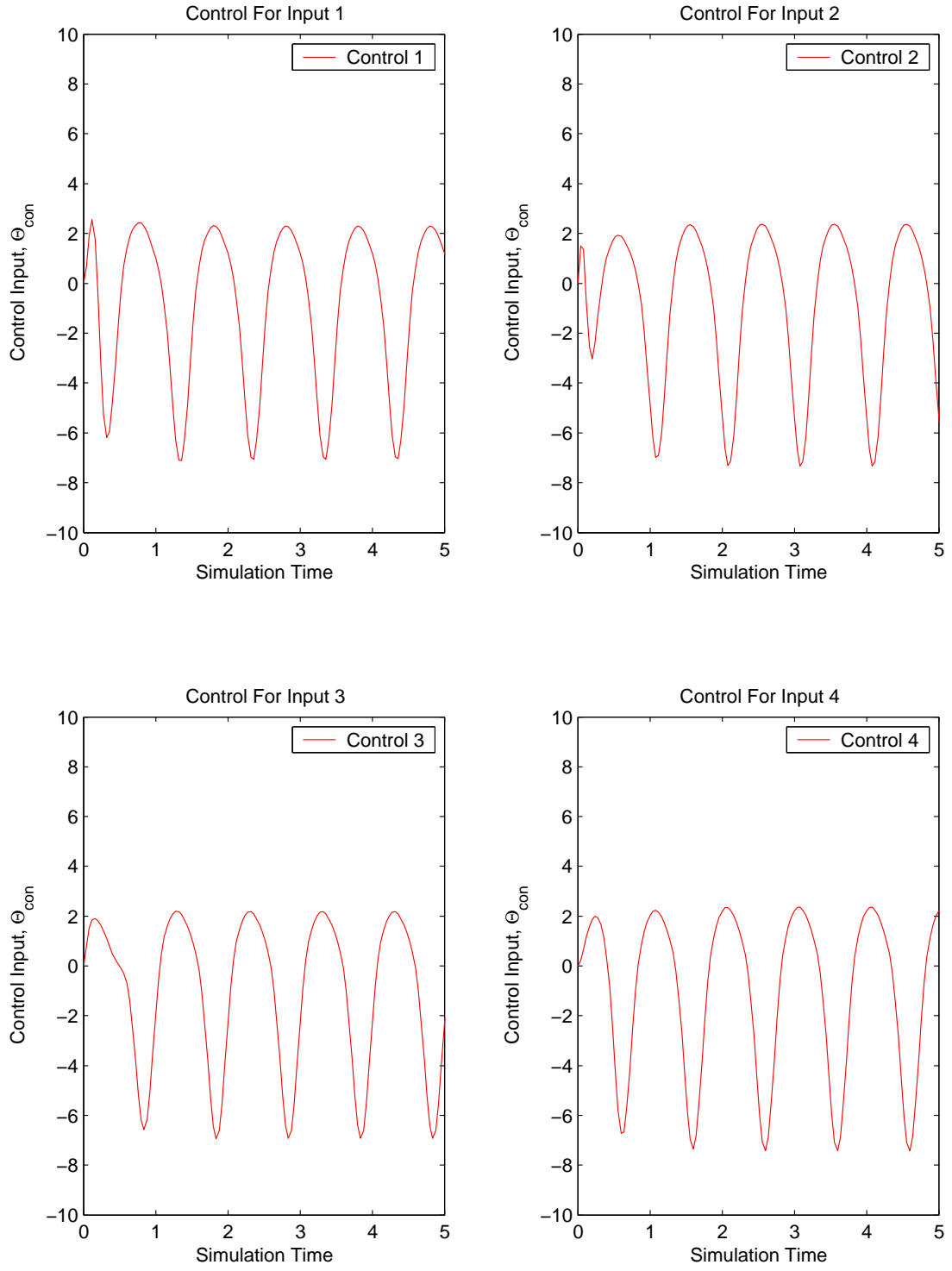


Figure E.7: Control Usage for case  $\omega_f = 0.4\omega_p$ ,  $S_v = 3$

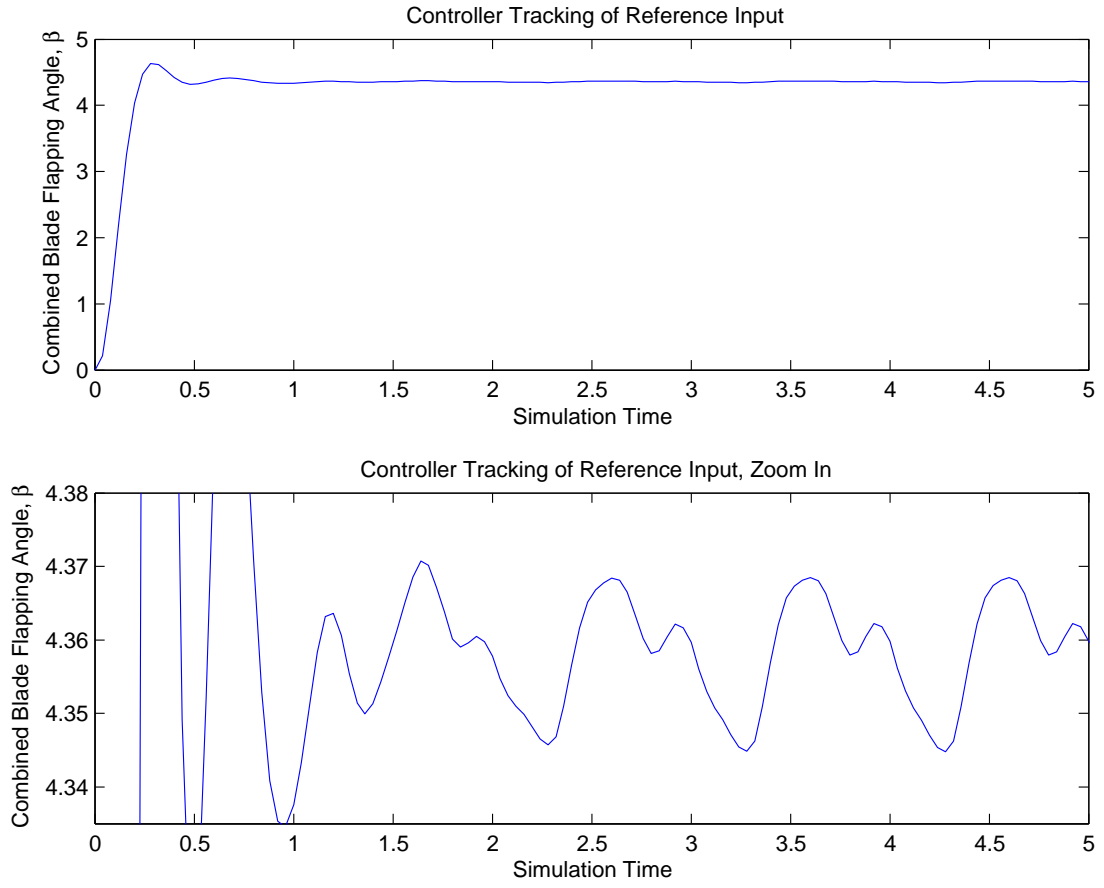


Figure E.8: Tracking Performance of Vibration Controller for case  $\omega_f = 0.4\omega_p$ ,  $S_v = 3$

Case 3	
Controller Design Parameters	
Input Frequency, $\omega_f$	Noise spectral density, $S_v$
$\omega_f = .3\omega_p$	$S_v = 3$

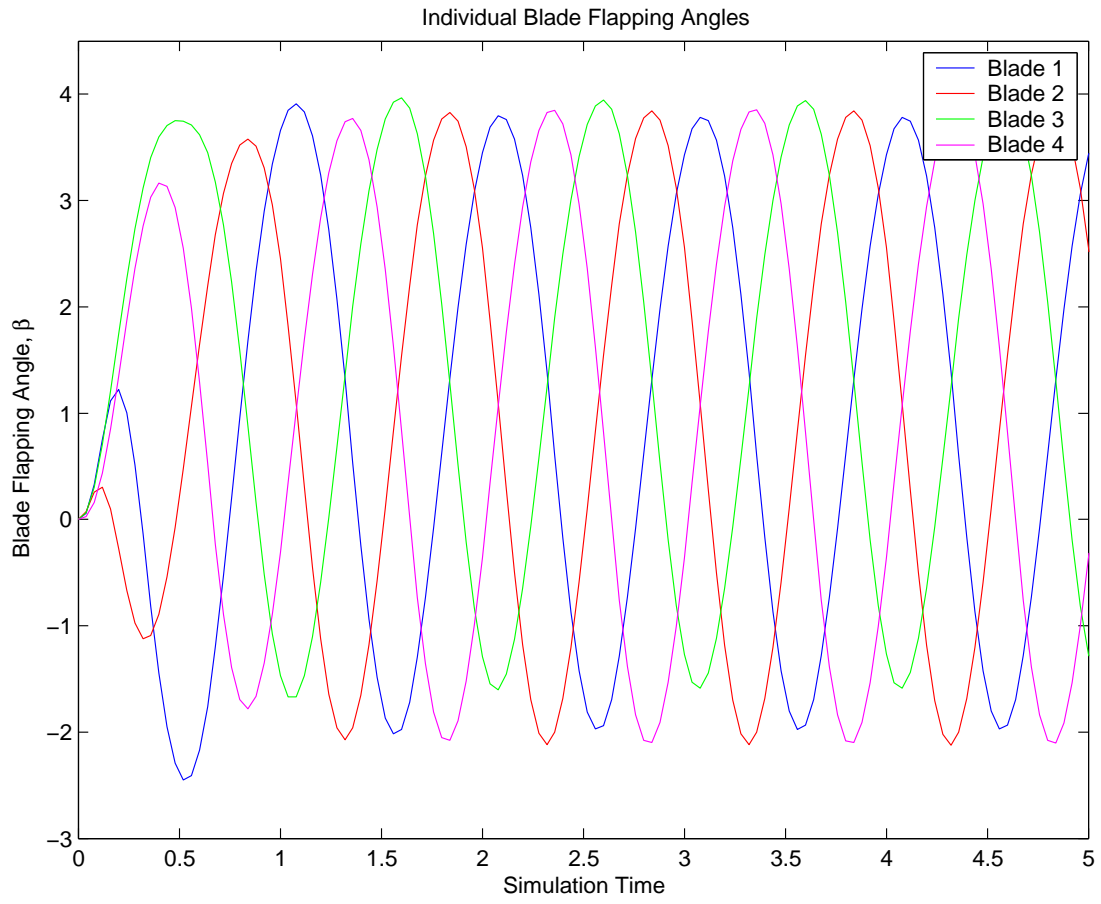


Figure E.9: Individual Flap Angles,  $\beta$ , for case  $\omega_f = 0.3\omega_p$ ,  $S_v = 3$

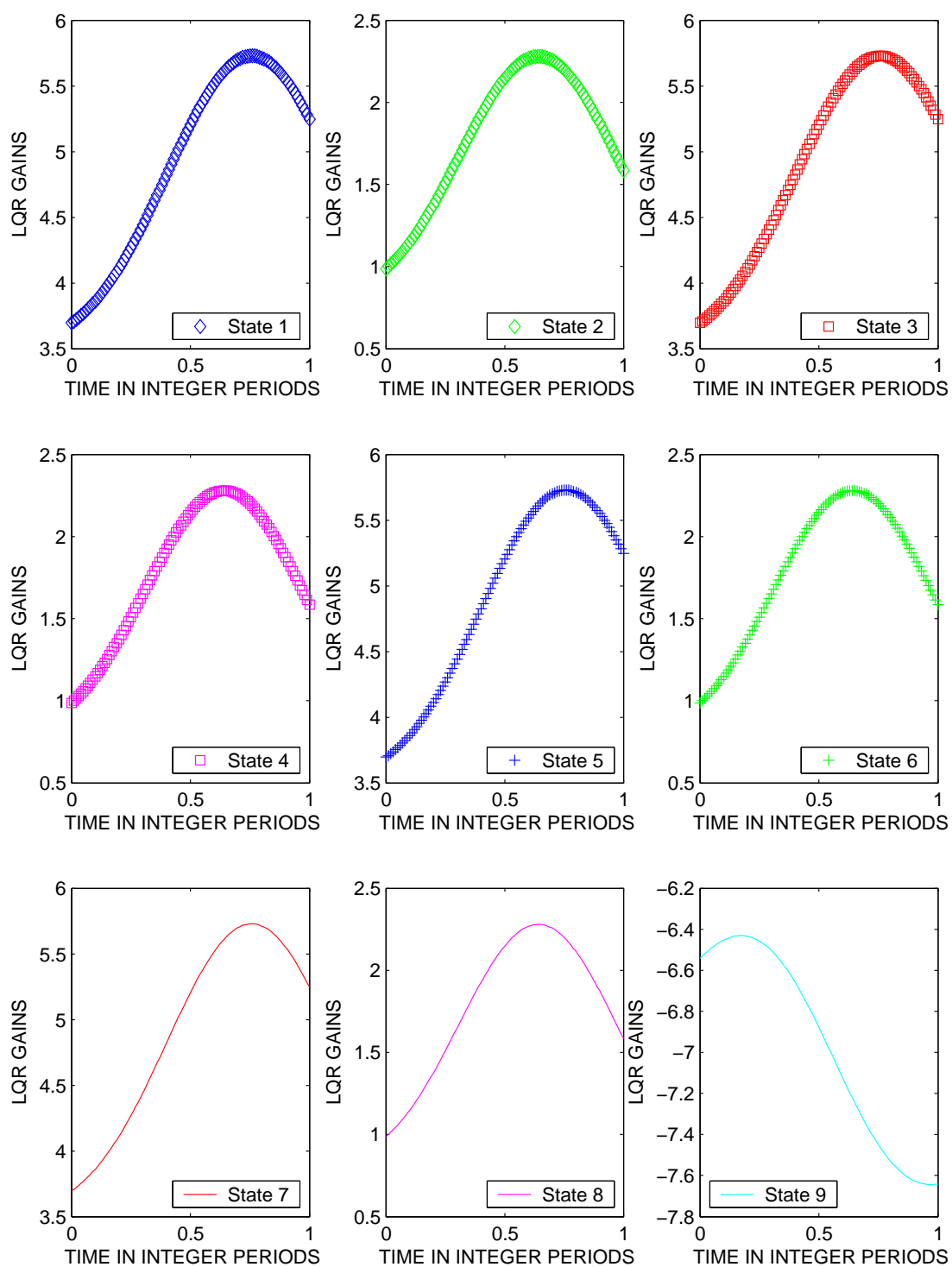


Figure E.10: All LQR Gains for case  $\omega_f = 0.3\omega_p$ ,  $S_v = 3$

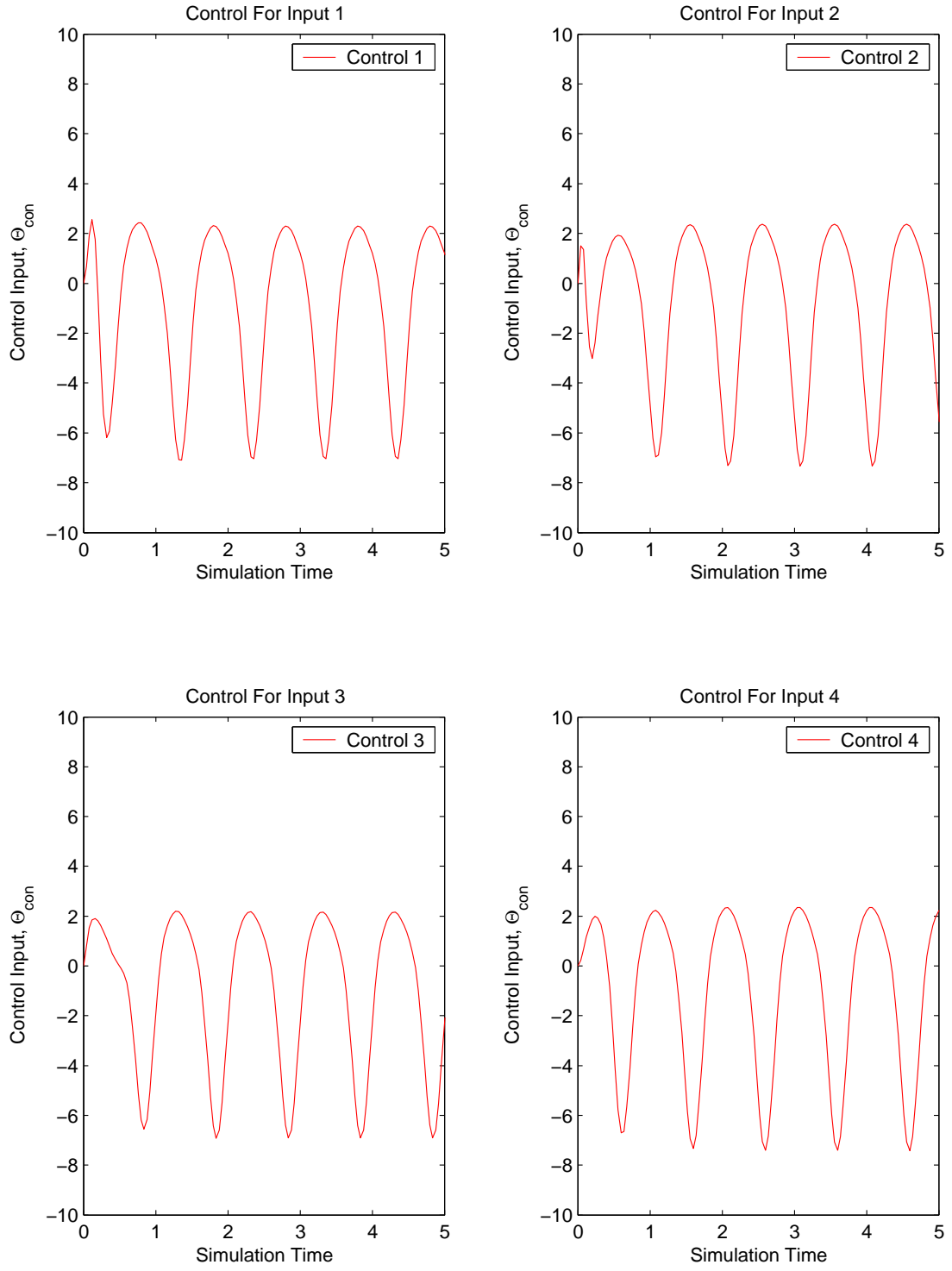


Figure E.11: Control Usage for case  $\omega_f = 0.3\omega_p$ ,  $S_v = 3$

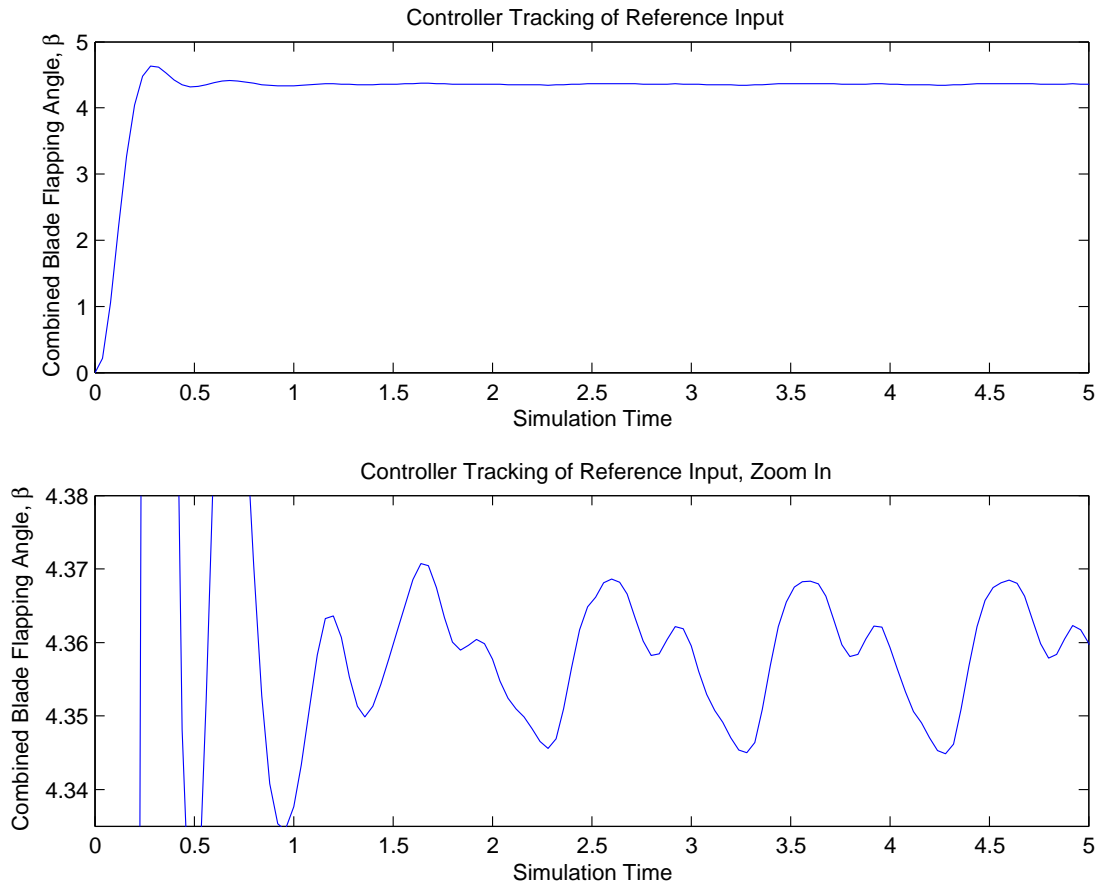


Figure E.12: Tracking Performance of Vibration Controller for case  $\omega_f = 0.3\omega_p$ ,  $S_v = 3$

Case 4	
Controller Design Parameters	
Input Frequency, $\omega_f$	Noise spectral density, $S_v$
$\omega_f = .2\omega_p$	$S_v = 3$

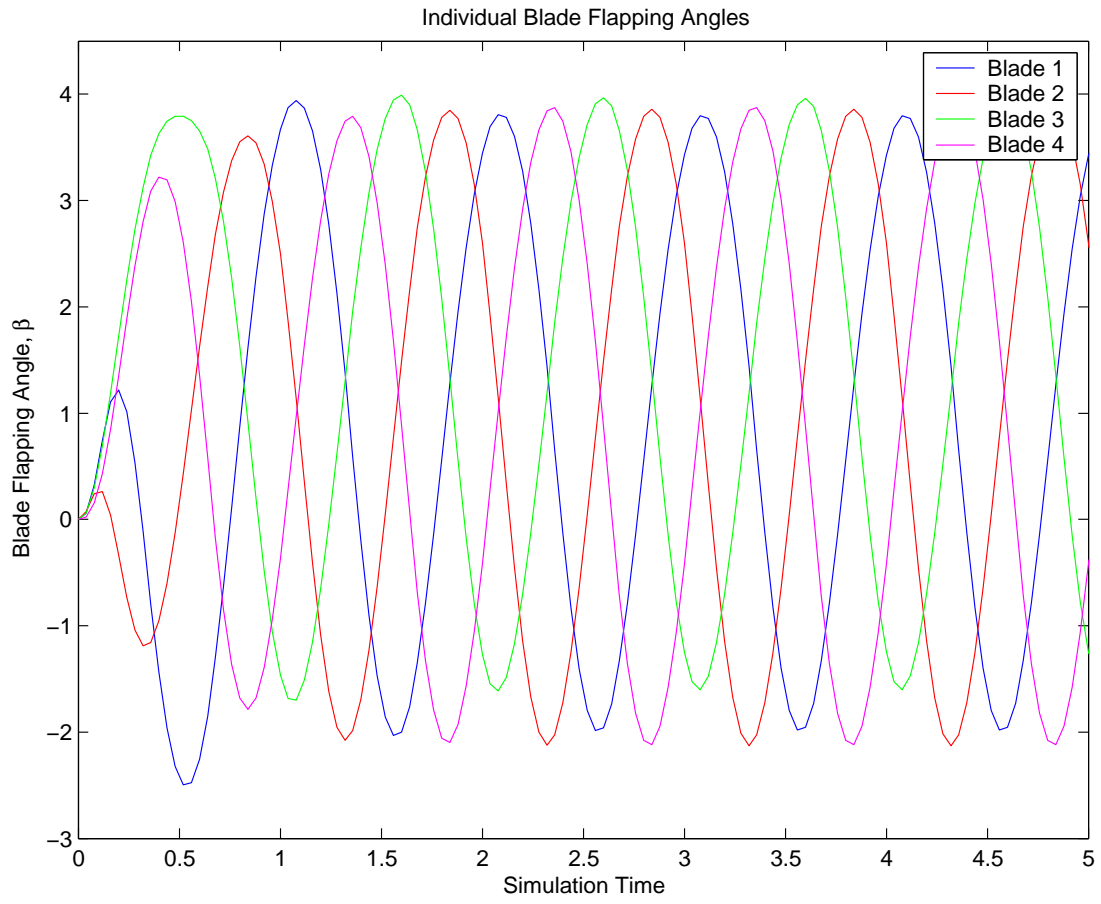


Figure E.13: Individual Flap Angles,  $\beta$ , for case  $\omega_f = 0.2\omega_p$ ,  $S_v = 3$

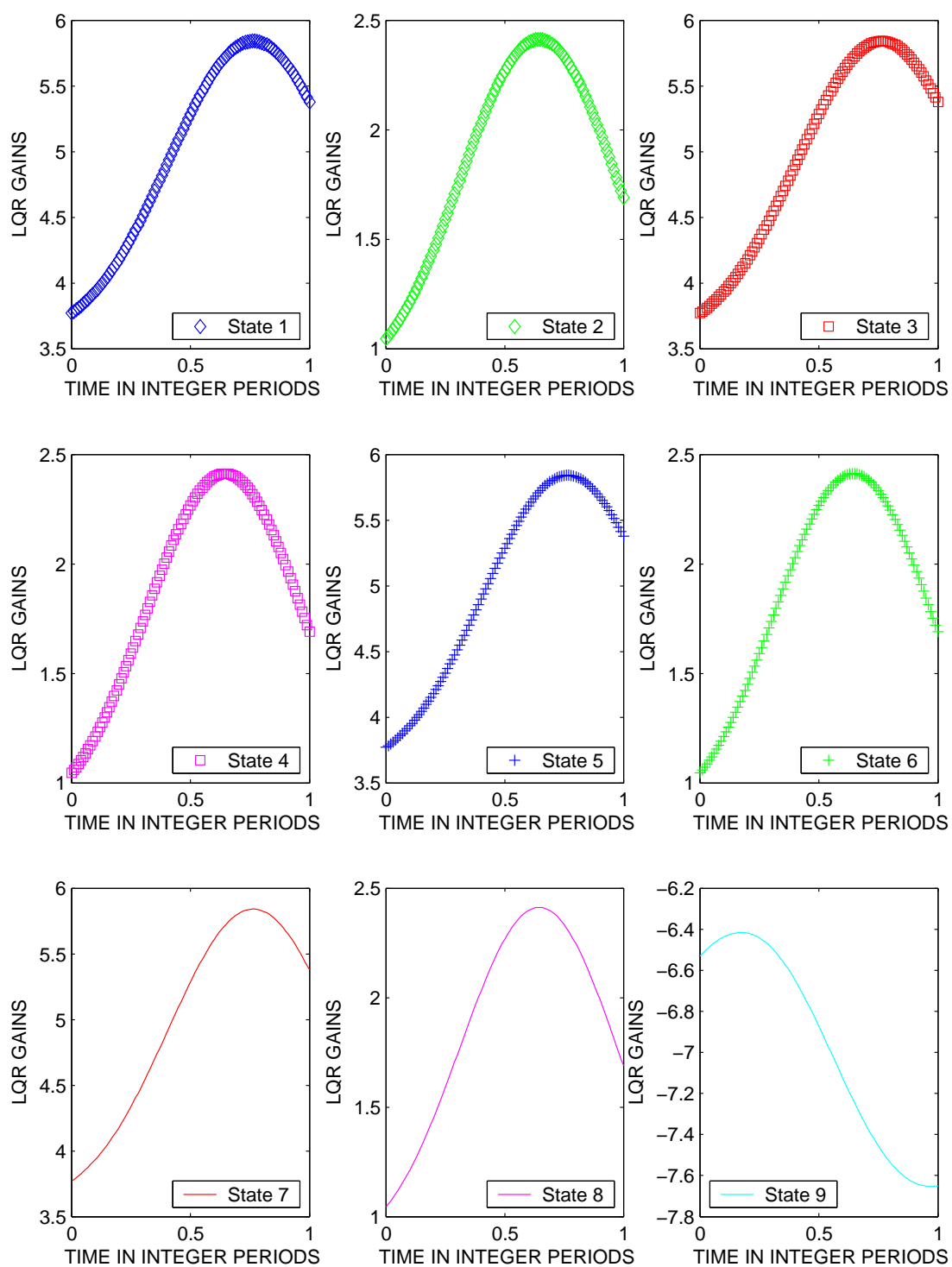


Figure E.14: All LQR Gains for case  $\omega_f = 0.2\omega_p$ ,  $S_v = 3$

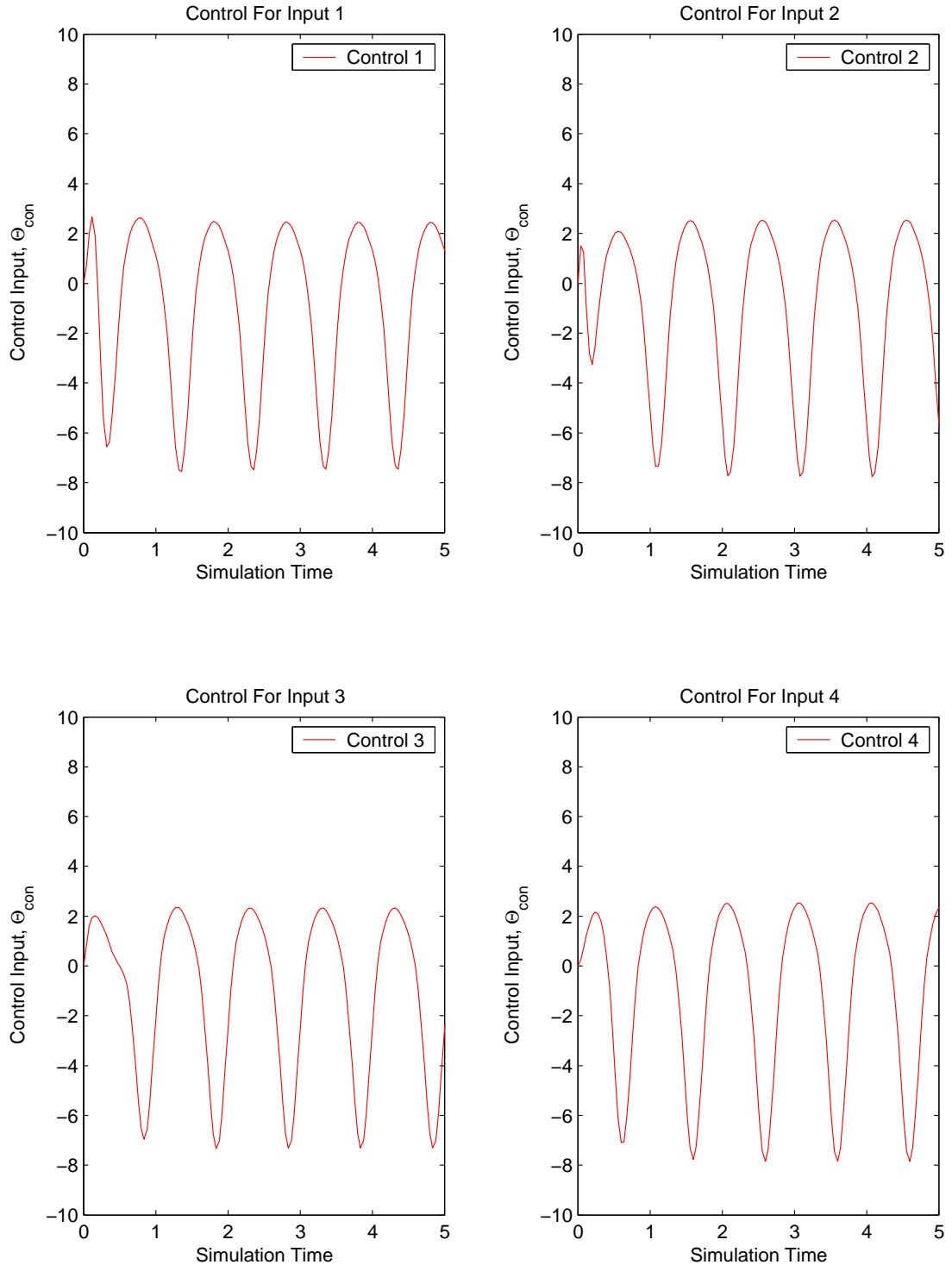


Figure E.15: Control Usage for case  $\omega_f = 0.2\omega_p$ ,  $S_v = 3$

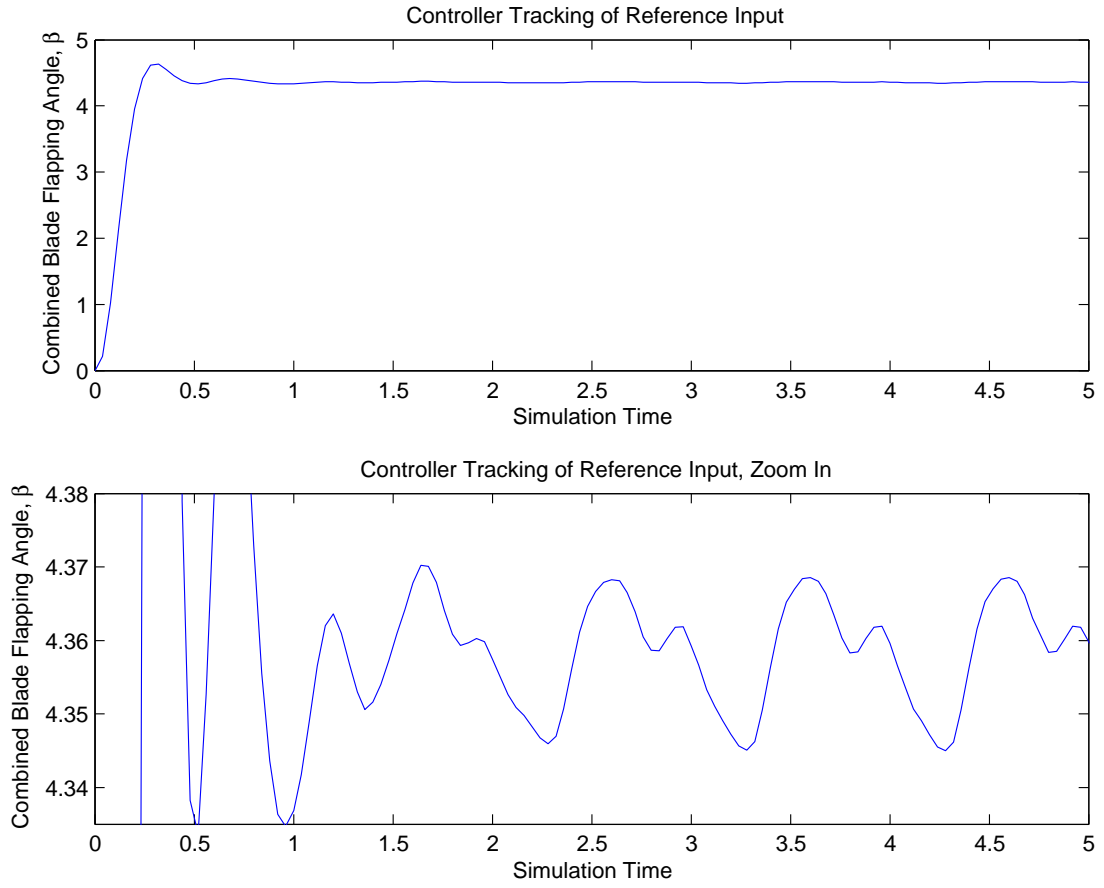


Figure E.16: Tracking Performance of Vibration Controller for case  $\omega_f = 0.2\omega_p$ ,  $S_v = 3$

Case 5	
Controller Design Parameters	
Input Frequency, $\omega_f$	Noise spectral density, $S_v$
$\omega_f = .1\omega_p$	$S_v = 3$

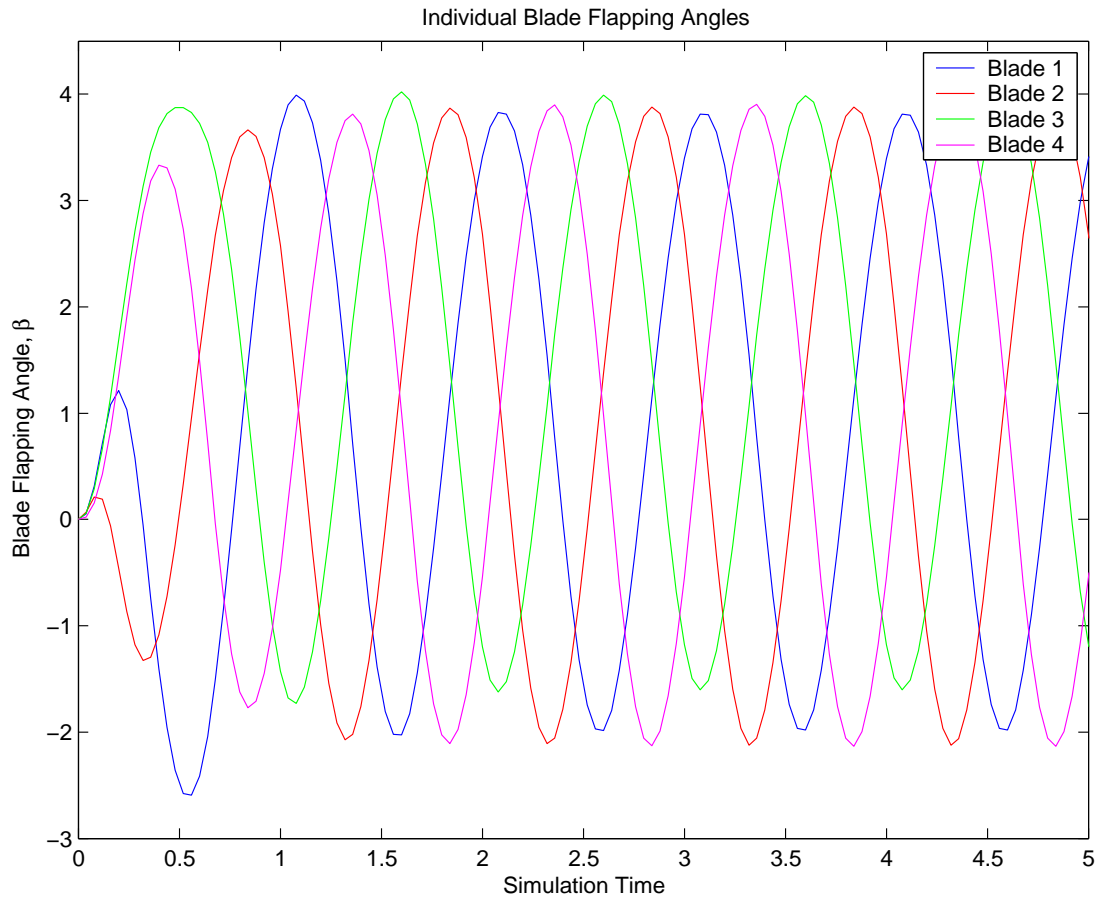


Figure E.17: Individual Flap Angles,  $\beta$ , for case  $\omega_f = 0.1\omega_p$ ,  $S_v = 3$

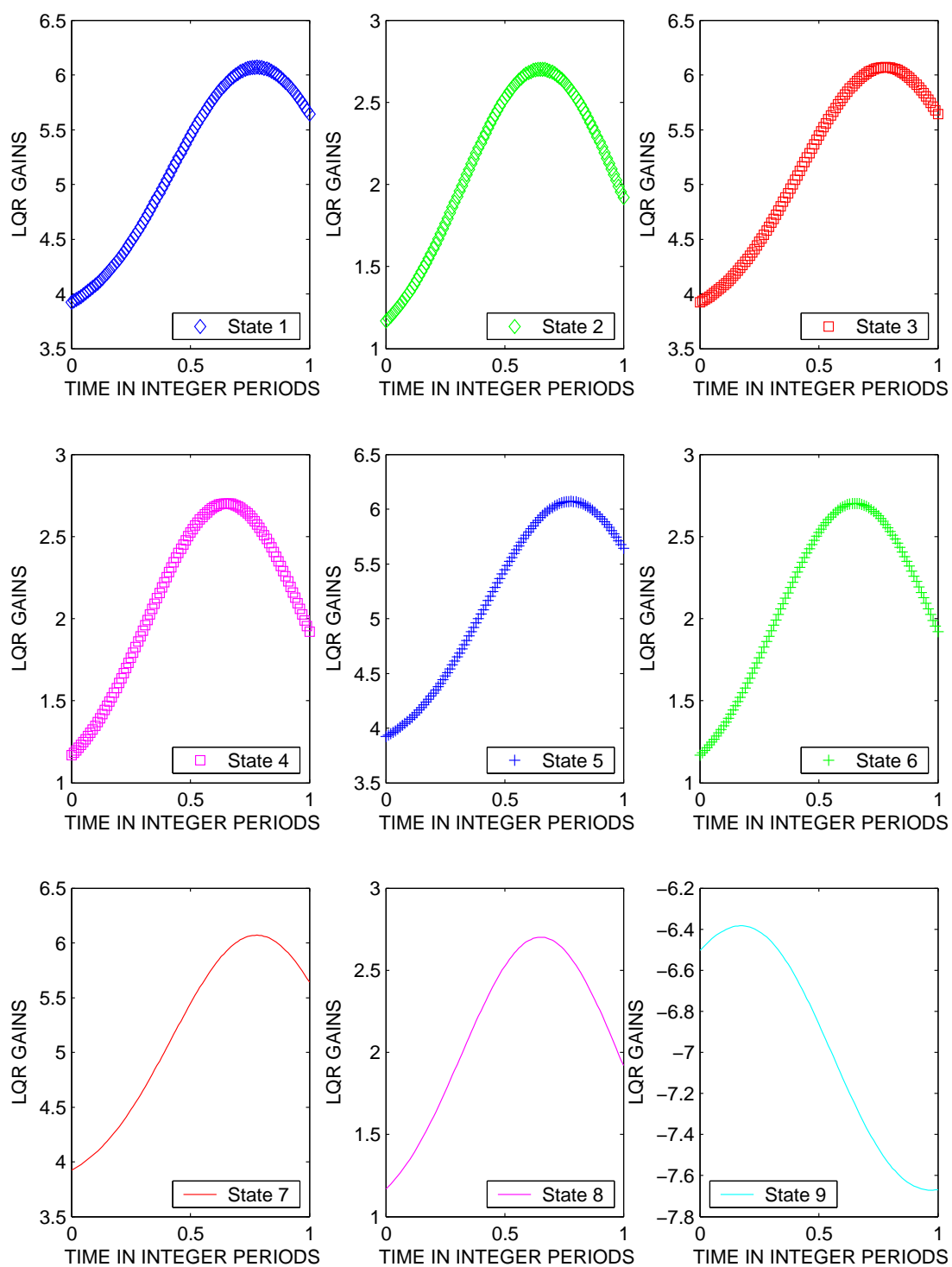


Figure E.18: All LQR Gains for case  $\omega_f = 0.1\omega_p$ ,  $S_v = 3$

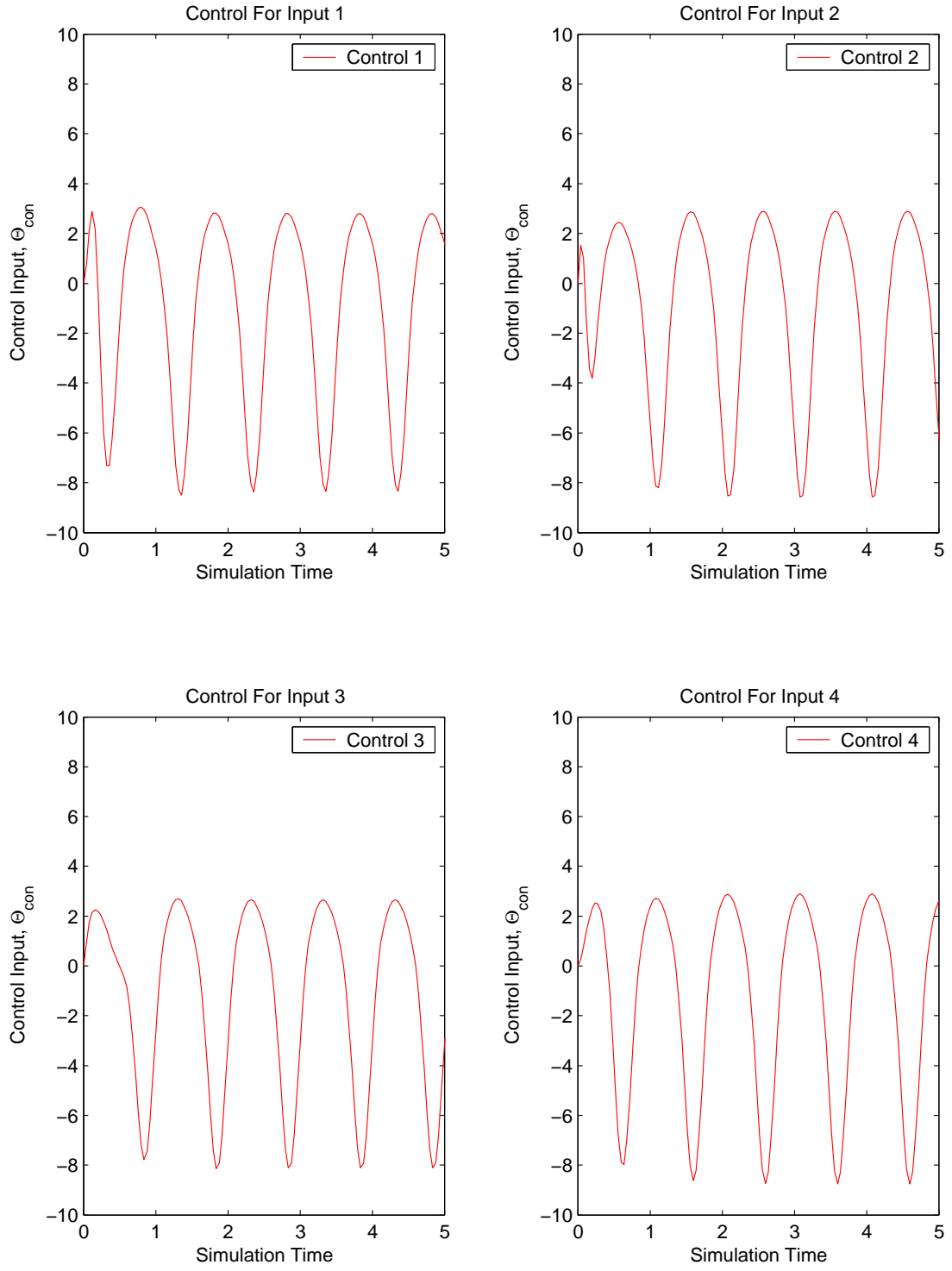


Figure E.19: Control Usage for case  $\omega_f = 0.1\omega_p$ ,  $S_v = 3$

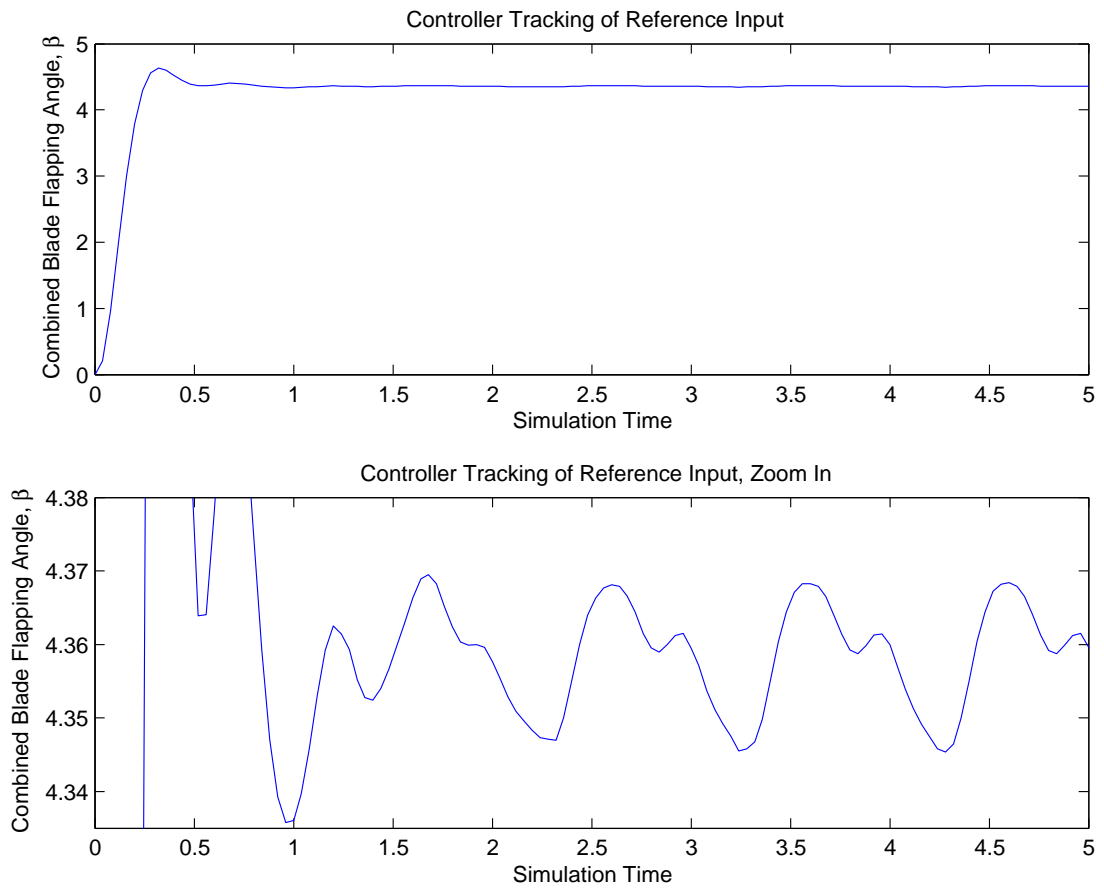


Figure E.20: Tracking Performance of Vibration Controller for case  $\omega_f = 0.1\omega_p$ ,  $S_v = 3$

Case 6	
Controller Design Parameters	
Input Frequency, $\omega_f$	Noise spectral density, $S_v$
$\omega_f = .05\omega_p$	$S_v = 3$

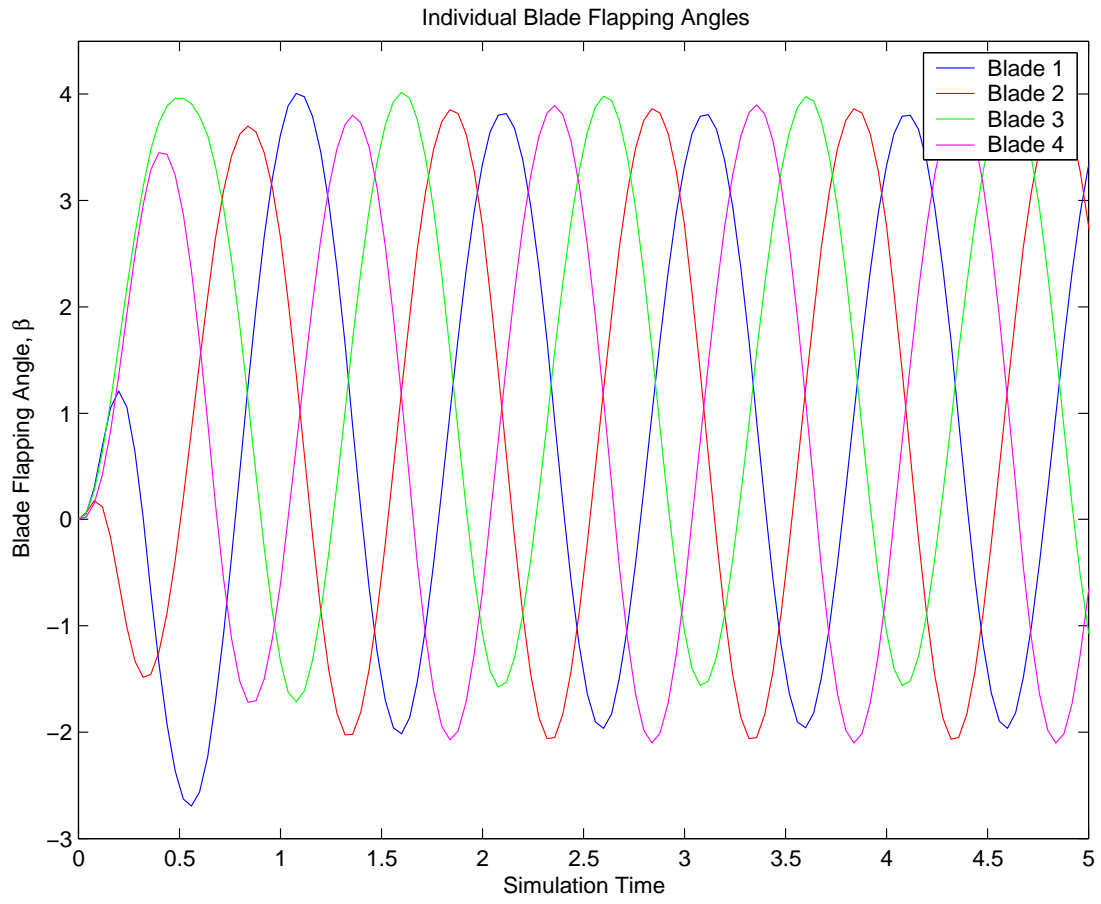


Figure E.21: Individual Flap Angles,  $\beta$ , for case  $\omega_f = 0.05\omega_p$ ,  $S_v = 3$

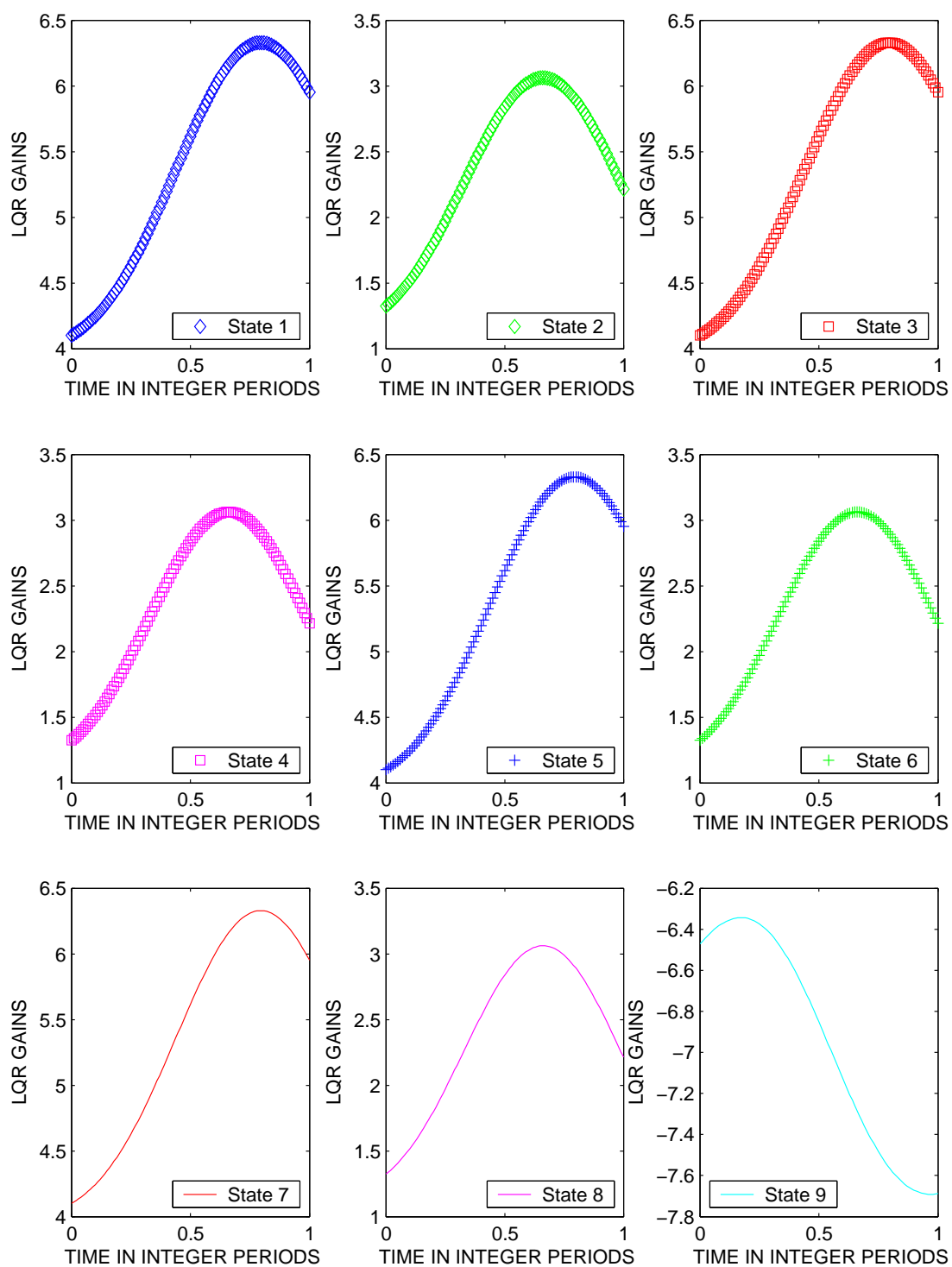


Figure E.22: All LQR Gains for case  $\omega_f = 0.05\omega_p$ ,  $S_v = 3$

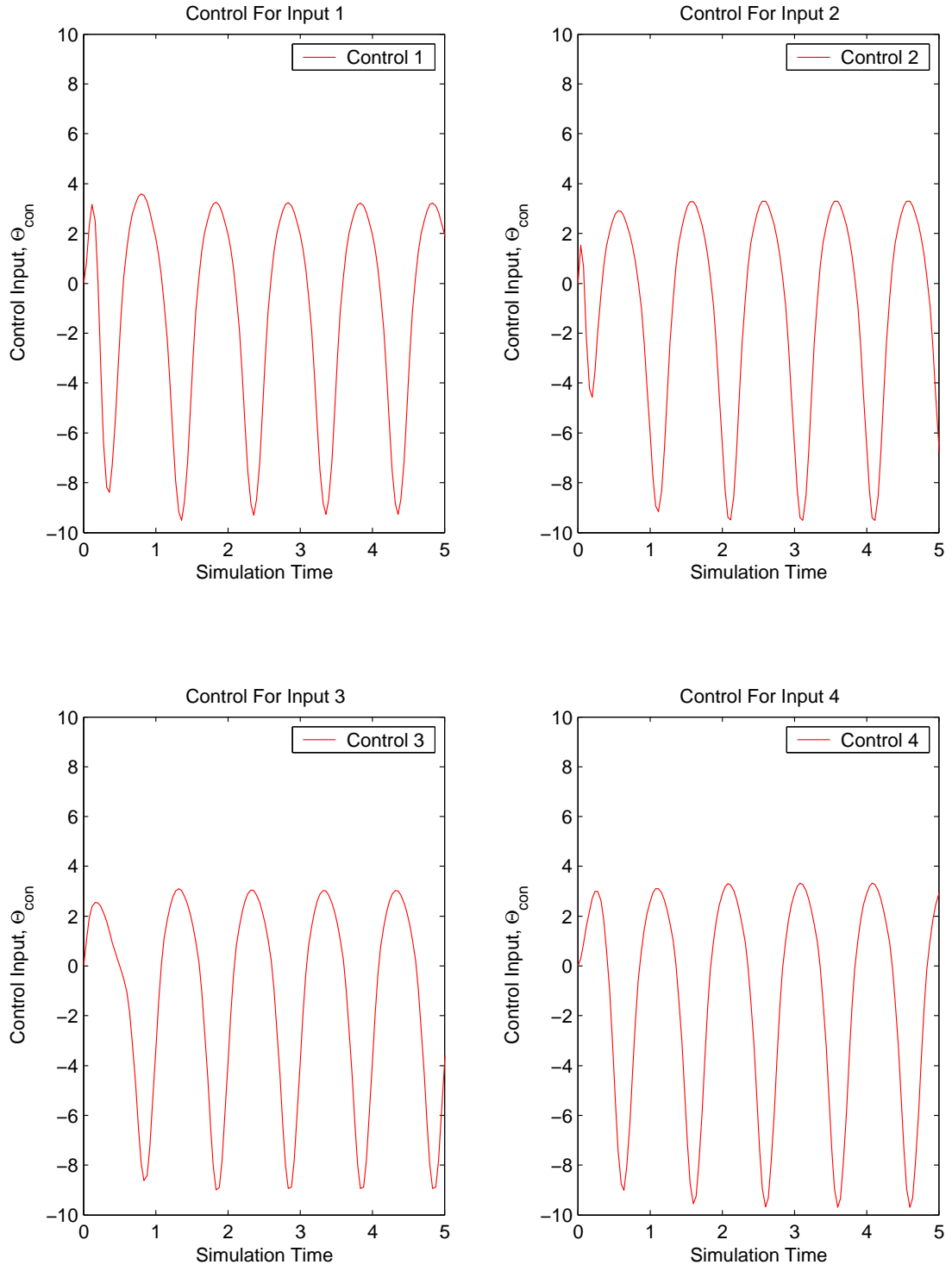


Figure E.23: Control Usage for case  $\omega_f = 0.05\omega_p$ ,  $S_v = 3$

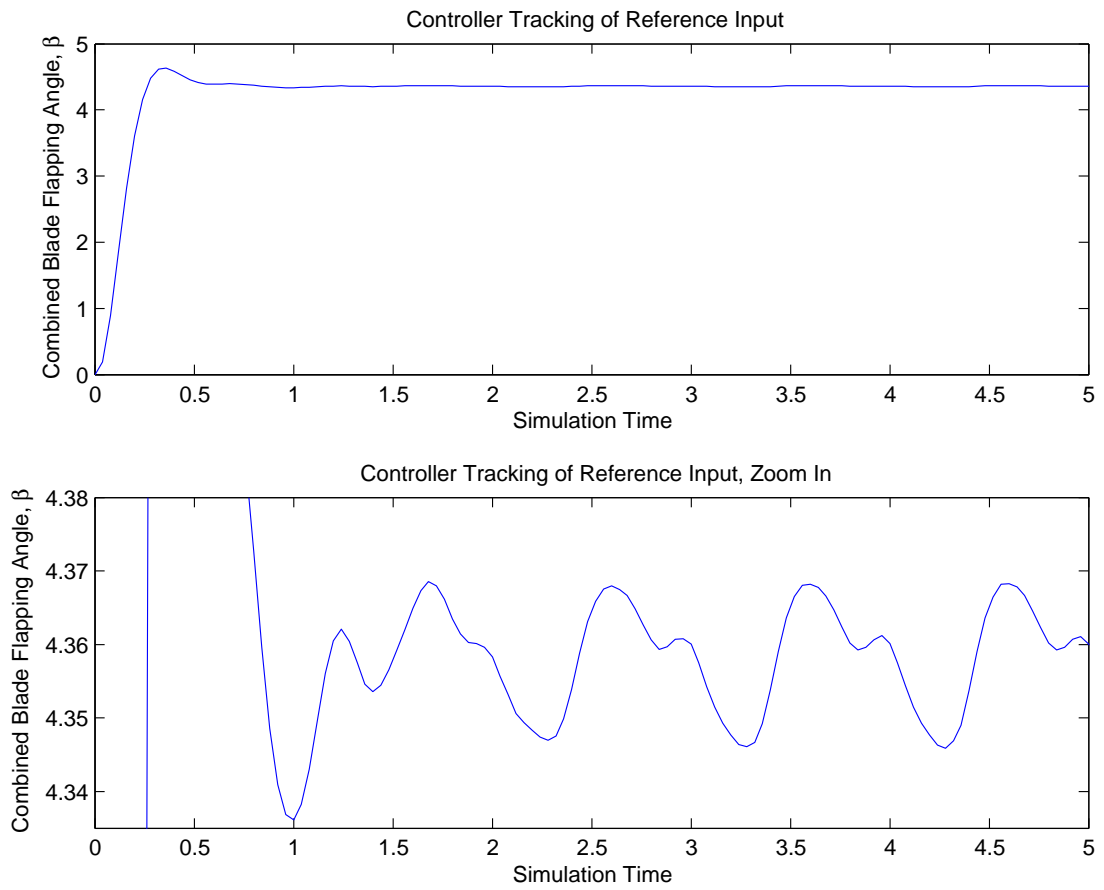


Figure E.24: Tracking Performance of Vibration Controller for case  $\omega_f = 0.05\omega_p$ ,  $S_v = 3$

Case 7	
Controller Design Parameters	
Input Frequency, $\omega_f$	Noise spectral density, $S_v$
$\omega_f = .0\omega_p$	$S_v = 3$

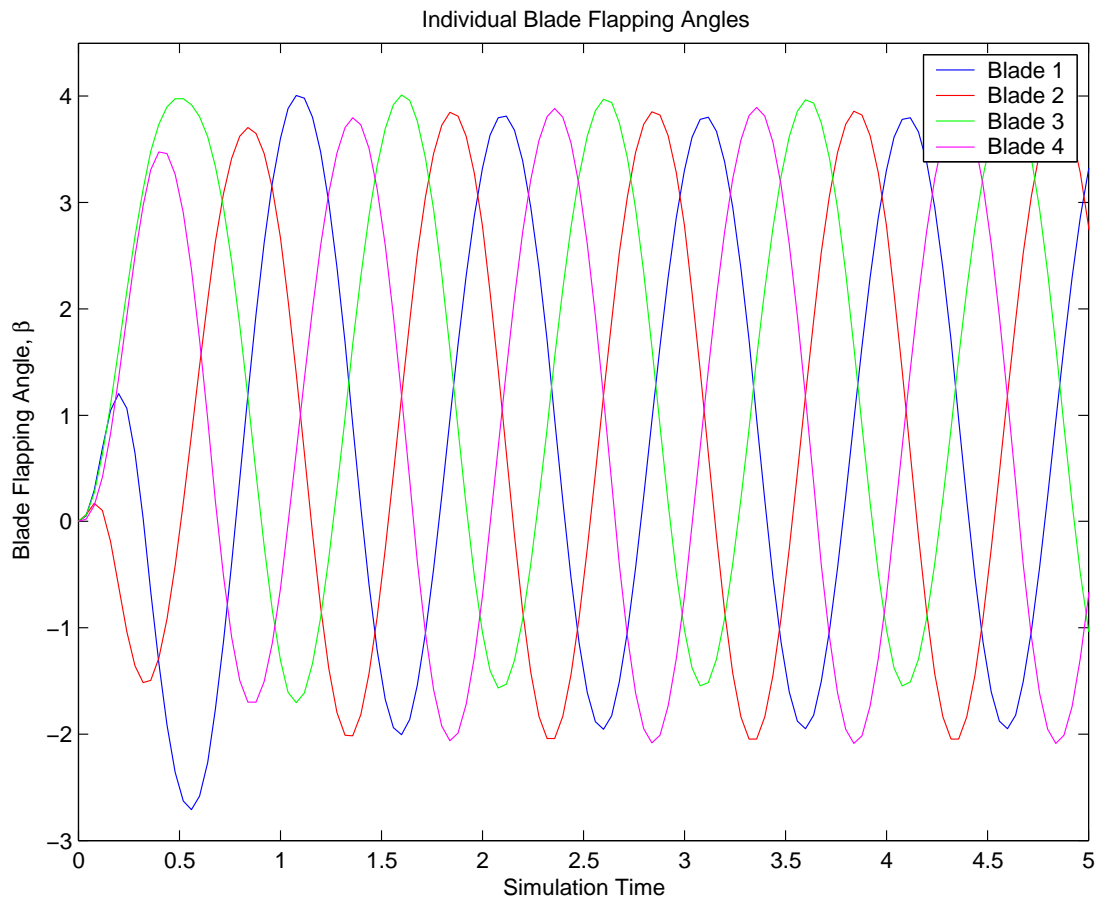


Figure E.25: Individual Flap Angles,  $\beta$ , for case  $\omega_f = 0.0\omega_p$ ,  $S_v = 3$

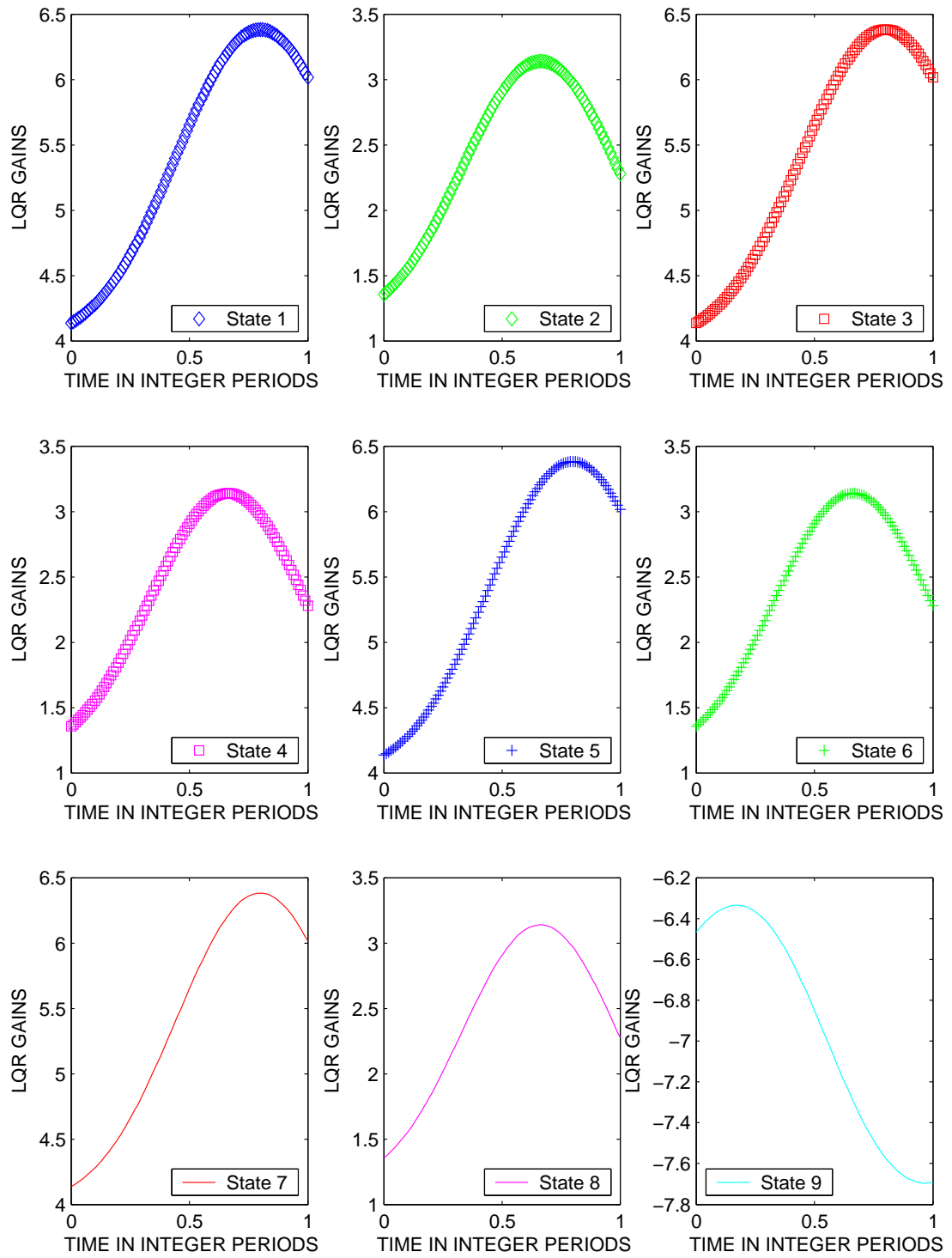


Figure E.26: All LQR Gains for case  $\omega_f = 0.0\omega_p$ ,  $S_v = 3$

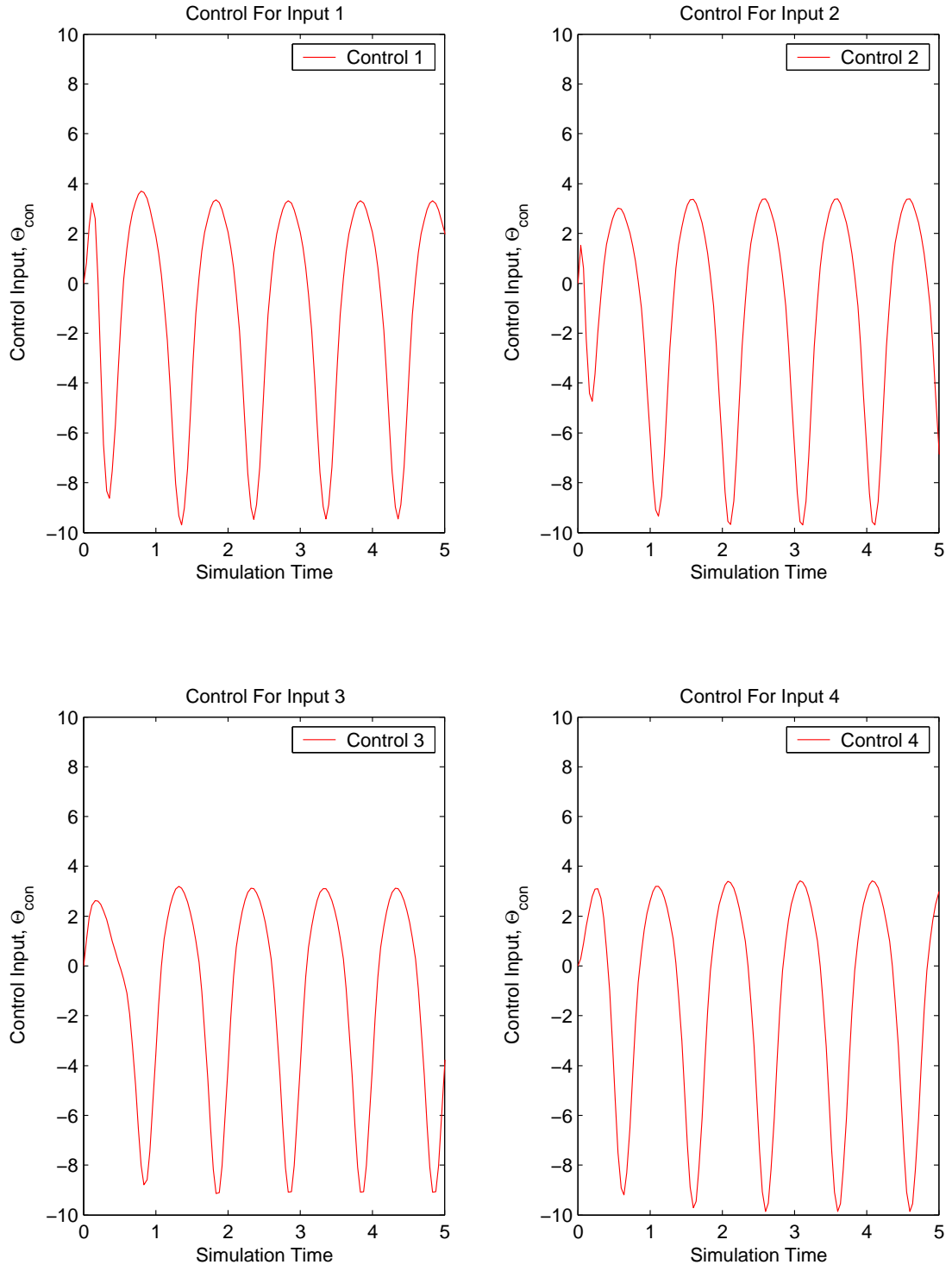


Figure E.27: Control Usage for case  $\omega_f = 0.0\omega_p$ ,  $S_v = 3$

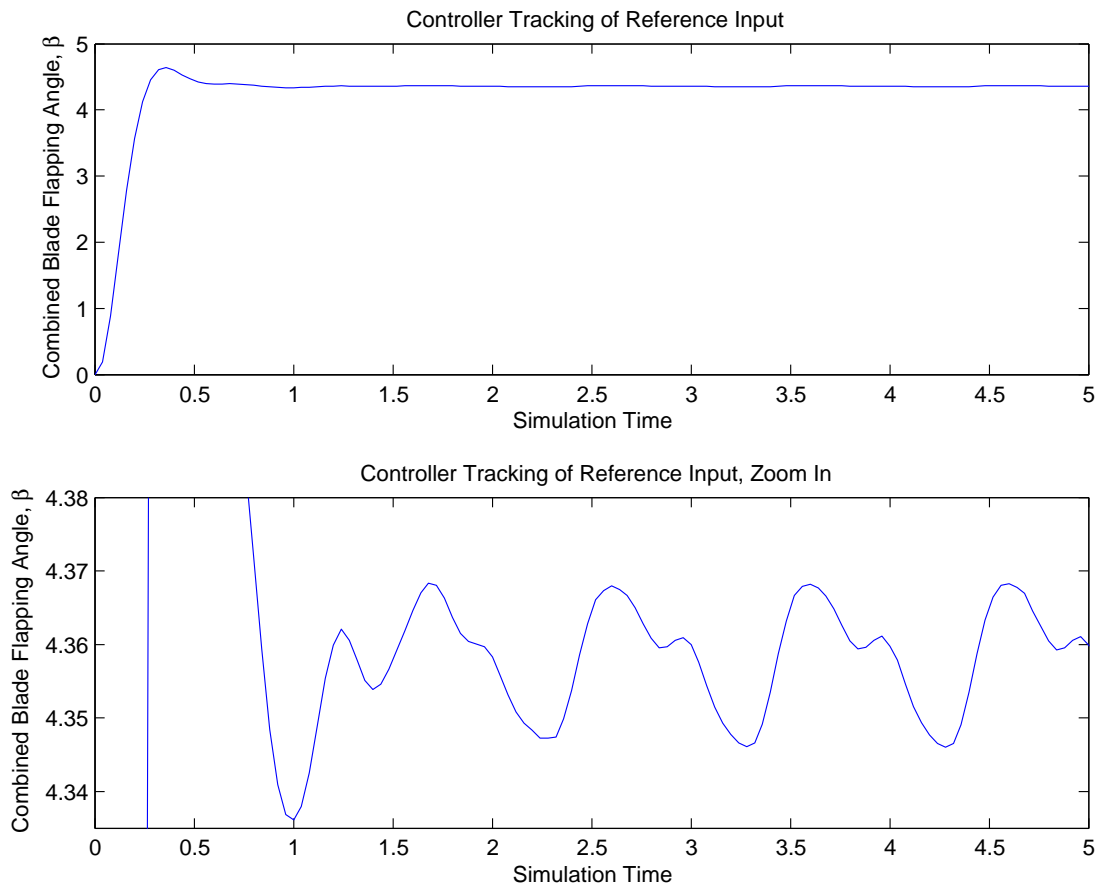


Figure E.28: Tracking Performance of Vibration Controller for case  $\omega_f = 0.0\omega_p$ ,  $S_v = 3$

## *Appendix F. Vibration Controller Comparison Plots, Noise Case*

$$S_v = 4$$

This appendix contains the plots of the individual flap angles, calculated LQR gains, control usage, and vibration controller performance as computed at specific cases of input frequency  $\omega_f$  and noise spectral density  $S_v$ . For the cases presented in this appendix, the range of values of input and measurement noise are  $\omega_f = \omega_p(0, 0.05, 0.1, 0.2, 0.3, 0.4, 0.5)$  and  $S_v = 4$  are used, which results in 7 individual cases. Each case will present four plots; one representing the individual flap angles of each blade after control is applied to eliminate the asymmetric lift, one for calculated LQR gains, one for control usage,  $\Theta_{con}$  for each blade, and one depicting the vibration controller performance in terms of matching the reference input.

Case 1	
Controller Design Parameters	
Input Frequency, $\omega_f$	Noise spectral density, $S_v$
$\omega_f = .5\omega_p$	$S_v = 4$

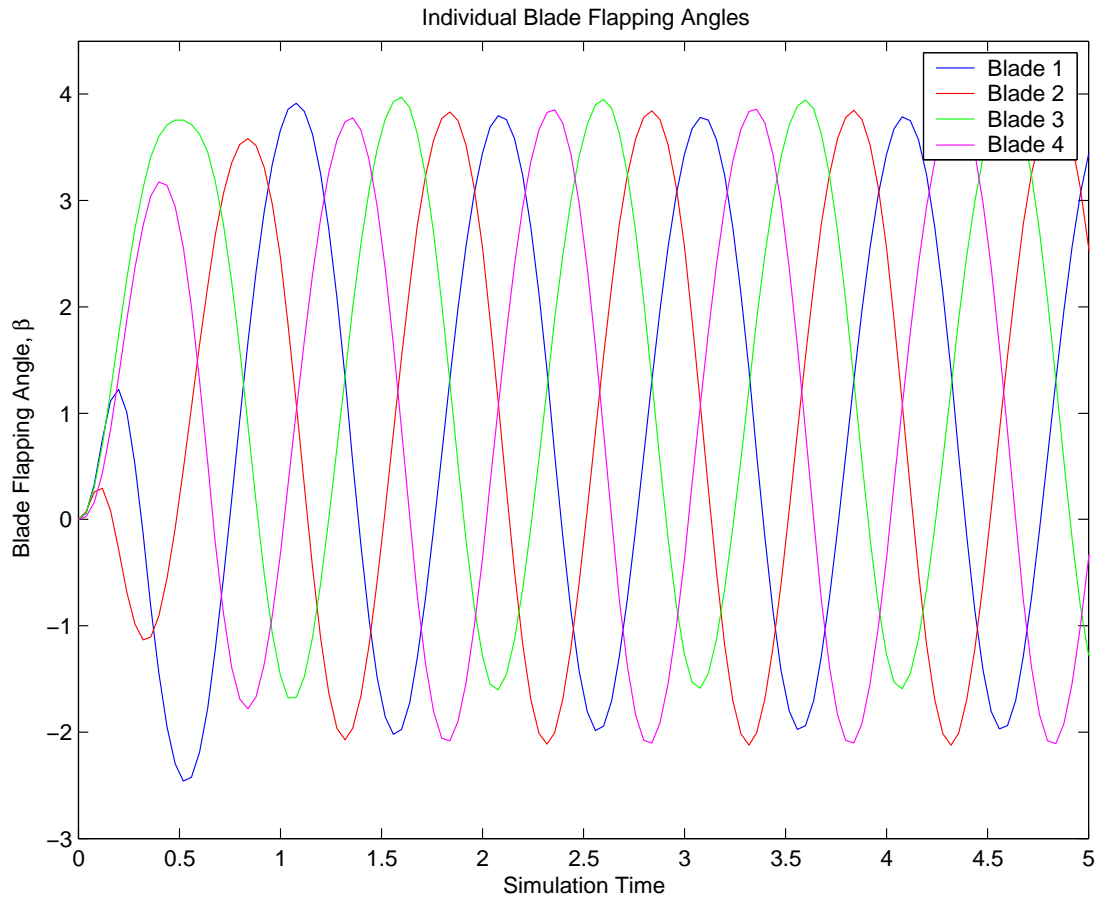


Figure F.1: Individual Flap Angles,  $\beta$ , for case  $\omega_f = 0.5\omega_p$ ,  $S_v = 4$

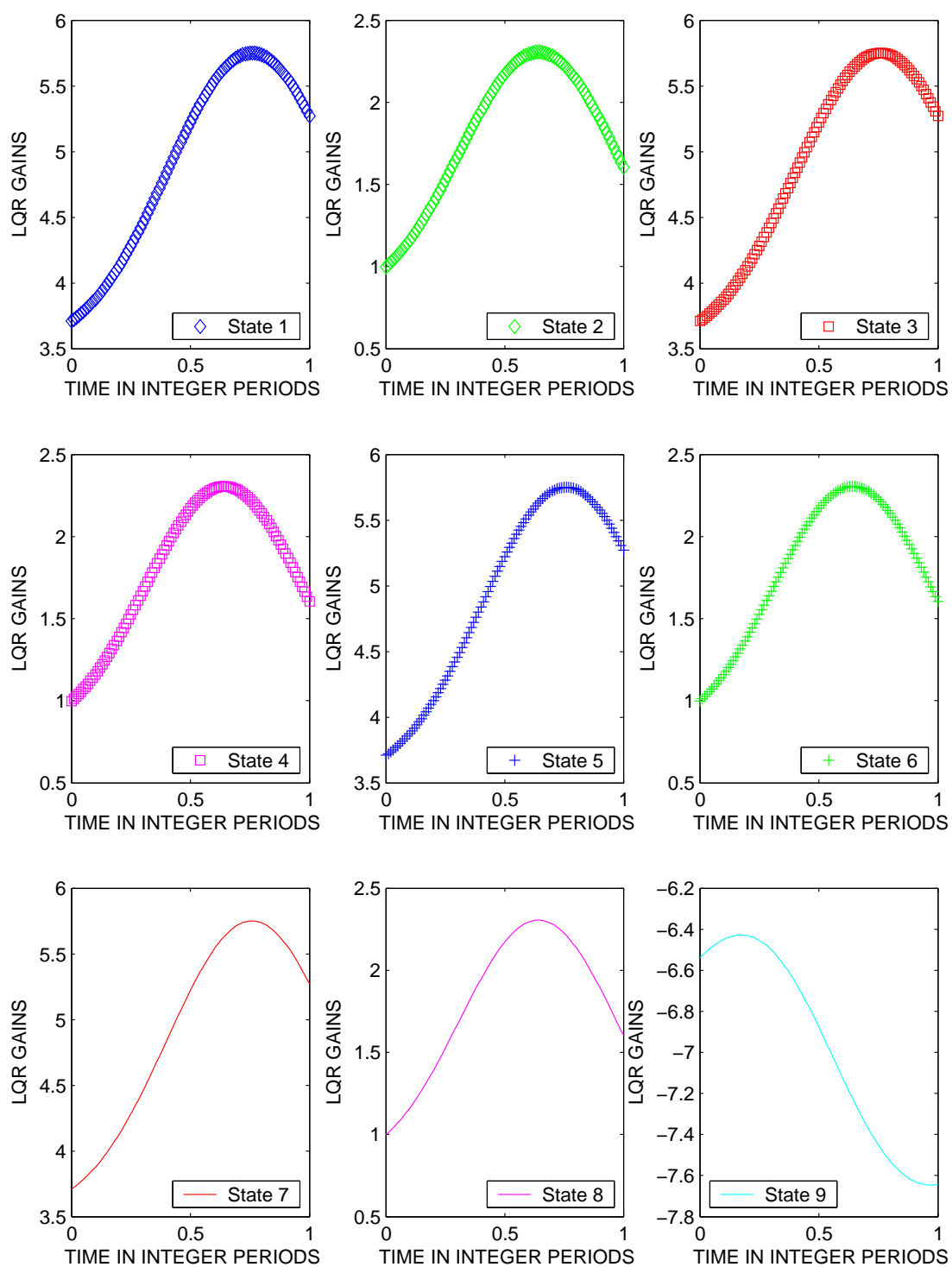


Figure F.2: All LQR Gains for case  $\omega_f = 0.5\omega_p$ ,  $S_v = 4$

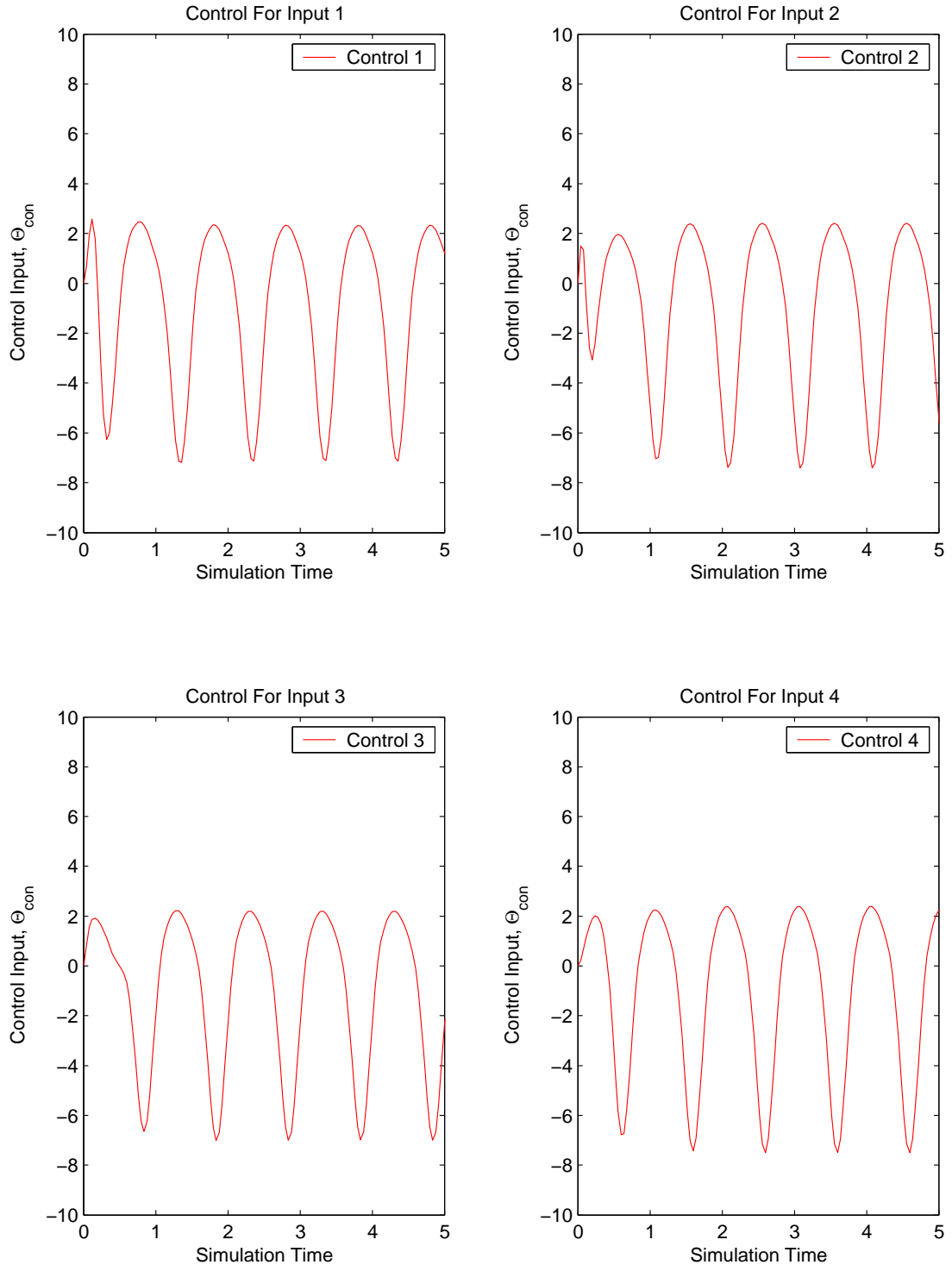


Figure F.3: Control Usage for case  $\omega_f = 0.5\omega_p$ ,  $S_v = 4$

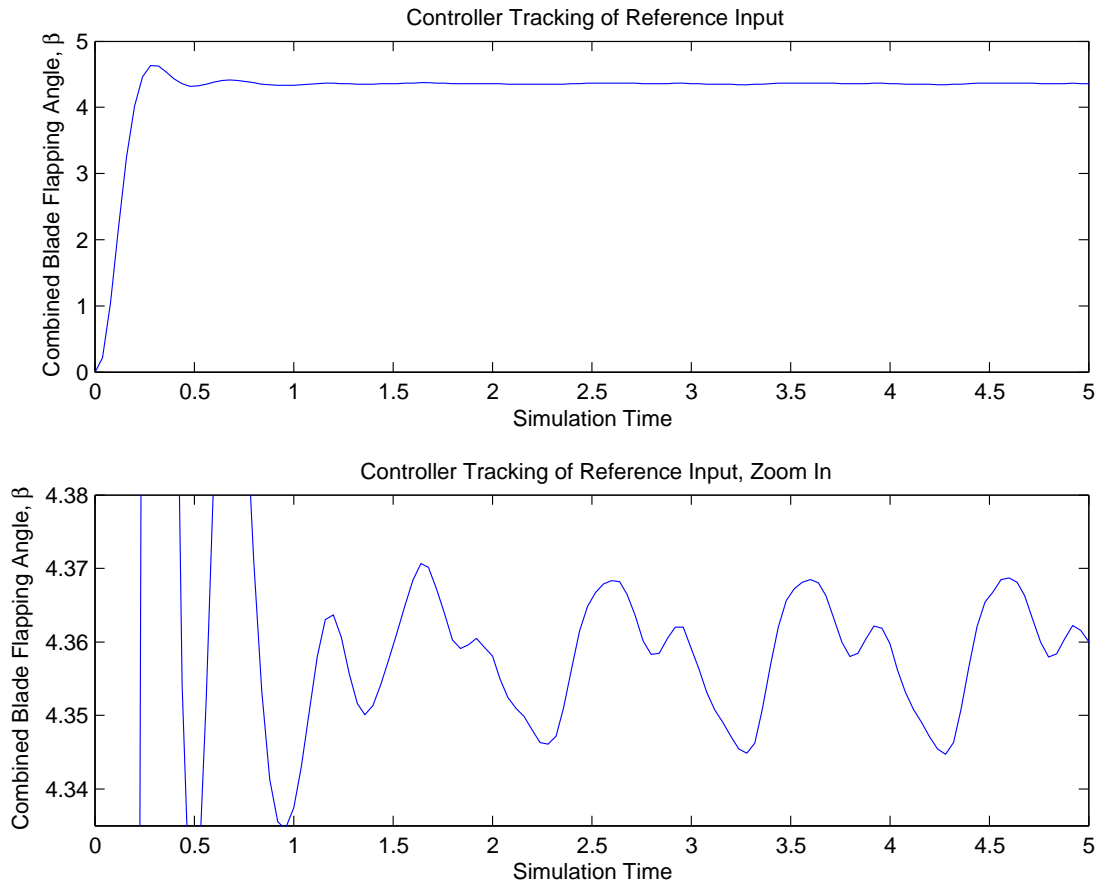


Figure F.4: Tracking Performance of Vibration Controller for case  $\omega_f = 0.5\omega_p$ ,  $S_v = 4$

Case 2	
Controller Design Parameters	
Input Frequency, $\omega_f$	Noise spectral density, $S_v$
$\omega_f = .4\omega_p$	$S_v = 4$

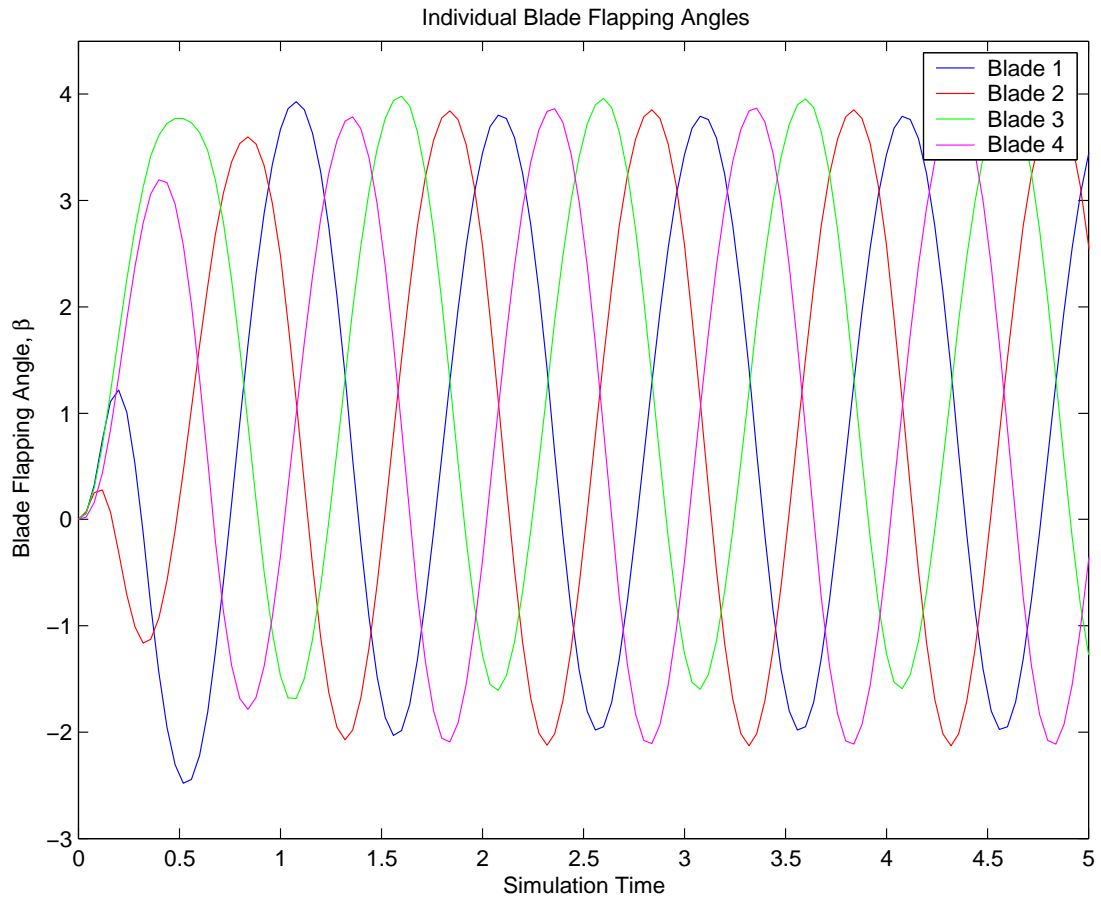


Figure F.5: Individual Flap Angles,  $\beta$ , for case  $\omega_f = 0.4\omega_p$ ,  $S_v = 4$

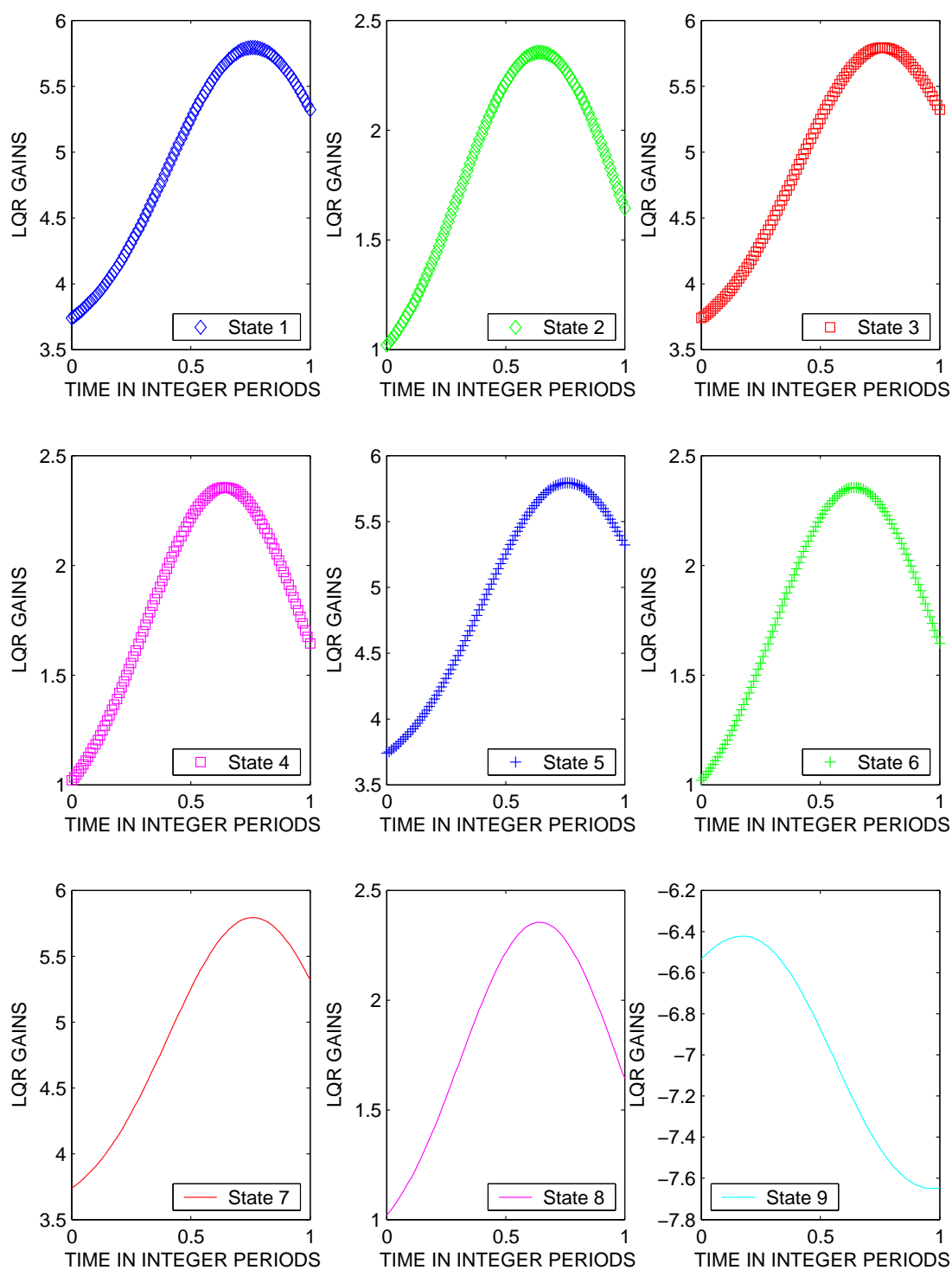


Figure F.6: All LQR Gains for case  $\omega_f = 0.4\omega_p$ ,  $S_v = 4$

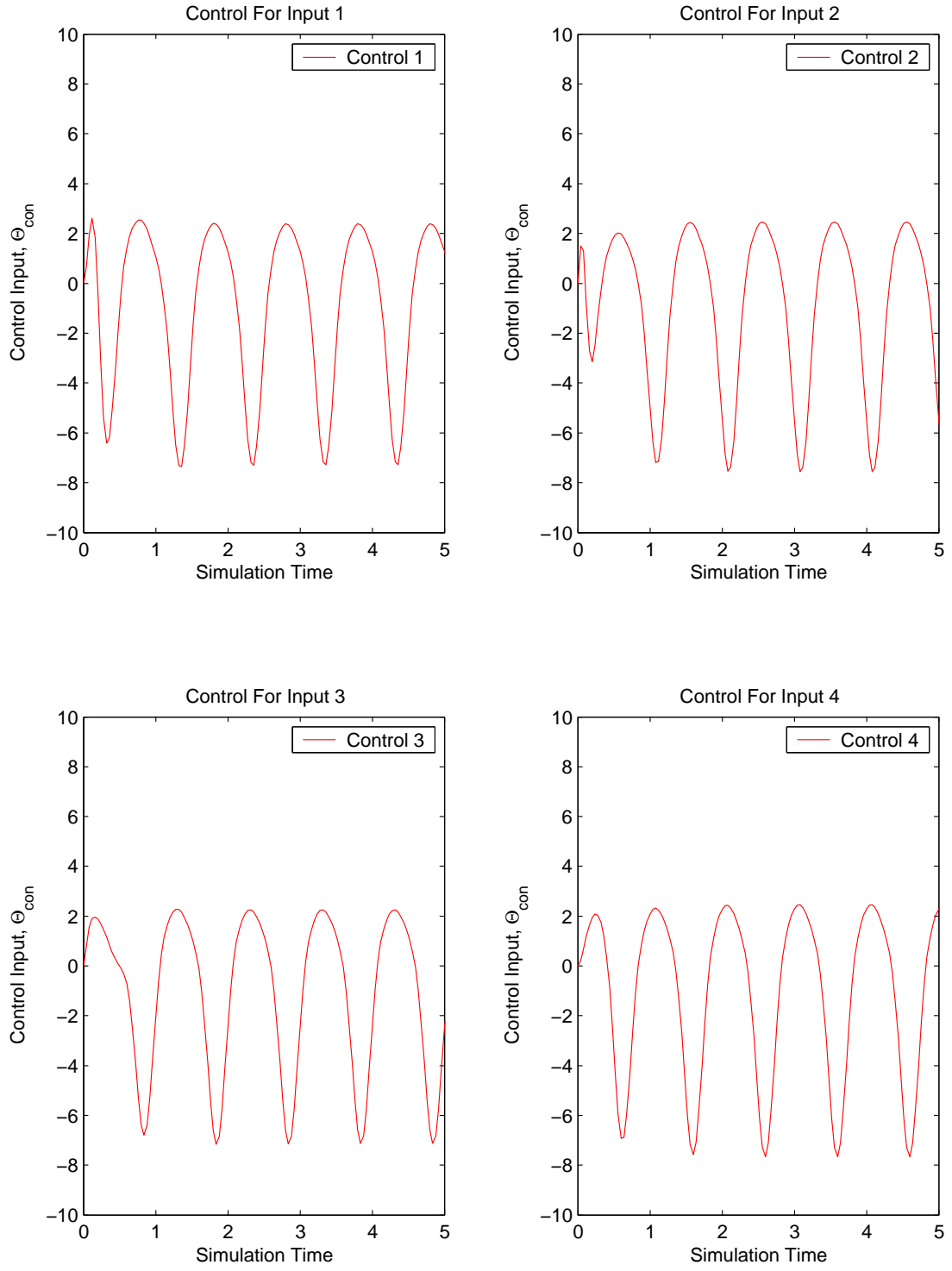


Figure F.7: Control Usage for case  $\omega_f = 0.4\omega_p$ ,  $S_v = 4$

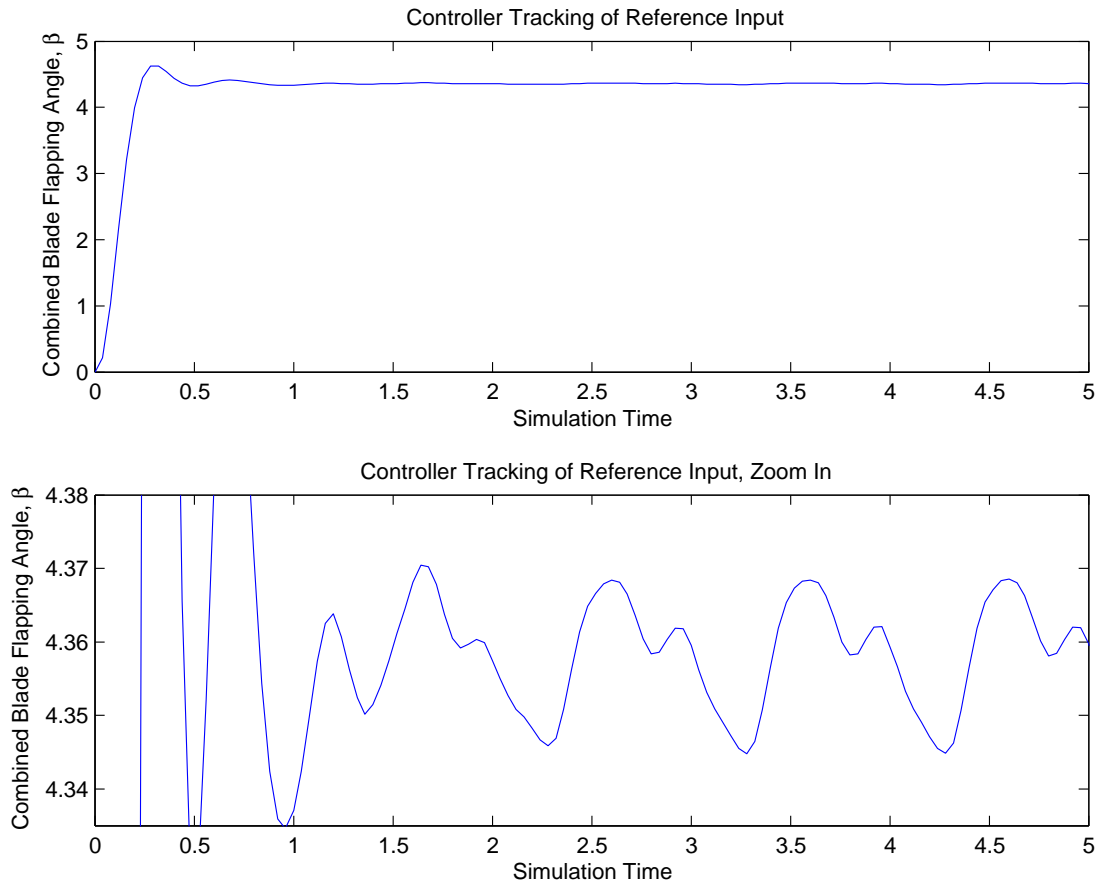


Figure F.8: Tracking Performance of Vibration Controller for case  $\omega_f = 0.4\omega_p$ ,  $S_v = 4$

Case 3	
Controller Design Parameters	
Input Frequency, $\omega_f$	Noise spectral density, $S_v$
$\omega_f = .3\omega_p$	$S_v = 4$

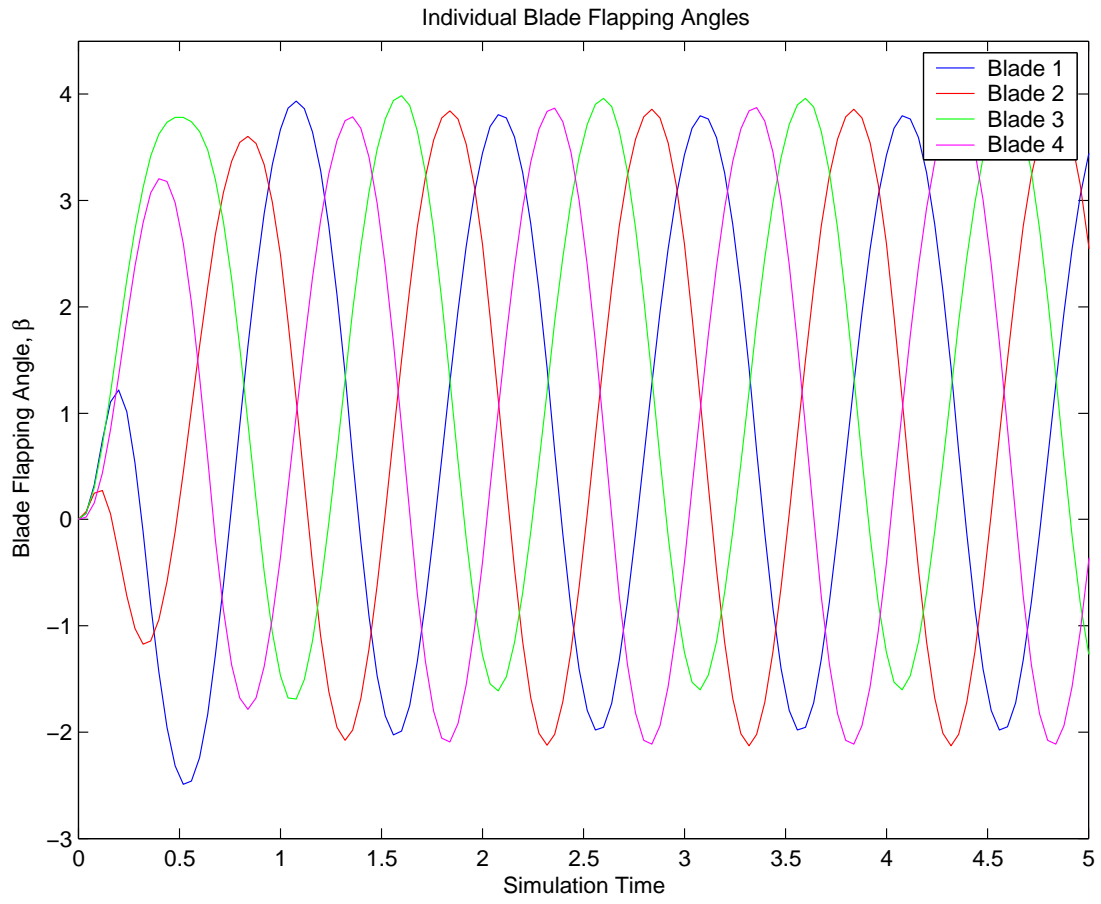


Figure F.9: Individual Flap Angles,  $\beta$ , for case  $\omega_f = 0.3\omega_p$ ,  $S_v = 4$

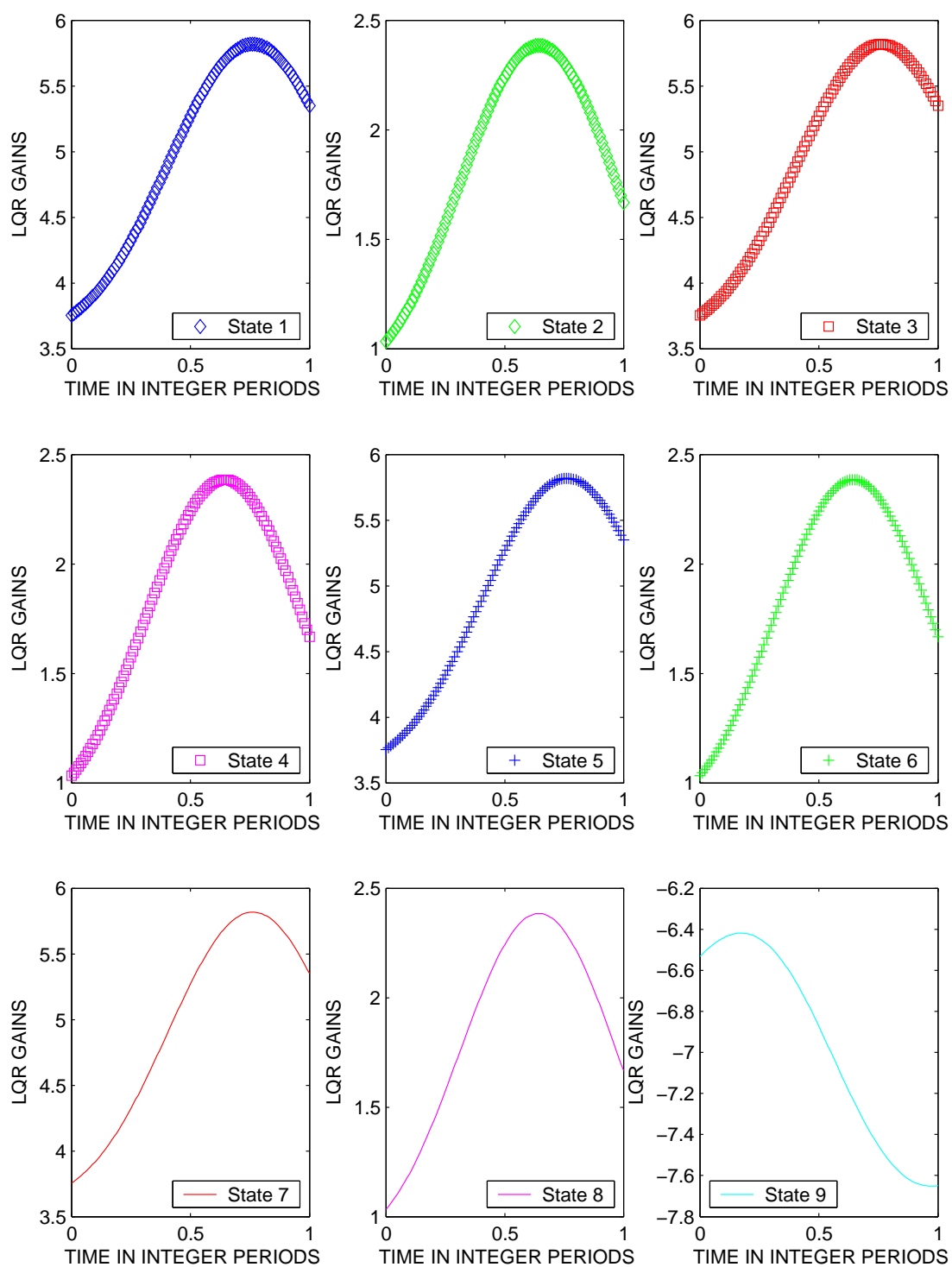


Figure F.10: All LQR Gains for case  $\omega_f = 0.3\omega_p$ ,  $S_v = 4$

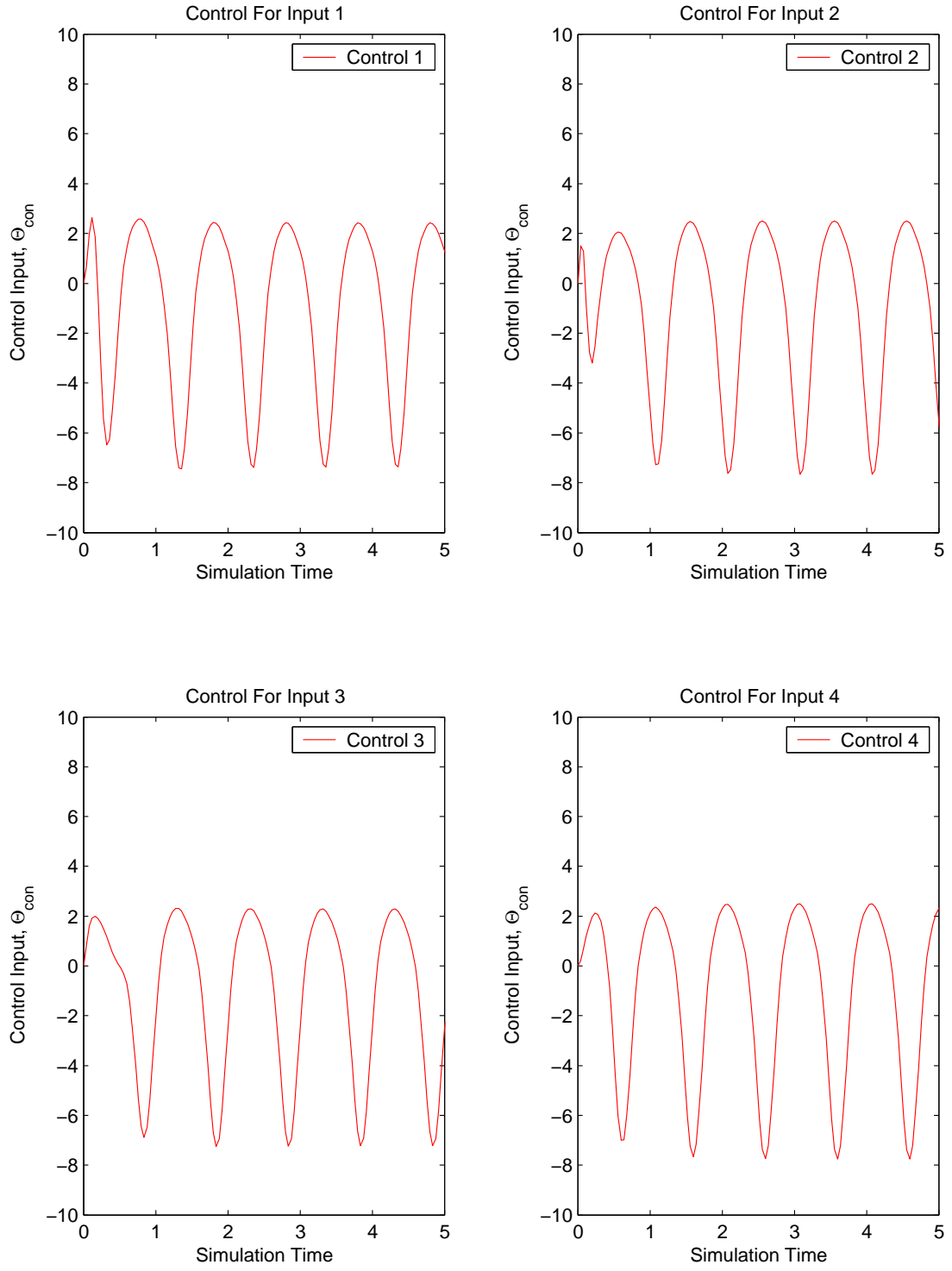


Figure F.11: Control Usage for case  $\omega_f = 0.3\omega_p$ ,  $S_v = 4$

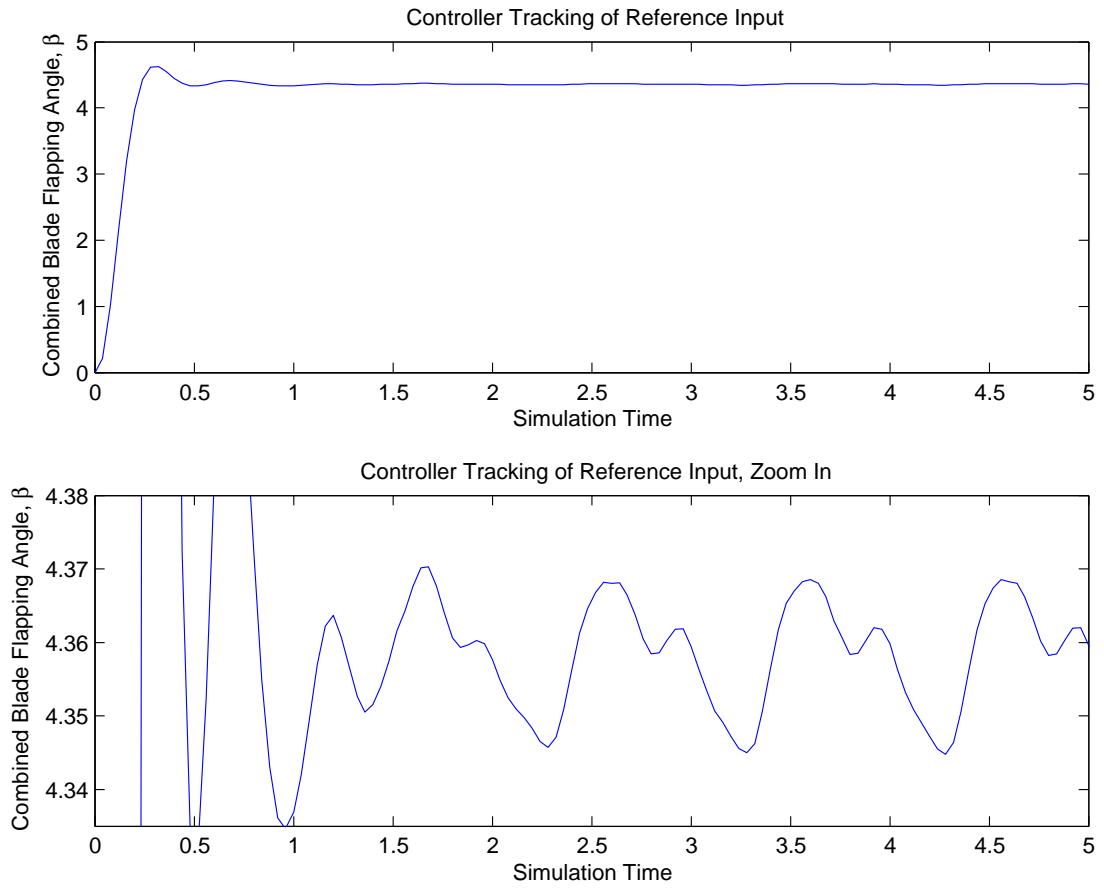


Figure F.12: Tracking Performance of Vibration Controller for case  $\omega_f = 0.3\omega_p$ ,  $S_v = 4$

Case 4	
Controller Design Parameters	
Input Frequency, $\omega_f$	Noise spectral density, $S_v$
$\omega_f = .2\omega_p$	$S_v = 4$

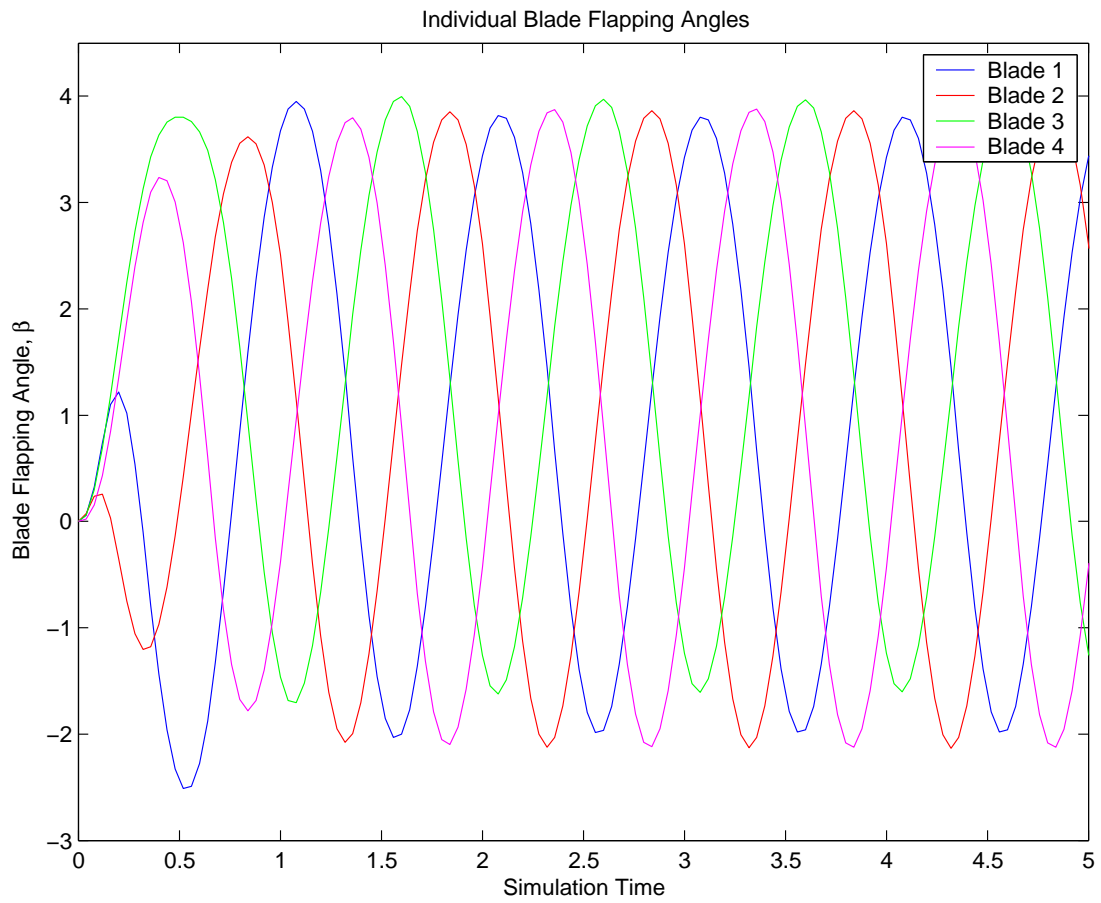


Figure F.13: Individual Flap Angles,  $\beta$ , for case  $\omega_f = 0.2\omega_p$ ,  $S_v = 4$

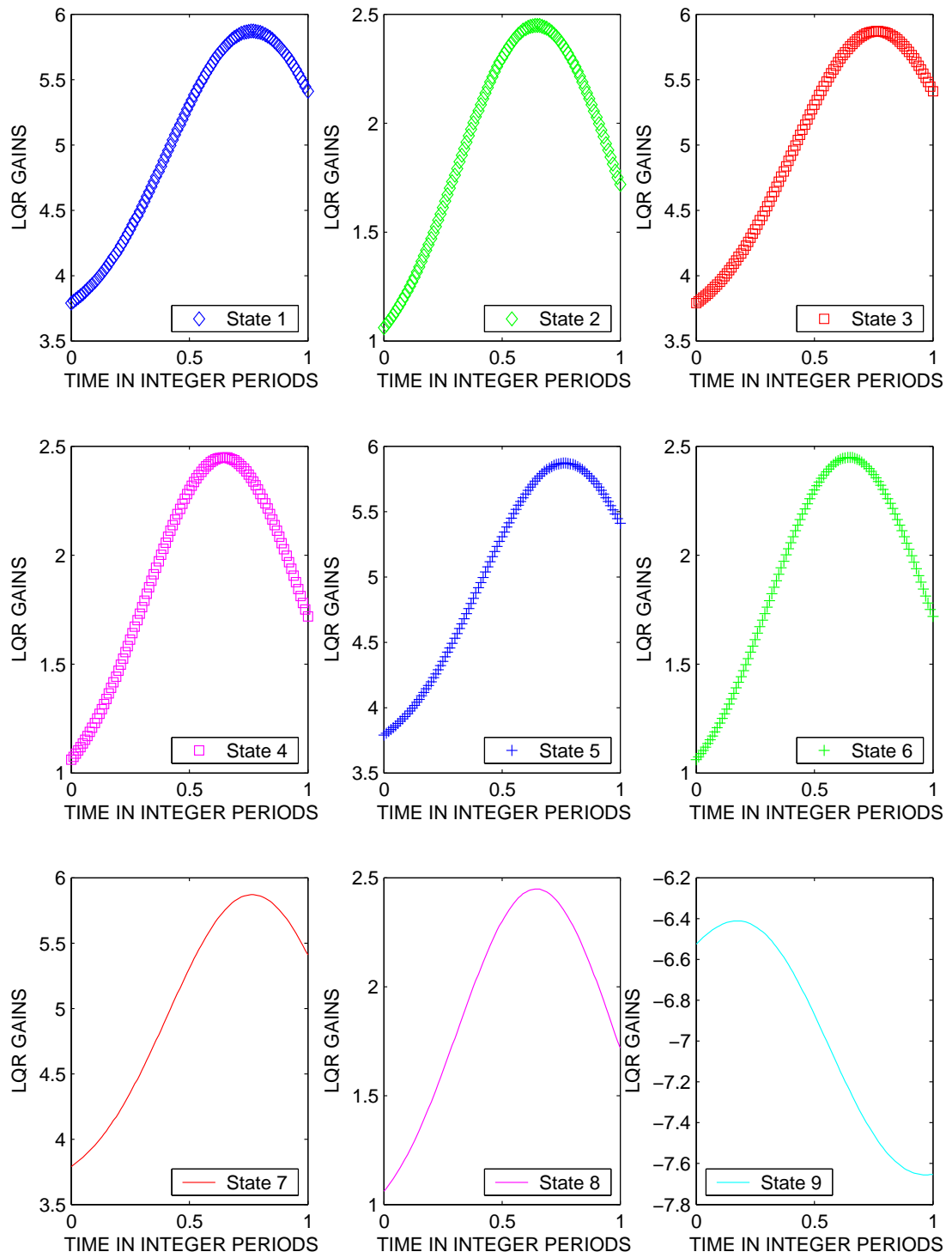


Figure F.14: All LQR Gains for case  $\omega_f = 0.2\omega_p$ ,  $S_v = 4$

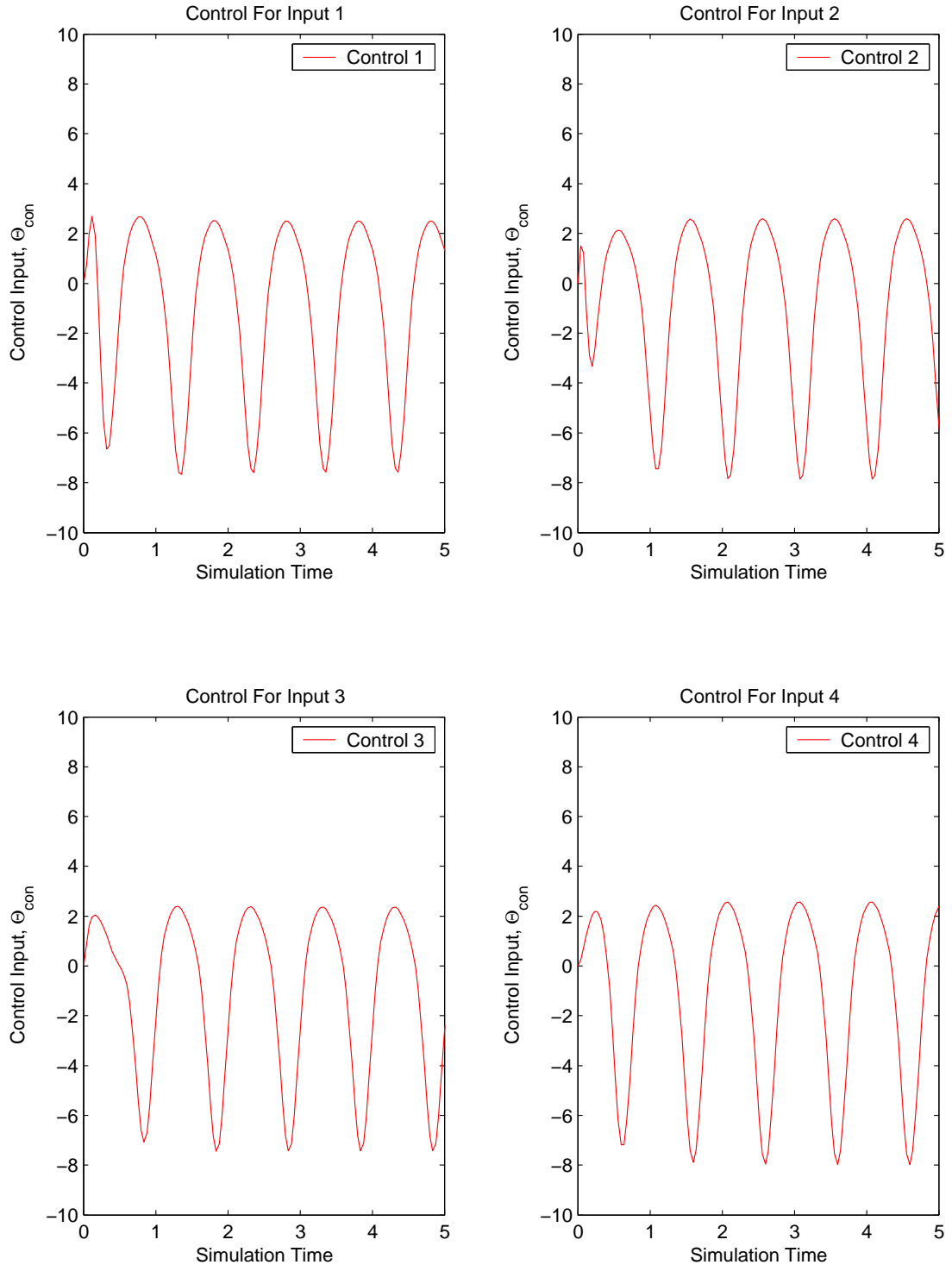


Figure F.15: Control Usage for case  $\omega_f = 0.2\omega_p$ ,  $S_v = 4$

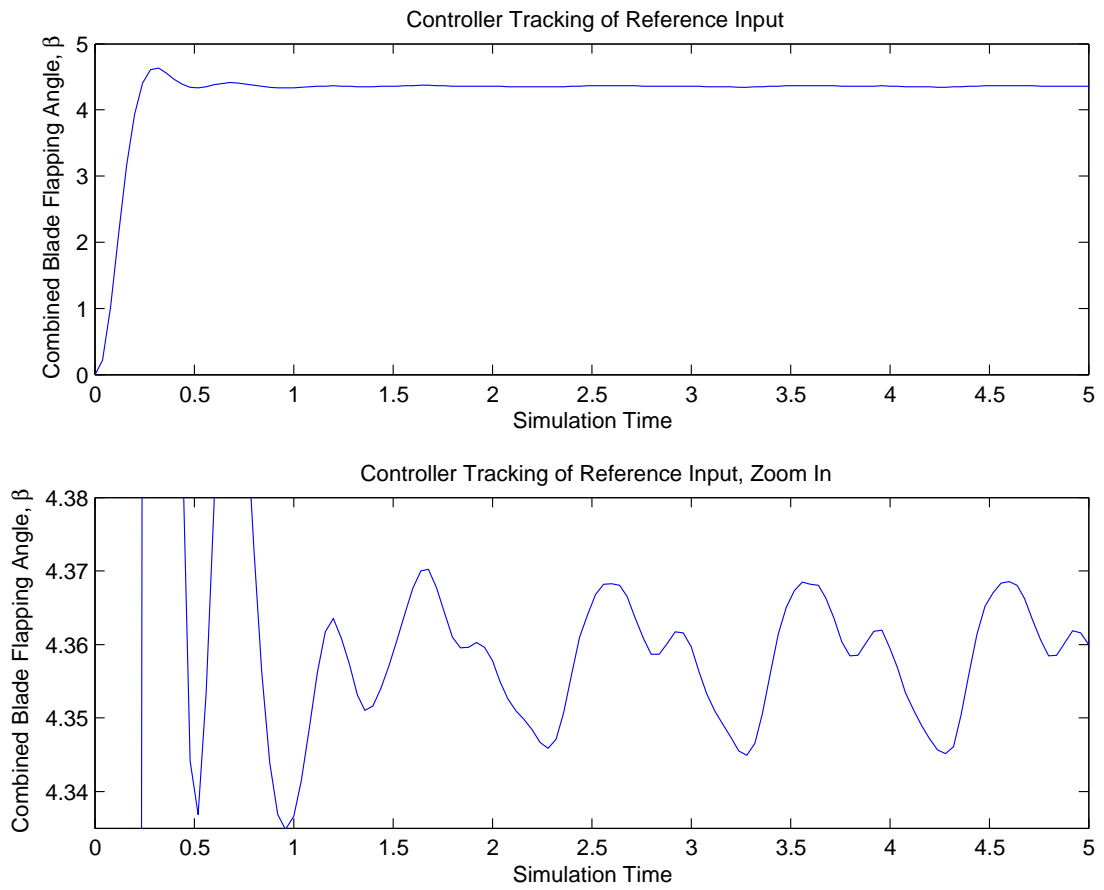


Figure F.16: Tracking Performance of Vibration Controller for case  $\omega_f = 0.2\omega_p$ ,  $S_v = 4$

Case 5	
Controller Design Parameters	
Input Frequency, $\omega_f$	Noise spectral density, $S_v$
$\omega_f = .1\omega_p$	$S_v = 4$

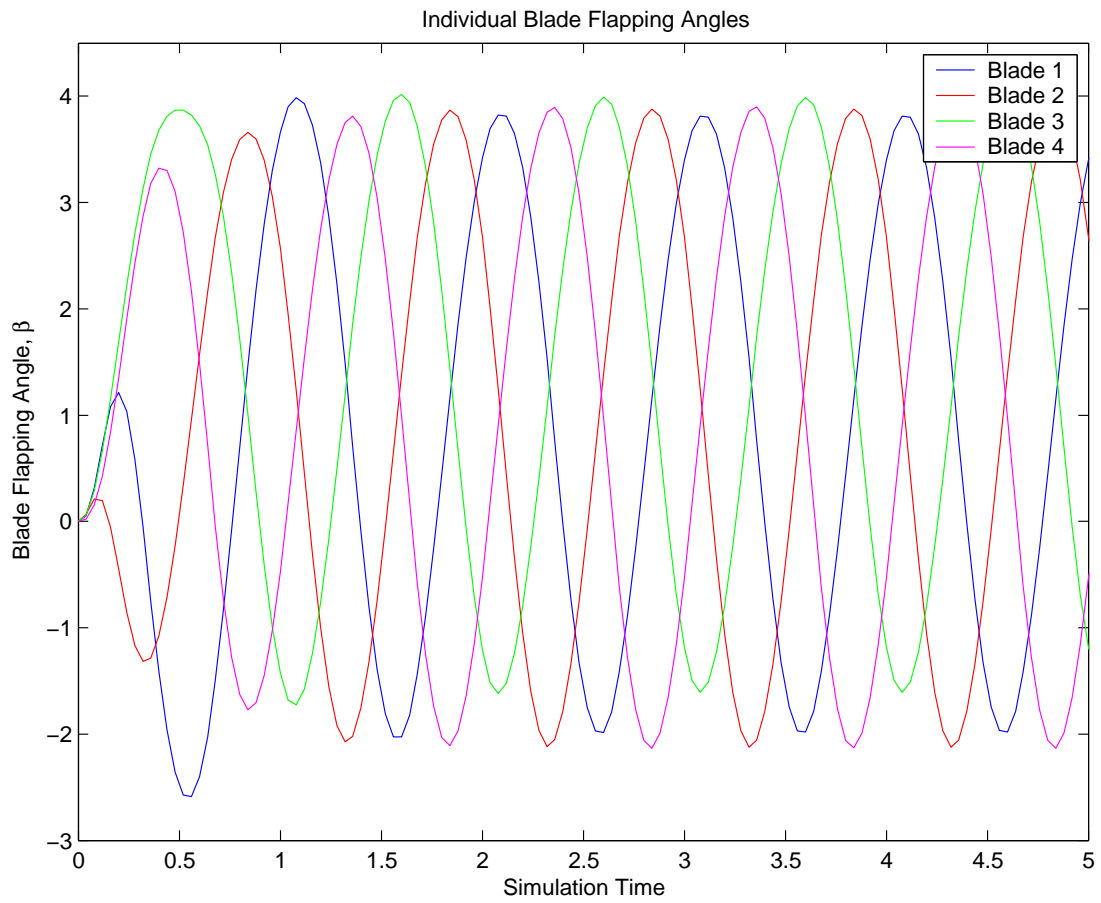


Figure F.17: Individual Flap Angles,  $\beta$ , for case  $\omega_f = 0.1\omega_p$ ,  $S_v = 4$

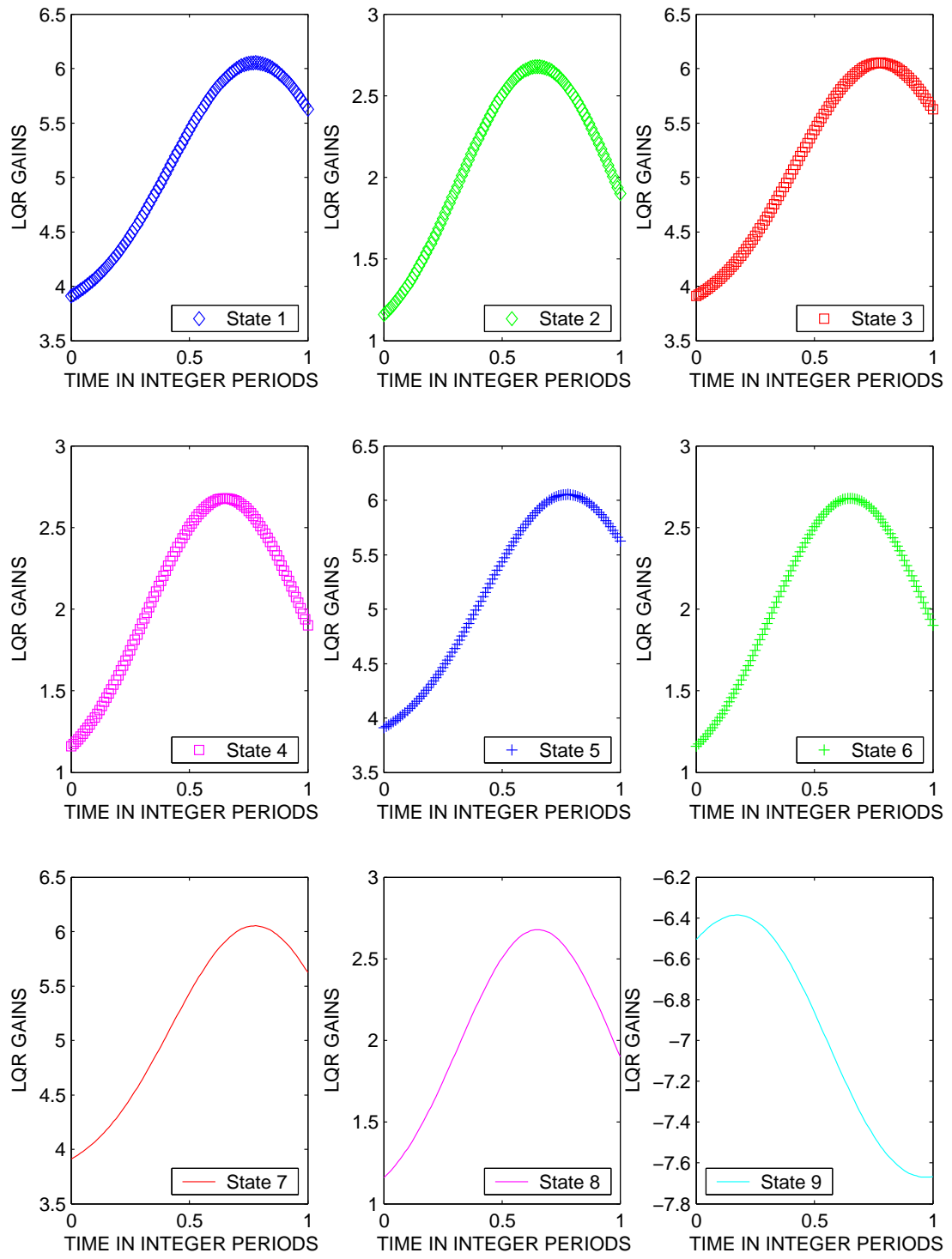


Figure F.18: All LQR Gains for case  $\omega_f = 0.1\omega_p$ ,  $S_v = 4$

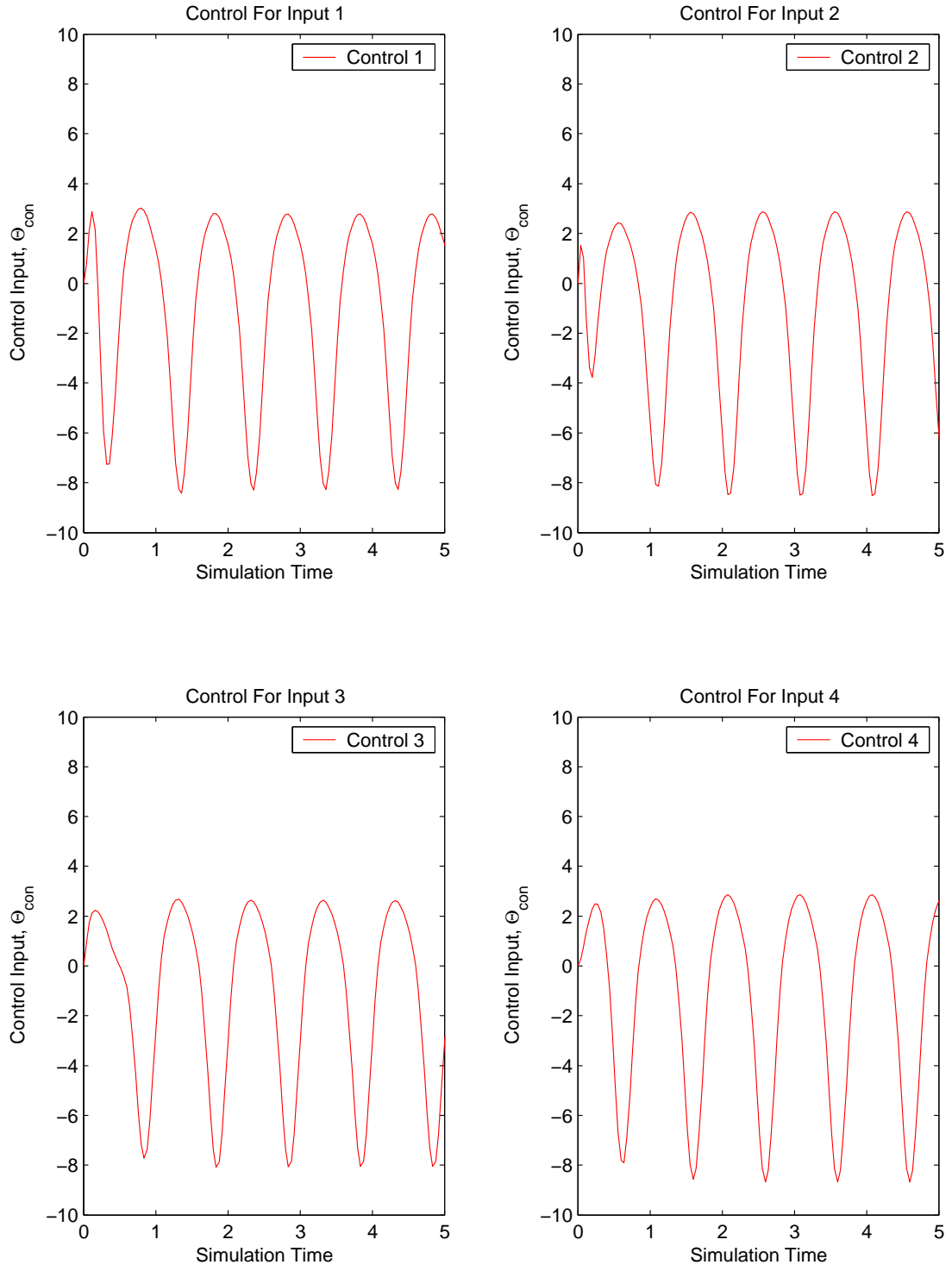


Figure F.19: Control Usage for case  $\omega_f = 0.1\omega_p$ ,  $S_v = 4$

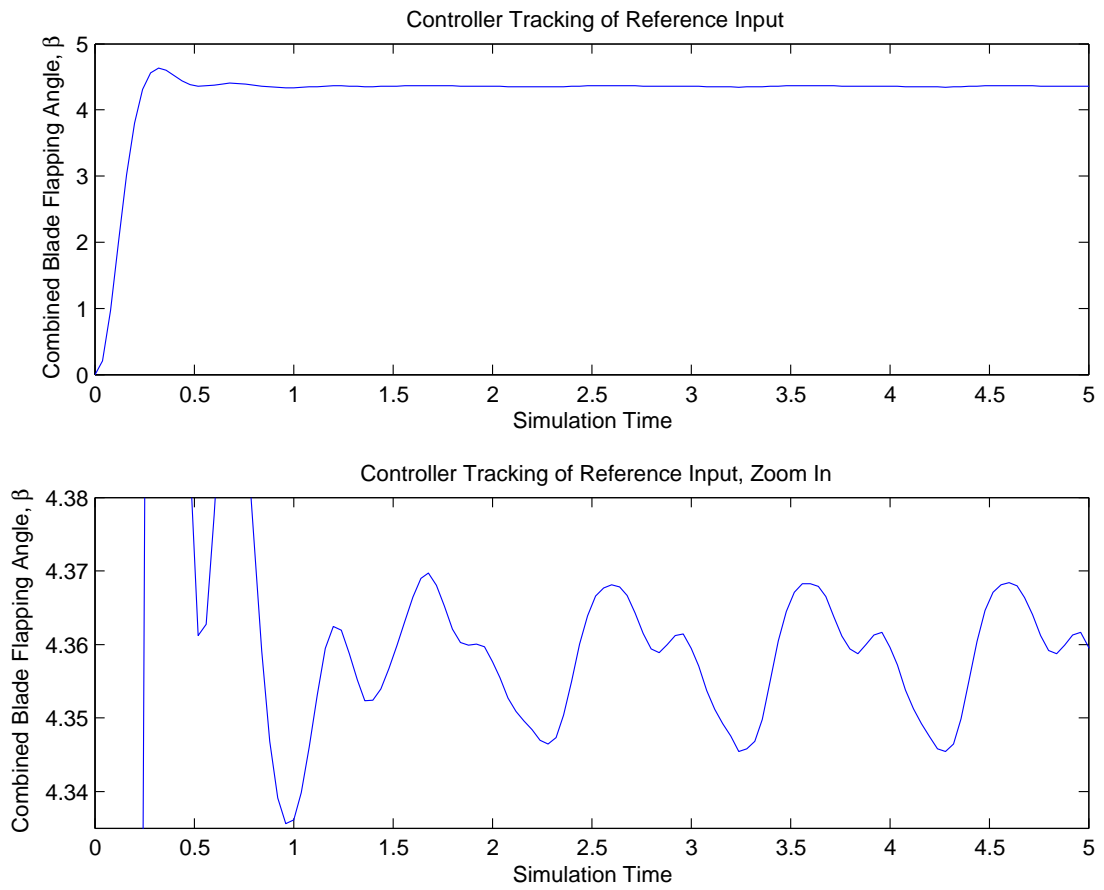


Figure F.20: Tracking Performance of Vibration Controller for case  $\omega_f = 0.1\omega_p$ ,  $S_v = 4$

Case 6	
Controller Design Parameters	
Input Frequency, $\omega_f$	Noise spectral density, $S_v$
$\omega_f = .05\omega_p$	$S_v = 4$

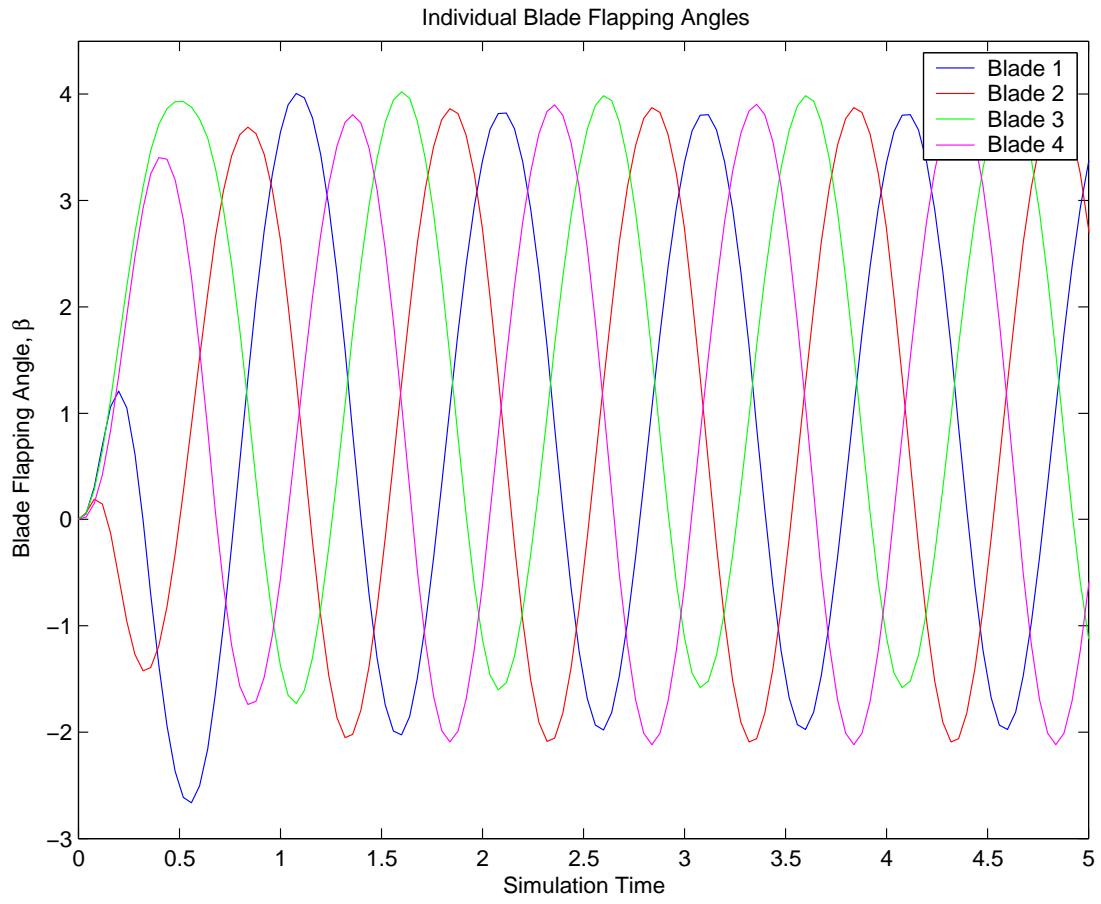


Figure F.21: Individual Flap Angles,  $\beta$ , for case  $\omega_f = 0.05\omega_p$ ,  $S_v = 4$

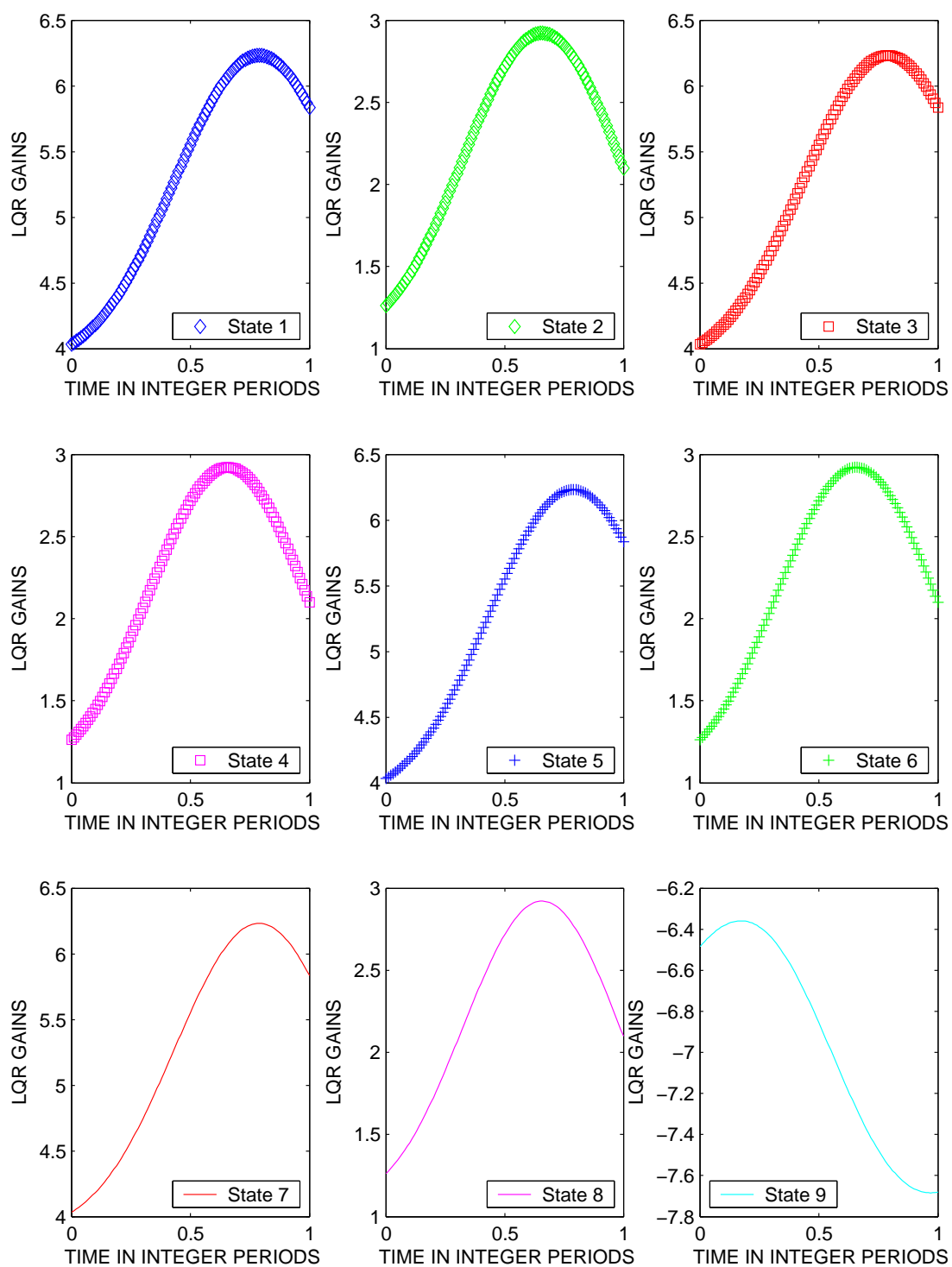


Figure F.22: All LQR Gains for case  $\omega_f = 0.05\omega_p$ ,  $S_v = 4$

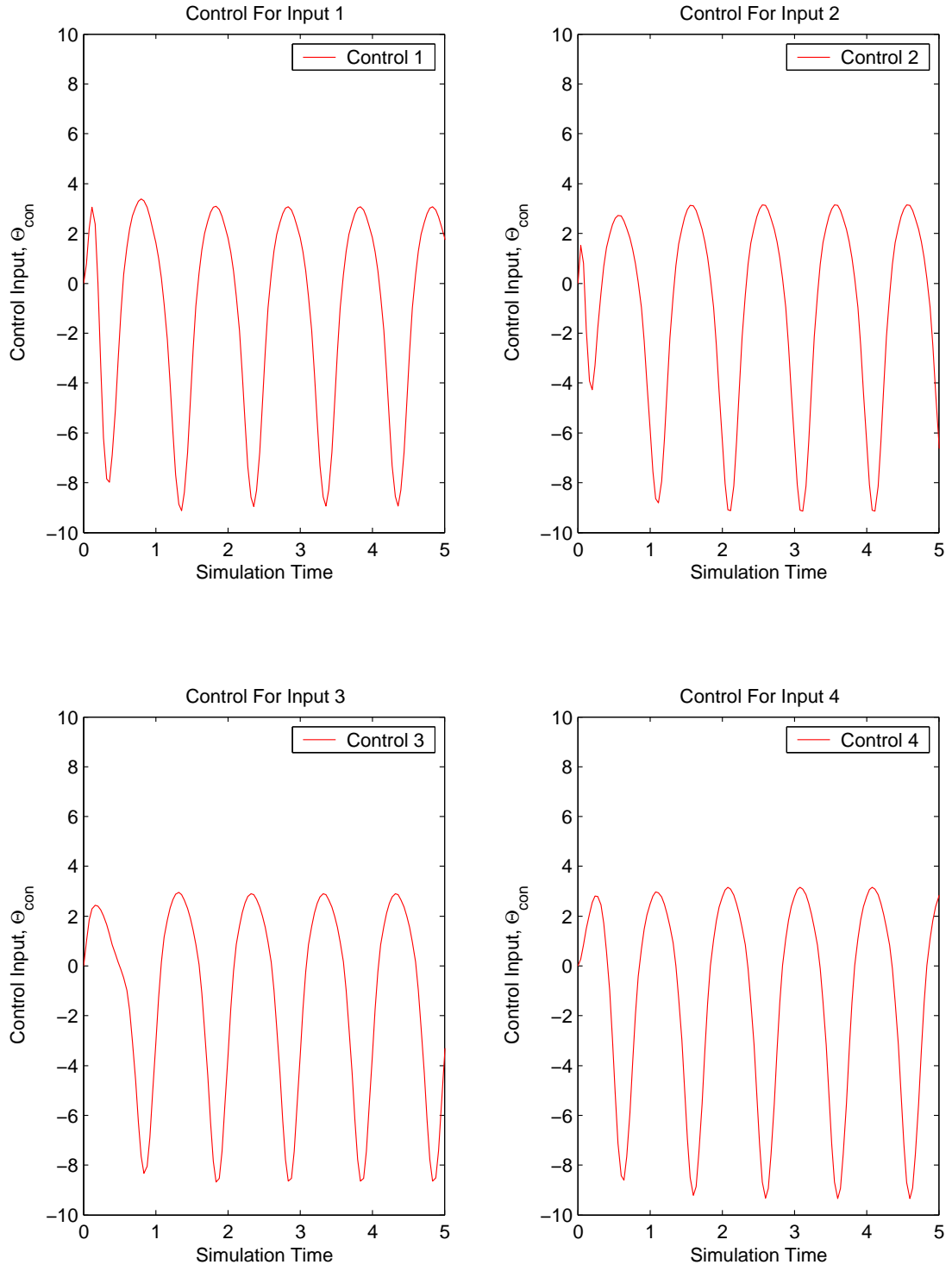


Figure F.23: Control Usage for case  $\omega_f = 0.05\omega_p$ ,  $S_v = 4$

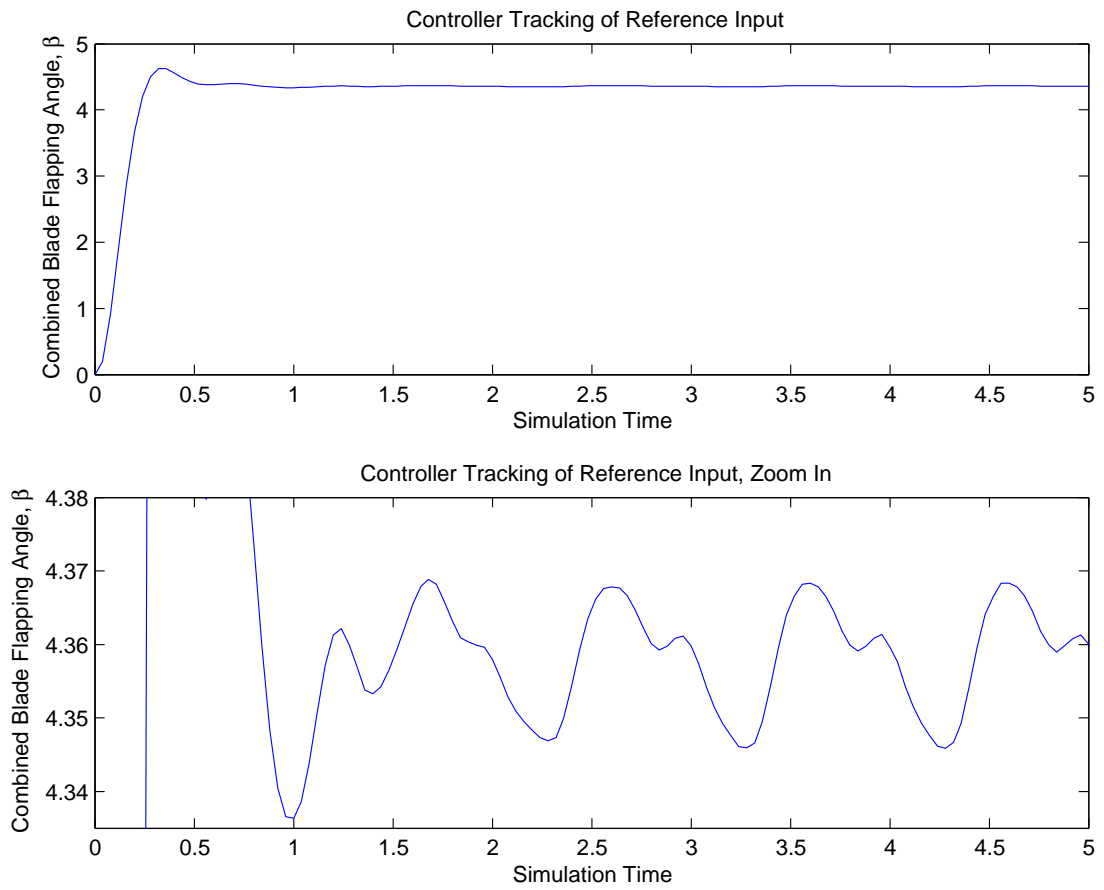


Figure F.24: Tracking Performance of Vibration Controller for case  $\omega_f = 0.05\omega_p$ ,  $S_v = 4$

Case 7	
Controller Design Parameters	
Input Frequency, $\omega_f$	Noise spectral density, $S_v$
$\omega_f = .0\omega_p$	$S_v = 4$

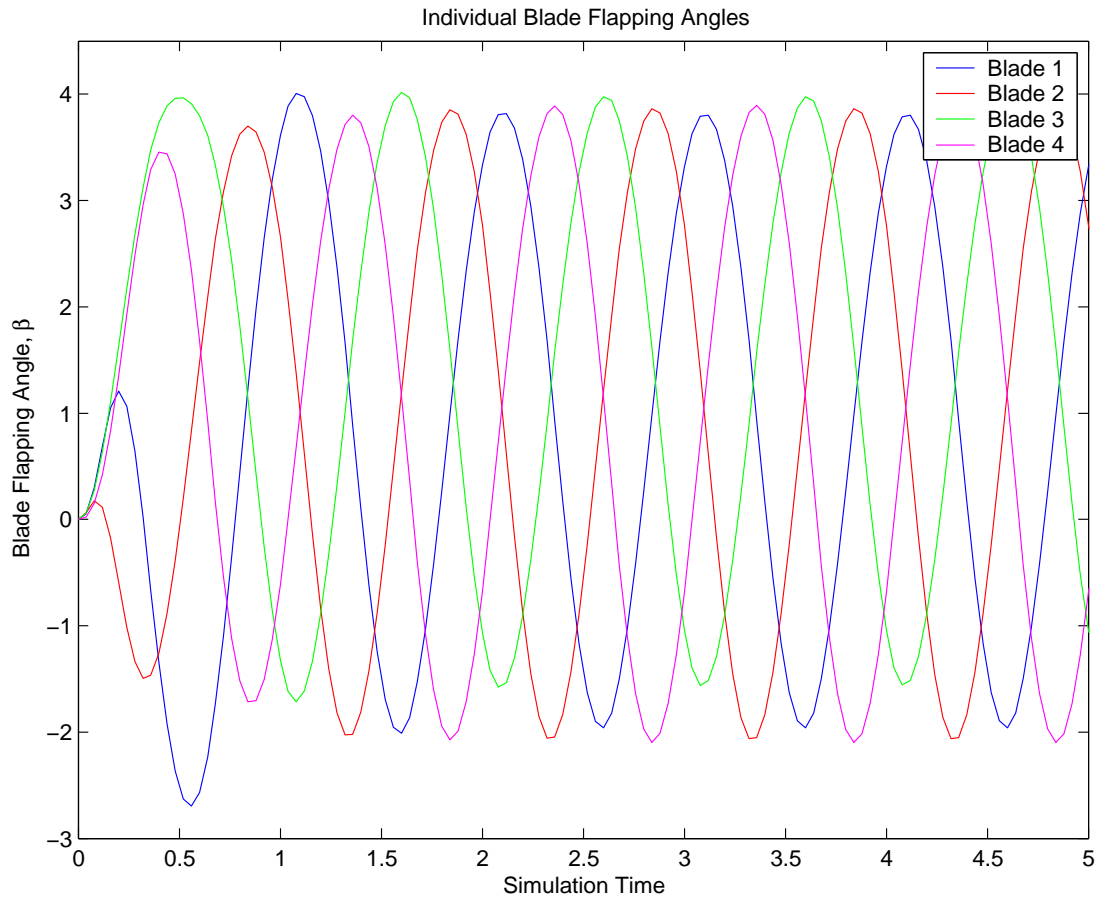


Figure F.25: Individual Flap Angles,  $\beta$ , for case  $\omega_f = 0.0\omega_p$ ,  $S_v = 4$

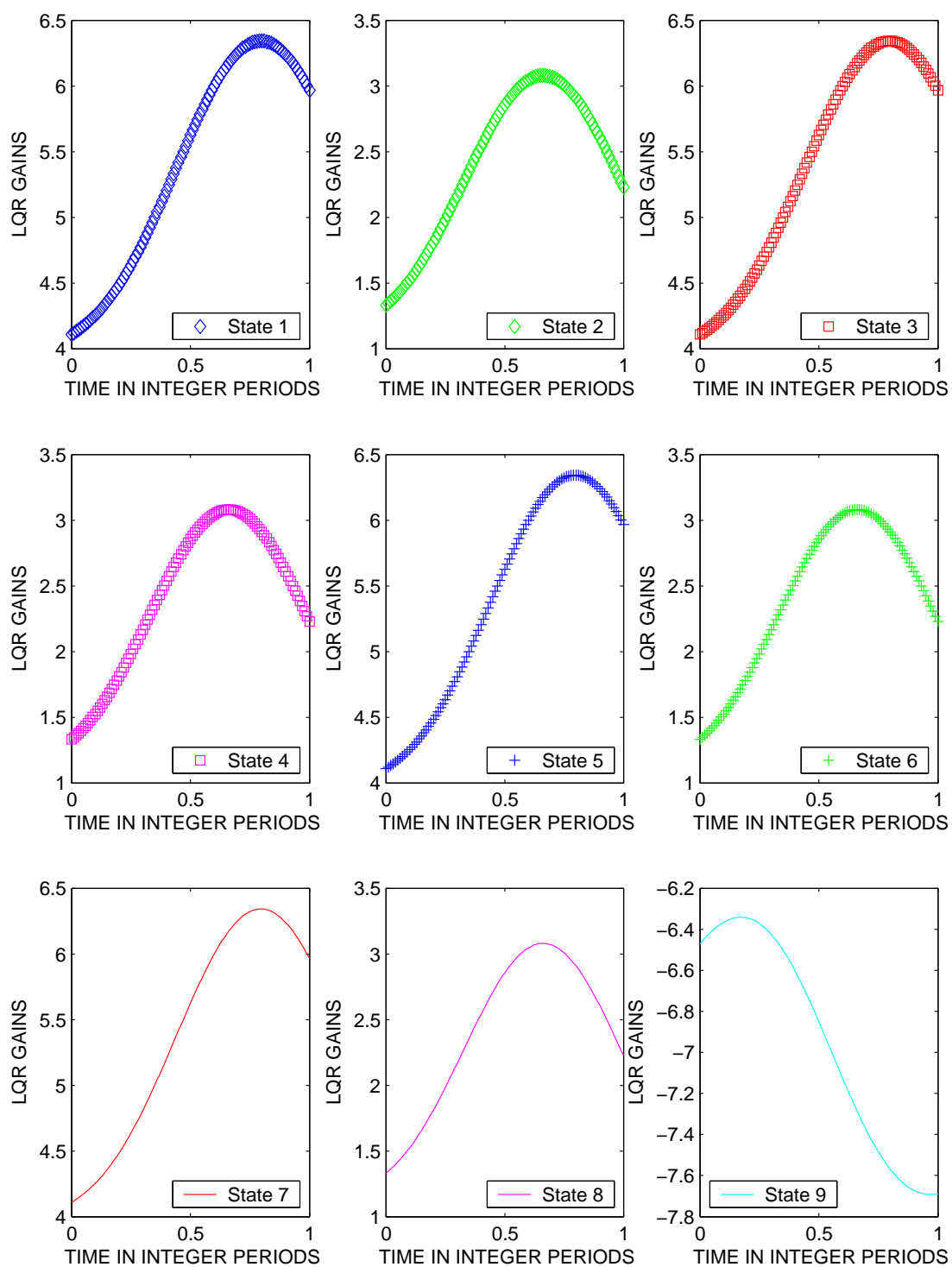


Figure F.26: All LQR Gains for case  $\omega_f = 0.0\omega_p$ ,  $S_v = 4$

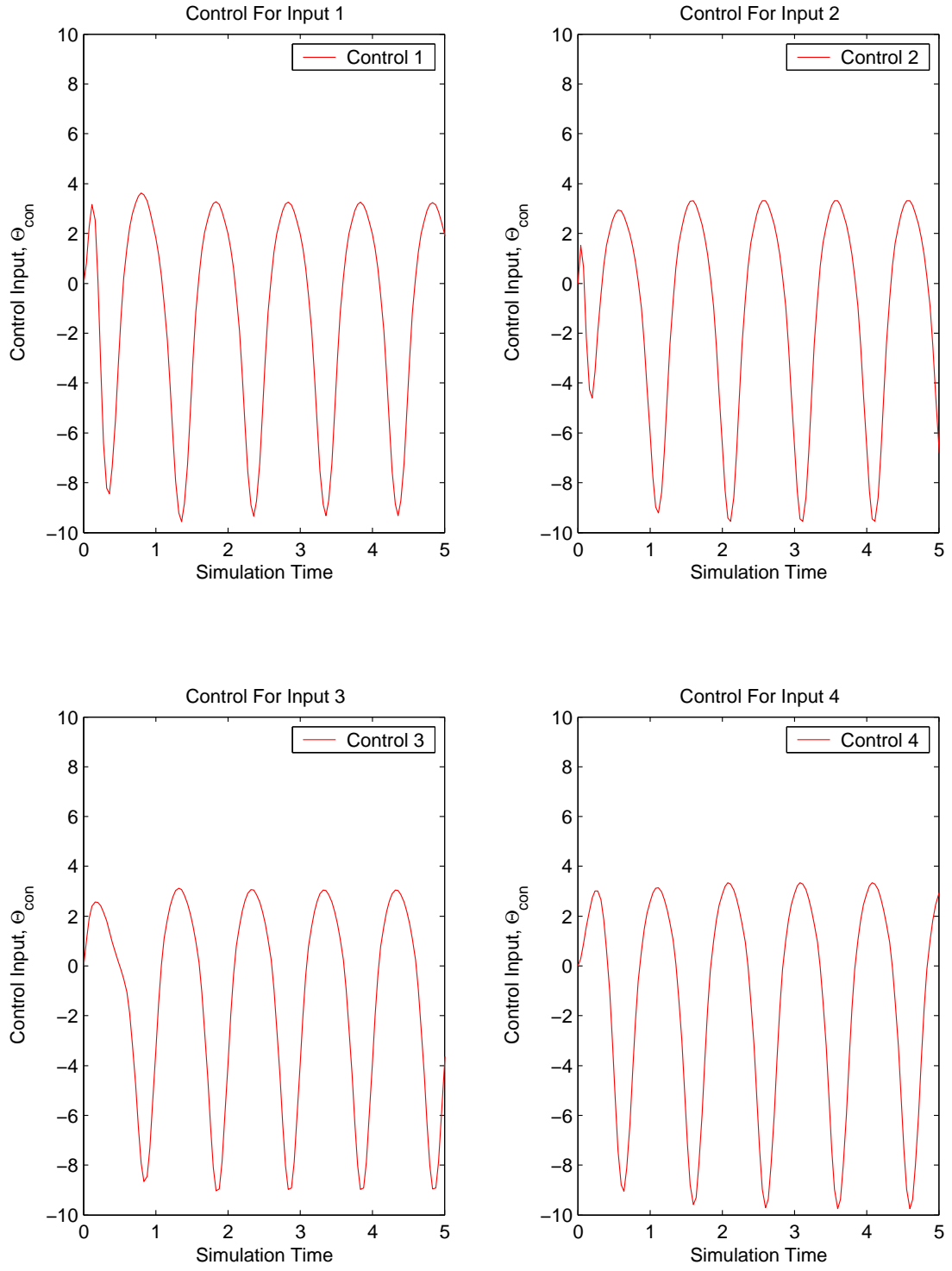


Figure F.27: Control Usage for case  $\omega_f = 0.0\omega_p$ ,  $S_v = 4$

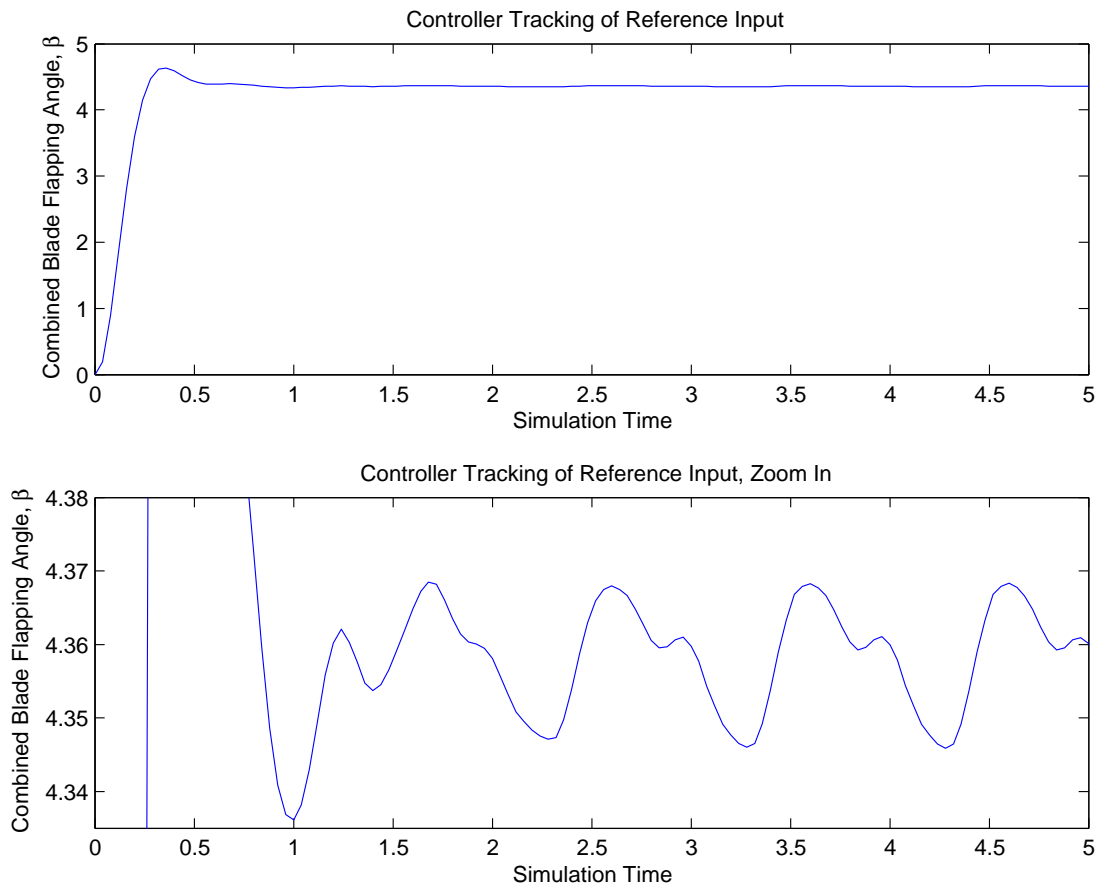


Figure F.28: Tracking Performance of Vibration Controller for case  $\omega_f = 0.0\omega_p$ ,  $S_v = 4$

*Appendix G. Cramer-Rao Bound Relationship to Maximum Control  
Requirements*

This appendix holds all of the plots generated by comparing the Cramer-Rao bound to the maximum negative control deflection for the range of input frequencies  $\omega_f = \omega_p(0, 0.05, 0.1, 0.2, 0.3, 0.4, 0.5)$ . Eight plots are presented to depict the maximum negative control deflection for each blade. Two plots are presented per blade, one for the noise case of  $S_v$  and the other for the case of  $S_v = 1, 2, 3, 4$ .

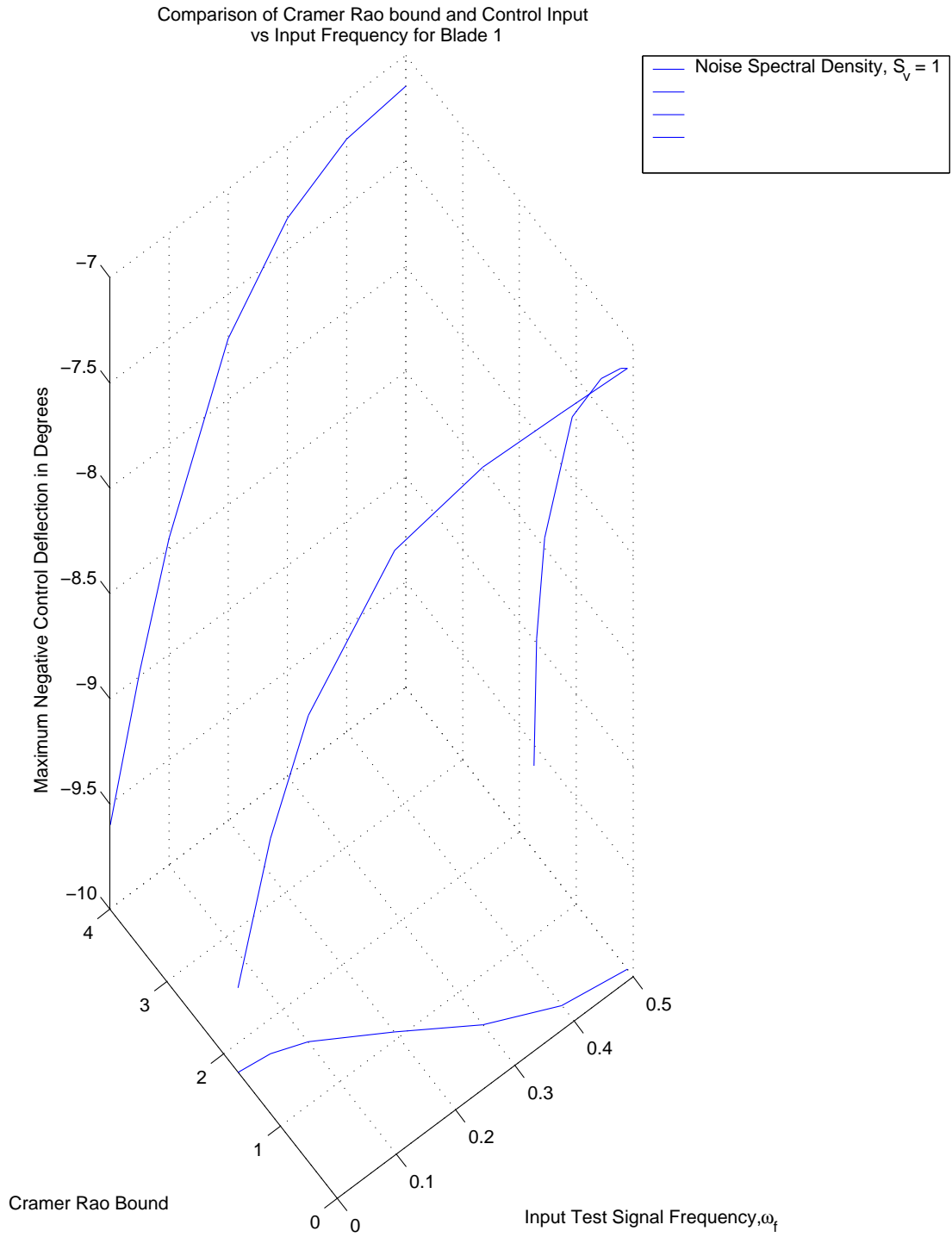


Figure G.1: Comparison of Cramer-Rao Bound to Maximum Negative Control Deflection For Blade 1:  $\omega_f = \omega_p(0, 0.05, 0.1, 0.2, 0.3, 0.4, 0.5)$ ,  $S_v = 1$

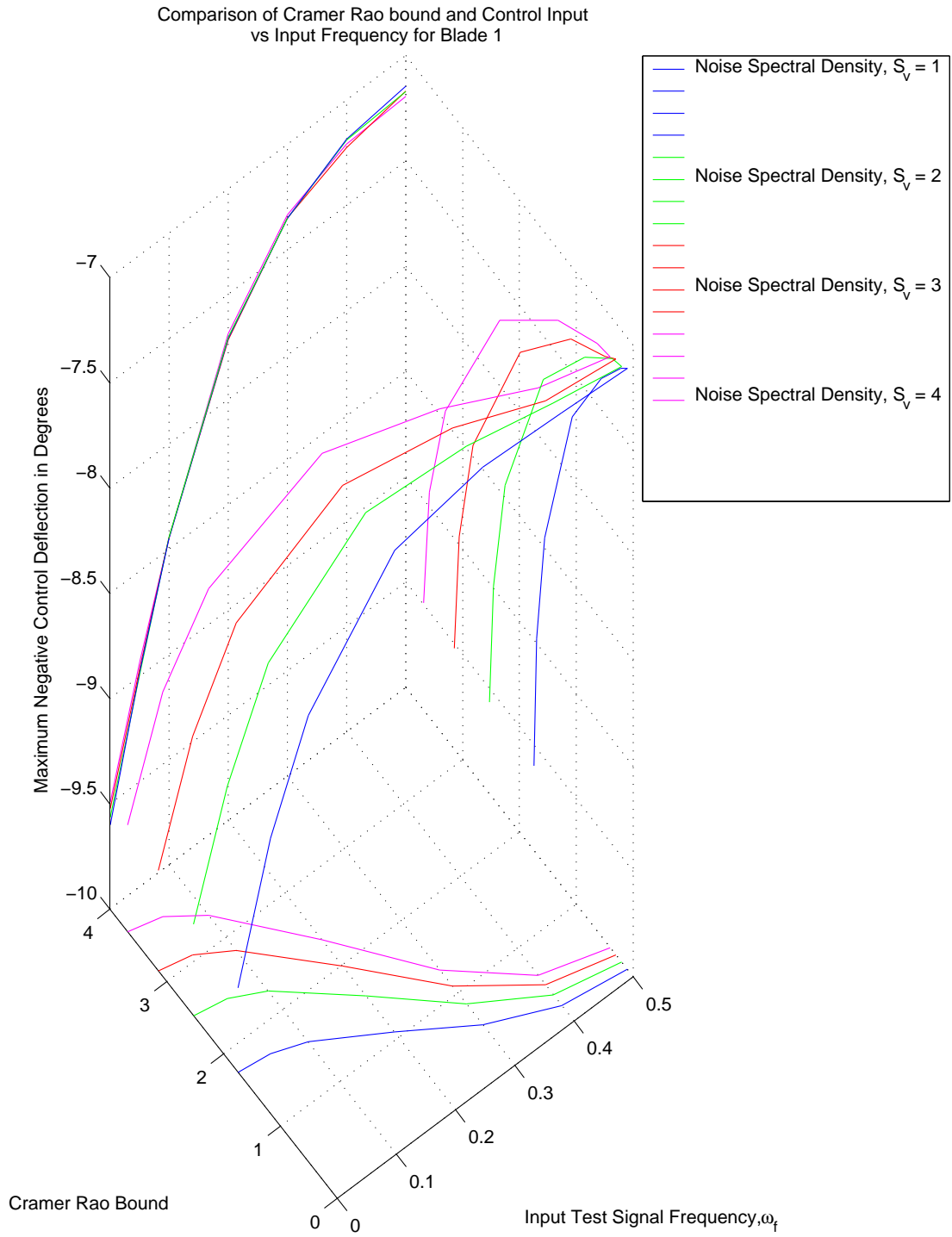


Figure G.2: Comparison of Cramer-Rao Bound to Maximum Negative Control Deflection For Blade 1:  $\omega_f = \omega_p(0, 0.05, 0.1, 0.2, 0.3, 0.4, 0.5)$ ,  $S_v = 1, 2, 3, 4$

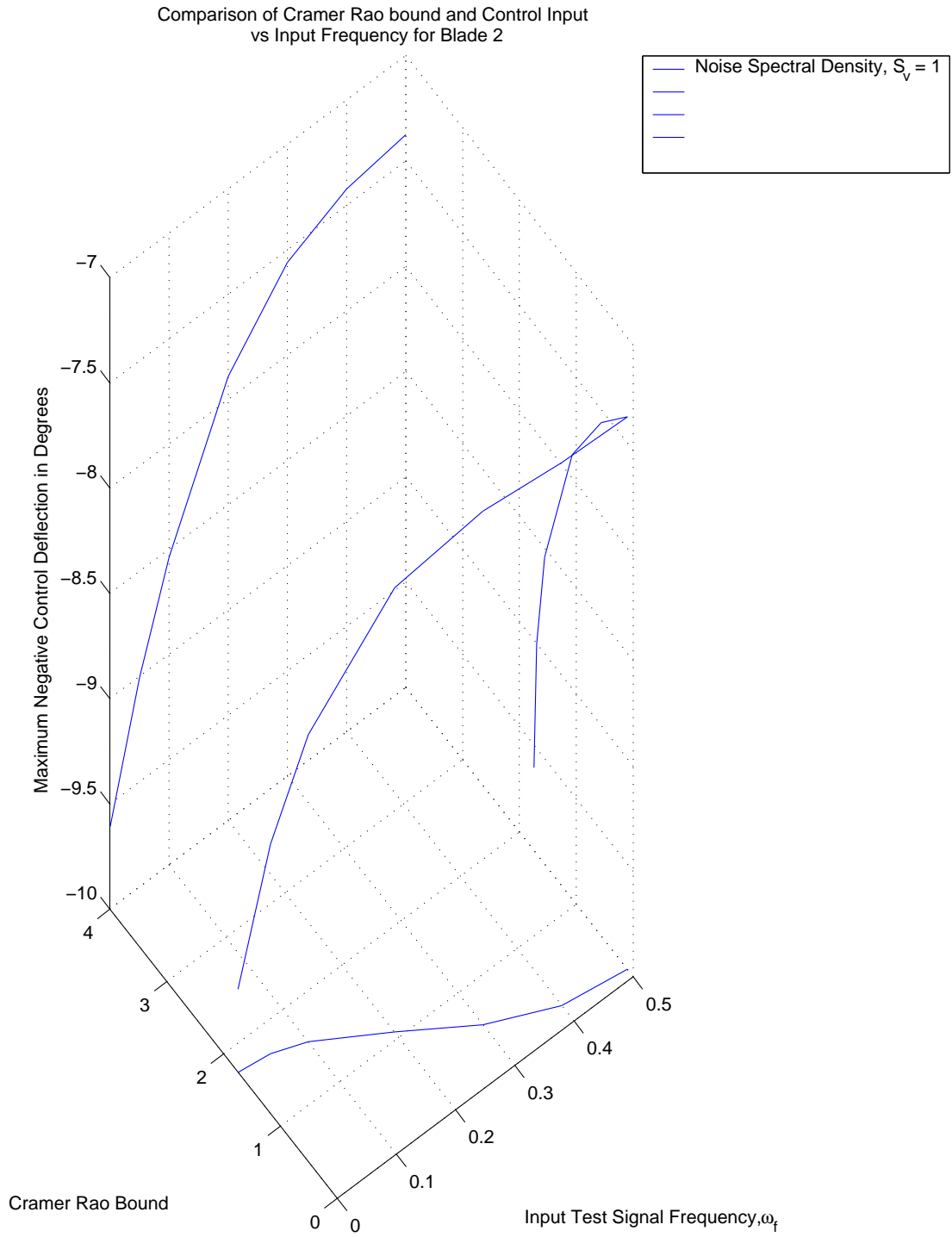


Figure G.3: Comparison of Cramer-Rao Bound to Maximum Negative Control Deflection For Blade 2:  $\omega_f = \omega_p(0, 0.05, 0.1, 0.2, 0.3, 0.4, 0.5)$ ,  $S_v = 1$

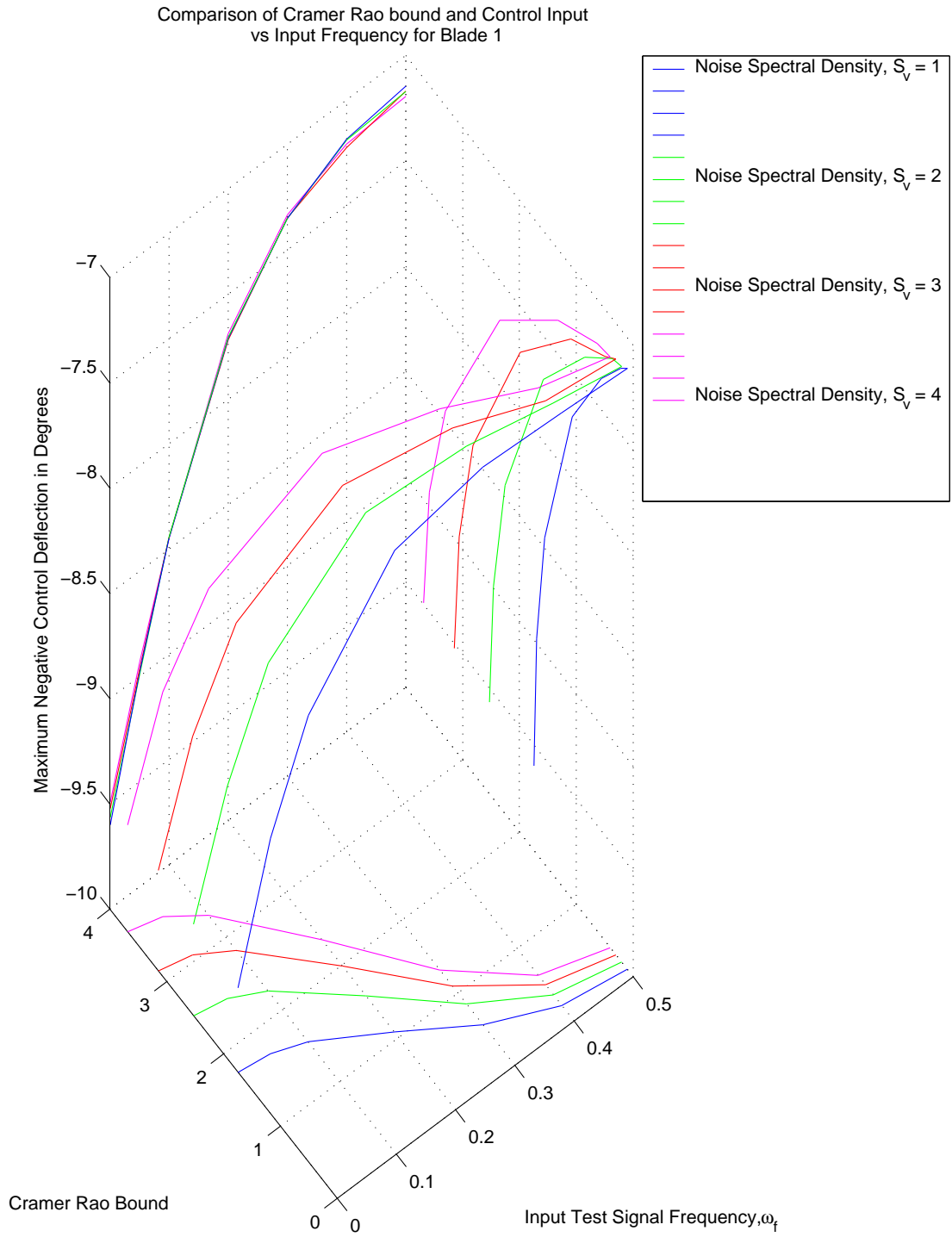


Figure G.4: Comparison of Cramer-Rao Bound to Maximum Negative Control Deflection For Blade 2:  $\omega_f = \omega_p(0, 0.05, 0.1, 0.2, 0.3, 0.4, 0.5)$ ,  $S_v = 1, 2, 3, 4$

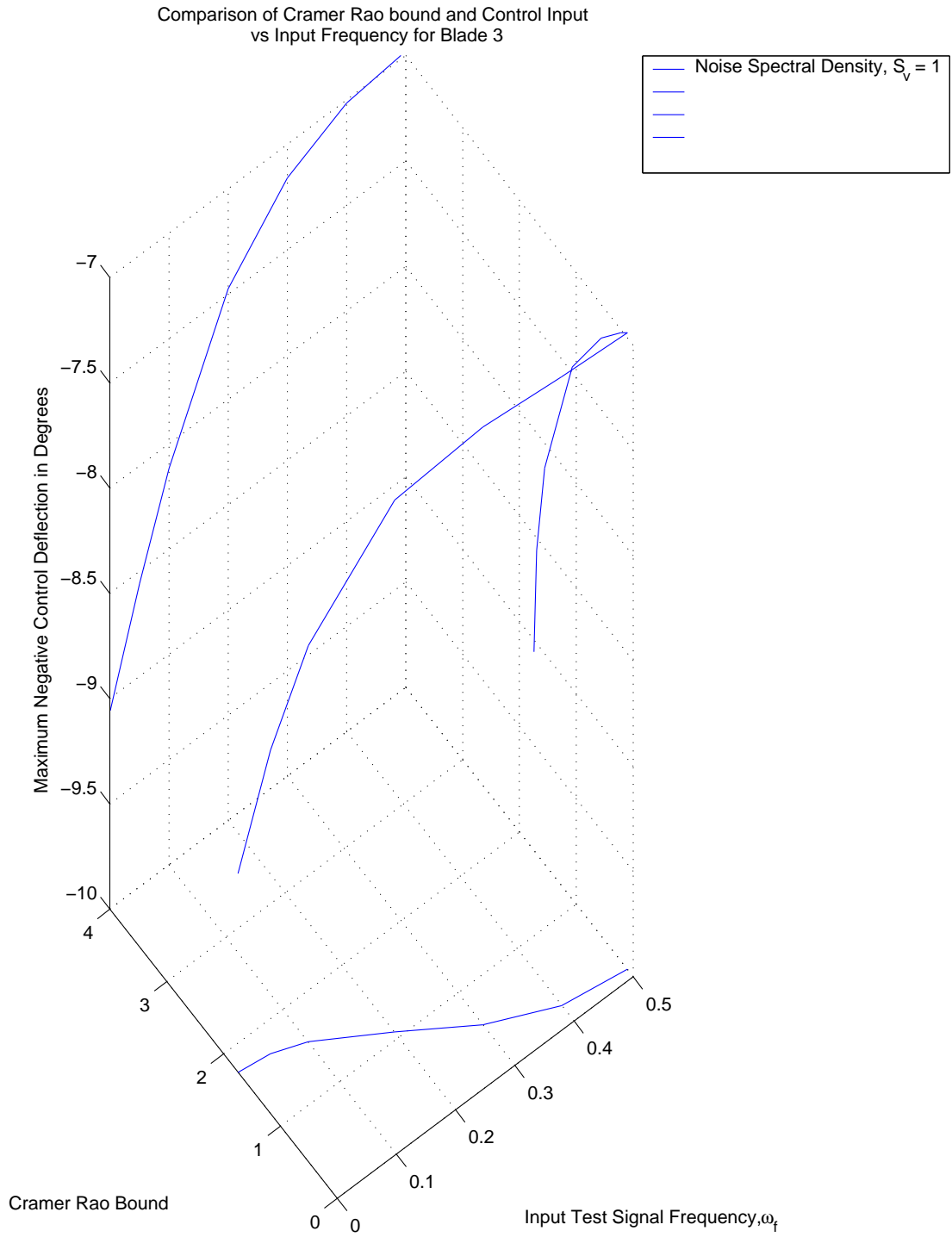


Figure G.5: Comparison of Cramer-Rao Bound to Maximum Negative Control Deflection For Blade 3:  $\omega_f = \omega_p(0, 0.05, 0.1, 0.2, 0.3, 0.4, 0.5)$ ,  $S_v = 1$

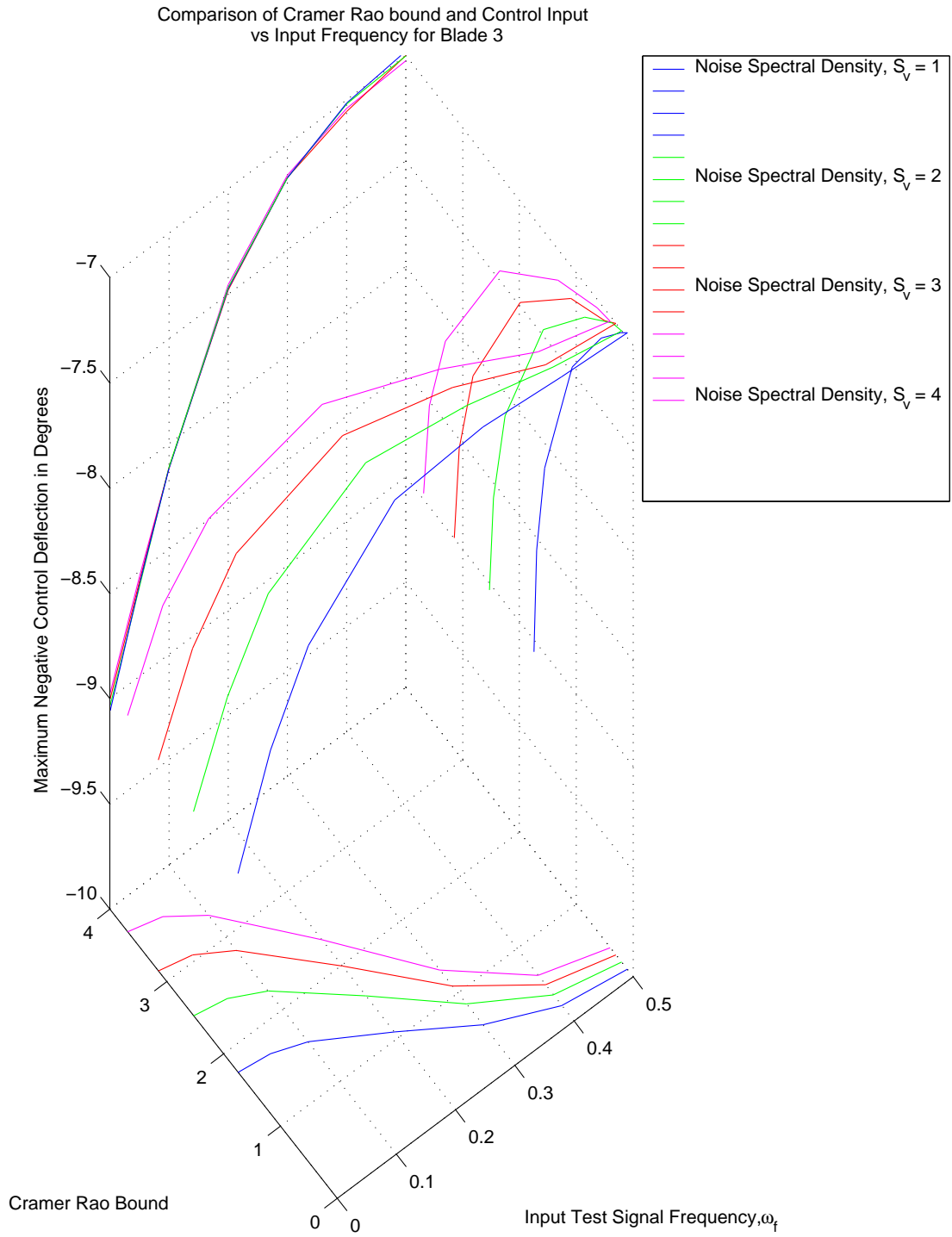


Figure G.6: Comparison of Cramer-Rao Bound to Maximum Negative Control Deflection For Blade 3:  $\omega_f = \omega_p(0, 0.05, 0.1, 0.2, 0.3, 0.4, 0.5)$ ,  $S_v = 1, 2, 3, 4$

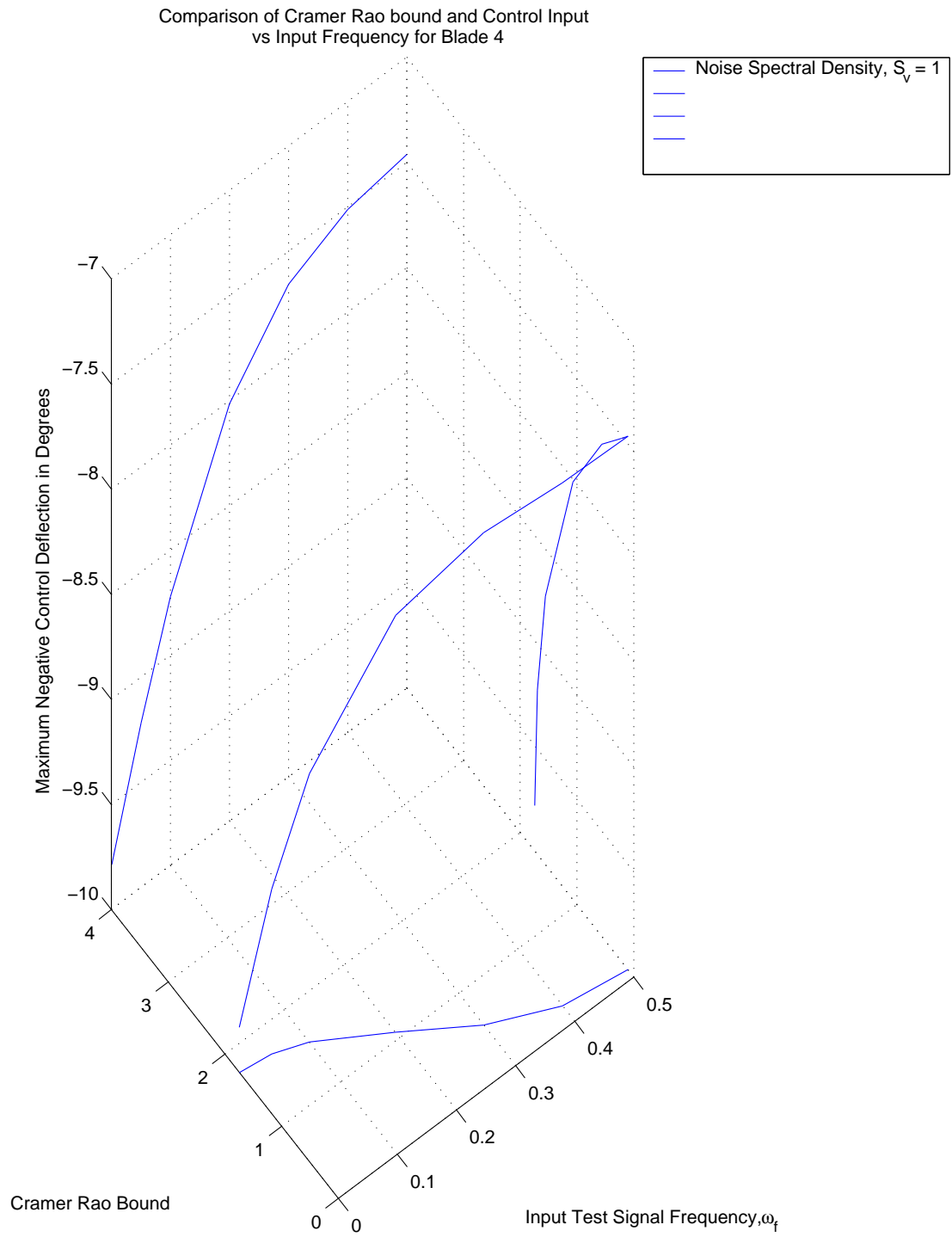


Figure G.7: Comparison of Cramer-Rao Bound to Maximum Negative Control Deflection For Blade 4:  $\omega_f = \omega_p(0, 0.05, 0.1, 0.2, 0.3, 0.4, 0.5)$ ,  $S_v = 1$

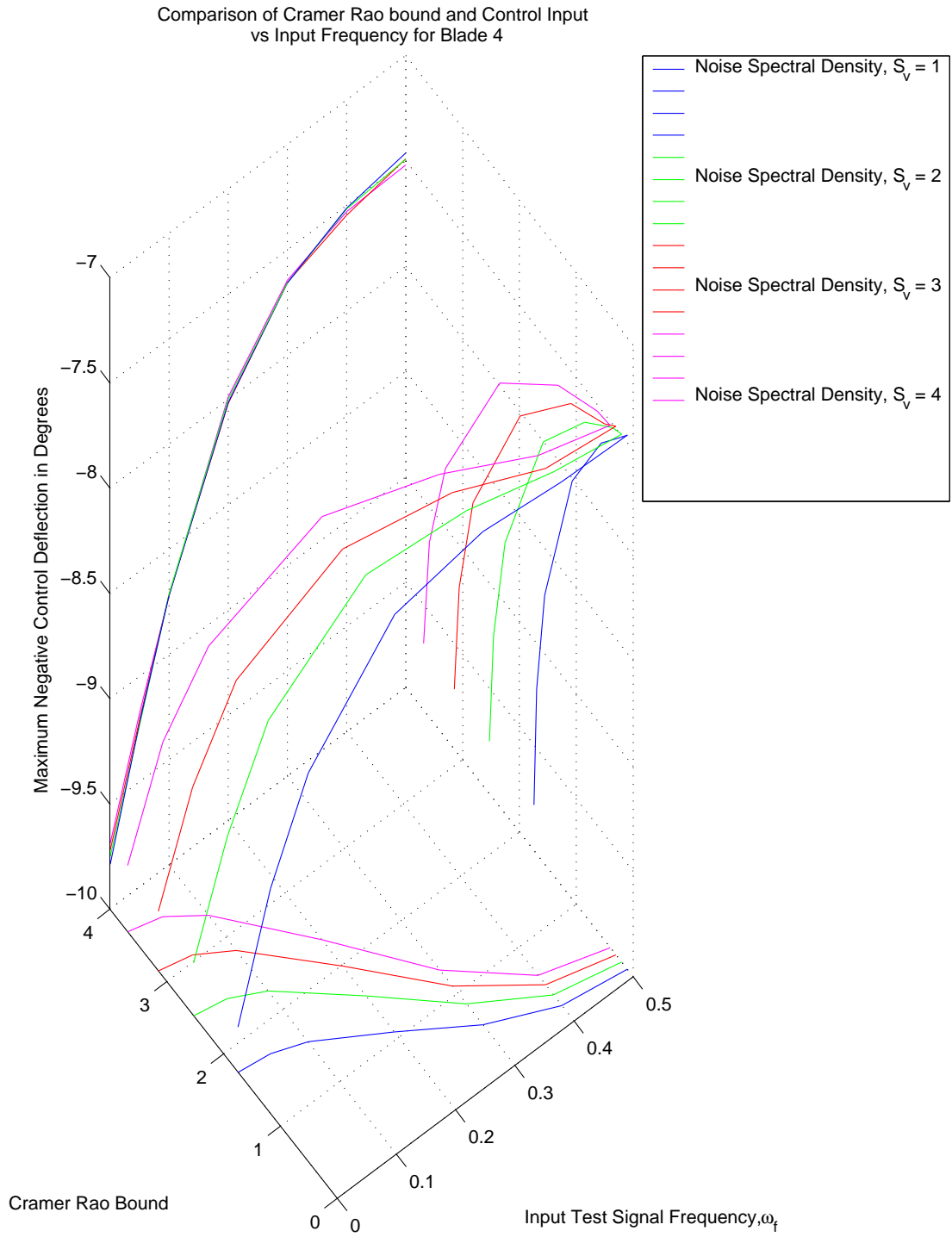


Figure G.8: Comparison of Cramer-Rao Bound to Maximum Negative Control Deflection For Blade 4:  $\omega_f = \omega_p(0, 0.05, 0.1, 0.2, 0.3, 0.4, 0.5)$ ,  $S_v = 1, 2, 3, 4$

## Bibliography

1. 6625-01-282-3746, NSN. *Operator's, Aviation Unit, and Intermediate Maintenance Manual Including Repair Parts and Special Tools List for Test Set, Aviation Vibration Analyzer (AVA)*. US Government, Washington, DC, pn 29313107 edition, 2002.
2. Burl, Jeff B. *Linear Optimal Control:  $H_2$  and  $H_\infty$  methods*. Addison Wesley, Menlo Park, first edition, 1998.
3. C. Jones, R. Celi. "Determination of Helicopter Rotor Damping From Simulated Data Using Frequency Domain System Identification". *Structures, Structural Dynamics and Materials Conference*. New Orleans, LA, 1995. Pp. 669-679.
4. Corporation, Align. *Trex 450XL Instruction Manual*. Align Corporation, www.align.com.tw, v1 edition, 2005.
5. D. Wroblewski, P. Berry, P. Grabill. "Neural Network System for Helicopter Rotor Smoothing". *IEEE Aerospace Conference Proceedings*. Big Sky, Montana, March 2000.
6. D. Wroblewski, T. Cook, R. Branhof. "Neural Networks for Smoothing of Helicopter Rotors". *American Helicopter Society 57<sup>th</sup> Annual Forum*. Washington, DC, May 2001.
7. Dieterich, O. "Application of Modern Control Technology for Advanced IBC Systems". *Proceedings of the 24<sup>th</sup> European Rotorcraft Forum*. Verneuil sur Seine, France, 1998. Pp. AS03.1-AS03.21.
8. Eric Bechhoefer, Dennis Power. "IMD HUMS Rotor Track and Balance". IEEE, October 2002.
9. Gelb, Arthur. *Applied Optimal Estimation*. The Analytical Sciences Corporation, Chantilly, Virginia, sixteenth edition, 1974.
10. George Casella, Roger L. Berger. *Statistical inference*. Duxbury, Pacific Grove, California, second edition, 2001.
11. Hill, G. "On the part of the lunar perigee which is a function of the mean motions of the sun and the moon". *Acta Mathematica*. 8:1-36 1886.
12. Hwang, Sunghwan. *Frequency Domain System Identification of Helicopter Rotor Dynamics Incorporating Models With Time Periodic Coefficient*. Phd thesis, University of Maryland at College Park, 1997.
13. J. Cooley, S. Tukey. "An Algorithm for the Machine Calculation of Complex Fourier Series". *Math. Compute.*, volume 19. 1965. Pp. 297-301.

14. Johnson, Lloyd. "Gary's Combat Aircraft Reference Guide". Internet Web Page, September 2001. Available at <http://www.inetres.com/gp/military/ar/rotor/AH-64.html>.
15. Johnson, Lloyd. "HISTORY: Helicopter Rotor Smoothing". DSS Micro Homepage, June 2005. Available at <http://www.dssmicro.com/theory/dsrothst.htm>.
16. Johnson, Wayne. *Helicopter Theory*. Dover, New York, dover eddition edition, 1994.
17. Juang, Jer-Nan. *Applied System Identification*. Prentice Hall, Englewood Cliffs, New Jersey, 1st edition, 1994.
18. Kunz, Donald L., Michael J. McNulty, Jeffrey L. Sorensen, and Kelly McCauley. "Effects of Age and Use on Apache Main Rotor Support Characteristics". *Proceedings of the AIAA/ASME/ASCE/AHS/ACS 36th Structures, Structural Dynamics, and Materials Conference*, AIAA Paper No. 95-1229. New Orleans, Louisiana, April 1995.
19. Mannchen, T. and K. Well. "Helicopter Vibration Reduction and Damping Enhancement Using Individual Blade Control". *Journal of Guidance, Control, and Dynamics*, 27(5), 2004. Pp. 760-766.
20. Mannchen, Thomas. *Helicopter Vibration Reduction Using Robust Control*. Phd thesis, Institut für Flugmechanik und Flugregelung, Universität Stuttgart, October 2003.
21. Martin T. Hagan, Mark Beale, Howard D. Demuth. *Neural Network Design*. International Thomson Publishing, New York, 1st edition, 1996.
22. Meirovitch, Leonard. *Fundamentals of Vibrations*. Mcgraw-Hill, New York, first edition, 1999.
23. Miller, Nathan A. *An Assessment of Modern Methods for Rotor Track and Balance*. Masters thesis, Graduate School of Engineering, Air Force Institute of Technology (AETC), Wright-Patterson AFB OH, April 2006. AFIT/GAE/ENY/06-M24.
24. Miller, Nathan A. and Donald L. Kunz. "A Comparison of Main Rotor Smoothing Adjustments Using Linear and Neural Network Algorithms". *Proceedings of the 62nd Annual Forum of the American Helicopter Society*, 1317-1322. Phoenix, Arizona, may 2006.
25. Nice, Norman S. *Control Systems Engineering*. Benjamin/Cummings, Redwood City, California, second edition, 1997.
26. Ogata, Katsuhiko. *Modern Control Engineering*. Prentice Hall, New Jersey, third edition, 1997.
27. P. Arcara, S. Bittanti and M. Lovera. "Active Control of Helicopter Rotors for Attenuation of Vibration in Forward Flight". *IEEE Transactions on Control Systems Technology*, 8(6), 2000. Pp. 883-894.

28. P. Grambill, L. Grant, J. Berry. "The US Army and National Guard Vibration Management Enhancement Program (VMEP): Data Analysis and Statistical Results". *American Helicopter Society 58<sup>th</sup> Annual Forum*. Montreal, Canada, June 2002.
29. P. Grambill, L. Grant, J. Berry. "Rotor Smoothing and Vibration Monitoring Results for the US Army VMEP". *American Helicopter Society 59<sup>th</sup> Annual Forum*. Phoenix, AZ, May 2003.
30. P. Grambill, R. Branhof, J. Berry. "Automated Helicopter Vibration Diagnostics for the US Army and National Guard". *American Helicopter Society 57<sup>th</sup> Annual Forum*. Washington, D.C., May 2001.
31. Raymond G. Kvaternik, Richard L. Bennett, Jer-Nan Juang. *Exploratory Studies in Generalized Predictive Control for Active Aeroelastic Control of Tiltrotor Aircraft*. National Aeronautics and Space Administration, Langley Research Center, Hampton, Virginia, 1st edition, 2000. NASA TM-2000-210552.
32. Reid, Gary J. *Linear System Fundamentals*. McGraw-Hill, New York, first edition, 1983.
33. Rensi, Michael J. *An Assessment of Modern Methods for Rotor Track and Balance*. Masters thesis, Graduate School of Engineering, Air Force Institute of Technology (AETC), Wright-Patterson AFB OH, April 2004. AFIT/GAE/ENY/04-J11.
34. Richard E Maine, Kenneth W. Iliff. *The Theory and Practice of Estimating the Accuracy of Dynamic Flight-Determined Coefficients*. National Aeronautics and Space Administration, Dryden Flight Research Center, Edwards, California, 1st edition, 1981.
35. Robinson, Mike. "Helicopter Track and Balance Theory". *Aircraft Maintenance Technology*, February, 1999.
36. S. Bittanti, F. Loritto and S. Strade. "An LQ Approach to Active Control of Vibration in Helicopters". *Journal of Dynamic Systems, Measurement, and Control*, 118, 1996. Pp. 482-488.
37. S. Webb, W. Wiesel, R. Calico. "Time-Periodic Control of a Multi-blade Helicopter". *Journal of Guidance*, 14, 1991. Pp. 1301-1308.
38. Strang, Gilbert. *Linear Algebra and its Applications*. Harcourt, Orlando, third edition, 1988.
39. Taitel, Howard J., Kourosh Danai, and D. Gauthier. "Helicopter Track and Balance With Artificial Neural Nets". *ASME Journal of Dynamic Systems, Measurement, and Control*, 117(2):226–231, jun 1995.
40. M. de Terlizzi, P.P. Friedmann. "Active Control of Vibration due to BVI and Experimental Correlation". *Proceedings of the 25<sup>th</sup> European Rotorcraft Forum*. Rome, Italy, 1999. Pp. G6.1-G6.16.

41. W. Baker, P. Millington. “Design and Evaluation of a Learning Augmented Longitudinal Flight Control System”. *Proceedings of the 32nd IEEE Conference on Decision and Control*. San Antonio, Texas, December 1993.
42. Wereley, Norman M. *Analysis and Control of Linear Periodically Time Varying Systems*. Phd thesis, Massachusetts Institute of Technology, February 1991.
43. Wroblewski, Dariuz, Robert W. Branhof, and Timothy Cook. “Neural Networks for Smoothing of Helicopter Rotors”. *Proceedings of the 57th Annual Forum of the American Helicopter Society*, 1587–1594. Washington, DC, may 2001.

<b>REPORT DOCUMENTATION PAGE</b>					<i>Form Approved</i> <i>OMB No. 0704-0188</i>	
The public reporting burden for this collection of information is estimated to average 1 hour per response, including the time for reviewing instructions, searching existing data sources, gathering and maintaining the data needed, and completing and reviewing the collection of information. Send comments regarding this burden estimate or any other aspect of this collection of information, including suggestions for reducing this burden to Department of Defense, Washington Headquarters Services, Directorate for Information Operations and Reports (0704-0188), 1215 Jefferson Davis Highway, Suite 1204, Arlington, VA 22202-4302. Respondents should be aware that notwithstanding any other provision of law, no person shall be subject to any penalty for failing to comply with a collection of information if it does not display a currently valid OMB control number. <b>PLEASE DO NOT RETURN YOUR FORM TO THE ABOVE ADDRESS.</b>						
<b>1. REPORT DATE (DD-MM-YYYY)</b> 27-04-2006 - 19-07-2007		<b>2. REPORT TYPE</b> Dissertation		<b>3. DATES COVERED (From — To)</b> Apr 2006 - Jul 2007		
<b>4. TITLE AND SUBTITLE</b>  <div style="text-align: center; padding: 10px;">Rotorcraft Smoothing Via Linear Time Periodic Methods</div>				<b>5a. CONTRACT NUMBER</b>		
				<b>5b. GRANT NUMBER</b>		
				<b>5c. PROGRAM ELEMENT NUMBER</b>		
<b>6. AUTHOR(S)</b>  Christopher S. Schulz, Capt, USAF				<b>5d. PROJECT NUMBER</b>		
				<b>5e. TASK NUMBER</b>		
				<b>5f. WORK UNIT NUMBER</b>		
<b>7. PERFORMING ORGANIZATION NAME(S) AND ADDRESS(ES)</b> Air Force Institute of Technology Graduate School of Engineering and Management 2950 Hobson Way WPAFB OH 45433-7765				<b>8. PERFORMING ORGANIZATION REPORT NUMBER</b>  AFIT/DS/ENY/07-10		
<b>9. SPONSORING / MONITORING AGENCY NAME(S) AND ADDRESS(ES)</b> Dr. John D. Berry US Army Research, Development, and Engineering Command, Aviation Engineering Directorate USA RDECOM AMSRD-AMR-AE-A Redstone Arsenal, AL 35989-5000				<b>10. SPONSOR/MONITOR'S ACRONYM(S)</b>		
				<b>11. SPONSOR/MONITOR'S REPORT NUMBER(S)</b>		
<b>12. DISTRIBUTION / AVAILABILITY STATEMENT</b>  Approval for public release; distribution is unlimited.						
<b>13. SUPPLEMENTARY NOTES</b>						
<b>14. ABSTRACT</b>  This research presents the development of an on line linear time periodic rotor vibration controller. The Cramer-Rao bound is developed for a linear time periodic system in order to identify the quality of identified system parameters, which are used in system models for controller development. The methods developed in this work allow model parameters can be verified for accuracy and likewise adjusted to improve controller accuracy.						
<b>15. SUBJECT TERMS</b>						
<b>16. SECURITY CLASSIFICATION OF:</b>			<b>17. LIMITATION OF ABSTRACT</b>	<b>18. NUMBER OF PAGES</b>	<b>19a. NAME OF RESPONSIBLE PERSON</b>	
a. REPORT	b. ABSTRACT	c. THIS PAGE			Dr. Donald L. Kunz	
U	U	U	UU	312	<b>19b. TELEPHONE NUMBER (include area code)</b> (937) 255-3636, ext 4548	